RAMAN SPECTROSCOPY TO DISTINGUISH TONGUE CANCER FROM HEALTHY TISSUE

Froukje L. J. Cals

Raman Spectroscopy to Distinguish Tongue Cancer From Healthy Tissue

Froukje Leontine Joris Cals

Raman Spectroscopy to Distinguish Tongue Cancer From Healthy Tissue

ISBN/EAN: 978-94-028-0590-1

Cover illustrations: Raman spectroscopic mapping experiments
Comic illustrations: Arjen Schumacher and Froukje Cals

Lay-out: Legatron Electronic Publishing
Printing: IPSKAMP Printing

Raman Spectroscopy to Distinguish Tongue Cancer From Healthy Tissue

Het gebruik van Raman spectrosopie om tongkanker van gezond weefsel te onderscheiden

Academisch proefschrift

ter verkrijging van de graad van doctor aan de
Erasmus Universiteit Rotterdam
op gezag van de
rector magnificus
Prof.dr. H.A.P. Pols
en volgens besluit van het College voor Promoties.

De openbare verdediging zal plaatsvinden op

woensdag 3 mei 2017 om 11.30 uur

door
Froukje Leontine Joris Cals
geboren te Merselo

Erasmus University Rotterdam

Promotor:	Prof.dr. R.J. Baatenburg de Jong, MD
Leescommissie:	Prof.dr. A. van der Lugt, MD Prof.dr. F.J. van Kemenade, MD Prof.dr. G.M. van Dam, MD
Copromotoren:	Dr. S. Koljenović, MD Dr. Ir. G. J. Puppels

Slap van de lach hangen wonderen over tafel, niet eens helemaal uitgevouwen

Tom, bedankt!

CONTENTS

1

General introduction

HEAD AND NECK CANCER

Epidemiology

Cancer is a major public health problem, with an estimated lifetime risk of 9% until the age of 60, increasing to 50% by the age of 95.[1] Among adults, it has beaten diseases of the circulatory system to become the leading cause of death. In 2013, 30% of all deaths in the Netherlands were ascribed to invasive cancers.[2] Two percent of these cancers originated in the head and neck, giving this region a place in the top ten deadliest cancers.[2]

The head and neck region includes the oral cavity (comprising the lips, anterior two-thirds of the tongue, floor of the mouth, gingiva, buccal mucosa, retromolar trigone, and hard palate), salivary glands, paranasal sinuses, pharynx, and larynx. The oral cavity and pharynx share the top position in head and neck cancer incidence, both accounting for 29% of cases.[1] Most head and neck cancers (90%) originate in the epithelial surface and show squamous cell differentiation; therefore, they are called head and neck squamous cell carcinomas (HNSCCs). Although this thesis focuses on squamous cell carcinomas of the oral cavity, in particular the tongue, a brief general overview of the carcinogenesis of a HNSCC will be useful here.

Carcinogenesis and metastasis

Transformation from normal squamous epithelium to HNSCC is a multistep process characterized by several alterations that are, in the beginning, not visible to the naked eye neither under the microscope. The accumulation of genetic and epigenetic events that results in the activation of oncogenes and the inactivation of tumor suppressor genes leads to uncontrolled cell proliferation.[3] This cell proliferation subsequently results in visible morphological changes, like a disorganized orientation, size, shape, and layering of the epithelial cells. This is known as dysplasia.[4] The more severe the dysplasia becomes, the greater the likelihood of progression into HNSCC.[3] Unfortunately, despite continuous efforts to standardize classification criteria, the grading of dysplasia is quite subjective, with low intra- and inter-observer reproducibility.[5]

In general, uncontrolled cell proliferation is followed by cells' resistance to death (apoptosis), their limitless replicative potential, and the sustained formation of new blood vessels (angiogenesis). Subsequent degradation of the basement membrane and loss of cell-cell/matrix attachment proteins leads to the invasion and infiltration of neoplastic epithelial cells into the subepithelial tissue,[6] which features the development of an invasive HNSCC. The metastatic cascade is initiated through the acquisition of several additional capabilities, like changes in the physical coupling of cells to their microenvironment and activation of extracellular proteases.[7] In this cascade the neoplastic cells multiply further, detach from their neighboring cells, and invade the surrounding tissue. After penetrating the blood and lymphatic vessels (intravasation), the neoplastic cells survive in the circulation (life in transit) and become trapped in the capillary beds of distant organs (arrest). The subsequent exit from the circulation (extravasation) allows colonization, and a metastasis is formed.[6]

ORAL CAVITY SQUAMOUS CELL CARCINOMA

Epidemiology and etiology

In the Netherlands, nearly 3000 invasive HNSCCs were diagnosed in 2015, of which 888 were located in the oral cavity. With 359 cases (40%), the tongue was the most common subsite.[2]

An oral cavity squamous cell carcinoma (OCSCC) occurs predominantly in alcohol- and tobacco-using adults (men > women), in their fifth and sixth decades of life.[8,9] Other identified risk factors are race, betel quid (paan) chewing, radiation, immune deficiencies, and prior upper aerodigestive tract cancer.[10,11] There has been ongoing debate regarding the influence of poor oral hygiene, chronic irritation, Human Papilloma Virus type 16 and 18, and diet, particularly the diets that are fat rich, low in fibers and lack antioxidants.[11,12]

Diagnosis and classification

Small-sized OCSCCs are mostly asymptomatic, while non-healing mucosal ulcerations, discomfort, referred ear pain, halitosis, hemoptysis, limited mobility of the tongue, weight loss, and neck swelling occur with more extensive tumors.[13] Optimal treatment of a patient with an OCSCC of the tongue depends on an accurate diagnosis. In the first place, physical examination including visual inspection and palpation are combined with imaging modalities such as magnetic resonance imaging (MRI) or computed tomography.[13] Subsequently, histopathological confirmation of the diagnosis is performed.

In the internationally accepted TNM classification, the size and extent of a histopathologically proven tumor (T1 – T4) is combined with the presence of nodal (N0 – N3) and distant metastases (M0 – M1).[14,15] The nodal status is defined using imaging techniques, such as MRI, computed tomography and ultrasound guided fine needle aspiration cytology.[13,16] The presence of distant metastasis is evaluated by either computed tomography of the thorax or positron emission tomography.[17] Considering that in 3% of cases simultaneous carcinomas occur in the upper aerodigestive tract,[18] a panendoscopy is often carried out to screen for them.

The TNM classification is a dual system that includes a clinical (pretreatment) classification, which is designated 'cTNM', and a final pathological (postoperative) classification, designated 'pTNM'.[15]

Treatment

Currently available treatment modalities for OCSCCs include surgery, radiotherapy, chemotherapy, targeted (bio) therapy, or a combination of these. The cTNM classification is, among other, used as a basis for the choice of treatment.[19,20] Other factors that influence choice of treatment are related to the characteristics of the primary tumor and the patient. Relevant tumor characteristics are: subsite, exact location, depth of invasion, proximity and invasion to bone, previous treatment and histology (differentiation grade). Patient factors include age, medical condition, tolerance, acceptance, compliance, lifestyle, and other socioeconomic considerations. Factors related to the treatment team will also be considered in treatment planning.

Intraoperative assessment of resection margins

The majority of OCSCCs of the tongue are treated with surgical excision.[20] The ultimate goal of surgical treatment is to eradicate the cancer and to preserve or restore form and function. Often, a 1 cm margin around the tumor is taken,[21] in order to obtain adequate microscopic resection margins. Adequate microscopic resection margins are defined as a distance of more than 5 mm between tumor border and resection surface, according to the guidelines of the Royal College of Pathologists.[22] Adequate resection margins are an important predictor for disease control and survival.[14,23-27] Survival improves with each additional millimeter of tumor-free tissue in the resection margins.[28] Nevertheless, literature shows that in current practice up to 85% of OCSCCs are inadequately resected (tumor-positive margins: less than or equal to 1 mm, or close margin: between 1 and 5 mm).[26,29]

As mentioned above, many imaging techniques are available preoperatively to help the surgeon plan the tumor resection. During the operation, the surgeon attempts to define the borders of the tumor by visual inspection and tissue palpation. Additionally, a frozen section procedure can be used for intraoperative histopathological examination of suspicious regions in the resection surface (Figure 1A – E).[30] Although state-of-the-art, this procedure has major limitations. The diagnostic accuracy of the frozen section method depends on how well the tissue samples from the suspected inadequate margin represents the complete resection margin.[24,27,31] Often the samples are taken from the epithelial margins, because these are more accessible and the tissue is relatively compact. However, up to 87% of all tumor-positive margins in the oral cavity tumor resections are located in the subepithelial tissue,[32] which makes sampling the epithelial margin of limited value. Moreover, due to the fact that the frozen section procedure is time-consuming and laborious,[33] only a small portion of the resection margin can be evaluated, inevitably leading to a sampling error. Despite these limitations, additional resections based on frozen sections can result in an increased rate of tumor-free margins[34] and thereby improve outcomes for many patients.[27,31,35]

Postoperative assessment

Based on the results of the final, histopathological (postoperative) examination of the resection specimen (pTNM) a decision is made for further treatment and a prognostic estimation can be made.[36] The resection specimen is pathologically evaluated to check whether the resection margins are adequate. Moreover, postoperative assessment also defines other histopathological parameters (tumor differentiation grade, invasion depth, presence of perineural and lymphovascular invasion, and extra nodal growth).[37] This routine histopathological procedure is based on thin sections from formalin-fixed and paraffin-embedded tissue, which are stained with haematoxylin and eosin (H&E).[38] If needed immunohistochemical-staining procedures are used to obtain additional information.[39]

The pTNM is the basis for decisions regarding the need for adjuvant therapy (postoperative radiotherapy and/or chemotherapy). Major criteria for postoperative radiotherapy include tumor-positive margins (less than or equal to 1 mm), lymph node metastases with extra nodal growth, or more than two lymph node metastases. The patient receives postoperative radiotherapy preferably within six weeks after surgery. In case of the following minor criteria postoperative radiotherapy is also recommended: pT3 – pT4 tumors (more than 4 cm in diameter and/or invading surrounding structures), perineural growth or close resection margins (between 1 and 5 mm).[40]

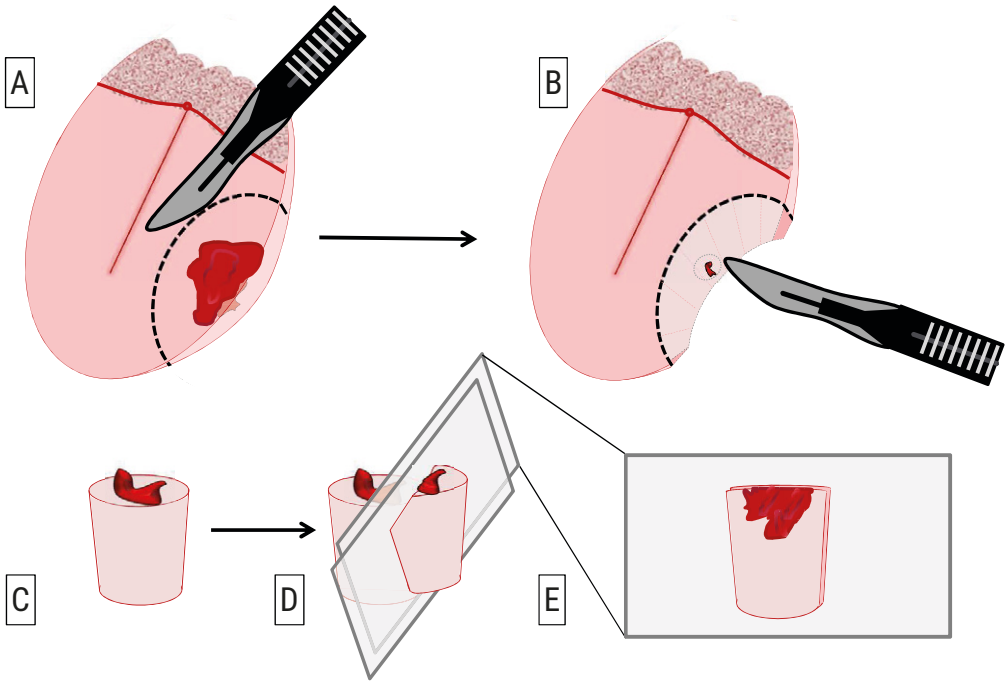

Figure 1. A: Schematic overview of a tongue with an OCSCC on its left edge. B: Sampling of a suspicious region in the wound bed. C: Tissue sample. D: Cutting a frozen tissue section from the sample. E: Frozen tissue section showing residual tumor.

Prognosis

The still increasing OCSCC incidence rates (especially in women in developed countries)[41,42] and the high disease-related mortality are reasons for concern. Recent decades have brought several advances in therapy, in the form of enhanced surgery, (postoperative) radiotherapy, chemotherapy, targeted (bio) therapy or a combination. However, still only half of the patients diagnosed with an OCSCC will survive the five years following diagnosis.[19,43-45]

This poor prognosis is mostly attributable to late diagnoses of primary and of recurrent tumors.[46,47] Large and extensive tumors are harder to excise with adequate resection margins and are associated with increased regional and distant metastases.[26,48] However, also early OCSCCs show high numbers of inadequate resection margins.[26] Of the many factors that may affect the clinical outcome (such as tumor site, pTNM classification, histopathological parameters, patient's age and comorbidity) only the resection margin can be controlled by the surgeon and pathologist.[26,49-51] Therefore, comprehensive intraoperative (histopathological) assessment can be of great value.

Although a gradually increasing number of publications is seen which emphasize the need for such comprehensive intraoperative assessment of the resection margins, this practice is not yet well adapted. One important prerequisite is the presence of a dedicated team of head and neck surgeons and pathologists.

ROOM FOR IMPROVEMENT

A technique for the intraoperative evaluation of all resection margins (especially in the subepithelial, soft tissue margins) might increase the number of adequate resections and thereby improve patient outcome. Optical imaging techniques are capable of characterizing tissues in real-time and can potentially fulfill this need.

OPTICS

Light

Optics describes the behavior and properties of light, and the interaction of light with matter. For optical imaging, nearly all types of electromagnetic radiation (EMR) can be used. The broad spectrum of EMR ranges from ionizing radiation (gamma rays and X-rays) through ultraviolet, visible light, infrared, microwaves, and radiofrequency waves.[52] Visible light is usually defined as having a wavelength in the range of 390 – 780 nm. When visible white light is dispersed through a prism it gets separated into different colors with shorter wavelengths and longer wavelengths (Figure 2).

In the 17th century, Isaac Newton was one of the first scientists to theorize that light is not only a wave phenomenon, but may also be interpreted as a stream of high-speed, submicroscopic particles, which we now call photons.[53] Subsequently it has been discovered that photons in a vacuum travel in harmonic waves at a constant speed (c), the speed of light, which is 299 792 458 ms^{-1}.[52] Light can interact with matter by absorption and by elastic and inelastic scattering.[52] The manner in which light interacts with matter depends on the nature of the molecules and atoms in the matter.

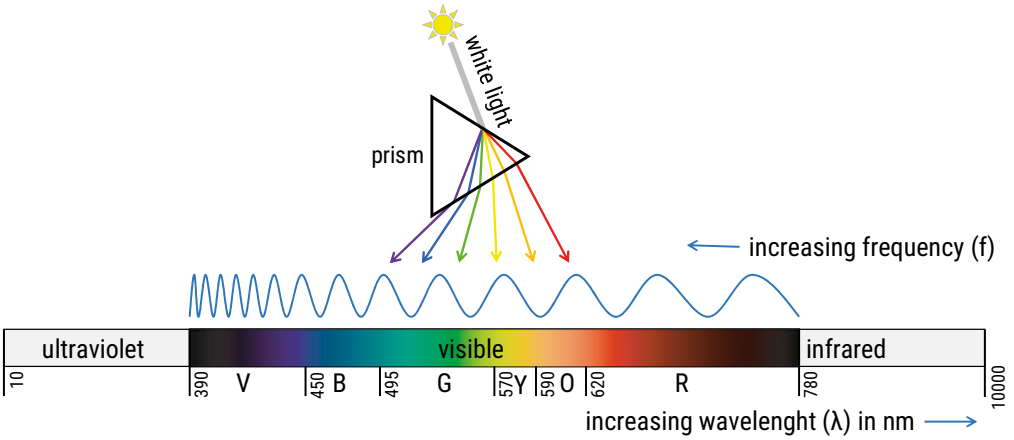

Figure 2. Part of electromagnetic radiation spectrum.

Absorption

Absorption is the simplest phenomenon that can occur when matter is illuminated by light. An atom is composed of a nucleus (protons and neutrons) and one or more electrons that are bound to this nucleus.[54] Atoms can attach to one or more other atoms by chemical bonds. At room temperature most electrons move around their nuclei in the lowest possible energy state, called the ground state. If an electron in the ground state is hit by a photon, the photon can be absorbed, transferring its energy and promoting the electron to a higher energy level, the excited state.[52] Electrons in an excited state will, over time, give off their obtained energy and return to their ground state. Most excited state energy resulting from absorption is converted into heat when the electron falls back to its ground state. However, in many atoms a portion of the stored energy can be re-emitted as light. When this happens immediately, this emission is known as fluorescence. When atoms gradually release their obtained energy to return to the ground state, it is called phosphorescence.[55]

Scattering

Scattering is, together with absorption, the second physical process that contributes to the visible appearance of matter.[55] The distribution of scattered light provides unique information about the illuminated atoms and molecules. Scattering can occur in two different ways (Figure 3).

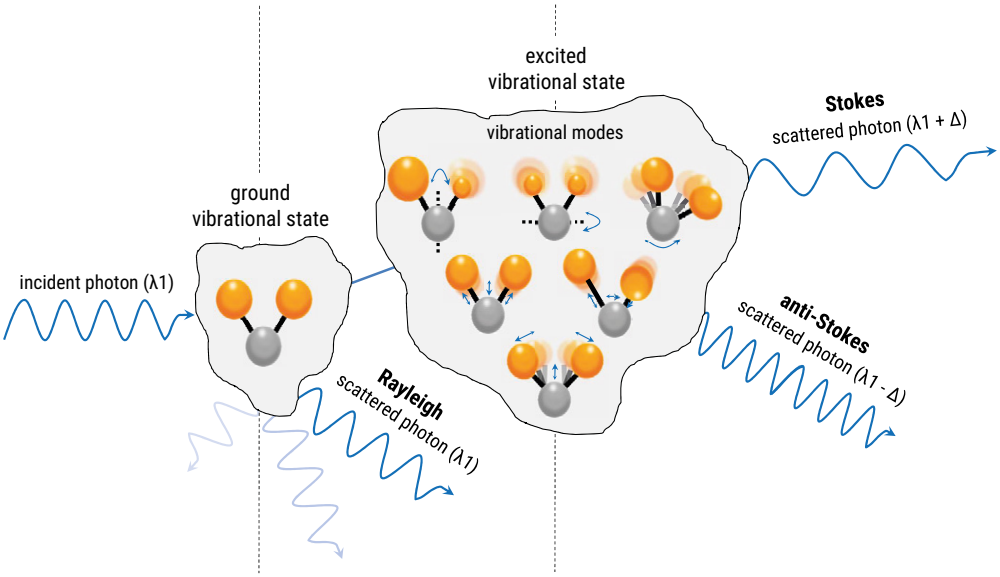

Figure 3. Schematic overview of the different scattering processes.

Elastic scattering

Elastic scattering of light occurs when no energy is transferred in the scattering event. On collision with matter, photons can be scattered in any direction without change of their energy (Figure 3).[52] The

frequency of the incident light is then the same as the scattered light's frequency. This type of scattering is called Rayleigh scattering after Lord Rayleigh, who was the first to correctly attribute scattering to tiny particles like atoms and molecules.[56]

Inelastic scattering

Only a fraction (1 in 10^6 to 1 in 10^8 photons) of incident photons undergo inelastic scattering.[57] In this so-called Raman scattering process, energy is tranferred from incident light to the illuminated molecules. This causes frequency shifts in the scattered light (Figure 3). These frequency shifts are predominantly caused by changes of the vibrational state of a molecule.

The exact photon energy needed to excite a molecular vibration is, among other things, determined by the mass and the strength of the chemical bonds of the atoms that are involved in the vibration.[57] Chemicals bonds can be regarded as stiff springs that can be stretched and bent. Vibrational modes are often given descriptive names, such as symmetric and asymmetric stretching, scissoring, rocking, wagging, and twisting (Figure 3). For instance, contrary to stretching, rocking, wagging, and twisting modes do not change the chemical bond lengths, but only their angles. Rocking is distinguished from wagging by the fact that, following it, the atoms remain in the same plane.

Molecules may have a great number of independent vibrational modes (3N-6 for a non-linear molecule consisting of N atoms).[58] The unique combination of vibrational levels means that the inelastic scattering of a molecule is highly molecule specific.

Stokes and anti-Stokes

Inelastic scattering can either cause a decrease or an increase of the energy of the scattered photon (Figure 3). The energy of a photon can be transferred to a molecule, which raises it to an excited vibrational state. This results in a decreased light frequency and increased wavelength. Vice versa, if the molecule transfers energy to the photon, the light frequency will increase and the scattered light will have a shorter wavelength than the incident light.[57] This latter way of scattering is only possible if the molecule is already in an excited vibrational state. This is rare at room temperature, since most molecules are then in their ground vibrational state.

These two types of inelastic scattering are known as Stokes (shifts to longer wavelengths) and anti-Stokes (shifts to shorter wavelengths) scattering.[57] At room temperature, anti-Stokes scattering causes a very weak signal compared to Stokes scattering. Therefore Stokes scattering is mostly used for analysis applications,[59] including the research described in this thesis.

RAMAN SPECTROSCOPY

Back to the beginning

The phenomenon of inelastic photon scattering is nowadays used as an optical characterization technique, known as Raman spectroscopy. In 1923 the phenomenon of Raman scattering was predicted on theoretical grounds by the Austrian physicist Adolf Gustav Smekal.[60] Experimental evidence for the effect

was first reported by the Indians Chandrasekhara Venkata Raman and Kariamanickam Srinivasa Krishna in 1928.[61] Sir C.V. Raman was later rewarded with the Nobel Prize in Physics in 1930. The complete story of achieving the Nobel Prize was published in 1998 by Singh et al.[62]

It took more than 60 years before Raman spectroscopy was applied in biosciences. Only after the invention of the laser in 1960,[63] it was possible to use incident light of a sufficient intensity to obtain a satisfactory Raman signal. Despite this innovation, several hours of signal collection were still needed to obtain a good quality Raman spectrum. The second major technological improvement essential for the practical use of Raman spectroscopy was the development of charge coupled device (CCD) in 1970,[64] which has been used as a detector in Raman spectroscopy since 1987.

Raman spectroscopy is very well suited for use in microscopic analysis. Since it is a scattering technique, tissue specimens do not need to be fixed or labelled, and can in principle be studied *in vivo*. The combination of Raman spectroscopy with a confocal microscope was first introduced by Puppels et al. in 1990.[65] Through the small confocal measurement volume, the collection of Raman spectra from inside cells was shown to be possible.

Instrumentation

The instrumentational requirements for Raman experiments are: 1) an excitation source, 2) focusing and collection optics, 3) a spectrometer, and 4) a personal computer (Figure 4).[58] The monochromatic light and excitation source currently most used is a laser. The lower the excitation wavelength of the laser, the stronger the Raman spectral intensities that can be obtained. However, when using an excitation wavelength between 250 nm and 700 nm, the Raman spectrum will be hampered by fluorescence, which is orders of magnitude stronger in intensity than the Raman scattered light.[66] Therefore, an excitation wavelength in the near infrared (NIR) region, 785 nm, is often used. This wavelength ensures minimal spectral interference from tissue fluorescence, limited chance of tissue damage, and enables deeper penetration of the light into the tissue.[58]

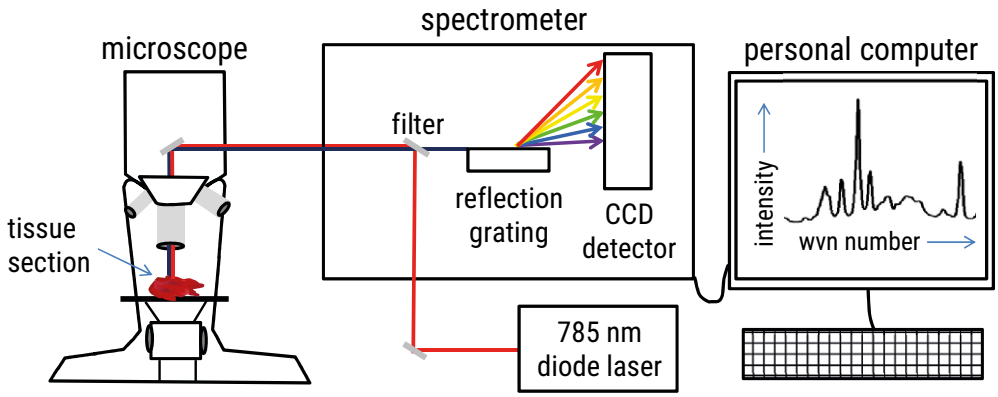

Figure 4. Instrumentation required for Raman spectroscopic experiments.

For the measurements on tissue sections described in this thesis, a microscope objective is used to focus the laser light onto the sample, and Raman scattered light is collected through the same objective. The scattered light is recorded by a spectrometer. First, the much stronger Rayleigh scattered light has to be suppressed. This suppression is accomplished by the use of an optical filter, which allows only minimal transmission of shorter wavelengths (laser), while longer wavelengths (Raman shifts) are optimally transmitted. Then, the transmitted light is separated in different wavelengths. This works by the same principle by which a prism divides white light into different colors, or wavelengths.[52] However, nowadays most spectrometers employ reflecting gratings rather than prisms. Next, the separated wavelength components are projected onto a sensitive, NIR optimized CCD camera, which works as a multichannel detector. Finally, a personal computer with dedicated software is used to display the Raman spectra.

Raman spectrum

The frequency shifts of the inelastically scattered light are specific to the illuminated molecule and are constant for that particular molecule, i.e. they are independent of the wavelength of excitation.[57] In a Raman spectrum (Figure 4), the intensity of the Stokes scattered light is plotted along the y-axis and the corresponding frequency shift along the x-axis. Since the frequency is equal to the number of waves in a distance of 299 792 458 meters; this is a very large number. Therefore, the frequency shift is generally expressed as the number of waves in one centimeter, called the wavenumber.[57] Wavenumber shifts in cm^{-1} are calculated according to the formula:

$$\Delta\ cm^{-1} = (1/\lambda_0 - 1/\lambda_s)$$

λ_0 = excitation wavelength in cm
λ_s = wavelength of backscattered light in cm

A Raman spectrum is highly molecule specific. Furthermore, Raman scattering is a linear process, which means the number of Raman scattered photons is directly proportional to the intensity of the incident light and to the number of irradiated molecules. Thus, the intensity of a Raman peak is proportional to the concentration of the respective molecule.[67] The position, shape, and intensity of the peaks in a Raman spectrum (Figure 5) provide detailed, quantitative information about the overall molecular composition of a sample.[66] This allows an objective characterization of cells and tissues.[58]

Analysis of Raman spectrum

Raman spectroscopic information is obtained mostly from two different spectral regions. The wavenumber region with the most detailed biochemical information lies between 400 – 2000 cm^{-1}, called the fingerprint region.[57] The high wavenumber (HWVN) region, which lies between 2000 – 4000 cm^{-1}, contains less spectroscopic information, originating mostly from CH-, OH- and NH-stretching vibrations. In this thesis only the fingerprint region is studied.

Analysis of a Raman spectrum of tissue is complex, due to the large number of partly overlapping Raman peaks. However, as mentioned above, a Raman tissue spectrum can be used as a tissue-specific spectroscopic fingerprint. To classify or subdivide spectral classes, unsupervised classification methods can be applied that use the spectral differences in these fingerprints. The unsupervised methods require

no a priori knowledge of group similarities. Examples of unsupervised methods are K-means cluster analysis (KCA) and hierarchical cluster analysis (HCA).[68] In supervised methods pattern recognition is used for the creation of models based on previously known labeling. An example of a supervised method is (hierarchical) linear discriminant analysis ((h)LDA).[69] (h)LDA is often used in combination with principal component analysis (PCA).[70] Such PCA-LDA models can be trained to identify or classify unknown Raman tissue spectra. This way of fingerprint analysis is often used in clinical diagnostics.

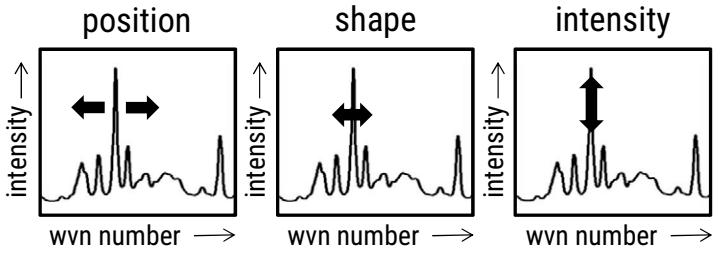

Figure 5. The position, shape, and intensity of the peaks in a Raman tissue spectrum provide a tissue-specific spectroscopic fingerprint.

A different approach to analyze the complex Raman tissue spectra is to decompose them. In this way, detailed information about the molecular composition of the measured tissue can be obtained. This is possible in a qualitative manner, by visual comparison of the peaks in the tissue spectrum with the features of pure-compound reference spectra. A more quantitative and objective approach is the use of fitting procedures that find the best (linear) combinations of known pure-compound reference spectra to approximate the tissue spectrum.[71] The fit coefficients of the pure-compound reference spectra relate to the relative concentrations of these compounds in the analyzed tissue spectrum.

For an accurate fitting procedure, multiple pure-compound reference spectra are needed. These pure compounds have to represent the main components of the investigated tissue. Generally, there are five principle chemical classes within biological tissues that can contribute to the Raman tissue spectra: proteins, lipids, nucleotides, carbohydrates, and amino acids.[29] This type of analysis is used to obtain more insight into the molecular composition of tissues and the differences in the composition of different tissues.

RAMAN SPECTROSCOPIC APPLICATIONS

To date, a number of publications have demonstrated the potential of Raman spectroscopy for tissue characterization and tumor detection in several anatomical regions,[72] including the oral cavity.[73-81] The technique is especially suited for intraoperative use, since it is nondestructive, reproducible, quick to perform without pretreatment or labelling, and suitable for use with fiber-optic probes.[82-85]

Most previously published Raman studies have focused on the analysis of tissue-specific spectroscopic fingerprints, using Raman signals from relatively large tissue volumes. However, oral tissue is not homogeneous, it is comprised of different histological structures and layers.[86] The various tissue structures have their own molecular compositions and, as a consequence, their own specific Raman features. All structures present in the measurement volume will contribute to the overall Raman spectrum. This must be taken into account when developing tissue classification algorithms based on Raman spectroscopy. A thorough understanding of the spectral contributions of the different tissue structures is essential for optimizing the discriminatory power of the technique.

MORPHOLOGY OF THE TONGUE

To create a solid foundation for Raman spectroscopic applications in head and neck oncological surgery and pathology, the spectral features of the main histological structures in the tongue need to be elucidated. The main tissue layers and structures of the tongue are illustrated in Figure 6 (inspired by the descriptions in Mills et al.).[86] The mucosa includes the squamous epithelium and lamina propria. The squamous epithelium of oral tongue shows regional variations in structure and keratin expression based on its function.[86] The dorsum of the tongue (i.e. superior side) is exposed to the forces of mastication and is covered with (para)keratinized squamous epithelium, whereas the ventral side (i.e. inferior side) is not keratinized. The epithelial thickness also varies dependent on sex, age, and tobacco- and alcohol consumption habits.[87,88] The basement membrane forms the interface between the basal epithelial layers and the lamina propria. The lamina propria is a delicate layer situated beneath the surface squamous epithelium and basement membrane, which contains few elastic and collagenous connective tissue (CT) fibers and is rich in blood vessels, lymphatics, and (sensory branches of) nerves. It also contains scattered lymphocytes that can migrate through the squamous epithelium.

The layer under the mucosa is called the submucosa. The submucosa is composed of CT, in which muscle fibers, adipose tissue, nerves, larger blood vessels, and lymphatics are distributed. The distribution of these tissue structures varies throughout the tongue.[89] Numerous minor salivary glands (predominantly mucinous) characterize the submucosa of the inferior side of the tongue. Taste buds are present in large numbers on the superior side and lateral edges of the tongue.[86]

SCOPE OF THIS THESIS

The main goal of this thesis is to provide a solid foundation for further development of Raman spectroscopic applications in head and neck oncology. This is a multistep process in which we want to investigate and understand the Raman spectroscopic features that distinguish the epithelial (keratinocytic) component of a tongue OCSCC from its surrounding tissue (referred to as non-tumorous or healthy tissue).

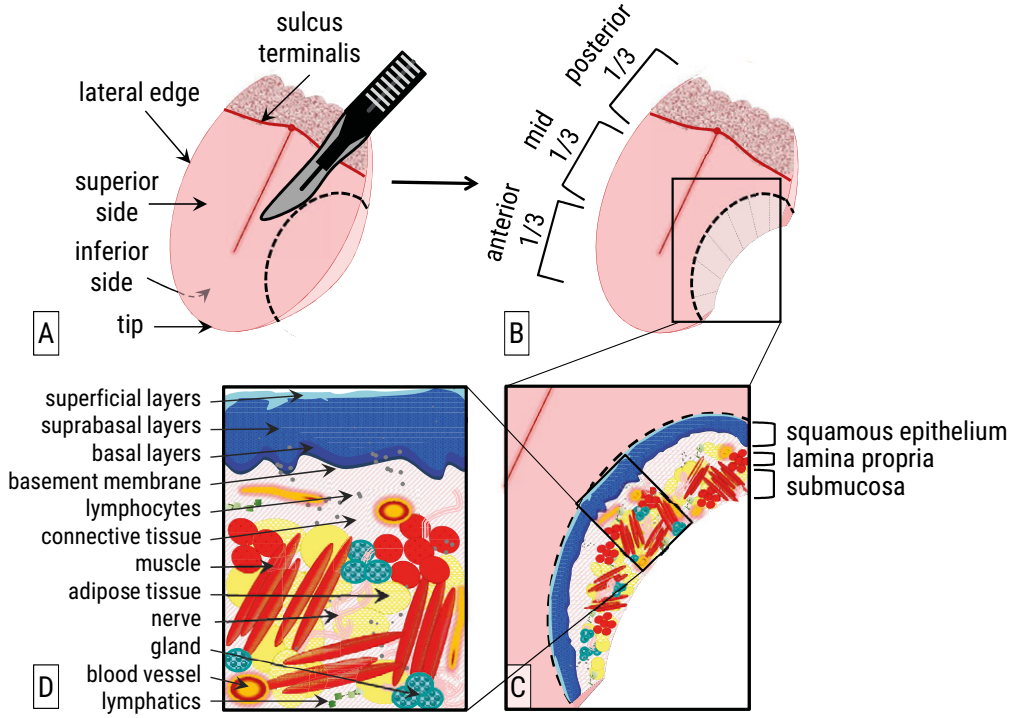

Figure 6. A: Schematic overview of a tongue. B: Cross section (lateral edge). C: Main histological tissue layers. D: Main histological structures.

First, we aimed to develop a standardized method to collect and analyze detailed Raman spectral information of OCSCC and the individual non-tumorous tissue structures in the tongue, as described in Chapter 2. Next, the potential of Raman spectroscopy to distinguish between the characteristic Raman features of OCSCC and the individual non-tumorous tissue structures is investigated in Chapter 3. In Chapter 4, these results are used for the development of a 'tumor' versus 'non-tumorous tissue' classification model. Lastly, in Chapter 5 the Raman spectra of OCSCC and individual non-tumorous tissue structures are analyzed in terms of the quantitative information they contain about the tissue's molecular composition. In Chapter 6 an overview is given of the pure-compound reference spectra used for this analysis.

To conclude, in this thesis the strengths and limitations of Raman spectroscopy, regarding its OCSCC-detecting potential in tongue, are elucidated.

REFERENCES

1. Integraal kankercentrum Nederland. *The dutch cancer registry*. http://www.cijfersoverkanker.nl/ [accessed 2016].
2. WHO. *Mortality database*. http://apps.who.int/healthinfo/statistics/mortality/whodpms/ [accessed 2016].
3. Califano, Van Der Riet, et al. (1996) *Genetic progression model for head and neck cancer: Implications for field cancerization.* Cancer Research. 56(11):2488-2492.
4. Pindborg. *Histological typing of cancer and precancer of the oral mucosa.* 2nd ed. (1997)
5. Fleskens, Slootweg. (2009) *Grading systems in head and neck dysplasia: Their prognostic value, weaknesses and utility.* Head & Neck Oncology. 1(1):11-19.
6. Hanahan, Weinberg. (2011) *Hallmarks of cancer: The next generation.* Cell. 144(5):646-674.
7. Hanahan, Weinberg. (2000) *The hallmarks of cancer.* Cell. 100(1):57-70.
8. Blot, Mclaughlin, et al. (1988) *Smoking and drinking in relation to oral and pharyngeal cancer.* Cancer Research. 48(11):3282-3287.
9. Gupta, Murti, et al. (1996) *Epidemiology of cancer by tobacco products and the significance of TSNA.* Critical Reviews in Toxicology. 26(2):183-198.
10. Van Oijen, Slootweg. (2000) *Oral field cancerization: Carcinogen-induced independent events or micrometastatic deposits?* Cancer Epidemiology, Biomarkers and Prevention. 9(3):249-256.
11. Warnakulasuriya. (2009) *Causes of oral cancer – an appraisal of controversies.* British Dental Journal. 207(10):471-475.
12. Zandberg, Bhargava, et al. (2013) *The role of human papillomavirus in nongenital cancers.* Cancer Journal for Clinicians. 63(1):57-81.
13. Barnes. *Pathology and genetics of head and neck tumours.* 3rd ed. (2005)
14. Binahmed, Nason, et al. (2007) *The clinical significance of the positive surgical margin in oral cancer.* Oral Oncology. 43(8):780-784.
15. Sobin. *Tnm classification of malignant tumours.* 7th ed. (2009)
16. Baatenburg De Jong, Rongen, et al. (1991) *Ultrasound-guided fine-needle aspiration biopsy of neck nodes.* Archives Otolaryngology Head Neck Surgery. 117(4):402-404.
17. De Bree, Deurloo, et al. (2000) *Screening for distant metastases in patients with head and neck cancer.* Laryngoscope. 110(3):397-401.
18. Brockstein. *Head and neck cancer.* 1st ed. (2003)
19. Erasmus MC. *Treatment.* https://erasmusmc-kno.shinyapps.io/treatmentsApp/ [accessed 2017].
20. Shah, Gil. (2009) *Current concepts in management of oral cancer-surgery.* Oral Oncology. 45(0):394-401.
21. National Comprehensive Cancer Network (NCCN). *Head and neck cancers.* https://www.nccn.org/professionals/physician_gls/f_guidelines.asp [accessed 2016].
22. Helliwell. (2013) *Standards and datasets for reporting cancers.*
23. Al-Rajhi, Khafaga, et al. (2000) *Early stage carcinoma of oral tongue: Prognostic factors for local control and survival.* Oral Oncology. 36(6):508-514.
24. Priya, D'cruz, et al. (2012) *Cut margins and disease control in oral cancers.* Journal of Cancer Research and Therapeutics. 8(1):74-79.
25. Slootweg, Hordijk, et al. (2002) *Treatment failure and margin status in head and neck cancer. A critical view on the potential value of molecular pathology.* Oral Oncology. 38(5):500-503.
26. Smits, Koljenovic, et al. (2015) *Resection margins in oral cancer surgery: Room for improvement.* Head & Neck. 38(1):E2197-2203.
27. Varvares, Poti, et al. (2015) *Surgical margins and primary site resection in achieving local control in oral cancer resections.* Laryngoscope. 125(10):2298-2307.
28. Nason, Binahmed, et al. (2009) *What is the adequate margin of surgical resection in oral cancer?* Oral Surgery, Oral Medicine, Oral Pathology, Oral Radiology and Endodontology. 107(5):625-629.
29. Dillon, Brown, et al. (2015) *How does the close surgical margin impact recurrence and survival when treating oral squamous cell carcinoma?* Journal of Oral and Maxillofacial Surgery. 73(6):1182-1188.
30. American Society of Clinical Oncology. *Oral and oropharyngeal cancer: Treatment options.* http://www.cancer.net/cancer-types/oral-and-oropharyngeal-cancer/treatment-options [accessed 2016].
31. Ribeiro, Godden, et al. (2003) *Do frozen sections help achieve adequate surgical margins in the resection of oral carcinoma?* International Journal of Oral and Maxillofacial Surgery. 32(2):152-158.

32. Woolgar, Triantafyllou. (2005) *A histopathological appraisal of surgical margins in oral and oropharyngeal cancer resection specimens.* Oral Oncology. 41(10):1034-1043.
33. Dinardo, Lin, et al. (2000) *Accuracy, utility, and cost of frozen section margins in head and neck cancer surgery.* Laryngoscope. 110(10):1773-1776.
34. Pathak, Nason, et al. (2009) *Impact of use of frozen section assessment of operative margins on survival in oral cancer.* Oral Surgery, Oral Medicine, Oral Pathology, Oral Radiology and Endodontology. 107(2):235-239.
35. Patel, Goldstein, et al. (2010) *Impact of positive frozen section microscopic tumor cut-through revised to negative on oral carcinoma control and survival rates.* Head & Neck. 32(11):1444-1451.
36. Kolokythas, Park, et al. (2015) *Squamous cell carcinoma of the oral tongue: Histopathological parameters associated with outcome.* International Journal of Oral and Maxillofacial Surgery. 44(9):1069-1074.
37. Woolgar. (2006) *Histopathological prognosticators in oral and oropharyngeal squamous cell carcinoma.* Oral Oncology. 42(3):229-239.
38. Rosai. *Surgical pathology* 10th ed. (2011)
39. Ransohoff, Wood, et al. (2016) *Third party assessment of resection margin status in head and neck cancer.* Oral Oncology. 57(6):27-31.
40. Nwhht. (2004) *Mondholte- en orofarynxcarcinoom.*
41. Braakhuis, Visser, et al. (2009) *Oral and oropharyngeal cancer in the netherlands between 1989 and 2006: Increasing incidence, but not in young adults.* Oral Oncology. 45(9):E85-89.
42. Patel, Carpenter, et al. (2011) *Increasing incidence of oral tongue squamous cell carcinoma in young white women, age 18 to 44 years.* Journal of Clinical Oncology. 29(11):1488-1494.
43. Amit, Yen, et al. (2013) *Improvement in survival of patients with oral cavity squamous cell carcinoma: An international collaborative study.* Cancer. 119(24):4242-4248.
44. Ferlay, Soerjomataram, et al. (2015) *Cancer incidence and mortality worldwide: Sources, methods amd major patterns in globocan 2012.* International Journal of Cancer. 136(5):E359-386.
45. Karim-Kos, De Vries, et al. (2008) *Recent trends of cancer in europe: A combined approach of incidence, survival and mortality for 17 cancer sites since the 1990s.* European Journal of Cancer. 44(10):1345-1389.
46. Al-Swiahb, Chen, et al. (2010) *Clinical, pathological and molecular determinants in squamous cell carcinoma of the oral cavity.* Future Oncology. 6(5):837-850.
47. Taghavi, Yazdi. (2015) *Prognostic factors of survival rate in oral squamous cell carcinoma: Clinical, histologic, genetic and molecular concepts.* Archives of Iranian Medicine. 18(5):314-319.
48. Spiro, Huvos, et al. (1986) *Predictive value of tumor thickness in squamous carcinoma confined to the tongue and floor of the mouth.* American Journal of Surgery. 152(4):345-350.
49. Datema, Ferrier, et al. (2010) *Impact of comorbidity on short-term mortality and overall survival of head and neck cancer patients.* Head & Neck. 32(6):728-736.
50. Baatenburg De Jong, Hermans, et al. (2001) *Prediction of survival in patients with head and neck cancer.* Head & Neck. 23(9):718-724.
51. Van Der Schroeff, Steyerberg, et al. (2012) *Prognosis: A variable parameter: Dynamic prognostic modeling in head and neck squamous cell carcinoma.* Head & Neck. 34(1):34-41.
52. Hecht. *Optics*. 4th ed. (2002)
53. Newton. *Opticks.* 4th ed. (1730)
54. Bettelheim. *Introduction to general, organic and biochemistry.* 10th ed. (2012)
55. Wisconsin-Madison. (2005) *Absorption, emission, reflection and scattering.*
56. Ball. (2001) *Rayleigh and Raman scattering. Spectroscopy.* 16 (2):28-30.
57. Koningstein. *Introduction to the theory of the Raman effect.* 1st ed. (1972)
58. Mason. *Fluorescent and luminescent probes for biological activity.* 2nd ed. (1999)
59. Srinivasan. *Vibrational spectroscopic imaging for biomedical applications.* 1st ed. (2010)
60. Smekal. (1923) *Zur quantentheorie der dispersion. Naturwissenschaften.* 11(43):873-875.
61. Raman. (1928) *A new type of secondary radiation.* Nature. 121(501-502):365.
62. Singh. (1998) *Sir c.V. Raman and the story of the nobel price.* Current science. 75(965.
63. Maiman. (1960) *Stimulated optical radiation in ruby.* Nature. 187(8):493-494.
64. Boyle. (1970) *Charge coupled semiconductor devices.* Bell systems technical journal. 49(4):587-593.
65. Puppels, De Mul, et al. (1990) Studying single living cells and chromosomes by confocal Raman microspectroscopy. Nature. 347(6290):301-303.

66. Carey. (1999) *Raman spectroscopy, the sleeping giant in structural biology, awakes.* Journal of Biological Chemistry. 274(38):26625-26628.

67. Hanlon, Manoharan, et al. (2000) *Prospects for in vivo Raman spectroscopy.* Physics in Medicine and Biology. 45(2):R1-59.

68. Jain. *Algorithms for clustering data* 1st ed. (1988)

69. Tabachnick. *Using multivariate statistics.* 6th ed. (1996)

70. Jolliffe. *Principal component analysis.* 2nd ed. (2002)

71. Lawson. Solving least squares problems. 1st ed. (1995)

72. Evers, Hendriks, et al. (2012) *Optical spectroscopy: Current advances and future applications in cancer diagnostics and therapy.* Future Oncology. 8(3):307-320.

73. Carvalho, Bonnier, et al. (2015) *Raman micro-spectroscopy for rapid screening of oral squamous cell carcinoma.* Experimental and Molecular Pathology. 98(3):502-509.

74. Deshmukh, Singh, et al. (2011) *Raman spectroscopy of normal oral buccal mucosa tissues: Study on intact and incised biopsies.* Journal of Biomedical Optics. 16(12):127004-127010.

75. Guze, Short, et al. (2011) *Comparison of molecular images as defined by Raman spectra between normal mucosa and squamous cell carcinoma in the oral cavity.* Journal of Raman Spectroscopy. 42(6):1232-1239.

76. Knipfer, Motz, et al. (2015) Raman difference spectroscopy: *A non-invasive method for identification of oral squamous cell carcinoma: Publisher's note.* Biomedical Optics Express. 6(7):3252-3265.

77. Krishna, Majumder, et al. (2014) *In vivo Raman spectroscopy for detection of oral neoplasia: A pilot clinical study.* Journal of Biophotonics. 7(9):690-702.

78. Malini, Venkatakrishna, et al. (2006) *Discrimination of normal, inflammatory, premalignant, and malignant oral tissue: A Raman spectroscopy study.* Biopolymers. 81(3):179-193.

79. Su, Sun, et al. (2012) *Raman spectral properties of squamous cell carcinoma of oral tissues and cells.* Laser Physics. 22(1):311-316.

80. Venkatakrishna. (2001) *Optical pathology of oral tissue: A Raman spectroscopy diagnostic method.* Current science. 80(5):665-670.

81. Wu, Xu, et al. (2001) *Distinguishing malignant from normal oral tissues using ftir fiber-optic techniques.* Biopolymers. 62(4):185-192.

82. Davies, Connolly, et al. (2015) *Point of care optical diagnostic technologies for the detection of oral and oropharyngeal squamous cell carcinoma.* Surgeon. 13(6):321-329.

83. Green, Cobb, et al. (2014) *Optical diagnostic techniques for use in lesions of the head and neck: Review of the latest developments.* British Journal of Oral and Maxillofacial Surgery. 52(8):675-680.

84. Jerjes, Upile, et al. (2011) *The future of medical diagnostics: Review paper.* Head & Neck Oncology. 3(38):1-8.

85. Singh, Ibrahim, et al. (2016) *Recent advances in optical diagnosis of oral cancers: Review and future perspectives.* Head & Neck. 38(1):1-9.

86. Mills. *Histology for pathologists.* 3rd ed. (2004)

87. Valentine, Scott, et al. (1985) *A histological analysis of the early effects of alcohol and tobacco usage on human lingual epithelium.* Journal of Oral Pathology. 14(8):654-665.

88. Sasaki. (1994) *Histomorphometric analysis of age-related changes in epithelial thickness and langerhans cell density of the human tongue.* Tohoku Journal Experimental Medicine. 173(3):321-336.

89. Miller, Watkin, et al. (2002) *Muscle, adipose, and connective tissue variations in intrinsic musculature of the adult human tongue.* Journal of Speech Language and Hearing Research. 45(1):51-65.

2

Method development: Raman spectroscopy-based histopathology of oral mucosa

Froukje L. J. Cals, Tom C. Bakker Schut, Senada Koljenović, Gerwin J. Puppels and Robert J. Baatenburg de Jong

Journal of Raman spectroscopy 2013; DOI 10.1002/jrs.4318

ABSTRACT

An earlier and more accurate detection of (small) cancerous and precancerous lesions in the oral cavity is essential to improve the prognosis of oral cavity squamous cell carcinomas. Raman spectroscopy is being pursued as a potential method to realize this improvement, since the technique provides objective information on a biochemical level and can be used for real-time guidance of the diagnostic procedure.
Since oral mucosal tissue is inhomogeneous and comprises different layers and histological structures, a good understanding of the signal contributions of the individual layers and structures is required for an accurate interpretation of *in vivo* measured tissue spectra. The aim of this study was to create a standardized method to collect and analyze the spectral contributions of individual histopathological structures in oral mucosa.
The method is based on Raman micro spectroscopic mapping of unstained frozen tissue sections and subsequent histopathological annotation of the features in the resulting Raman images. The obtained annotated Raman spectra were used as input in an unsupervised hierarchical cluster analysis in order to determine the spectral characteristics and variance within one histopathological structure.
The described method resulted in an annotated database of Raman spectral characteristics of individual histopathological structures encountered in oral tissue. This database can be used as input for the development of classification and quantification algorithms, in order to achieve a high specificity and sensitivity for clinical diagnostic instruments. Additionally, this database can be used to optimize the exact location and measurement volume of *in vivo* measurements.

INTRODUCTION

Oral cavity squamous cell carcinomas (OCSCC) are a source of concern, not only because of the still increasing incidence (especially in women in developed countries), but also because of the high disease-related mortality. Every year 640 000 new cases of OCSCC are diagnosed worldwide, and only half of these patients will survive 5 years.[1,2] Over the past decades, only marginal improvements in 5-year-survival rates were achieved through advances in therapy (surgery, radiotherapy, chemotherapy, or a combination of these).[3] The relatively poor prognosis is mostly attributed to late diagnosis of primary and recurrent tumors, which leads to a higher risk of residual tumor after surgery and, consequently to the development of regional and distant metastases.[4-6] The gold standard for diagnosis of OCSCC is histopathological evaluation of biopsy tissue samples. Unfortunately, histopathological diagnosis of (pre)cancerous oral lesions is subjective[7] despite continuing efforts to standardize the criteria for classification of the disease. Moreover, the diagnostic accuracy depends on how well the biopsy material represents the actual suspected lesion. To improve the prognosis of these patients, earlier and more accurate detection of (small) cancerous and precancerous lesions in the oral cavity is essential. An objective technique for tissue characterization that can be used for real-time guidance of the diagnostic procedure would therefore be helpful.

Raman spectroscopy is an optical technique which may be able to provide an alternative for, or adjunct to, conventional diagnostic modalities in head and neck oncology.[8-10] Raman spectroscopy does not require sample preparation, is nondestructive, and can be used *in vivo*.[11,12] Because of these attractive properties there has been much interest in the use of Raman spectroscopy in cancer detection in recent years. To date, a number of publications have appeared which have shown that diseased and normal tissue samples, from a variety of organs, can be differentiated by means of Raman spectroscopy.[13-18]

Raman spectroscopic research also entered the field of head and neck oncology.[19-28] Malini et al. studied 50 normal, 50 malignant, 10 inflammatory, and 5 premalignant oral samples. They recorded a total of 216 spectra using a diode laser (SDL-8530 and a HR320 spectrograph) and concluded that key features of spectra of normal tissues can be attributed to lipids, whereas pathological tissue spectra were dominated by proteins.[24] Singh et al. have found similar results, after comparing the spectra from 10 normal and 10 tumor samples from the oral cavity, using a fiber optic probe coupled Raman spectrometer.[26] By means of Raman confocal micro spectrometry, Su et al. identified specific spectral markers associated with DNA and protein vibrational modes, which exhibited discrimination power for cancer sample identification.[28] These results demonstrate the strong diagnostic potential of Raman spectroscopy in head and neck oncology.

Most Raman studies published to date have focused on intact (non-sectioned) oral tissue samples, using relatively large measurement volumes. However, it is important to realize that a Raman spectrum of a tissue sample is dependent on the exact location, and size of the tissue volume from which the signal is collected. Since oral mucosal tissue is inhomogeneous and comprises different layers and histological structures,[29] a good understanding of the signal contributions of individual layers and structures is required for an accurate interpretation of *in vivo* tissue spectra with large measurement volumes. For that reason, spectral characteristics of individual histo(patho)logical structures of normal and diseased oral

mucosa need to be elucidated, before Raman spectroscopic diagnosis can be implemented in real-time clinical practice.

The aim of this study was to create a standardized method to collect and analyze the spectral contributions of individual histopathological structures in oral mucosa. The method is based on Raman micro spectroscopic mapping of frozen tissue sections and histopathological annotation of the features in the resulting Raman images. The method provides clear insight into how well Raman and histopathological results correlate, as well as into the variance in biochemical composition of individual histopathological structures. This should provide a more solid foundation for the development of classification and quantification algorithms, in order to achieve a high specificity and sensitivity for clinical diagnostic instruments.

MATERIALS AND METHODS

Sample handling and sample preparation

This study was approved by the Medical Ethics Committee of the Erasmus MC Cancer Institute, University Medical Center Rotterdam. At the Department of Otorhinolaryngology and Head and Neck Surgery of the Erasmus MC Cancer Institute, University Medical Center Rotterdam, tissue samples were collected from patients who had undergone surgical resection because of a primary squamous cell carcinoma (SCC) of the edge of the tongue. In total, three samples of tumor tissue and three samples of normal appearing mucosa (adjacent to the tumor) were collected from three patients after given informed consent. Samples were collected from resection material within 60 minutes after surgical excision. These samples were snap frozen by immersion in isopentane and subsequently in liquid nitrogen and kept at -80˚C until further use. Figure 1 shows the next steps of the sample handling and sample preparation.

The frozen tissue samples were mounted on a cryotome stage using CryoCompound (KP-CryoCompound, Klinipath B.V., and The Netherlands) (Figure 1B). Adjacent 6 µm (Figure 1C) and 20 µm (Figure 1D) thick sections were cut. The 6 µm sections were stained with haematoxylin and eosin (H&E) for histopathological evaluation, which served to select regions of interest for Raman mapping experiments (Figure 1E). Corresponding regions in the unstained 20 µm sections were identified (Figure 1F). Prior to Raman measurements, the 20 µm tissue sections were placed on fused silica slides and were allowed to dry at the room temperature. These unfixed, unstained tissue sections were used for Raman spectroscopic mapping experiments without further treatment (Figure 1G). After completing the experiments, the 20 µm tissue sections were routine stained with H&E (Figure 1H) to enable precise histopathological correlation (Figure 1I) with the resulting pseudo color Raman images (Figure 1J).

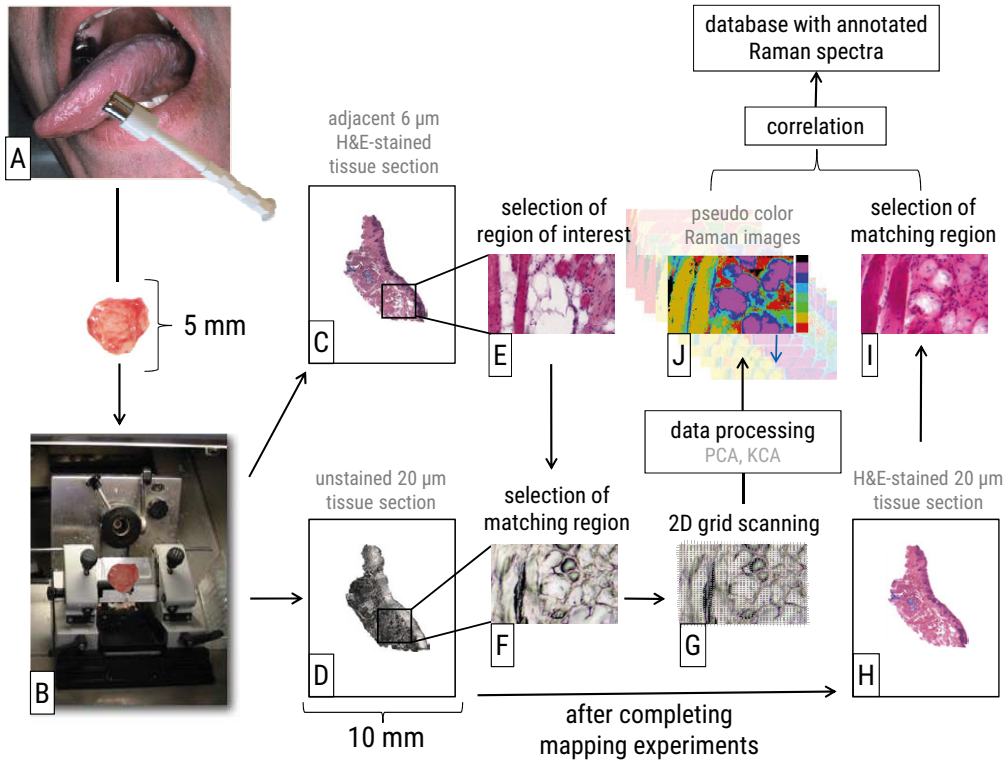

Figure 1. A: Biopsy sample from a suspected lesion of the tongue. B: Frozen tissue sample mounted on a cryotome stage. C: Adjacent 6 µm H&E-stained tissue section. D: 20 µm unstained tissue section. E: Region of interest selected for Raman mapping experiments. F: Corresponding region in unstained section. G: Point-by-point scanning in a 2D grid. J: Pseudo color Raman images. H: Afterwards H&E-stained 20 µm section. I: Mapped region.

Raman spectroscopic mapping experiments

A flowchart, including all steps needed to collect and analyze spectral information about individual histopathological structures in oral mucosa, is shown in Figure 2. All steps are described in detail in the following sections. For clarity, the steps and the ultimate results are summarized in this paragraph.

A total of 20 Raman mapping experiments were performed on multiple tissue sections. The selected region in the 20 µm thick unstained tissue section was scanned point-by-point in a two-dimensional grid. After pre-processing of the collected spectra, K-means cluster analysis (KCA) was applied to the dataset. Spectra within one cluster were assigned the same color, resulting in a pseudo color Raman image. After completing the measurements, the 20 µm section was H&E stained.[30] Each differently colored area, and thus each K-means cluster average, in the Raman image was then histopathologically annotated. Next, the annotated Raman spectra of all experiments together were used as input in an unsupervised hierarchical cluster analysis (HCA). The HCA results provide a clear insight into the level of correlation between Raman and histopathological results, and allow determination of a spectral average and standard deviation for each histopathological annotation.

Scanning procedure

A near infrared (NIR) multichannel Raman micro spectrometer, built in-house, was used to collect the Raman spectra of the tissue sections as described earlier.[31] Briefly, 30 to 60 mW of laser power (785 nm) was focused on the 20 µm tissue section through an 80x microscope-objective. The Raman scattered light was collected through the same objective and guided to a NIR optimized spectrometer (model HPRM 2500, RiverD International B.V., Rotterdam, The Netherlands), dispersed, and subsequently imaged on a charge coupled device (CCD) camera. Data were collected in the wavenumber interval from 310 to 2530 cm^{-1} with a spectral resolution of 4 cm^{-1}. Automatic scanning of sections was enabled by a xyz-motorized, computer-controlled sample stage (Leica DM STC, Cambridge, UK). The laser light was focused in the tissue section to a spot of about 1 – 2 μm^2. For each Raman mapping experiment, a selected region in the tissue section was scanned point-by-point in a two-dimensional grid with a step size of 2 µm and an acquisition time of 1 second per point. Moving the stage together with focusing took another second per point, resulting in a total measurement time of 2 seconds per point. Twenty Raman mapping experiments were performed on the six tissue sections. The scanned areas ranged between 212 192 µm and 602 802 µm in size, resulting in 10 176 to 120 700 points per mapping experiment. Thus, the time to measure an individual experiment varied between 15 and 67 h.

Data processing and data analysis

The Raman data were processed and analyzed with software developed in-house that operated in a MATLAB environment (MATLAB 7.3, MathWorks, MA, USA) and used the multivariate toolbox PLS-toolbox 7.0.0c (EigenVector Research, WA, USA). The data processing and analysis consisted of three consecutive steps that are described in detail below. The first two steps were applied to all individual mapping experiments separately, and in the last step, the annotated Raman spectra of all experiments were combined and analyzed together.

Data processing

The goal of data processing was to ensure that the processed spectra are a true representation of the local tissue molecular composition, so that the spectra of multiple experiments were comparable with respect to relevant biochemical differences.

Cosmic ray event removal

First, the cosmic ray events in the raw data (CCD readouts) were identified using a threshold filter and removed by interpolating the data over the affected CCD channels.

Calibration

The raw data were then calibrated and corrected for the wavelength-dependent signal detection efficiency of the Raman setup as described earlier.[32] Briefly, we calibrated the wavenumber range of the setup using the internal standards of the HPRM. The interfering background Raman signals originating from the optical elements in the laser-light delivery pathway were separately measured and subtracted. The detection efficiency was corrected using a NIST Relative Intensity Correction Standard (SRM 2241, NIST, USA). Finally, all spectra were interpolated to the range of 360 – 2450 cm^{-1} wavenumbers.

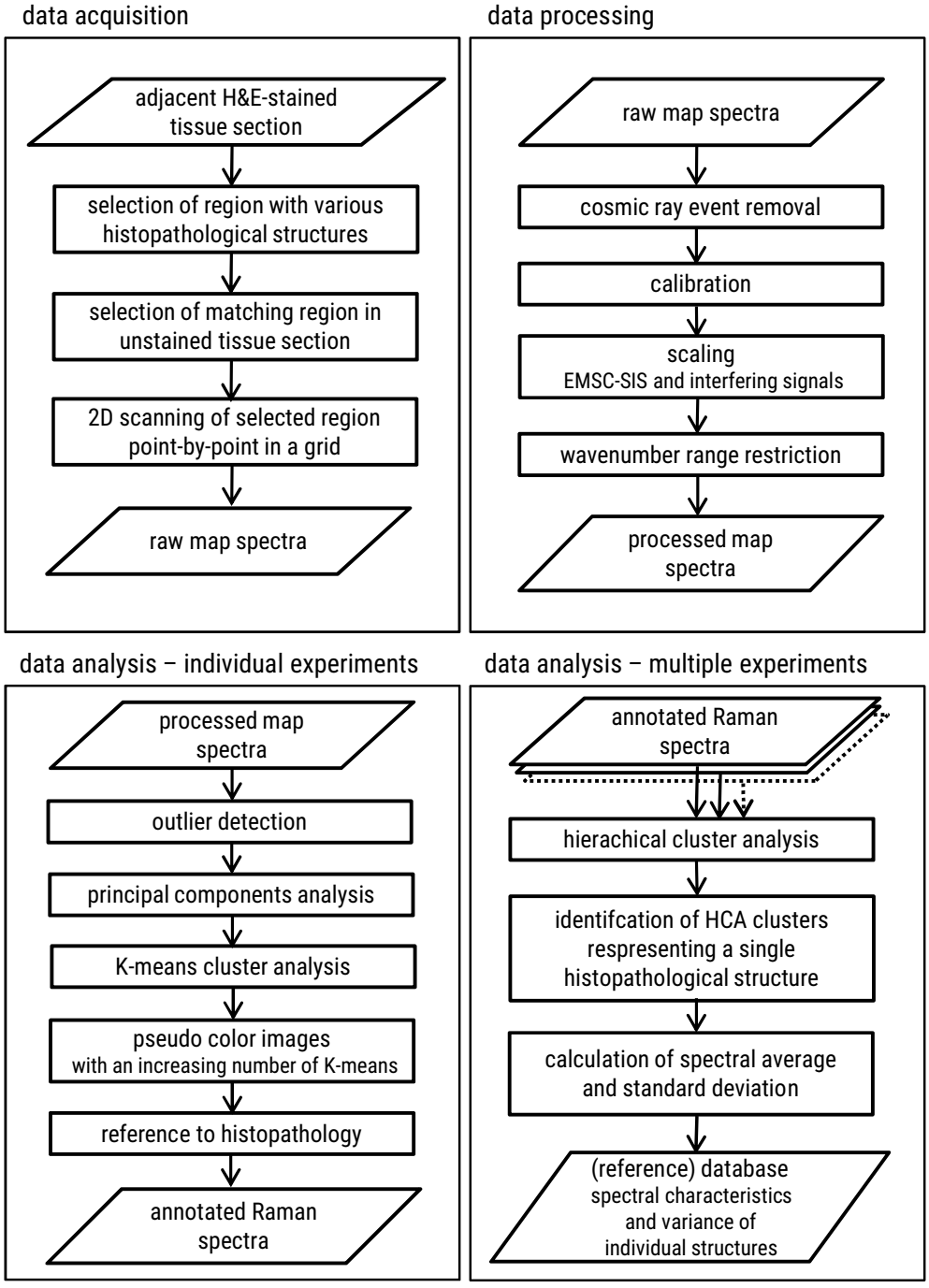

Figure 2. Flowchart of all steps used to collect and analyze spectral information about individual histopathological structures in oral mucosa (see text for a detailed description).

Scaling

After calibration, spectra are comparable from experiment to experiment but may show considerable differences in intensity and in spectral features that are considered to be non-informative, such as signals arising from the fused silica tissue carrier. A spectral scaling procedure called extended multiplicative signal correction procedure combined with spectral interference subtraction (EMSC-SIS)[33] was used to eliminate all the non-informative interfering signals, and to scale the spectra on the basis of informative biochemical content only.

- EMSC-SIS: EMSC-SIS uses a fitting procedure which estimates contributions of known spectral sources in a measured spectrum. We identified the following sources; [1] relevant informative biological signal contributions, and non-informative interfering contributions from [2] the fused silica tissue carrier RiverD International B.V., Rotterdam, The Netherlands [3] CryoCompound, [4] blood, [5] β-carotene, [6] hydroxyapatite, and [7] background fluorescence. Reference spectra of [2 – 6] were measured from pure compounds (Sigma–Aldrich Chemie B.V., The Netherlands). The contribution of [7] was modelled as a seventh-order polynomial. A tissue prototype spectrum was calculated after manual correction for any non-informative interfering contributions of [2 – 6], as described earlier.[33] The tissue prototype spectrum, which serves as the reference for relevant informative biological signal contributions [1] was also used to detect spectral outliers.
- Interfering signals: The contributions of [2 and 3] were considered to be non-informative for histopathological correlation, since none of these are biologically found in untreated oral mucosa. The contributions of [4, 5 and 6] represented biological signals that were considered non-informative, since these signals showed a large influence on the scaling procedure, resulting in non-informative differences between similar histopathological structures in different Raman experiments. The contribution of [7] fluorescence was considered to be non-specific information.

Wavenumber range restriction

The wavenumber range of the spectra was restricted to the fingerprint region (400 – 1800 cm^{-1}) which is considered the most informative region for biological Raman signals.

Data analysis – individual experiments

After data processing, each mapping experiment was analyzed to obtain a pseudo color Raman image, which was used for histopathological annotation. In order to achieve this, the processed spectra were subjected to a KCA.

Outlier detection

As a first step in the individual experiment analysis, all spectral outliers were eliminated because these can have a significant effect on the cluster analysis results. Two types of outliers were automatically identified: [1] low quality spectra (based on high scaling factors to tissue prototype from the EMSC-SIS scaling procedure) and [2] spectra with a non-biological signature (based on low correlation to the tissue prototype).

Principal component analysis

The remaining spectra were transformed by principal component analysis (PCA).[34] PCA is a mathematical procedure to transform a set of possibly correlated variables into a set of scores on linearly uncorrelated variables called principal components (PCs). PCA is also used to decrease the amount of data to enable further analysis. The first PC accounts for the major direction of variance in the data set, and each next PC has the highest possible variance that is uncorrelated with the previous components. In this way, each subsequent PC represents a decreasing amount of variance in the data set. As the PCs are ordered in importance, a significant reduction of the dataset without significant loss of information can be realized by restricting the number of PCs that are taken into account.

K-means cluster analysis

The first 20 PCA scores of all spectra of an individual experiment, where PC 20 accounts for less than 0,5% of the variance present in the dataset, were then grouped using KCA,[35] with a Euclidian distance measured to define the distance between the spectral scores. KCA is a heuristic partitioning clustering technique that does not always find the optimal solution, but the algorithm is computationally fast with large amounts of data and gives acceptable results.

KCA started with a user-defined number of cluster centers that, in our implementation, were selected by uniform sampling of the PCA space of the data set. Each single spectrum was then assigned to the closest cluster center, thus forming the first partitioning of the data. In the next step, new cluster centers were calculated by taking the mean of all spectra assigned to that cluster. Subsequently, each spectrum was again assigned to the closest cluster center, thus forming the second partitioning of the data. This process was repeated until a stable solution was reached for the requested amount of K-means clusters.

Correlation to histopathology

From the KCA results, a pseudo color Raman image can be generated by assigning a color to each cluster and plotting the cluster membership of each spectrum as a colored pixel at its measurement position. A trained pathologist evaluated the scanned regions in the H&E-stained 20 µm tissue sections and determined which morphological histopathological structures were present. Afterwards, for each experiment, the optimal amount of K-means clusters was defined, based on the best match between the pseudo color Raman image and the present histopathological structures. Correlating a too low number of K-means clusters resulted in heterogeneous clusters that represented more than one specific histopathological structure. However, correlating a too high number of K-means clusters resulted in clusters that were annotated equally, and in very small clusters (representing a small amount of points in the grid) that could not be correlated to histopathology. Thus, the choice of the optimal number of K-means clusters was determined empirically, by defining the best match as the cluster result with [1] the lowest amount of clusters possible without presence of Raman clusters comprising different histopathological structures, and [2] the lowest amount of equally annotated and/or uncorrelated clusters.

In this way, for each individual experiment, a specific number of K-means clusters was defined of which each cluster was either annotated as a specific histopathological oral tissue structure, or annotated as

undetermined. The K-means cluster averages serve as histopathologically annotated Raman spectra, and are hereafter called annotated Raman spectra.

Data analysis – multiple experiments

The cluster results of the KCA of all individual maps were used as input for an unsupervised HCA. The goal of this analysis was to determine a spectral average and standard deviation for each individual histopathological structure. The analysis also shows whether clusters with the same histopathological annotation, but from different Raman mapping experiments, form one or more spectroscopic subgroups. This provides an insight into the variance in biochemical composition of individual histopathological structures.

Hierarchical cluster analysis

All annotated Raman spectra in the database were used as input for a HCA. HCA is a non-heuristic clustering method to find the best subdivision in clusters at each possible division level.[35] HCA finds the optimal solution for a given clustering algorithm and distance measure, but the algorithm is computationally slow (full enumeration) and cannot be used with large amounts of data. HCA can be divisive, starting from the complete set, or agglomerative, starting from the individual observations. Here, we used an agglomerative algorithm (Ward's method) with the squared Pearson's correlation coefficient (R^2) between two spectra as proximity measure (and ($1-R^2$) as distance measure). The output of HCA is a membership matrix (N x N, where N is the number of spectra) that represents the clustering at each level of agglomeration.

Identification of HCA clusters representing individual histopathological structures

The HCA membership matrix was used to identify the HCA clusters that only contain annotated Raman spectra with the same histopathological annotation. Starting from the highest level, where all annotated Raman spectra are within one HCA cluster, we analyzed the splitting of the input data in an ascending number of HCA clusters, in order to identify the largest possible clusters that consist of reference spectra with identical histopathological annotation.

Calculation of spectral average and standard deviation

The identification procedure described above results in multiple clusters per histopathological structure. The spectral characteristics define which annotated Raman spectra cluster together, instead of the histopathological annotations. In this way, the procedure preserves information that would be lost by simple averaging all equally annotated Raman spectra. Each HCA cluster represents a spectroscopic subgroup of a specific histopathological structure. When averaging all HCA clusters of an individual structure, a spectral average and standard deviation can be calculated that represents the overall molecular composition of that histopathological structure. The standard deviation provides an insight into the variance in biochemical composition within individual histopathological structures.

RESULTS

Histopathological evaluation of tissue sections

Twenty Raman mapping experiments were performed on unstained, unfixed sections of three normal tongue tissue samples and three samples with OCSCC, taken from three patients. Different histopathological structures were identified on the adjacent sections that were routinely stained (i.e. H&E). An example of the histology of normal tongue tissue is given by Figure 3. Figure 3A shows a low magnification micrograph of a transversally cut tongue tissue section with the epithelium (indicated E), lamina propria (indicated LP), and submucosa (indicated SM). Higher magnification of the epithelium and lamina propria (Figure 3B) shows that the basal epithelial layers (indicated BEL) are relatively darker compared to the epithelium layers towards the surface (indicated suprabasal layers, SBL). This is due to the fact that the basal epithelial cells have less cytoplasm.[29] The lamina propria is a delicate layer of loose connective tissue (indicated LCT) and contains capillaries, lymphatics and peripheral nerves. Figure 3C shows the underlying supportive layer, termed submucosa, in more detail. Submucosa is mostly composed of dense connective tissue (indicated DCT) and contains larger blood vessels, peripheral nerves, lymphatic vessels, adipose tissue (indicated A), and seromucous glands. The mucosa and submucosa are bound to the underlying smooth muscle tissue (indicated M) by connective tissue fibers.

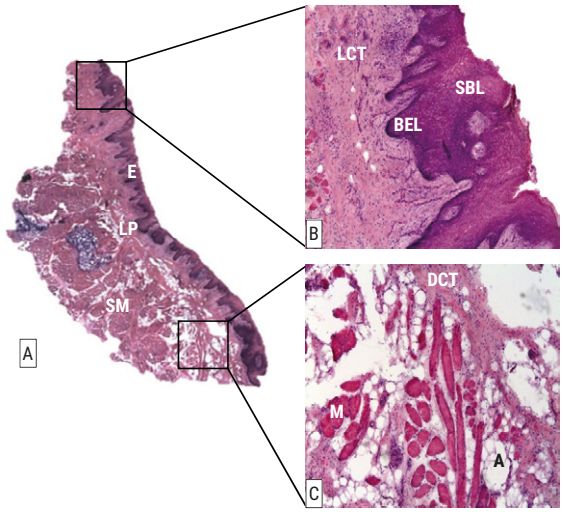

Figure 3. A: Microphotograph (original magnification 16x) of an H&E-stained section showing a transversally cut sample of normal oral tongue tissue, with stratified squamous epithelium (indicated E), underlying lamina propria (indicated LP), and submucosa (indicated SM). In panel B and C, the histological structures are shown in more detail (original magnification 40x). B: The basal epithelial layers (indicated BEL) can be distinguished from suprabasal layers (indicated SBL), and the underlying loose connective tissue (indicated LCT) in the lamina propria. C: Within the submucosa, dense connective tissue (indicated DCT), adipose tissue (indicated A), and smooth muscle tissue (indicated M) can be appointed.

Correlation between Raman images and histopathological structures

For Raman mapping experiments, the regions of interest, containing different histopathological structures, were selected in the unstained tissue sections by correlation to the adjacent H&E-stained sections. The acquired Raman spectra of each experiment were analyzed by PCA, followed by KCA. This resulted in pseudo color Raman images after assigning a color to each cluster, as described in the materials and

methods section. After all mapping experiments were completed, the 20 µm tissue sections were routine stained for histopathological correlation with the Raman images. This procedure was performed by an experienced pathologist. For each individual experiment, the optimal number of K-means clusters was defined, based on the best match between the pseudo color Raman image and the histopathological structures present.

In Figure 4, this procedure is illustrated using the results of one mapping experiment. Figure 4A shows the magnified photograph of the scanned region in the afterwards H&E-stained section. Based on histological evaluation, three different tissue layers/structures were distinguished; [I] central part of well-differentiated OCSCC, [II] peripheral part of well-differentiated OCSCC, and [III] peritumoral stroma. In Figures 4B – 4H, the pseudo color Raman images of this experiment are shown with an increasing number of K-means clusters (ranging 2 – 8). Using K-means 2, 3, 4, or 5 for correlation resulted in clusters that combined more than one histopathological structure (Figures 4B – 4E). In these Raman images, the peripheral part of well-differentiated OCSCC was not represented in a separate cluster, in contrary to the image with K-means 6 (Figure 4F). Using an even higher amount of K-means clusters (Figures 4G – 4H) resulted in multiple K-means clusters that were assigned the same histopathological annotation, as well as in a higher number of uncorrelated clusters that could not be assigned a specific histopathological annotation. The optimal number of K-means clusters in this experiment was therefore 6 (Figure 4F). Next, clusters 2, 3, and 4 were annotated as peritumoral stroma, cluster 5 as peripheral part of well-differentiated OCSCC, and cluster 6 as central part of well-differentiated OCSCC. The spectrum of the first cluster contained too much noise and was therefore excluded from further analysis. Another two examples are shown in Figure 5 and 6.

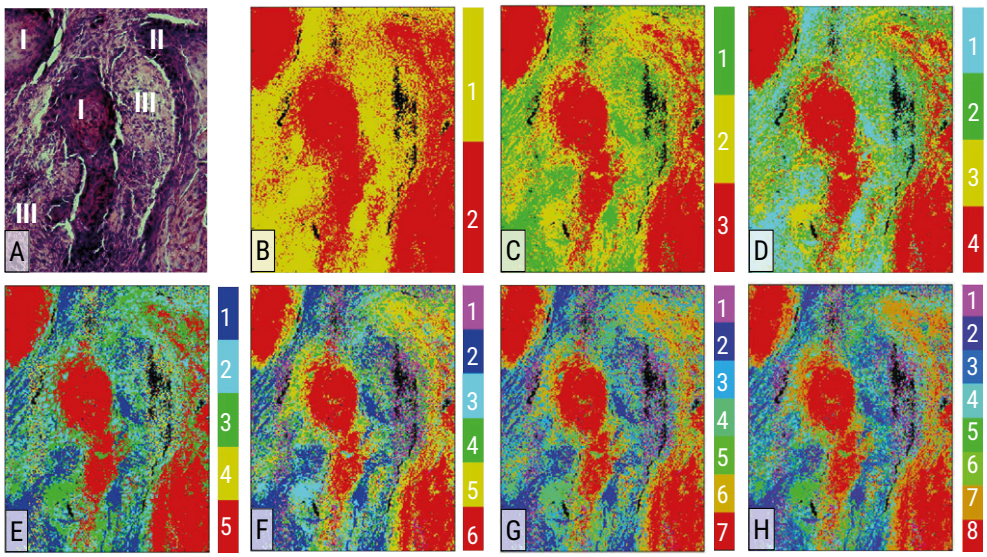

Figure 4. A: Microphotograph (original magnification 100x) of an H&E-stained section of the scanned tissue region. Three different tissue layers/structures were distinguished; [I] central part of well-differentiated OCSCC, [II] peripheral part of well-differentiated OCSCC, and [III] peritumoral stroma. B – H: pseudo color Raman images of this experiment are shown with an increasing number of K-means clusters (ranging 2 – 8). The best correlation, representing all identified histopathological structures in a separate cluster, was defined at 6.

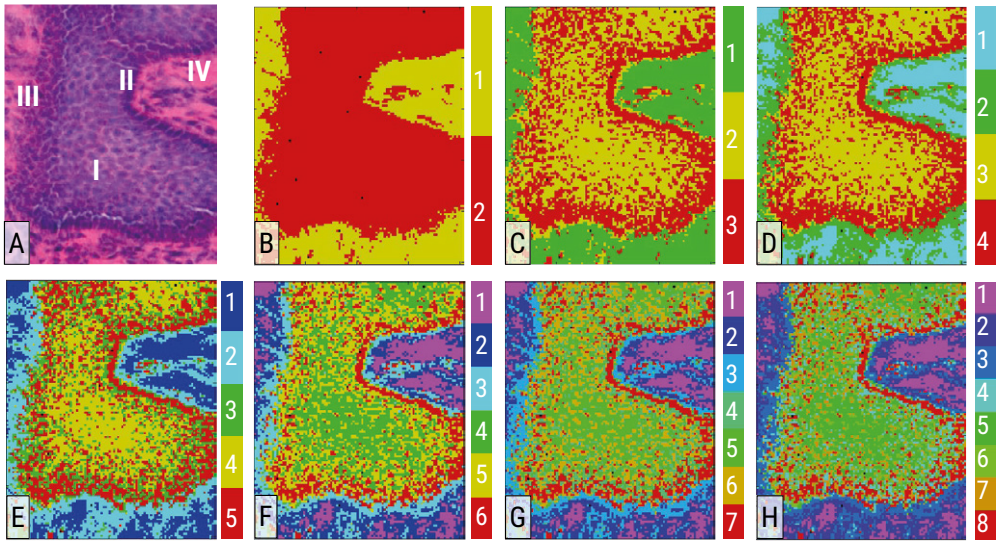

Figure 5. A: Microphotograph (original magnification 100x) of an H&E-stained section of the scanned tissue region. Four different tissue layers/structures were distinguished; [I] superficial layers of squamous epithelium, [II] basal layers of squamous epithelium, [III] lymphocyte rich CT, and [IV] dense connective tissue. B – H: pseudo color Raman images of this experiment are shown with an increasing number of K-means clusters (ranging 2 – 8). The best correlation, representing all identified histopathological structures in a separate cluster, was defined at 6.

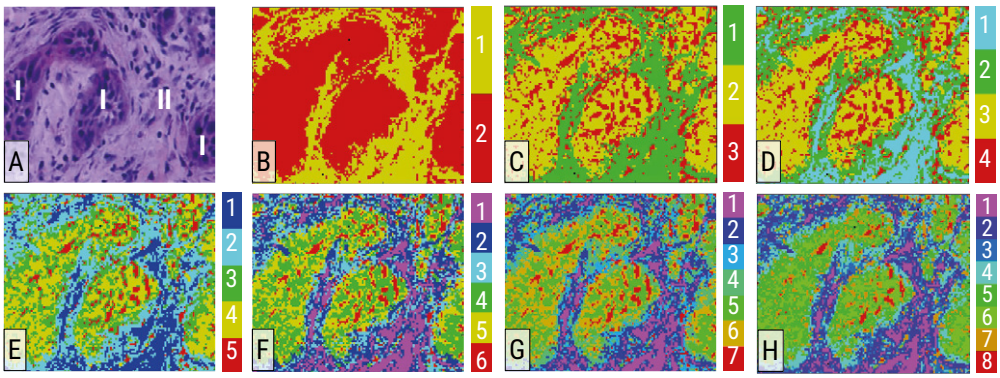

Figure 6. A: Microphotograph (original magnification 100x) of an H&E-stained section of the scanned tissue region. Two different tissue layers/structures were distinguished; [I] poorly differentiated OCSCC and [II] peritumoral stroma. B – H: pseudo color Raman images of this experiment are shown with an increasing number of K-means clusters (ranging 2 – 8). The best correlation, representing all identified histopathological structures in a separate cluster, was defined at 7.

In this way, for each individual experiment, a specific amount of K-means clusters was defined (ranging between 5 and 12), resulting in 140 Raman spectra obtained from the 20 mapping experiments. In total 17 K-means clusters, mostly consisted of just a small amount of pixels, could not be correlated to a

specific structure. Another 9 K-means clusters represented an interface region in between two different histopathological structures. These could neither be annotated as a specific structure. The remaining 114 K-means clusters were annotated as one of the 19 specific histopathological oral tissue structures.

Spectral characteristics and standard deviation of different histopathological structures

In order to determine a spectral average and spectral variance of individual histopathological structures, all annotated Raman spectra were used as input for the HCA. Table 1 shows the results of this HCA. An alphabetical enumeration of the 19 identified histopathological structures is shown in the first column. The second column shows the total number of annotated Raman spectra per histopathological structure acquired from all 20 mapping experiments. In the third column, the number of selected HCA clusters that only comprised Raman spectra with the same annotation is shown. It is clear that for each histopathological structure, multiple HCA clusters were found. The final columns show of how many annotated Raman spectra these HCA clusters consisted. This overview shows that within one histopathological structure, multiple spectroscopic subgroups were present. These spectroscopic subgroups were used to calculate a spectral average with standard deviation, as described in the materials and methods section.

Previous steps are illustrated using the results obtained from one tissue sample. Bright-field microscopic image of the unstained tissue section of this normal oral sample are shown in Figure 7A. In this section, three regions including a variety of histopathological structures were selected for Raman mapping experiments. Figures 7B – 7D shows the magnified images of the unstained regions that were scanned. The pseudo color Raman images (Figures 7E – 7G) are shown that represented the best match to the corresponding regions in the afterwards stained tissue section (Figures 7H – 7J). A comparison between these images reveal that they correlate very well.

Figure 8 shows the averaged spectra of the histopathological structures that were present in the three prior illustrated mapping experiments. Although it was expected that the standard deviation, which is illustrated by a grey shadow around the spectra, was larger whenever more HCA clusters were found, all the standard deviations are remarkably small. No discriminative spectral subgroups could be appointed in these histopathological structures. This might be due to a limited number of annotated Raman spectra obtained from the different samples and patients in the current database. Nevertheless, it enabled us to point out a number of characteristic peaks (highlighted by yellow bars) that differ between these mean spectra. Especially, the slopes between 784 and 938 cm^{-1}, as well as between 1206 and 1370 cm^{-1} are characteristic for each of these histological structures. These slopes look quite alike in the mean spectra of basal and of suprabasal layers of epithelium. Both mean spectra of epithelium are furthermore distinguishable from others by their peaks at 526, 546, 784, 828, 942, 958, 1128, 1318 and 1340 cm^{-1}. Similar looking spectra of (bronchial) epithelium were published before.[16X]

	Histopathological annotation	Number of Raman clusters	Number of HCA clusters	Composition of HCA clusters				
				1	2	3	6	17
1	adipose tissue	7	2	1			1	
2	basal epithelial layers	7	7	7				
3	capillaries	2	2	2				
4	central part of well differentiated OCSCC	1	1	1				
5	collagen fibers	9	7	5	2			
6	dense connective tissue	13	11	9	2			
7	epithelial layer of gland	1	1	1				
8	loose connective tissue	22	13	6	5	2		
9	lymphocyte rich connective tissue	7	6	5	1			
10	lymphocyte rich peritumoral stroma	4	4	4				
11	peripheral nerve	2	1		1			
12	peripheral part of well differentiated OCSCC	1	1	1				
13	peritumoral stroma	15	10	6	3	1		
14	poorly differentiated OCSCC	4	2		2			
15	smooth muscle	3	3	3				
16	superficial layers of epithelium	2	2	2				
17	suprabasal layers of epithelium	11	9	8		1		
18	well differentiated OCSCC with hyperkeratosis	1	1	1				
19	well differentiated OCSCC with parakeratosis	2	1		1			
	interface	9	9	9				
	ignored	17	1					1
	total	**140**	**94**					

Table 1. The results of the HCA are shown.

First column: an alphabetical enumeration of the 19 identified histopathological structures. Second column: total number of annotated Raman spectra per histopathological structure acquired from all 20 mapping experiments. Third column: number of selected HCA clusters that only comprised Raman spectra with the same annotation. Final column: number of annotated Raman spectra included in the HCA clusters.

As expected, the spectra of loose (indicated in light grey) and dense (indicated in dark grey) connective tissue also represent more or less the same molecular composition, when compared to the other structures. These spectra are recognized by their peaks at 570, 820, 858, 876, 922, 1248 cm^{-1}, which are mostly appointed to collagen contribution).[36] The spectral difference between loose and dense connective tissue is based on differences in the amount of contribution of collagen. Adipose tissue (indicated in orange) is the easiest to recognize on its mean spectrum because of some distinctive peaks at 874, 972 1064, 1082, 1264, 1304, 1440, and 1746 cm^{-1}. All these peaks are attributed to lipids),[36] which confirm the correlation with the histological origin. The averaged spectrum of smooth muscle, although just based upon three annotated Raman spectra, show characteristic peaks at 488, 758, 904, 1046, 1104, 1278, 1304, and 1398 cm^{-1}. These peaks can be partly attributed to glycogen (488 and 1046 cm^{-1}) and collagen type I (1278 and 1304 cm^{-1}).[36] A similar looking spectrum of smooth muscle was published before.[16] Using the described

method, distinguishable and characteristic averaged spectra and standard deviation were calculated of a total of 19 individual histopathological structures encountered in oral mucosal samples. This created database will be supplemented in the future by all spectroscopic features present in histopathological structures of oral mucosa. This will be the scope of our future work.

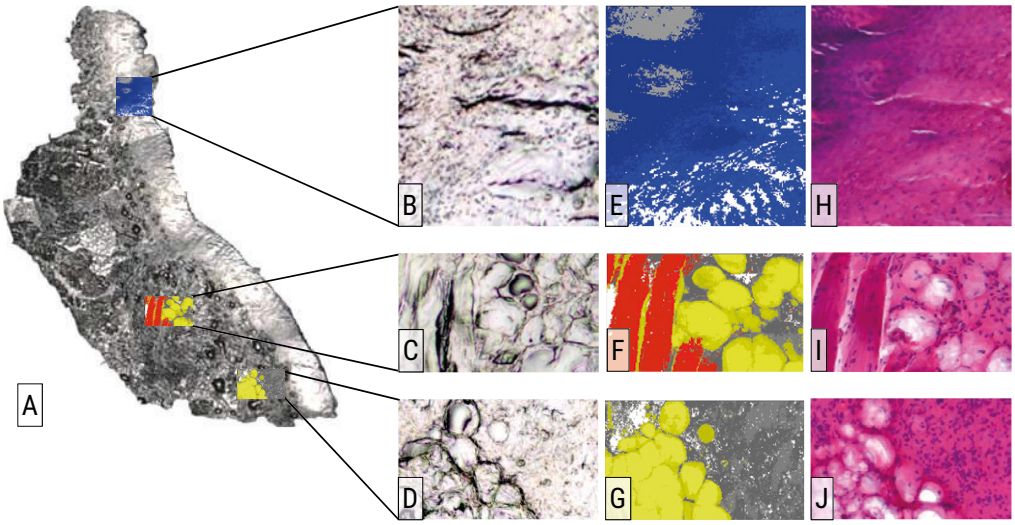

Figure 7. A: In this tissue section, three regions including a variety of histopathological structures were selected for Raman mapping experiments. B – D: show the magnified microphotographs (original magnification 100x) of the unstained regions that were scanned point-by-point. E – G: pseudo color Raman images, which represent the optimal number of K-m means clusters. H – J: microphotographs (original magnification 100x) of the afterwards stained tissue section.

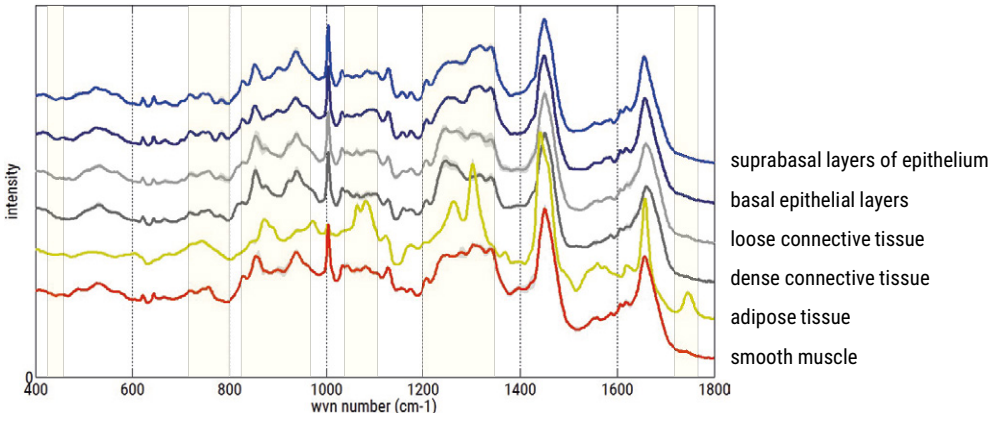

Figure 8. The averaged spectra of the histopathological structures from the Raman mapping experiments shown in Figure 7. The standard deviation is shown in grey shadow around the spectral average. A number of characteristic peaks (highlighted by yellow bars) can be appointed for each spectrum.

DISCUSSION

An earlier and more accurate detection of (small) cancerous and precancerous lesions in the oral cavity is essential to improve the prognosis of OCSCC. Raman spectroscopy is being pursued as a potential technique to realize this improvement, since the technique provides objective information on a biochemical level and can be used for real-time guidance of the diagnostic procedure. To apply Raman spectroscopy for *in vivo* diagnosis of oral mucosal lesions, it is essential to discriminate accurately between normal and malignant transformed tissue. Previous studies repeatedly indicated that the main difference between normal and malignant tissue samples was attributed to lipid features in normal tissue spectra and protein features in the spectra of malignant tissue.[20,21,24,26,28] Our results indicate that this may be due to differences in tissue morphology, rather than to differences in molecular composition.

As OCSCC originates in the epithelial surface, a malignant mucosal sample shows squamous cell differentiation and has an increased epithelium thickness.[29] When a Raman spectrum is obtained from an intact (non-sectioned) normal sample, it may therefore gather more signals from the structures in the deeper tissue layers, in relation to a malignant tissue sample. As mentioned above, previous studies repeatedly concluded that spectral features of normal tissue had predominant lipid signatures. This was particularly indicated by two sharp features assigned to = C-H cis stretch and CH2 twist respectively (1260 and 1300 cm^{-1}), a strong CH2 bend (1440 – 1450 cm^{-1}), a sharp peak in the spectral region of C = C stretch vibrations (1656 – 1660 cm^{-1}) and ester bands (1740 – 1750 cm^{-1}).[21,24,26,28,37] Comparing these peak positions to our calculated mean spectra, strong similarities were detected with the mean spectrum of adipose tissue. Since the deeper submucosal layer is composed of among others adipose tissue, the lipid-dominated spectra of normal samples may be explained by differences in epithelium thickness. However, an increase in epithelial thickness does not automatically imply the presence of carcinoma, and therefore incorrect classification of a sample can occur. Classification algorithms based on lipid to protein ratios may therefore result in diagnostic models with low specificity.

In order to build a diagnostic model with a high specificity, we devised a method to obtain (characteristic) spectral signatures of all histopathological structures that can contribute to an *in vivo* spectrum. The used method of Raman mapping experiments, followed by KCA, resulted in pseudo color Raman images that could be clearly correlated to the afterwards H&E-stained sections. We demonstrated that Raman correlates well with the current gold standard, histopathology. By using the unsupervised HCA, a spectral subdivision in equally annotated Raman spectra occurred. This suggests that Raman results contain even more specific information than histopathology. Within one histopathological structure, some unexplained biochemical variance is present that might be caused by patient, sample, or other structural characteristics. The described method resulted in a database that can be supplemented in future, in order to answer these questions.

The scanning step size of 2 μm enabled us to obtain information about the molecular composition on a cellular level. Moreover, it limited the amount of spectral contribution of neighboring structures, resulting in the purest possible spectral information. However, it also limited the size of the scanned regions within the tissue sections per experiment.

The Raman tissue characterization method described here was devised using a relatively small amount of samples. We are currently using the described method to create an extensive database of histopathologically annotated Raman spectra of oral mucosa and mucosal lesions, based on larger numbers of samples. This database can serve to analyze the spectral characteristics and variance of all histopathological structures in more detail. Specific spectral subgroups within one structure can be selected, which leads to additional useful information for the development of classification and quantification algorithms, in order to improve data interpretation of *in vivo* tissue spectra.

We conclude that *in vitro* Raman mapping experiments, followed by KCA and HCA, can be used as a reproducible method to obtain, identify, and define the spectral characteristics of individual histopathological structures in oral mucosal tissue. As a result, a distinguishable spectral average, including a standard deviation can be calculated for each structure. This provides an insight into the presence of spectral variance within one structure.
We expect that the knowledge of the spectral characteristics of individual histopathological structures will help to develop an accurate diagnostic model that can be used to identify suspect lesions within the oral cavity. We believe that our method provides an essential contribution to the research field on new diagnostic tools in head and neck oncology.

REFERENCES

1. Baatenburg De Jong, Hermans, et al. (2001) *Prediction of survival in patients with head and neck cancer.* Head & Neck. 23(9):718-724.
2. Van Der Schroeff, Steyerberg, et al. (2012) *Prognosis: A variable parameter: Dynamic prognostic modeling in head and neck squamous cell carcinoma.* Head & Neck. 34(1):34-41.
3. Parkin, Bray, et al. (2005) *Global cancer statistics, 2002.* Cancer Journal for Clinicians. 55(2):74-108.
4. Al-Swiahb, Chen, et al. (2010) *Clinical, pathological and molecular determinants in squamous cell carcinoma of the oral cavity.* Future Oncology. 6(5):837-850.
5. Leemans, Tiwari, et al. (1993) *Regional lymph node involvement and its significance in the development of distant metastases in head and neck carcinoma.* Cancer. 71(2):452-456.
6. Rautava, Luukkaa, et al. (2007) *Squamous cell carcinomas arising from different types of oral epithelia differ in their tumor and patient characteristics and survival. Oral Oncology.* 43(9):911-919.
7. Abbey, Kaugars, et al. (1995) *Intraexaminer and interexaminer reliability in the diagnosis of oral epithelial dysplasia.* Oral Surgery Oral Medicine Oral Pathology. 80(2):188-191.
8. Harris, Rennie, et al. (2010) *Raman spectroscopy in head and neck cancer.* Head & Neck Oncology. 2(26):1-6.
9. Jerjes, Upile, et al. (2011) *The future of medical diagnostics: Review paper.* Head & Neck Oncology. 3(38):1-8.
10. Upile, Jerjes, et al. (2009) *Head and neck optical diagnostics: Vision of the future of surgery.* Head & Neck Oncology. 1(25):1-9.
11. Caspers, Lucassen, et al. (2001) *In vivo confocal Raman microspectroscopy of the skin: Noninvasive determination of molecular concentration profiles.* Journal of Investigative Dermatology. 116(3):434-442.
12. Bakker Schut, Witjes, et al. (2000) *In vivo detection of dysplastic tissue by Raman spectroscopy.* Analytical Chemistry. 72(24):6010-6018.
13. Barman, Dingari, et al. (2012) *Selective sampling using confocal Raman spectroscopy provides enhanced specificity for urinary bladder cancer diagnosis.* Analytical and Bioanalytical Chemistry. 404(10):3091-3099.
14. Bergholt, Zheng, et al. (2010) *Raman endoscopy for in vivo differentiation between benign and malignant ulcers in the stomach.* Analyst. 135(12):3162-3168.
15. Bergholt, Zheng, et al. (2011) *In vivo diagnosis of esophageal cancer using image-guided Raman endoscopy and biomolecular modeling.* Technology in Cancer Research and Treatment. 10(2):103-112.
16. Koljenovic, Bakker Schut, et al. (2004) *Raman microspectroscopic mapping studies of human bronchial tissue.* Journal of Biomedical Optics. 9(6):1187-1197.
17. Mahadevan-Jansen, Mitchell, et al. (1998) *Near-infrared Raman spectroscopy for in vitro detection of cervical precancers.* Photochemical and Photobiology. 68(1):123-132.
18. Nijssen, Bakker Schut, et al. (2002) *Discriminating basal cell carcinoma from its surrounding tissue by Raman spectroscopy.* Journal of Investigative Dermatology. 119(1):64-69.
19. Deshmukh, Singh, et al. (2011) *Raman spectroscopy of normal oral buccal mucosa tissues: Study on intact and incised biopsies.* Journal of Biomedical Optics. 16(12):127004-127010.
20. Guze, Short, et al. (2009) *Parameters defining the potential applicability of Raman spectroscopy as a diagnostic tool for oral disease.* Journal of Biomedical Optics. 14(1):161-169.
21. Krishna, Sockalingum, et al. (2004) *Micro-Raman spectroscopy for optical pathology of oral squamous cell carcinoma.* Applied spectroscopy reviews. 58(9):1128-1135.
22. Lau, Huang, et al. (2005) *Raman spectroscopy for optical diagnosis in the larynx: Preliminary findings.* Lasers in Surgery and Medicine. 37(3):192-200.
23. Lin, Cheng, et al. (2012) *Optical diagnosis of laryngeal cancer using high wavenumber Raman spectroscopy.* Biosensors and Bioelectronics. 35(1):213-217.
24. Malini, Venkatakrishna, et al. (2006) *Discrimination of normal, inflammatory, premalignant, and malignant oral tissue: A Raman spectroscopy study.* Biopolymers. 81(3):179-193.
25. Oliveira, Bitar, et al. (2006) *Near-infrared Raman spectroscopy for oral carcinoma diagnosis.* Photomedicine and Laser Surgery. 24(3):348-353.
26. Singh, Deshmukh, et al. (2012) *Raman spectroscopy in head and neck cancers: Toward oncological applications.* Journal of Cancer Research and Therapeutics. 8(2):S126-132.

27. Stone, Stavroulaki, et al. (2000) *Raman spectroscopy for early detection of laryngeal malignancy: Preliminary results.* Laryngoscope. 110(10):1756-1763.
28. Su, Sun, et al. (2012) *Raman spectral properties of squamous cell carcinoma of oral tissues and cells.* Laser Physics. 22(1):311-316.
29. Mills. *Histology for pathologists.* 3rd ed. (2004)
30. Rosai. *Surgical pathology* 10th ed. (2011)
31. Van De Poll, Romer, et al. (2001) *Raman spectroscopic evaluation of the effects of diet and lipid-lowering therapy on atherosclerotic plaque development in mice.* Arteriosclerosis, Thrombosis and Vascular Biology. 21(10):1630-1635.
32. Mason. *Fluorescent and luminescent probes for biological activity.* 2nd ed. (1999)
33. Martens, Stark. (1991) E*xtended multiplicative signal correction and spectral interference subtraction: New preprocessing methods for near infrared spectroscopy.* Journal of Pharmaceutical and Biomedical Analysis. 9(8):625-635.
34. Jolliffe. *Principal component analysis.* 2nd ed. (2002)
35. Jain. *Algorithms for clustering data* 1st ed. (1988)
36. Movasaghi. (2007) *Raman spectroscopy of biological tissues.* Applied spectroscopy reviews. 42(5):493 -541.
37. Wu, Volponi, et al. (2011) *In vivo lipidomics using single-cell Raman spectroscopy.* Proceeding of the National Academy of Sciences. 108(9):3809-3814.

3

Investigation of the potential of Raman spectroscopy for oral cancer detection in surgical margins

Froukje L. J. Cals, Tom C. Bakker Schut, José A. Hardillo,
Robert J. Baatenburg de Jong, Senada Koljenović and Gerwin J. Puppels

Laboratory investigation 2015; DOI 10.1038/labinvest.2015.85

ABSTRACT

The poor prognosis of oral cavity squamous cell carcinoma (OCSCC) patients is associated with residual tumor after surgery. Raman spectroscopy has the potential to provide an objective intra-operative evaluation of the surgical margins. Our aim was to understand the discriminatory basis of Raman spectroscopy at a histological level. In total, 127 pseudo color Raman images were generated from unstained thin tissue sections of 25 samples (11 OCSCC and 14 healthy) of 10 patients. These images were clearly linked to the histopathological evaluation of the same sections after hematoxylin and eosin-staining. In this way, Raman spectra were annotated as OCSCC or as a surrounding healthy tissue structure (i.e. squamous epithelium, connective tissue (CT), adipose tissue, muscle, gland, or nerve). These annotated spectra were used as input for linear discriminant analysis (LDA) models to discriminate between OCSCC spectra and healthy tissue spectra. A database was acquired with 88 spectra of OCSCC and 632 spectra of healthy tissue. The LDA models could distinguish OCSCC spectra from the spectra of adipose tissue, nerve, muscle, gland, CT, and squamous epithelium in 100%, 100%, 97%, 94%, 93%, and 75% of the cases, respectively. More specifically, the structures that were most often confused with OCSCC were dysplastic epithelium, basal layers of epithelium, inflammation- and capillary-rich CT, and connective and glandular tissue close to OCSCC. Our study shows how well Raman spectroscopy enables discrimination between OCSCC and surrounding healthy tissue structures. This knowledge supports the development of robust and reliable classification algorithms for future implementation of Raman spectroscopy in clinical practice.

INTRODUCTION

Inadequate surgery (tumor-positive (≤ 1 mm) or close (> 1 and ≤ 5 mm) resection margins) for oral cavity squamous cell carcinomas (OCSCCs) varies between 30 and 85%.[1] This indicates that currently used visual inspection and tissue palpation by the surgeon are not sufficient to define the borders of the tumor intraoperatively. Frequently, frozen tissue sections are taken during surgery to evaluate whether the margins are tumor-free (so-called frozen tissue section procedure). Although state of the art, this procedure has major limitations such as time-consuming whereby only a small percentage (1 – 5%) of the resection margin can be evaluated.[2] The consequences of tumor-positive resection margins are significant since this often leads to revision surgery, the need for adjuvant therapy (postoperative radiotherapy), and higher morbidity and mortality.[3,4]

Therefore, several optical diagnostic modalities have entered the field of head and neck oncology in the last decades, aiming to support the surgeon in achieving tumor-free resections. The most studied optical techniques include fluorescence,[5-8] optical coherence tomography,[9,10] elastic light scattering spectroscopy,[11] (high resolution) micro endoscopy[12,13] and Raman spectroscopy.[14,15]

Raman spectroscopy is especially suited for intraoperative use since this nondestructive technique does not need any pretreatment or labeling of the tissue. Previously, several groups investigated the potential application of Raman spectroscopy for tumor detection in the head and neck region,[16-18] including the oral cavity.[19-26] Based on the results of *ex vivo* and *in vivo* measurements of oral tissue, it was repeatedly concluded that spectra from normal tissue were recognized by their high lipid content, whereas the spectra from malignant tissue were characterized by their protein features.[20,21,23,25] However, the interpretation of the previously published measurements is not straightforward because no exact correlation was made between the histopathological structures in the tissue volume from which the Raman signal was obtained, and the Raman results.

The different layers and structures in healthy oral cavity tissue have their own specific molecular composition and as a consequence their own specific Raman features. OCSCC of the tongue can be surrounded by any of the different healthy tissue structures. In previous research, we developed a method of collecting detailed spectral information of individual histopathological structures based on *in vitro* Raman mapping experiments.[27]

In the current study, we used that method to create a spectral database that comprises OCSCC and healthy tissue structures of the tongue. We investigated how well the tissue spectra enable discrimination between OCSCC and surrounding healthy tissue structures. We discuss how these results would affect development of classification algorithms and future implementation of Raman spectroscopy in clinical practice.

MATERIALS AND METHODS

Sample handling and sample preparation

This study was approved by the Medical Ethics Committee (MEC-2011-450) of the Erasmus MC Cancer Institute, University Medical Center Rotterdam. At the Department of Otorhinolaryngology and Head and Neck Surgery of the Erasmus MC Cancer Institute, University Medical Center Rotterdam, 25 tissue samples were collected from 10 patients who had undergone surgical resection of a primary OCSCC of the tongue. All patients gave informed consent.

In total, 11 samples contained OCSCC and surrounding healthy tissue structures. These samples were harvested from the surgical resection specimen, more specifically from the center of the macroscopically visible tumor. The 14 normal samples that contained only healthy tissue structures, were harvested from two different locations. Eight samples were harvested from the surgical resection specimen, more specifically from normal-appearing mucosa adjacent to the tumor i.e., between the tumor border and the resection border (Figure 1). Six samples were collected from the contralateral (not-affected site) edge of the tongue.

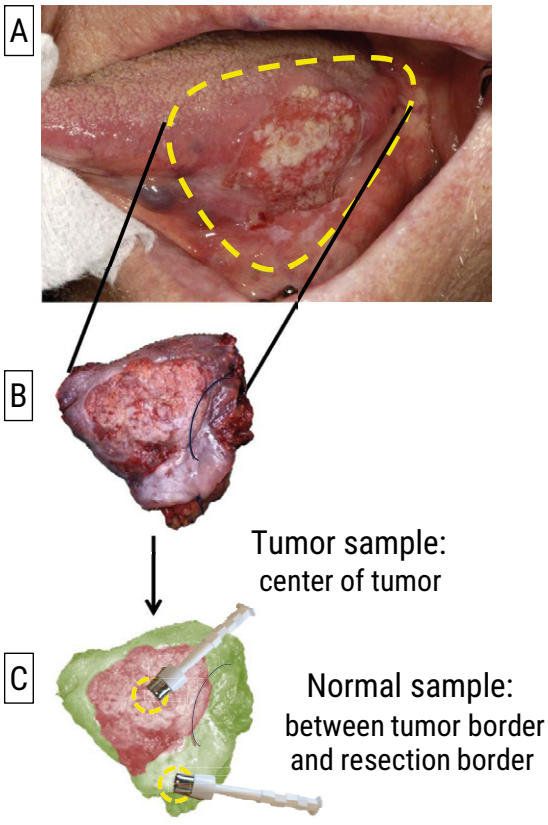

Figure 1. A: OCSCC of the tongue. B: Resection specimen. C: Tumor sample was harvested from the center of the macroscopically visible tumor, and normal sample was taken between the tumor border and the resection border.

All samples were at least 5 × 5 mm in size. Samples from the surgical resection specimen were taken within 60 minutes after surgical excision. Contralateral samples were taken during surgery. The samples were snap frozen by immersion in isopentane and subsequently in liquid nitrogen, and kept at −80°C until further use.

For Raman mapping experiments, the frozen tissue samples were mounted on a cryotome stage using CryoCompound (KP-CryoCompound, Klinipath B.V., the Netherlands). Adjacent 6 µm and 20 µm-thick sections were cut. The 6 µm sections were stained with haematoxylin and eosin (H&E) for histopathological evaluation.[28] The H&E-stained sections were used to select regions for Raman mapping experiments. Corresponding regions were then identified in the unfixed, unstained 20 µm sections that were placed on fused silica windows. These 20 µm sections were allowed to dry at the room temperature and used for the Raman mapping experiments without further treatment. After completing the mapping experiments, the 20 µm sections were also H&E stained.

Raman spectroscopic mapping experiments

Raman spectroscopic mapping experiments were performed using a SpectraCell RA Bacterial Strain Analyzer (RiverD International B.V., Rotterdam, the Netherlands). This instrument was designed as a fully automated inverted confocal Raman microscope for analyzing bacterial samples. After modification of the software, it was used for point-by-point Raman mapping of tissue sections. Each measured point (pixel) represents an individual spectrum.

For each mapping experiment, the selected region was scanned point-by-point in a two-dimensional grid with a step size of 5 µm, and an acquisition time of 1 second per point. About 100 mW of laser light (785 nm) was focused to a spot of 2 µm in diameter, using a custom made infinity corrected objective with an NA of 0,7 and a magnification of 14 (RiverD International B.V.). Raman scattered light was collected in the wavenumber interval from 300 to 2500 cm^{-1} with a spectral resolution of 4 cm^{-1}, using a custom made reflection grating with 1650 lines/mm (RiverD International B.V.).

Data preprocessing

The data preprocessing is described in detail in previous work.[27] Briefly, for each individual mapping experiment, the Raman data were processed and analyzed with software developed in-house that operates in a MATLAB environment (MATLAB 7.5.0 (R2007b), MathWorks, MA, USA) and uses the multivariate toolbox PLS-toolbox 7.0.0c (EigenVector Research, WA, USA). After removing cosmic ray events, the raw data were calibrated. Extended multiplicative signal correction combined with spectral interference subtraction[29] was used to eliminate all non-informative interfering signals, comprising signal of the fused silica window, CryoCompound, blood, carotenoid (Sigma-Aldrich Chemie B.V., The Netherlands), hydroxyapatite (Sigma-Aldrich Chemie B.V., The Netherlands), and background fluorescence, as described earlier.[27] The contributions of carotenoid and hydroxyapatite represented biological signals that were considered non-informative, since these signals showed a large influence on the scaling procedure, resulting in non-informative differences between similar histopathological structures in different Raman experiments. Finally, the wavenumber range of the spectra that were included in the data-analysis was restricted to the 400 – 1800 cm^{-1}.

Data processing

Processing of the Raman map spectra was done as described in previous work.[27] Briefly, principal components analysis (PCA) was used to reduce the data set without significant loss of information.[30] All data were mean-centered before PCA. The first 20 PCA scores accounted for more than 99,5% of the variance present. These PCA scores were grouped using K-means cluster analysis (KCA).[31] From the KCA results, a pseudo color Raman image was generated by assigning a color to each cluster and by plotting the cluster membership of each spectrum as a colored pixel at its measurement position.

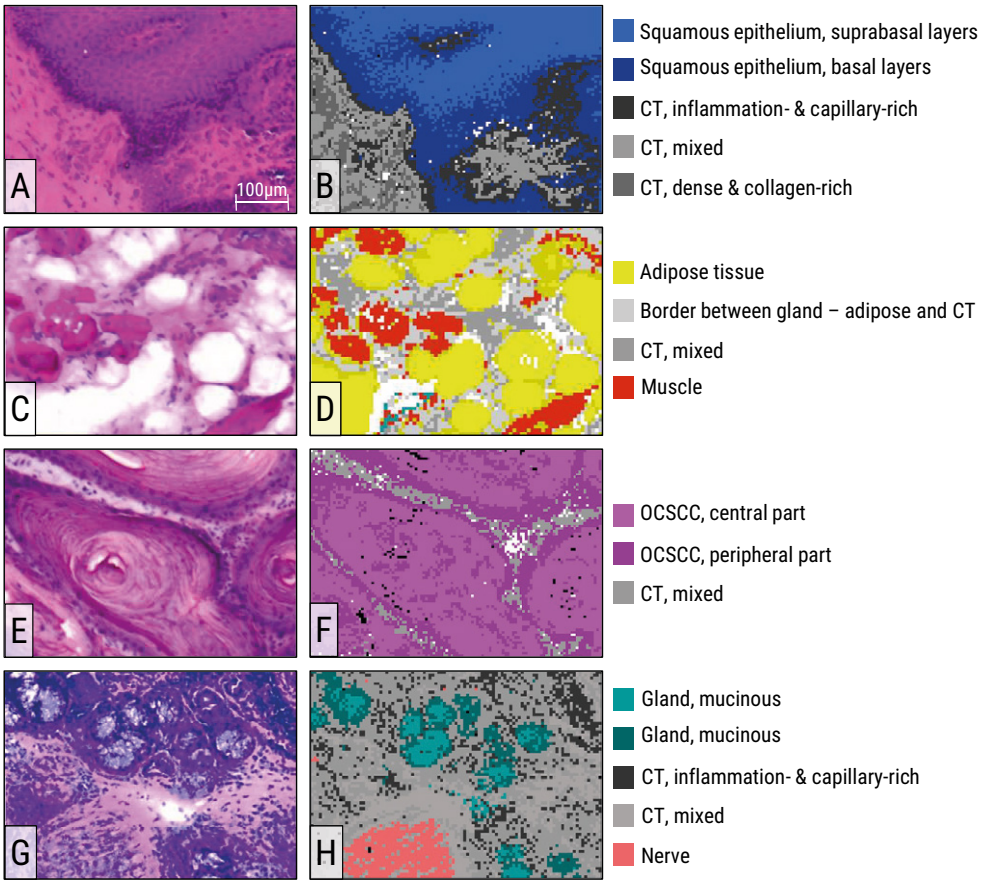

Figure 2. A, C, E and G: H&E-stained tissue sections. B, D, F and H: corresponding pseudo color images. The K-means cluster averages were annotated as one of the following tissue structures: OCSCC (central part, peripheral part, or not otherwise specified), squamous epithelium (superficial layers, suprabasal layers, or basal layers), CT (dense and collagen-rich, mixed, or inflammation- and capillary-rich), gland (mucinous or serous), muscle, adipose tissue, or nerve.

Histopathologically annotated Raman spectra

After the Raman mapping experiment and H&E staining, a trained pathologist identified the histopathological structures that were present in the scanned region. For each experiment, the optimal number of K-means clusters was defined, based on the best match between histopathological structures that were present in the mapped region and the pseudo color Raman image, as described in detail earlier.[27] Figure 2 shows representative examples of H&E-stained sections and their corresponding pseudo color Raman images (Figure 2). The pathologist was blinded for the corresponding spectra.

These K-means cluster averages were selected on the basis of sufficient signal-to-noise ratio, and on an adequate cluster size to allow histopathological annotation. The signal was calculated as the peak height at CH2 (1448 cm^{-1}), and the noise was estimated from the signal part between 1770 and 1800 cm^{-1} where no signal is present. Clusters with a signal-to-noise ratio < 30 were excluded, to ensure that low spectral quality was of no influence to the model, especially for small clusters consisting of few spectra. The cluster size was expressed as percentage (number of representing pixels/total number of pixels in the map). A percentage of ≤ 5% was used as an exclusion criterion.

The remaining K-means cluster averages were then annotated as one of the following tissue structures: [1] OCSCC, [2] squamous epithelium, [3] connective tissue (CT), [4] gland, [5] muscle, [6] adipose tissue, or [7] nerve, as shown in Figure 2. The K-means cluster averages served as histopathologically annotated Raman spectra, and are hereafter called annotated Raman spectra.

The annotated Raman spectra were further subdivided based on the histopathological heterogeneity of corresponding tissue areas. In this way the OCSCC spectra were subdivided in: [1a] central part, [1b] peripheral part, or [1c] OCSCC not otherwise specified (n.o.s.). Squamous epithelium spectra were subdivided in: [2a] superficial layers, [2b] suprabasal layers, or [2c] basal layers. The CT contains varying amounts of collagen (bundles), blood vessels, and lymphocytes. Accordingly, three subtypes were distinguished: [3a] dense and collagen-rich CT, [3b] mixed CT, and [3c] inflammation-and capillary-rich CT. This second subtype contains loose CT, CT with less collagen, CT with blood vessels, or a mixture of different CT subtypes. Gland spectra were subdivided in: [4a] mucinous and [4b] serous. Figure 3 shows an H&E-stained tissue section which illustrates these subdivisions.

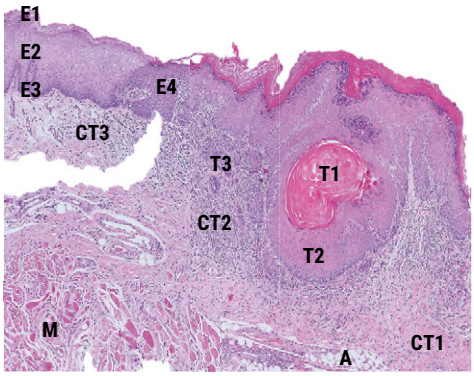

Figure 3. Microphotograph (magnification × 16) of an H&E-stained tissue section of a tumor sample. The squamous epithelium can be divided into three layers; superficial layers (E1), suprabasal layers (E2), and basal layers (E3). The epithelium changes toward the right into dysplastic epithelium (E4). An OCSCC (T1 – T3) arises from this dysplasia and can be divided into central part (T1) and peripheral part (T2) or not otherwise specified (n.o.s.) (T3). The underlying lamina propria and submucosa consist of CT that can be divided into dense and collagen-rich CT (CT1), inflammation- and capillary-rich CT (CT2), or mixed CT (CT3). Adipose tissue (A) and muscle tissue (M) are also found in the submucosa.

A second subdivision of the OCSCC spectra was based on the differentiation grade of the measured tumor: [I] moderately differentiated, [II] moderately to poorly differentiated, or [III] poorly differentiated OCSCC.[32] A second subdivision of the squamous epithelium spectra was based on the presence or absence of dysplastic changes; [i] dysplasia, or [ii] no dysplasia.[32] Finally, the spectra of the healthy tissue structures ([2] squamous epithelium, [3] CT, [4] gland, [5] muscle, [6] adipose tissue, and [7] nerve) were subdivided depending on their distance to OCSCC. Spectra that were measured in normal (tumor-free) samples were divided in: [A] harvested contralateral (not-affected site of the tongue), [B] harvested adjacent to OCSCC (between tumor border and resection border). Healthy tissue structures that were measured in samples that contained regions of OCSCC were annotated as [C] close to the tumor. Spectra that could not be histologically annotated were excluded.

Hierarchical cluster analysis

The annotated Raman spectra of all experiments together were used as input in an unsupervised hierarchical cluster analysis (HCA). The output of HCA is a membership matrix (N × N, where N is the number of spectra) that represents the clustering at each level of agglomeration.[31] The HCA results were used to determine the spectral average and standard deviation, for each histopathological annotation as described earlier.[27] The spectral average represents the overall molecular composition of a histopathological structure. The standard deviation provides insight into the variance in biochemical composition within the histopathological structure.

Linear discriminant analysis

To investigate how well the tissue spectra enabled discrimination between OCSCC and the six surrounding healthy tissue structures, a linear discriminant analysis (LDA) was used.[33] Six separate LDA models were made, using the scores of the PCA of the annotated Raman spectra as input variables. Each model was tested by leave-one-patient-out (LOPO) analysis, i.e. the models were trained using a subset of nine patients and tested on the remaining one patient. For each model, the optimal number of input parameters was determined by the best result in the LOPO analysis. To prevent overfitting of the LDA model, the amount of input parameters was in all cases smaller than half the number of annotated Raman spectra in the smallest group. The classification accuracy (proportion of true results, both true positives and true negatives) served as a measure for discriminative power.

RESULTS

Histopathologically annotated database

A total of 127 Raman mapping experiments were performed on 25 samples from 10 patients (11 samples contained OCSCC and surrounding healthy tissue structures, and 14 samples contained only healthy tissue structures). The scanned areas ranged between 405 × 150 µm and 1005 × 470 µm. The step size of 5 µm resulted in 2700 to 24 426 pixels per experiment (mean number of pixels per experiment: 11 538).

The optimal number of K-means clusters varied between 4 and 20, resulting in a total of 1114 K-means clusters.
Seven hundred-twenty K-means clusters were annotated based on histopathological correlation of the scanned tissue regions. In total 88 K-means clusters were annotated as OCSCC, 140 as squamous epithelium, 396 as CT, 41 as muscle, and 33 as adipose tissue. Gland and nerve were both underrepresented in our samples with 17 and 5 annotated Raman spectra, respectively. The spectral averages and standard deviations of these seven histopathological tissue structures are shown in Figure 4.

In total, 394 K-means cluster averages were excluded from further analysis. These excluded K-means clusters represented 17% of the total number of pixels of all experiments together. Examples of the excluded K-means spectra are shown in Supplementary Figure S1. First, 216 K-means clusters did not pass the inclusion criteria. For 62 clusters, the signal-to-noise ratio was < 30. The average signal-to-noise ratio of all included spectra was 279 (range: 52 – 999). The other 154 clusters only represented a few pixels (≤ 5%) in the scanned regions which made exact histopathological correlation impossible. Another 178 K-means clusters were excluded to prevent addition of non-representative contribution to the spectral averages. These include 65 clusters that represented borders between two different tissue structures, and that therefore reveal a composition of the spectral features of both tissue structures. For 83 clusters, no reliable correlation with histopathology was possible, because these clusters consisted of single pixels dispersed throughout several tissue structures in the pseudo color Raman images. For 20 clusters, contamination or tissue loss during the cutting and H&E staining procedure prevented a reliable correlation. Last, 17 clusters were excluded because they represented structures that were rarely encountered in our samples, such as parakeratotic layers of epithelium and gland's duct.

Distinction between OCSCC and its surrounding healthy tissue structures

To investigate how well OCSCC could be distinguished from the six healthy tissue structures, we made six separate LDA models based on the whole spectrum (i.e. OCSCC vs squamous epithelium; OCSCC vs CT; OCSCC vs gland; OCSCC vs muscle; OCSCC vs adipose tissue, and OCSCC vs nerve). The results of each classification model are given below.

OCSCC vs squamous epithelium

Similar to the OCSCC spectrum (pink spectrum Figure 5A), the average spectrum of squamous epithelium (blue spectrum Figure 5A) is dominated by proteins (peaks at 668, 782, 830, 936, 1004, 1156, 1174, 1208, 1302, 1316, 1448, 1514, and 1656 cm-1).[34] The major differences between these spectra are caused by the more intense peaks at 902, 936, and 1656 cm^{-1} in the squamous epithelium spectrum, and the more intense peaks at 878, 990, 1064, and 1448 cm^{-1} in the average OCSCC spectrum (enlarged details in Figure 5B). The LDA model classified 39 of the 140 squamous epithelium spectra as OCSCC, and 17 out of 88 OCSCC spectra as squamous epithelium (Figure 5C). This resulted in a classification accuracy of 75%.

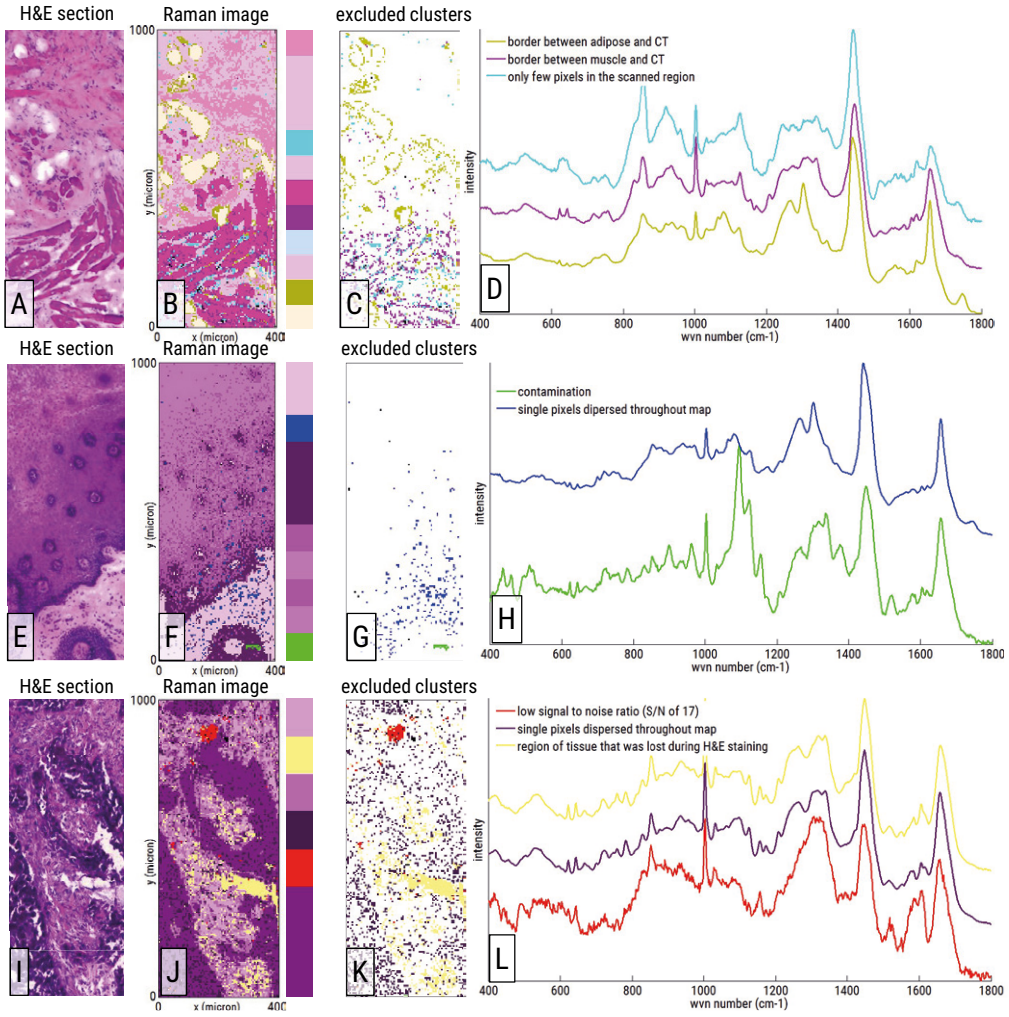

Figure S1. A, E and I: Microphotograph (magnification 16x) of scanned regions in H&E-stained tissue sections. B, F and J: corresponding pseudo color Raman images. C, G and K: K-means clusters that could not be histologically annotated and were therefore excluded from further analysis. D, H and L: Corresponding spectral averages of excluded K-means clusters.

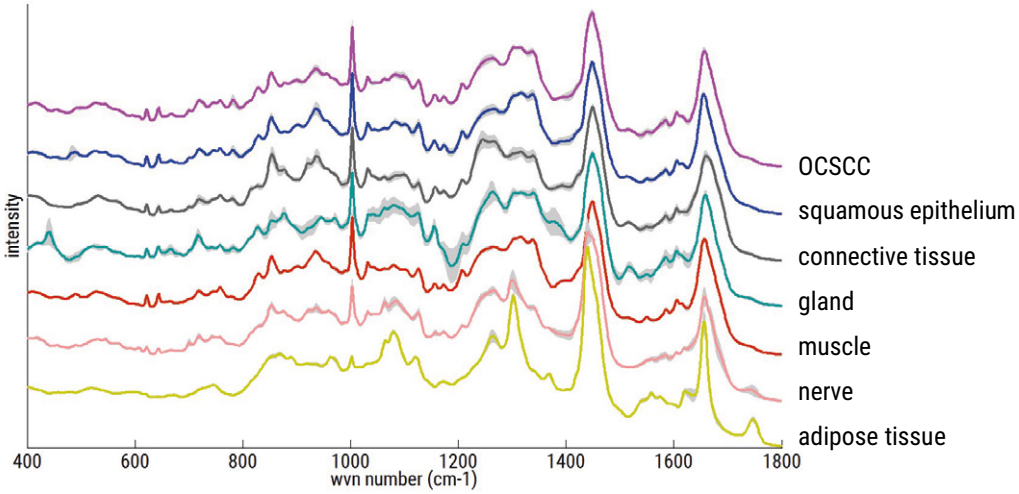

Figure 4. Average spectra ± standard deviation of all individual histopathological structures; OCSCC (pink), squamous epithelium (blue), connective tissue (gray), gland (teal), muscle (red), nerve (salmon), and adipose tissue (yellow).

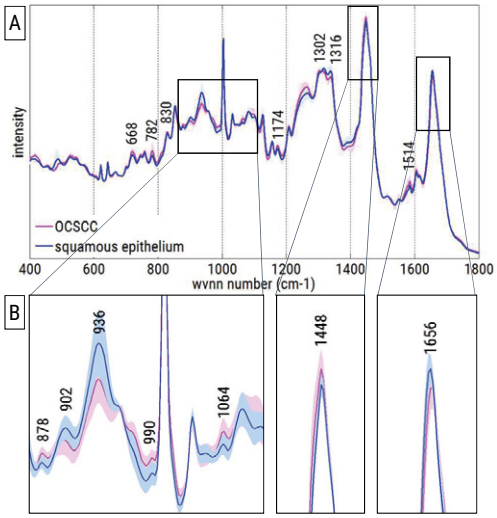

C

Raman classification	histopathological annotation: OCSCC	histopathological annotation: squamous epithelium
OCSCC	71	39
squamous epithelium	17	101
% correct	81	72
accuracy	75%	

Figure 5. A: The average spectra ± standard deviation of OCSCC (pink) and squamous epithelium (blue). B: Enlarged details showing the most striking differences. C: Confusion table.

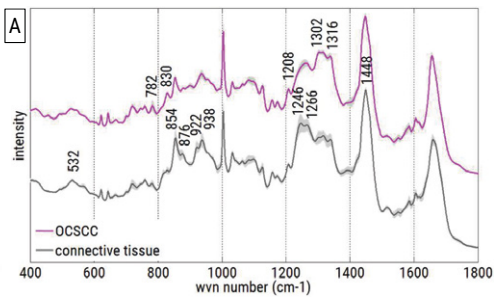

B

Raman classification	histopathological annotation: OCSCC	histopathological annotation: connective tissue
OCSCC	76	21
connective tissue	12	375
% correct	86	95
accuracy	93%	

Figure 6. A: The average spectra ± standard deviation of OCSCC (pink) and CT (gray). B: Confusion table.

OCSCC vs CT

The most discriminative region of the mean CT spectrum (gray spectrum Figure 6A) is attributed to collagen (peaks at 532, 854, 876, 922, 938, 1246, 1266, and 1448 cm^{-1}).[34] The LDA model classified 21 out of 396 CT spectra as OCSCC, and 12 out of 88 OCSCC spectra as CT (Figure 6B). This resulted in a classification accuracy of 93%.

OCSCC vs gland

Glandular tissue was not often encountered in our samples. Since the mean spectrum was based on spectra of two different types of gland tissue (serous and mucinous) the standard deviation was larger than in other tissue types (Figure 4). Nevertheless the characteristic peaks (440, 718, 874, 1042, 1114, 1156, 1376, and 1518 cm^{-1}) of the mean gland spectrum (teal spectrum Figure 7A) were striking compared with the average OCSCC spectrum (pink spectrum Figure 7A). The LDA model classified 6 out of 17 gland spectra as OCSCC, but none of the 88 OCSCC spectra as gland (Figure 7B), resulting in a classification accuracy of 94%.

OCSCC vs muscle

The spectral features of OCSCC (pink spectrum Figure 8A) and muscle (red spectrum Figure 8A) are quite similar; however some clear differences are visible. Peaks at 546, 782, 1084, and 1096 cm^{-1} were present in the average OCSCC spectrum but were absent in the muscle spectrum. The peaks at 936, 1042, and 1396 cm^{-1} were more intense in the muscle spectrum, compared with the OCSCC spectrum (enlarged details in Figure 8B). The LDA model classified 1 out of 41 muscle spectra as OCSCC, and 3 out of 88 OCSCC spectra as muscle (Figure 8C), resulting in a classification accuracy of 97%.

OCSCC vs adipose tissue and OCSCC vs nerve

The average spectra of nerve (salmon spectrum Figure 9A) and adipose tissue (yellow spectrum Figure 9A) mainly represent lipids (peaks at 962, 1064, 1080, 1302, 1368, 1440, 1558, 1656, and 1744 – 1748 cm^{-1}),[34] whereas the average spectrum of OCSCC (pink spectrum Figure 9A) is dominated by protein signals (peaks at 668, 782, 830, 936, 1004, 1156, 1174, 1208, 1316, 1448, 1514, and 1656 cm^{-1}).[34] Thanks to these large differences in lipid protein ratios both LDA models showed a classification accuracy of 100% (Figure 9B).

Analysis of misclassifications by the use of subdivisions

Highly accurate discrimination between OCSCC and the majority of healthy tissue structures was possible (CT: 93%, gland: 94%, muscle: 97%, adipose tissue: 100%, and nerve: 100%), with the exception of squamous epithelium (75%). A detailed overview of the misclassifications is given in Table 1.

The spectra of OCSCC, squamous epithelium, CT, and gland, each showed a large variance around their mean (Figure 4). This reflects the heterogeneity in their histopathological annotations. To understand the cause of the misclassifications, we used further subdivisions of these tissue structures (as described in the materials and methods section).

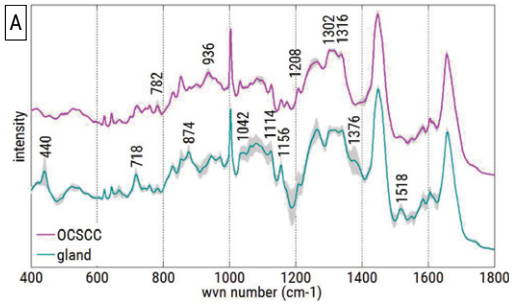

B

Raman classification	histopathological annotation: OCSCC	histopathological annotation: gland
OCSCC	88	6
gland	0	11
% correct	100	65
accuracy	94%	

Figure 7. A: The average spectra ± standard deviation of OCSCC (pink) and gland (teal). B: Confusion table.

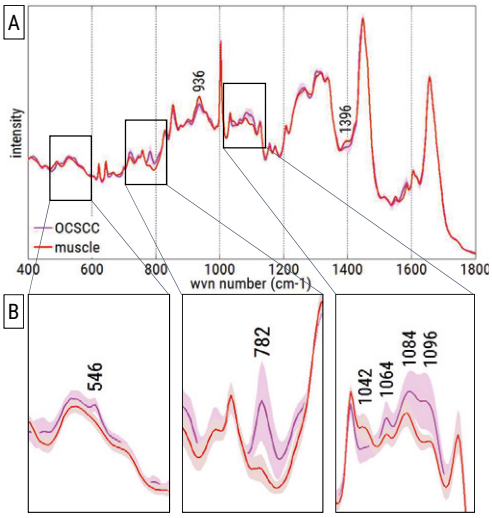

C

Raman classification	histopathological annotation: OCSCC	histopathological annotation: muscle
OCSCC	85	1
muscle	3	40
% correct	97	98
Accuracy	97%	

Figure 8. A: The average spectra ± standard deviation of OCSCC (pink) and muscle (red). B: Enlarged details showing the most striking differences. C: Confusion table.

Misclassifications in squamous epithelium

Of the 140 spectra annotated as squamous epithelium, 101 were correctly classified (72%), and 39 were misclassified as OCSCC. The spectra that represented the superficial layers were more often correctly classified as epithelium (84% (37/44)), than the suprabasal layers (78% (31/40)) or basal layers (59% (33/56)), as shown in Supplementary Figure S2.

Spectra that represented squamous epithelium without dysplasia were more often correctly classified as squamous epithelium (78% (87/111)), than the squamous epithelium with dysplasia (48% (14/29)) (Supplementary Figure S2).

The percentage of correct classifications was higher for squamous epithelium in the contralateral normal samples (91% (31/34)), than in the adjacent harvested normal samples (58% (40/69)), or than for squamous epithelium from the samples that contained OCSCC (81% (30/37)) (Table 1). This might be related to previous observation since less dysplasia was seen in the contralateral samples.

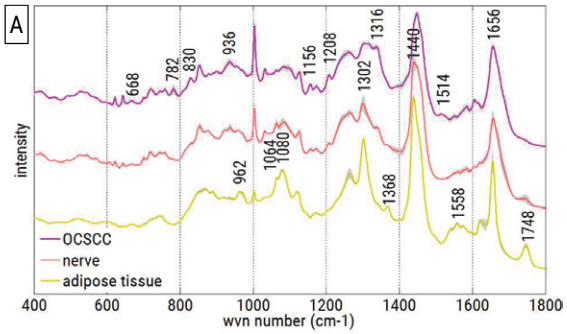

B

Raman classification	histopathological annotation: OCSCC	adipose tissue	nerve
OCSCC	88	0	0
adipose tissue	0	33	-
nerve	0	-	5
% correct	100	100	100
accuracy	100%		

Figure 9. A: The average spectra ± standard deviation of OCSCC (pink), adipose tissue (yellow) and nerve (salmon). B: Confusion table.

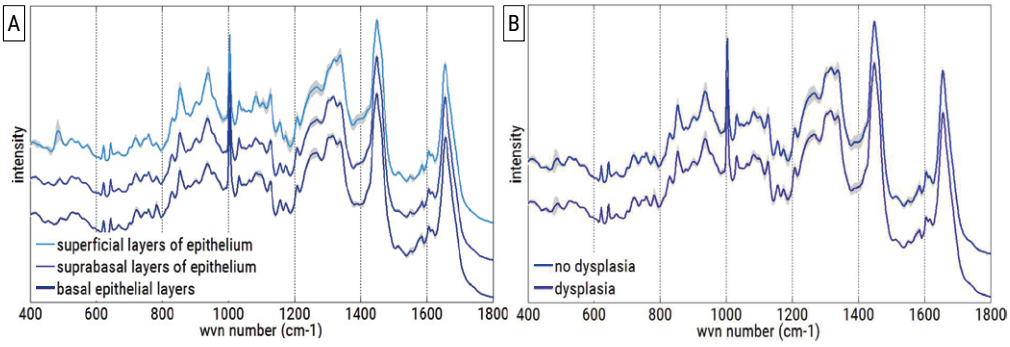

C

Raman classification	histopathological annotation: squamous epithelium	superficial layers	suprabasal layers	basal layers	no dysplasia	dysplasia
OCSCC	101	37	31	33	87	14
squamous epithelium	39	7	9	23	24	15
% correct	72	84	78	59	78	48

Figure S2. A and B: Average spectra ± standard deviation of subdivisions in squamous epithelium. C: Confusion table.

Misclassifications in CT

Of the 396 spectra annotated as CT, 375 were correctly classified (95%) and 21 were misclassified as OCSCC. The spectra that represented dense and collagen-rich CT were correctly classified as CT in 100% (62/62), whereas mixed CT was correctly classified in 97% (269/278) and inflammation-and capillary-rich CT in 79% (44/56), as shown in Supplementary Figure S3.

The percentage of correct classifications was lowest for CT in the samples containing OCSCC (92% (144/157)), than for CT measured in normal samples harvested adjacent to OCSCC (between tumor border and resection border) (97% (134/138)) or harvested contralateral (not-affected site of the tongue) (96% (97/101)) (Table 1).

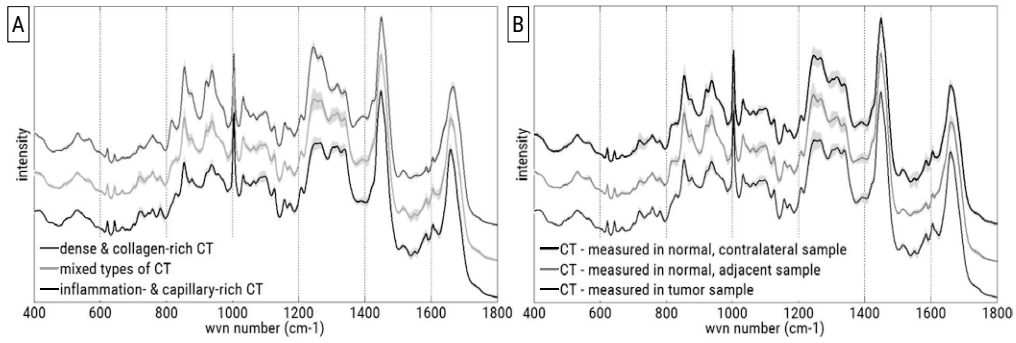

C

Raman classification	histopathological annotation: CT	dense & collagen-rich	mixed types	inflamm. & capillary-rich	normal, contralateral sample	normal, adjacent sample	tumor sample
OCSCC	375	62	269	44	97	134	144
CT	21	0	9	12	4	4	13
% correct	95	100	97	79	96	97	92

Figure S3. A and B: Average spectra ± standard deviation of subdivisions in CT. C: Confusion table.

Misclassifications in gland

Of the 17 spectra annotated as gland, 11 were correctly classified (65%) and 6 were misclassified as OCSCC. The mucinous gland spectra were more often correctly classified as OCSCC (79% (11/14)), than the serous gland spectra (0% (0/3)), as shown in Supplementary Figure S4.

The percentage of correct classifications was higher for gland measured in the contralateral normal samples (100% (5/5)), than measured in adjacent harvested normal samples (86% (6/7)) or than samples containing OCSCC 0% (0/5)) (Table 1).

		Correct	%	Annotations	Correct	%	Subdivision	Correct	%
Samples containing only healthy tissue structures	Harvested **contralateral** (from not-affected site of the tongue)	170/177	96%	**squamous epithelium**	31/34	91%	superficial layers	10/10	100%
							suprabasal layers	9/9	100%
							basal layers	12/15	80%
				CT	97/101	96%	dense & collagen- rich	21/21	100%
							mixed types	75/77	97%
							inflamm. & capill.- rich	1/3	33%
				gland	5/5	100%	mucinous	5/5	100%
				muscle	16/16	100%			
				adipose tissue	20/20	100%			
				nerve	1/1	100%			
				excluded	136				
	Harvested **adjacent** to OCSCC (from surgical resection specimen; between tumor border and resection border)	222/257	86%	**squamous epithelium**	40/69	58%	superficial layers	16/23	70%
							suprabasal layers	13/20	65%
							basal layers	11/26	42%
				CT	134/138	97%	dense & collagen- rich	31/31	100%
							mixed types	87/89	98%
							inflamm. & capill.- rich	16/18	89%
				gland	6/7	86%	mucinous	6/7	86%
				muscle	26/27	96%			
				adipose tissue	13/13	100%			
				nerve	3/3	100%			
				excluded	106				

	Correct	%	Annotations	Correct	%	Subdivision	Correct	%
Samples containing OCSCC and healthy tissue structures	183/208	88%	**squamous epithelium**	30/37	81%	superficial layers	11/11	100%
						suprabasal layers	9/11	82%
						basal layers	10/15	67%
			CT	144/157	92%	dense & collagen- rich	10/10	100%
						mixed types	107/112	96%
						inflamm. & capill.- rich	27/35	77%
			gland	0/5	0%	mucinous		
						serous		
			muscle	8/8	100%			
			nerve	1/1	100%			
			excluded	152				

Table 1. The number of correct classified spectra per histological annotation is shown.
Distinction was made between the normal samples (containing only healthy tissue structures) that were harvested contralateral (not-affected site of the tongue) and that were harvested adjacent to OCSCC (between tumor border and resection border), and tumor samples that contained OCSCC and healthy tissue structures.

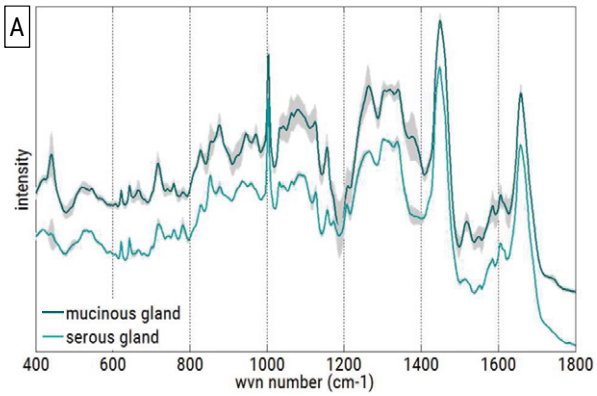

B

Raman classification	histopathological annotation: gland	mucinous	serous
OCSCC	6	3	3
gland	11	11	0
% correct	65	79	0

Figure S4. A: Average spectra ± standard deviation of subdivisions in gland. B: Confusion table.

Misclassifications in OCSCC

OCSCC vs squamous epithelium

Out of 88 spectra annotated as OCSCC, 71 were correctly classified (81%), and 17 were classified as squamous epithelium by the (OCSCC vs squamous epithelium) LDA model.

The spectra that represented the peripheral part were more often correctly classified as OCSCC (91% (21/23)) than the central part (72% (13/18)) or the OCSCC n.o.s. (79% (37/47)), as shown in Supplementary Figures S5A and S5C.

OCSCC vs CT

Out of 88 spectra annotated as OCSCC, 76 were correctly classified (86%) and 12 were classified as CT by the (OCSCC vs CT) LDA model.

The OCSCC spectra that represented the central part were correctly classified in 100% (18/18). More misclassifications occurred in the peripheral part 78% (18/23)), and in OCSCC n.o.s. (85% (40/47)), as shown in Supplementary Figures S5A and S5D.

Differentiation grade

In both distinctions (OCSCC vs squamous epithelium and OCSCC vs CT) the percentage of correct classifications was higher in the poorly differentiated OCSCC (93% (28/30)) and (90% (27/30)), than in the

moderately differentiated OCSCC (81% (29/36) and 83% (30/36)) and moderately to poorly differentiated OCSCC (64% (14/22) and 86% (19/22) (Supplementary Figures S5B – S5D).

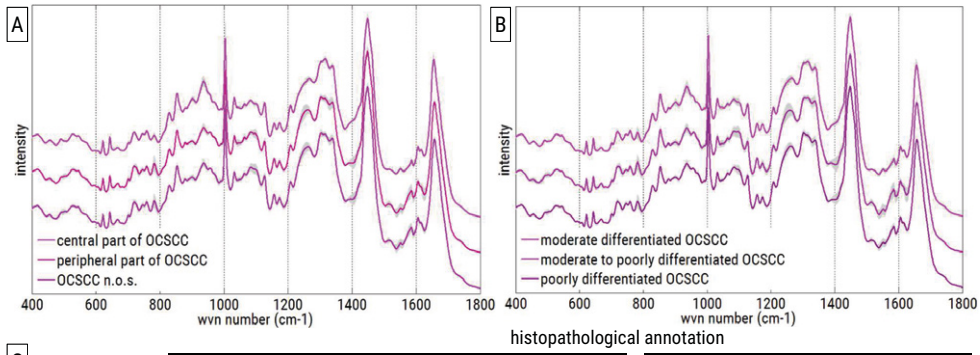

histopathological annotation

C

Raman classification	OCSCC	central part	peripheral part	OCSCC n.o.s.	moderately	moderate to poorly	poorly
OCSCC	71	13	21	37	29	14	28
epithelium	17	5	2	10	7	8	2
% correct	81	72	91	79	81	64	93

histopathological annotation

D

Raman classification	OCSCC	central part	peripheral part	OCSCC n.o.s.	moderately	moderate to poorly	poorly
OCSCC	76	18	18	40	30	19	27
CT	12	0	5	7	6	3	3
% correct	86	100	78	85	83	86	90

Figure S5. A and B: Average spectra ± standard deviation of subdivisions in OCSCC. C and D: Confusion tables.

DISCUSSION

Our ultimate goal is to develop an algorithm that helps the surgeon to achieve tumor-free resection margins and as a result improve the outcome of patients with OCSCC. The future implementation of such classification algorithm in clinical practice is dependent on the discriminatory power of Raman spectroscopy. To understand the discriminatory basis of Raman spectroscopy at a histological level, we performed experiments in which spectra and tissue locations (from which the spectra were obtained) were clearly linked. This has enabled us to identify which healthy tissue structures were difficult to distinguish from OCSCC.

OCSCC can be spectrally distinguished from most subepithelial healthy tissue structures with high accuracy (≥ 97% correct discrimination between OCSCC and adipose tissue, nerve, and muscle). Squamous epithelium, CT, and gland were the healthy tissue structures that were most often confused with OCSCC.

Most misclassifications occurred in the distinction between OCSCC and squamous epithelium, especially in the basal layers of epithelium, the dysplastic squamous epithelium, and in the epithelium measured in the samples that contained OCSCC. This is not surprising because OCSCC originates in the epithelial surface (Figure 3). In carcinogenesis, stem cells located in the basal layers of the epithelium acquire genetic alterations, followed by clonal expansion.[35] Normal epithelium alters in dysplastic epithelium, which is more often seen adjacent to invasive oral carcinomas[36] and is considered to be a premalignant disease. As a consequence, the biochemical composition of both tissue structures shows high similarity. Due to clonal expansion of stem cells in the basal layers, the lamina propria is pushed away, and invasion through the basal membrane follows. An OCSCC can develop from well differentiated to moderately differentiated to poorly differentiated OCSCC.[37,38] In each step the similarity with the original squamous epithelium will become smaller. This might explain that moderately differentiated OCSCC is more often correctly classified.

Irrespective of the distance to OCSCC, inflammation- and capillary-rich CT was most often misclassified in the OCSCC vs CT model. This type of CT is more often seen close to tumor (Figure 3). This is caused by two reasons: [1] tumor development is accompanied by an immune response that leads to massive tumor infiltration by inflammatory cells[39] and [2] a relatively higher amount of capillaries is present in the CT around the tumor because OCSCC creates new blood supply by stimulating endothelial cell proliferation and formation of new blood vessels.[40] This can probably explain why most misclassifications occurred in this type of CT as well as the higher percentage misclassifications in the CT in the samples containing tumor.

Furthermore, the higher percentage of misclassifications in the peripheral part of OCSCC might be explained by the epithelial-mesenchymal transition (EMT). EMT occurs at the periphery of a tumor and is characterized by the loss of epithelial characteristics.[41] EMT has a role in invasion and metastasis of cancer cells.[42]

However, the clinical relevance of these possible misclassifications is questionable. First, the imperfect discrimination between OCSCC and squamous epithelium will not necessarily influence the potential for intraoperative application of Raman spectroscopy. The majority of residual tumor is namely located in the subepithelial, deeper tissue layers. Woolgar et al.[43] described that < 2% of the resection specimens had solely an involved mucosal margin, whereas 87% of the involved margins was located in the deep soft tissue. In the future it might be an option to develop an algorithm that deals with the real clinical problem by excluding squamous epithelium and discriminating tumor only from the subepithelial healthy structures.

Second, regarding the misclassifications in the CT, it has to be mentioned that in clinical practice a margin of at least 1 cm around the tumor is resected to ensure an adequate resection. A part of inflammation- and capillary-rich CT, as well as the CT close to the tumor will most likely be resected anyway within the 1 cm margin, independent on an intraoperative classification by Raman. However, for algorithm development, this is important to know since over resection (and as a result a less functional organ) by expanding the border beyond the 1 cm margin is also not desirable.

In this study, we determined how well Raman spectroscopy enables discrimination between OCSCC and surrounding healthy tissue structures. This provided knowledge that supports the development of robust and reliable classification algorithms for future implementation of Raman spectroscopy in clinical practice.

REFERENCES

1. Smits, Koljenovic, et al. (2015) *Resection margins in oral cancer surgery: Room for improvement.* Head & Neck. 38(1):E2197-2203.
2. Dinardo, Lin, et al. (2000) *Accuracy, utility, and cost of frozen section margins in head and neck cancer surgery.* Laryngoscope. 110(10):1773-1776.
3. Al-Rajhi, Khafaga, et al. (2000) *Early stage carcinoma of oral tongue: Prognostic factors for local control and survival.* Oral Oncology. 36(6):508-514.
4. Priya, D'cruz, et al. (2012) *Cut margins and disease control in oral cancers.* Journal of Cancer Research and Therapeutics. 8(1):74-79.
5. Shin, Vigneswaran, et al. (2010) *Advances in fluorescence imaging techniques to detect oral cancer and its precursors.* Future Oncology. 6(7):1143-1154.
6. Keereweer, Sterenborg, et al. (2012) *Image-guided surgery in head and neck cancer: Current practice and future directions of optical imaging.* Head & Neck. 34(1):120-126.
7. Keereweer, Van Driel, et al. (2013) *Optical image-guided cancer surgery: Challenges and limitations.* Clinical Cancer Research. 19(14):3745-3754.
8. Francisco, Correr, et al. (2014) *Analysis of surgical margins in oral cancer using in situ fluorescence spectroscopy.* Oral Oncology. 50(6):593-599.
9. Wilder-Smith, Jung, et al. (2004) *In vivo optical coherence tomography for the diagnosis of oral malignancy.* Lasers in Surgery and Medicine. 35(4):269-275.
10. Hamdoon, Jerjes, et al. (2013) *Optical coherence tomography in the assessment of suspicious oral lesions: An immediate ex vivo study.* Photodiagnosis and Photodynamic Therapy. 10(1):17-27.
11. Sharwani, Jerjes, et al. (2006) *Assessment of oral premalignancy using elastic scattering spectroscopy.* Oral Oncology. 42(4):343-349.
12. Vila, Park, et al. (2012) *Discrimination of benign and neoplastic mucosa with a high-resolution microendoscope (hrme) in head and neck cancer.* Annual Surgical Oncology. 19(11):3534-3539.
13. Muldoon, Roblyer, et al. (2012) *Noninvasive imaging of oral neoplasia with a high-resolution fiber-optic microendoscope.* Head & Neck. 34(3):305-312.
14. Srinivasan. *Vibrational spectroscopic imaging for biomedical applications.* 1st ed. (2010)
15. Singh, Deshmukh, et al. (2012) *Raman spectroscopy in head and neck cancers: Toward oncological applications.* Journal of Cancer Research and Therapeutics. 8(2):S126-132.
16. Harris, Rennie, et al. (2010) *Raman spectroscopy in head and neck cancer.* Head & Neck Oncology. 2(26):1-6.
17. Hughes, Stone, et al. (2010) *Optical and molecular techniques to identify tumor margins within the larynx.* Head & Neck. 32(11):1544-1553.
18. Stone, Stavroulaki, et al. (2000) *Raman spectroscopy for early detection of laryngeal malignancy: Preliminary results.* Laryngoscope. 110(10):1756-1763.
19. De Veld, Bakker Schut, et al. (2005) *Autofluorescence and Raman microspectroscopy of tissue sections of oral lesions.* Lasers in Medical Science. 19(4):203-209.
20. Deshmukh, Singh, et al. (2011) *Raman spectroscopy of normal oral buccal mucosa tissues: Study on intact and incised biopsies.* Journal of Biomedical Optics. 16(12):127004-127010.
21. Guze, Pawluk, et al. (2015) *Pilot study: Raman spectroscopy in differentiating premalignant and malignant oral lesions from normal mucosa and benign lesions in humans.* Head Neck. 37(4):511-517.
22. Guze, Short, et al. (2011) *Comparison of molecular images as defined by Raman spectra between normal mucosa and squamous cell carcinoma in the oral cavity.* Journal of Raman Spectroscopy. 42(6):1232-1239.
23. Malini, Venkatakrishna, et al. (2006) *Discrimination of normal, inflammatory, premalignant, and malignant oral tissue: A Raman spectroscopy study.* Biopolymers. 81(3):179-193.
24. Oliveira, Bitar, et al. (2006) *Near-infrared Raman spectroscopy for oral carcinoma diagnosis.* Photomedicine and Laser Surgery. 24(3):348-353.
25. Singh, Deshmukh, et al. (2012) *In vivo Raman spectroscopic identification of premalignant lesions in oral buccal mucosa.* Journal of Biomedical Optics. 17(10):21-29.
26. Su, Sun, et al. (2012) *Raman spectral properties of squamous cell carcinoma of oral tissues and cells.* Laser Physics. 22(1):311-316.
27. Cals, Bakker Schut, et al. (2013) *Method development: Raman spectroscopy-based histopathology of oral mucosa.* Journal of Raman Spectroscopy. 44(7):963-972.

28. Rosai. *Surgical pathology* 10th ed. (2011)
29. Martens, Stark. (1991) *Extended multiplicative signal correction and spectral interference subtraction: New preprocessing methods for near infrared spectroscopy.* Journal of Pharmaceutical and Biomedical Analysis. 9(8):625-635.
30. Jolliffe. *Principal component analysis.* 2nd ed. (2002)
31. Jain. *Algorithms for clustering data* 1st ed. (1988)
32. Barnes. *Pathology and genetics of head and neck tumours*. 3rd ed. (2005)
33. Tabachnick. *Using multivariate statistics.* 6th ed. (1996)
34. Movasaghi. (2007) *Raman spectroscopy of biological tissues.* Applied spectroscopy reviews. 42(5):493 -541.
35. Braakhuis, Leemans, et al. (2004) *A genetic progression model of oral cancer: Current evidence and clinical implications.* Journal Oral Pathology Medicine. 33(6):317-322.
36. Slaughter, Southwick, et al. (1953) *Field cancerization in oral stratified squamous epithelium; clinical implications of multicentric origin.* Cancer. 6(5):963-968.
37. Hanahan, Weinberg. (2000) *The hallmarks of cancer.* Cell. 100(1):57-70.
38. Pindborg. *Histological typing of cancer and precancer of the oral mucosa.* 2nd ed. (1997)
39. Gasparoto, De Oliveira, et al. (2012) *Inflammatory events during murine squamous cell carcinoma development.* Journal of Inflammation. 9(1):1-11.
40. Choi, Myers. (2008) *Molecular pathogenesis of oral squamous cell carcinoma: Implications for therapy.* Journal of Dental Research. 87(1):14-32.
41. Sasahira, Kirita, et al. (2014) *Update of molecular pathobiology in oral cancer: A review. I*nternational Journal of Clinical Oncology. 19(3):431-436.
42. Weber, Xu, et al. (2007) *Microenvironmental genomic alterations and clinicopathological behavior in head and neck squamous cell carcinoma.* JAMA. 297(2):187-195.
43. Woolgar, Triantafyllou. (2005) *A histopathological appraisal of surgical margins in oral and oropharyngeal cancer resection specimens.* Oral Oncology. 41(10):1034-1043.

4

Development and validation of Raman spectroscopic classification models to discriminate tongue squamous cell carcinoma from non-tumorous tissue

Froukje L. J. Cals, Senada Koljenović, José A. Hardillo, Robert J. Baatenburg de Jong, Tom C. Bakker Schut, Gerwin J. Puppels

Oral oncology 2016; DOI 10.1016/oraloncology.2016.06.012

ABSTRACT

Currently, up to 85% of the oral resection specimens have inadequate resection margins, of which the majority is located in the deeper soft tissue layers. The prognosis of patients with oral cavity squamous cell carcinoma (OCSCC) of the tongue is negatively affected by these inadequate surgical resections. Raman spectroscopy, an optical technique, can potentially be used for intraoperative evaluation of resection margins. Our aim was to develop *in vitro* Raman spectroscopy-based tissue classification models that discriminate OCSCC of the tongue from (subepithelial) non-tumorous tissue.

Tissue classification models were developed using principal components analysis (PCA) followed by (hierarchical) linear discriminant analysis ((h)LDA). The models were based on a training set of 720 histopathologically annotated Raman spectra, obtained from 25 tongue samples (11 OCSCC and 14 normal) of 10 patients, and were validated by means of an independent validation set of 367 spectra, obtained from 19 tongue samples (6 OCSCC and 13 normal) of 11 patients.

A PCA-LDA tissue classification model 'tumor' versus 'non-tumorous tissue' (i.e. surface squamous epithelium, connective tissue, muscle, adipose tissue, gland and nerve) showed an accuracy of 86% (sensitivity: 100%, specificity: 66%). A two-step PCA-hLDA tissue classification model 'tumor' versus 'non-tumorous tissue' showed an accuracy of 91% (sensitivity: 100%, specificity: 78%).

In this study an accurate PCA-hLDA Raman spectroscopy-based tissue classification model for discrimination between OCSCC and (especially the subepithelial) non-tumorous tongue tissue was developed and validated. This model with high sensitivity and specificity may prove to be very helpful to detect tumor in the resection margins.

INTRODUCTION

Every year 300 000 new cases of oral cavity squamous cell carcinomas (OCSCCs) are diagnosed worldwide[1] and only half of these patients will survive 5 years.[2] The prognosis is negatively affected by inadequate surgical resections.[3-5] Nevertheless, it was recently shown that in current practice up to 85% of the oral resection specimens have inadequate resection margins (≤ 5 mm distance between tumor border and resection surface).[3,4]

During operation, the surgeon attempts to define the borders of the tumor by visual inspection and palpation. Additionally, a so-called frozen tissue procedure can be used for intraoperative histopathological examination of suspicious regions.[6] However, the diagnostic accuracy of the frozen section procedure depends on how well the sampled tissue represents the actual resection margin that is suspected to be inadequate.[7] Since in oral cavity up to 87% of all tumor-positive margins are located in the deeper soft tissue layers,[8] the common practice of taking samples of the epithelial margin is of limited value. Moreover, the sampling error is often inevitable because only a small portion of the resection margins can be evaluated by frozen sections, due to the fact that the procedure is too time-consuming and laborious.[9] Thus, an intraoperative tool that provides a real-time and objective evaluation of all resection margins (especially in the deeper soft tissue margins) may increase the number of adequate resections and thereby improve the prognosis of patients with OCSCC.

Raman spectroscopy is an optical technique that is suited for such intraoperative use because it is nondestructive and no pretreatment or labeling of the tissue is needed.[10] The technique is based on inelastic scattering of light by molecules.[11] A Raman spectrum contains characteristic peaks that are assigned to a corresponding molecular structure within the illuminated tissue. Thus, Raman spectroscopy enables tissue characterization based on objective molecular information.[12] Because of these attractive properties, there has been much interest in the use of Raman spectroscopy for differentiation between tumor and non-tumorous tissue[13-16] in the head and neck region,[17-20] including the oral cavity.[21-27]

Tongue, which is the most common subsite of OCSCC,[28] comprises different histological structures and layers,[29] all having their own specific Raman spectroscopic features. In order to provide a tool that detects OCSCC within the surrounding non-tumorous tongue tissue, a good understanding of all histological structures and their spectroscopic features is needed. Histopathologically annotated Raman spectra were used in our previous work[30] to enable distinction between OCSCC of the tongue and individual tissue structures, including those in the deeper soft tissue. Due to the large differences in lipid-protein ratio, a 100% accurate distinction was possible between OCSCC and adipose tissue, and OCSCC and nerve. Although the other deeper located healthy tissue structures (connective tissue (CT), gland and muscle) had a greater spectral similarity to the OCSCC spectrum, these structures were also spectrally distinguishable from OCSCC with high accuracy (93%, 94%, and 97% respectively). Furthermore, as might be expected by similarities in biochemical composition, the spectral features of OCSCC and surface squamous epithelium (i.e. non-tumorous squamous epithelium covering the surface of the tongue) were partly overlapping, resulting in a lower discriminatory power of 75%.[30]

The objective of our current study was to prove the potential of Raman spectroscopy in discriminating OCSCC from non-tumorous tongue tissue, by developing *in vitro* tissue classification models based on

spectral data of individual non-tumorous tissue structures. The accuracy of the models was validated by means of an independent dataset.

MATERIALS AND METHODS

Sample handling and sample preparation

At the department of Otorhinolaryngology and Head and Neck Surgery of the Erasmus MC Cancer Institute, University Medical Center Rotterdam, 44 tissue samples were collected from 21 patients who had undergone a surgical resection because of a primary OCSCC of the tongue. Informed consent was obtained prior to the operation according to the protocol approved by the Medical Ethics Committee (MEC-2011-450) of the Erasmus University Medical Center Rotterdam.

Seventeen samples (from 14 patients) contained OCSCC and non-tumorous tissue (i.e. surface squamous epithelium, CT, muscle, adipose tissue, gland and nerve). These samples were harvested from the fresh resection specimens, from a region with macroscopically visible tumor. The other 27 samples (from 19 patients) contained only non-tumorous tissue and were harvested from 2 locations: [1] 14 samples (from 12 patients) were taken from the resection specimen within a macroscopically normal-appearing region adjacent to the tumor, and [2] 13 samples (from 13 patients) were taken from the contralateral (not-affected) edge of the tongue.

All samples were at least 5 x 5 mm in size. Samples from the surgical resection specimens were taken within 60 minutes after surgical excision. Contralateral samples were taken during surgery. The samples were snap frozen by immersion in isopentane and subsequently in liquid nitrogen, and kept at -80˚C until further use.

Raman spectroscopic mapping experiments and annotated Raman spectra

The frozen tissue samples were mounted on a cryotome stage using CryoCompound (KP-CryoCompound, Klinipath B.V., The Netherlands), and 20 µm thick frozen tissue sections were cut, placed on fused silica windows and allowed to dry at room temperature. Raman mapping experiments were performed, using a SpectraCell RA Bacterial Strain Analyzer (RiverD International B.V., Rotterdam, The Netherlands). This instrument was designed as a fully automated inverted confocal Raman microscope for analyzing bacterial samples. After modification of the software it was used for point-by-point Raman mapping of tissue sections.

The data processing and data analysis has been described in detail previously.[31] The data analysis software was developed in-house and operates in a MATLAB environment (MATLAB 7.5.0 (R2007b), MathWorks, MA, USA) with the multivariate toolbox PLS-toolbox 7.0.0c (EigenVector Research, WA, USA). Briefly, about 100 mW of laser light (785 nm) was focused to a spot of 2 µm in diameter on the unfixed, unstained 20 µm thick frozen tissue sections. Selected regions were scanned point-by-point in a 2-dimensional grid with a step size of 5 µm and a spectral resolution of 8 cm^{-1}. Of each point a single spectrum was obtained, constricted to the wavenumber range of 400 – 1800 cm^{-1}. The spectra were grouped using K-means cluster analysis (KCA).[32] By assigning a color to each K-means cluster, pseudo

color Raman images were generated. After the Raman experiments tissue sections were stained with haematoxylin and eosin (H&E).[33] Comparison of these pseudo color Raman images with the H&E-stained tissue sections enabled histopathological annotation of the K-means cluster averages as [1] OCSCC, [2] surface squamous epithelium, [3] CT, [4] muscle, [5] adipose tissue, [6] gland or [7] nerve, as described in detail previously.[31] With OCSCC the epithelial (keratinocytic) component of the tumor is meant. Based on the observed histopathological heterogeneity, the annotated Raman spectra of surface squamous epithelium were subdivided into 3 layers (basal layer, suprabasal layer and superficial layer) and 2 epithelial subtypes (dysplastic and non-dysplastic), as described in detail previously.[30]

These histopathologically annotated K-means cluster averages are hereafter referred to as annotated Raman spectra. For further analysis, the spectra annotated as [1] were labeled as 'tumor' and the six individual non-tumorous tissues/tissue structures [2 – 7] were all marked as 'non-tumorous tissue'.

Development of tissue classification models

One half of the spectral database containing annotated Raman spectra of 10 patients (hereafter called the training set) was used to develop the tissue classification models. To ensure an accurate representation of all tissue structures, the training set was created such that each tissue structure was represented in at least three patients. For the development of tissue classification models principal component analysis (PCA)[34] was used, followed by (hierarchical) linear discriminant analysis ((h)LDA).[35]

In this study, two tissue classification models were developed (Figure 1).

- A PCA-LDA model 'tumor' (OCSCC) versus 'non-tumorous tissue' (i.e. surface squamous epithelium, CT, muscle, adipose tissue, gland and nerve).
- A two-step PCA-hLDA model 'tumor' versus 'non-tumorous tissue'. In the first step the spectra of adipose tissue and nerve were distinguished from all the other spectra. In the second step the spectra of surface squamous epithelium, CT, muscle and gland were distinguished from the spectra of OCSCC.

The best model parameters were selected based on the classification accuracy (proportion of true results (both true positives and true negatives) of a leave-one-patient-out (LOPO) analysis. In a LOPO analysis the classification models are built using the data of all patients in the training set but one, and tested on the data of the patient that was left out.

Validation of tissue classification models

The final tissue classification models were validated using the other half of the spectral database (hereafter called the validation set) that contained annotated Raman spectra of the samples of the 11 different patients not included in the training set.

The discriminative power of the tissue classification models was determined by a receiver operator characteristic (ROC) analysis where the true positive rate (sensitivity) is plotted against the false positive rate (1-specificity) for different values of the discrimination threshold. The area under the ROC curve (AUC) is a measure of discriminatory power of the tissue classification model. The maximum value for the AUC is 1,0 thereby indicating a (theoretically) perfect model (i.e. 100% sensitive and 100% specific). An AUC value of 0,5 indicates no discriminative value (i.e. 50% sensitive and 50% specific) and is represented by a straight, diagonal line extending from the lower left corner to the upper right. There are several scales

for AUC value interpretation, but ROC curves with an AUC of > 0,9 are generally interpreted as an excellent discriminative power, an AUC between 0,8 and 0,9 as good, between 0,7 and 0,8 as moderate and between 0,6 and 0,7 as poor.[36] The Youden index[37] is known as an optimal value of the discrimination threshold, yielding the highest combined sensitivity and specificity. However, the discrimination threshold can be chosen along the ROC curve, such that it provides the combination of sensitivity and specificity that is of greatest clinical value.

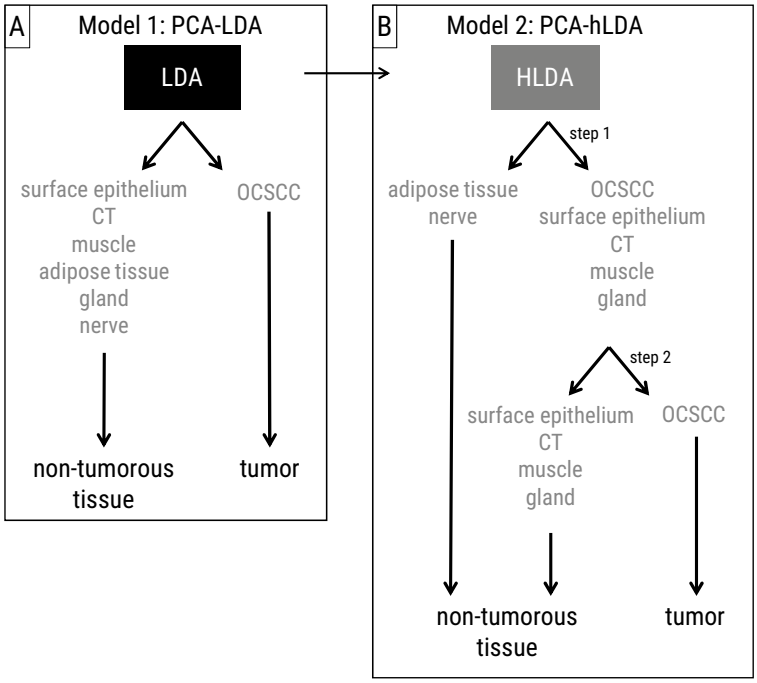

Figure 1. A: PCA-LDA tissue classification model 'tumor' versus 'non-tumorous tissue'. B: PCA-hLDA tissue classification model 'tumor' versus 'non-tumorous tissue'.

Tumor-heat maps

From the PCA-(h)LDA models, predictions of the posterior probability of being tumor were calculated for each individual point spectrum of each map. By coding this probability as a color between yellow and red, a heat map was generated for each measured Raman map.

RESULTS

Characteristics of the training set

The training set consisted of 127 Raman maps, obtained from 25 tissue samples from 10 patients. Of these 25 samples, 11 samples contained OCSCC as well as surrounding non-tumorous tissue structures (i.e. surface squamous epithelium, CT, muscle, adipose tissue, gland and nerve), and 14 samples contained non-tumorous tissue structures only. From the 14 tumor free samples, 8 originated from the resection specimen from a region with macroscopically normal-appearing mucosa adjacent to the tumor, and 6 from the contralateral (not-affected) edge of the tongue. The scanned areas ranged in size between 250 µm x 250 µm and 1005 µm x 470 µm. With a Raman measurement step size of 5 µm this resulted in 2700 – 18 894 point spectra per Raman map (mean number of spectra per map: 11 421). The optimal number of K-means clusters per map varied between 4 and 20.

In total 88 K-means clusters averages were annotated as 'tumor', and 632 K-means clusters averages were annotated as 'non-tumorous tissue' (140 surface squamous epithelium, 396 CT, 41 muscle, 33 adipose tissue, 17 gland and 5 nerve).

Characteristics of the validation set

The tissue classification models were validated using an independent dataset. This validation set consisted of 70 Raman maps, obtained from 19 samples from 11 patients that were not included in the training set. Of these 19 tissue samples, 6 samples contained OCSCC as well as surrounding non-tumorous tissue structures (i.e. surface squamous epithelium, CT, muscle, adipose tissue, gland and nerve), and 13 samples contained non-tumorous tissue structures only. From the 13 tumor free samples, 6 originated from the resection specimen from a region with macroscopically normal-appearing mucosa adjacent to the tumor, and 7 from the contralateral (not-affected) edge of the tongue. The scanned areas ranged in size between 250 µm x 100 µm and 1005 µm x 420 µm. With a Raman measurement step size of 5 µm this resulted in 1050 – 16 884 point spectra per Raman map (mean number of spectra per map: 9620). The optimal number of K-means clusters per map varied between 3 and 19.

In total 54 K-means clusters averages were annotated as 'tumor', and 313 K-means clusters averages were annotated as 'non-tumorous tissue' (62 surface squamous epithelium, 185 CT, 20 muscle, 32 adipose tissue, 9 gland and 5 nerve).

Validation of the tissue classification models

All results shown were generated using the validation set. Initially, a PCA-LDA model was built to distinguish 'tumor' from 'non-tumorous tissue' (i.e. surface squamous epithelium, CT, muscle, adipose tissue, gland and nerve). This model used five principal components (PCs) and showed a maximum classification accuracy of 86%. The ROC analysis showed an AUC of 0,90 (Figure 2). At a sensitivity of 100%, specificity reached 66%. The misclassifications with this discrimination threshold occurred for surface squamous epithelium (58/62), CT (11/185), muscle (15/20), adipose tissue (16/32), gland (4/9) and nerve (3/5) (Table 1).

Since previous published results indicated that certain individual non-tumorous tissue structures were easier to distinguish from OCSCC than others,[30] a PCA-hLDA model with two consecutive steps was built. In the first step the spectra of adipose tissue and nerve were distinguished from all the other spectra, using three PCs. In the second step the spectra of surface squamous epithelium, CT, muscle and gland were distinguished from the spectra of OCSCC, with an optimal number of 11 PCs. This model showed a maximum classification accuracy of 91%. The ROC analysis resulted in an AUC of 0,95 (Figure 2). At a sensitivity of 100% this model yielded a specificity of 78%. The misclassifications with this discrimination threshold occurred for surface squamous epithelium (51/62), CT (12/185) and gland (5/9) (Table 1).

				'tumor'	**'non-tumorous tissue'**					
	maximum accuracy	sensitivity	specificity	OCSCC	surface squamous epithelium	CT	muscle	adipose tissue	gland	nerve
Model 1: PCA-LDA 'tumor' versus 'non-tumorous tissue'	86%	100%	66%	0/54	58/62	11/185	15/20	16/32	4/9	3/5
Model 2: PCA-hLDA 'tumor' versus 'non-tumorous tissue'	91%	100%	78%	0/54	51/62	12/185	0/20	0/32	5/9	0/5

Table 1. Per tissue classification model the maximum accuracy, sensitivity (true positive rate) and specificity (true negative rate) are shown. The discrimination threshold is chosen such that a 100% sensitivity is obtained. The number of misclassified spectra per tissue structure have been further detailed in the last 7 columns.

Detailed histopathological evaluation of the misclassified surface squamous epithelium spectra revealed that 30 of the 32 spectra annotated as dysplastic epithelium were misclassified. Furthermore, all spectra (23/23) annotated as basal epithelial layers were misclassified. Analysis of the CT misclassifications showed that all misclassified CT spectra (12/12) were obtained from tissue samples containing OCSCC; i.e. from peritumoral stroma.

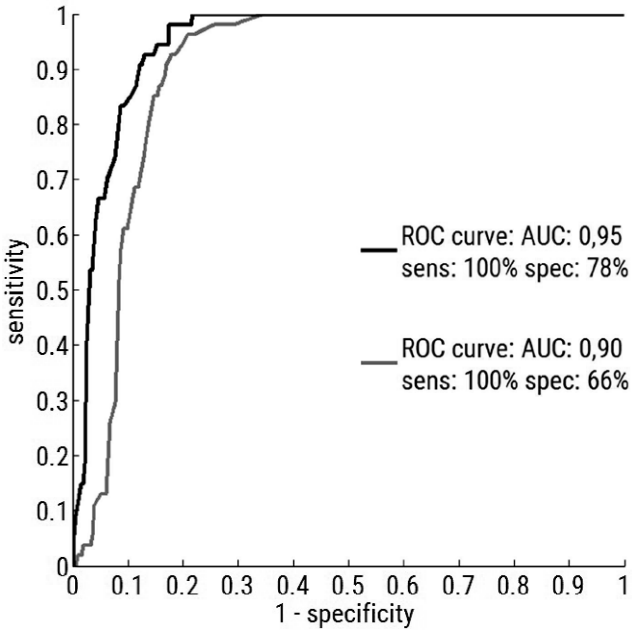

Figure 2. Receiver operator characteristic (ROC) analysis. Sensitivity is plotted against 1-specificity. The area under the ROC curve (AUC) is a measure of the discriminatory power of the classification models. Gray line: PCA-LDA model ('tumor' versus 'non-tumorous tissue'). Black line: 2-step PCA-hLDA model ('tumor' versus 'non-tumorous tissue').

Proof of principle: tumor-heat maps

To demonstrate the differences between the tissue classification models, heat maps were made. A representative example is shown in Figure 3. Figures 3A – 3C shows a mapped area with OCSCC and surrounding non-tumorous CT. Figures 3D – 3F shows non-tumorous tissue structures only. For more examples see Supplementary Figures S1 – S3.

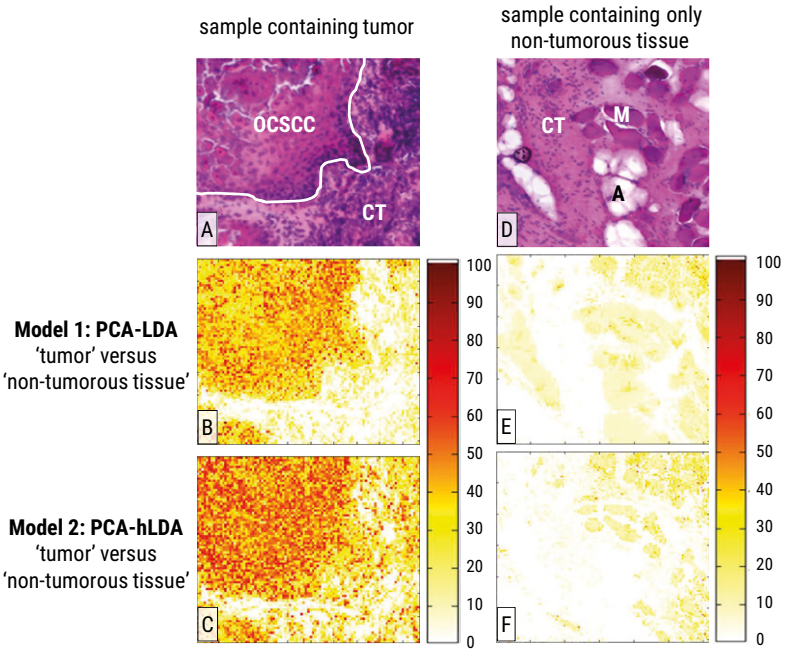

Figure 3. A: H&E-stained tissue section showing areas with OCSCC and surrounding CT. D: H&E-stained tissue section showing non-tumorous tissue (CT: connective tissue, M: muscle and A: adipose tissue). B – C and E – F: Posterior probability of being tumor was calculated for each individual point spectrum of each map and plotted as a color between yellow and red.

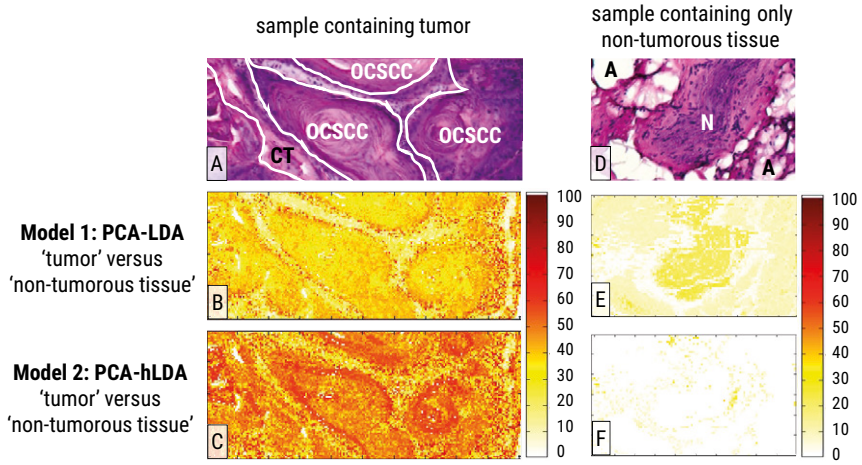

Figure S1. A: H&E-stained tissue section showing areas with OCSCC and surrounding CT. D: H&E-stained tissue section showing non-tumorous tissue (N: nerve and A: adipose tissue). B – C and E – F: Posterior probability of being tumor was calculated for each individual point spectrum of each map and plotted as a color between yellow and red.

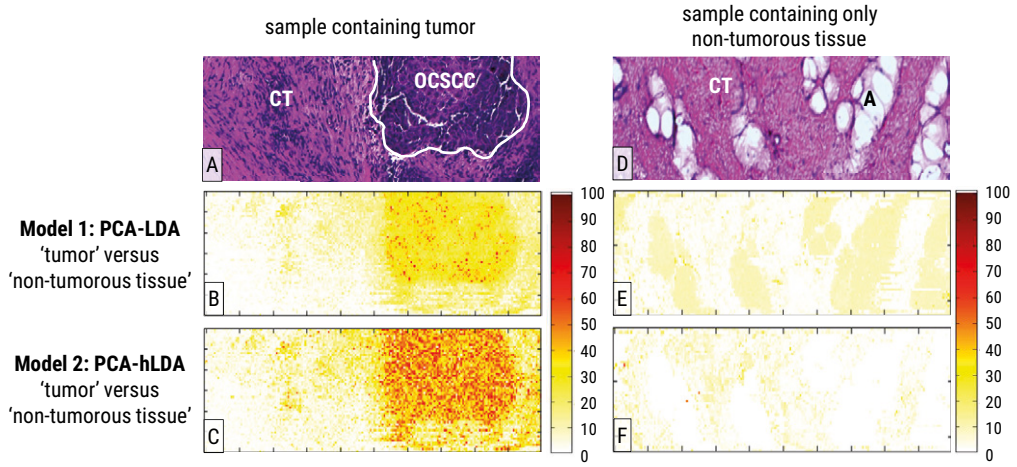

Figure S2. A: H&E-stained tissue section showing areas with OCSCC and surrounding CT. D: H&E-stained tissue section showing non-tumorous tissue (CT: connective tissue and adipose tissue). B – C and E – F: Posterior probability of being tumor was calculated for each individual point spectrum of each map and plotted as a color between yellow and red.

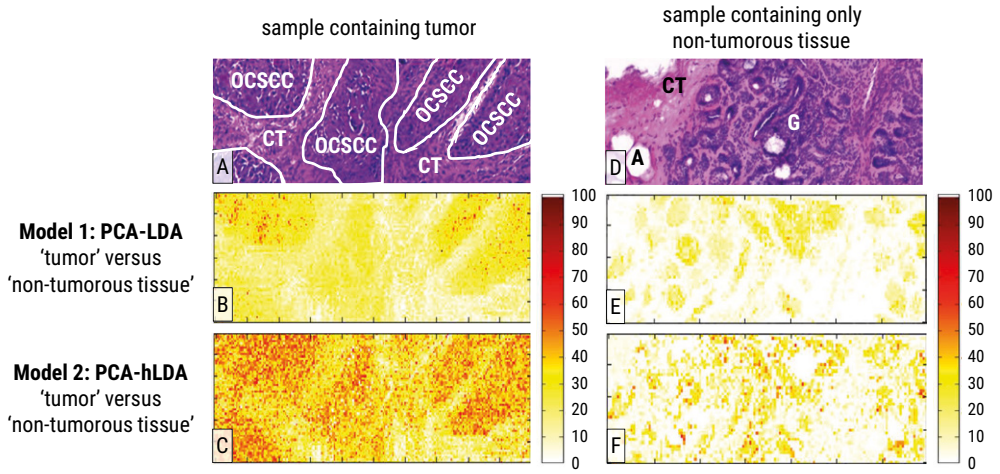

Figure S3. A: H&E-stained tissue section showing areas with OCSCC and surrounding CT. D: H&E-stained tissue section showing non-tumorous tissue (CT: connective tissue, G: gland and A: adipose tissue). B – C and E – F: Posterior probability of being tumor was calculated for each individual point spectrum of each map and plotted as a color between yellow and red.

DISCUSSION

Raman spectroscopy is a nondestructive, optical technique that does not need pretreatment or labeling to characterize tissue in real-time.[12] This makes the technique potentially very suitable for intraoperative application. *In vivo* recorded Raman spectra from intact (bulk) tissue will contain spectroscopic features from all histological structures and layers present in the entire illuminated volume.[22] To provide a solid foundation for the development of a diagnostic tool, spectroscopic knowledge about the entire target volume is mandatory. We therefore focus on the individual spectroscopic features of all histological structures present in tongue tissue. In previous work we investigated the potential of Raman spectroscopy for tongue cancer detection, by distinction between OCSCC spectra and spectra of individual non-tumorous tissue structures.[21] In this study, we used this knowledge to develop and validate 'tumor' versus 'non-tumorous tissue' classification models.

The use of Raman spectroscopy for characterization of normal and malignant tongue tissue was demonstrated by several authors[21,23,38] but an independently validated tissue classification model that distinguishes OCSCC from non-tumorous tongue tissue has not been published before. Singh et al. described a tumor classification model for another oral cavity subsite: buccal mucosa.[39] They performed *ex vivo* measurements on intact (bulk) buccal mucosa samples. With their validated PCA-LDA tissue classification model, eighty-seven percent overall accuracy was obtained when discriminating tumor tissue-spectra from normal tissue-spectra.[39] Although Raman results of different oral cavity subsites can show inherent spectral differences,[40] the accuracy of this buccal model and our tongue PCA-LDA tissue classification model was comparable. The higher accuracy (91%) of our second model can be explained by the use of a multistep hierarchical LDA. This proved to be more effective than a single step PCA-LDA model in the discrimination between tumor and non-tumorous tissue. The reason for this, is that in a PCA-hLDA model each discrimination step can be optimized separately.[35]

Compared to tissue classification models that are based on intact (bulk) tissue measurements our method uses the spectra of individual tissue structures. This makes it possible to explore the misclassifications of the developed models in detail and gain insight in their clinical relevance. All spectra annotated as basal epithelial layers were misclassified as tumor. This is not surprising because OCSCC originates from the surface squamous epithelium. In carcinogenesis, stem cells located in the basal epithelial layers acquire genetic alterations, followed by clonal expansion.[41] This explains the similarity in biochemical composition (and thus Raman spectra) of surface squamous epithelium and OCSCC. However, it is important to underline that the misclassifications of surface squamous epithelium spectra do not compromise the clinical value of our tissue classification model. Up to 87% of tumor-positive resections margins are located in the deeper soft tissue layers,[8] because tumor at the epithelium surface is visible and therefore often adequately resected. A Raman signature resembling squamous epithelium found in the deeper soft tissue is automatically suspicious of OCSCC.

In total 6,8% (17/251) of the non-tumorous tissue spectra that were obtained in the deeper soft tissue layers were misclassified. The majority (12/251) represented CT spectra that were obtained in the proximity (< 5 mm) of the tumor (also referred to as 'peritumoral stroma'). This might be explained by micro-environmental stromal changes that occur around a tumor. Tumor development is accompanied

by an immune response that leads to tumor infiltration by inflammatory cells[42] and neo-angiogenesis.[43] Hereby the biochemical composition of 'peritumoral stroma' differs from that of CT at a greater distance to the tumor. Though, these CT misclassifications are neither of clinical concern. In respect to the surgical aim which is to remove the tumor with an adequate margin of at least 5 mm of non-tumorous surrounding tissue, these false-positive classified spectra would in clinical practice not result in unnecessary resection of healthy tissue.

The developed PCA-hLDA classification model could directly be used for objective and automated assessment of frozen tissue sections. Unfortunately, current Raman mapping experiments take too much time to replace the routine frozen tissue section procedure. In our study, the scanning step size of 5 µm was chosen to obtain molecular information on a (sub)cellular level. Investigation of the detection limit (minimum amount of tumor cells necessary to be detected as tumor) will define whether this step size can be increased to reduce the measurement time without the loss of information. Furthermore, there are several other approaches proposed to reduce the current measurement time. Takamori et al. showed that the total mapping time was reduced by the combination of Raman spectroscopy with auto-fluorescence.[44] Auto-fluorescence, which has a high sensitivity and speed, but low specificity, was used to identify the areas in a tissue section that were suspicious for tumor and needed further detailed classification by Raman spectroscopy.

Use of intact fresh tissue (without making frozen sections) is another way to speed up the evaluation time, as described by Kong et al.[45] They also used a combination of Raman spectroscopy and auto-fluorescence, and demonstrated that an objective diagnosis of basal cell carcinoma was provided for non-sectioned tissue layers, faster than conventional histopathology and without the need for sample preparation. With this reduced measurement time intraoperative evaluation of all resection margins on the surgical specimen and/or in the wound bed is more achievable.

The classification model with an AUC of 0,95 from this study is the basis for further development of a Raman-spectroscopic diagnostic tool which can intraoperatively guide the surgeon to achieve adequate resection margins. Such tool can add to surgeon's experience (based on the visual inspection and palpation). The cut-off values of desired sensitivity and specificity may vary depending on the a-priori probability of suspicious tissue being tumor. Lower sensitivity and thus higher specificity may be accepted when a suspicious tissue to be resected had as low a-priori probability, combined with an expected functional loss or extended reconstruction.

In this study we developed and validated Raman spectroscopy-based *in vitro* tissue classification models for discrimination between OCSCC and (subepithelial) non-tumorous tongue tissue. A detailed analysis was made of the misclassifications to gain insight in their clinical relevance. We conclude that the high sensitivity and specificity of the PCA-hLDA classification model would be helpful in achieving adequate resection margins and that such clinical implementation is technically feasible.

REFERENCES

1. Ferlay, Soerjomataram, et al. (2015) *Cancer incidence and mortality worldwide: Sources, methods amd major patterns in globocan 2012.* International Journal of Cancer. 136(5):E359-386.
2. Karim-Kos, De Vries, et al. (2008) *Recent trends of cancer in europe: A combined approach of incidence, survival and mortality for 17 cancer sites since the 1990s.* European Journal of Cancer. 44(10):1345-1389.
3. Dillon, Brown, et al. (2015) *How does the close surgical margin impact recurrence and survival when treating oral squamous cell carcinoma?* Journal of Oral and Maxillofacial Surgery. 73(6):1182-1188.
4. Smits, Koljenovic, et al. (2015) *Resection margins in oral cancer surgery: Room for improvement.* Head & Neck. 38(1):E2197-2203.
5. Sutton, Brown, et al. (2003) *The prognostic implications of the surgical margin in oral squamous cell carcinoma.* International Journal of Oral and Maxillofacial Surgery. 32(1):30-34.
6. American Society of Clinical Oncology. *Oral and oropharyngeal cancer: Treatment options.* http://www.cancer.net/cancer-types/oral-and-oropharyngeal-cancer/treatment-options [accessed 2016].
7. Varvares, Poti, et al. (2015) *Surgical margins and primary site resection in achieving local control in oral cancer resections.* Laryngoscope. 125(10):2298-2307.
8. Woolgar, Triantafyllou. (2005) *A histopathological appraisal of surgical margins in oral and oropharyngeal cancer resection specimens.* Oral Oncology. 41(10):1034-1043.
9. Dinardo, Lin, et al. (2000) *Accuracy, utility, and cost of frozen section margins in head and neck cancer surgery.* Laryngoscope. 110(10):1773-1776.
10. Puppels, De Mul, et al. (1990) *Studying single living cells and chromosomes by confocal Raman microspectroscopy.* Nature. 347(6290):301-303.
11. Raman. (1928) *A new type of secondary radiation.* Nature. 121(501-502):365.
12. Srinivasan. *Vibrational spectroscopic imaging for biomedical applications.* 1st ed. (2010)
13. Koljenovic, Bakker Schut, et al. (2004) *Raman microspectroscopic mapping studies of human bronchial tissue.* Journal of Biomedical Optics. 9(6):1187-1197.
14. Kallaway, Almond, et al. (2013) *Advances in the clinical application of Raman spectroscopy for cancer diagnostics.* Photodiagnosis and Photodynamic Therapy. 10(3):207-219.
15. Koljenovic, Bakker Schut, et al. (2005) *Tissue characterization using high wave number Raman spectroscopy.* Journal of Biomedical Optics. 10(3):31116-31127.
16. Kong, Kendall, et al. (2015) *Raman spectroscopy for medical diagnostics-from in-vitro biofluid assays to in-vivo cancer detection.* Advances Drug Delivery Reviews. 89(7):121-134.
17. Harris, Rennie, et al. (2010) *Raman spectroscopy in head and neck cancer.* Head & Neck Oncology. 2(26):1-6.
18. Hughes, Stone, et al. (2010) *Optical and molecular techniques to identify tumor margins within the larynx.* Head & Neck. 32(11):1544-1553.
19. Stone, Stavroulaki, et al. (2000) *Raman spectroscopy for early detection of laryngeal malignancy: Preliminary results.* Laryngoscope. 110(10):1756-1763.
20. Upile, Jerjes, et al. (2009) *Head and neck optical diagnostics: Vision of the future of surgery.* Head & Neck Oncology. 1(25):1-9.
21. Carvalho, Bonnier, et al. (2015) *Raman micro-spectroscopy for rapid screening of oral squamous cell carcinoma.* Experimental and Molecular Pathology. 98(3):502-509.
22. Deshmukh, Singh, et al. (2011) *Raman spectroscopy of normal oral buccal mucosa tissues: Study on intact and incised biopsies.* Journal of Biomedical Optics. 16(12):127004-127010.
23. Guze, Pawluk, et al. (2015) *Pilot study: Raman spectroscopy in differentiating premalignant and malignant oral lesions from normal mucosa and benign lesions in humans.* Head Neck. 37(4):511-517.
24. Krishna, Majumder, et al. (2014) *In vivo Raman spectroscopy for detection of oral neoplasia: A pilot clinical study.* Journal of Biophotonics. 7(9):690-702.
25. Malini, Venkatakrishna, et al. (2006) *Discrimination of normal, inflammatory, premalignant, and malignant oral tissue: A Raman spectroscopy study.* Biopolymers. 81(3):179-193.
26. Singh, Deshmukh, et al. (2012) *In vivo Raman spectroscopic identification of premalignant lesions in oral buccal mucosa.* Journal of Biomedical Optics. 17(10):21-29.

27. Su, Sun, et al. (2012) *Raman spectral properties of squamous cell carcinoma of oral tissues and cells.* Laser Physics. 22(1):311-316.
28. Olaleye, Ekrikpo, et al. (2015) *Incidence and survival trends of lip, intra-oral cavity and tongue base cancers in south-east england.* Annual of the Royal College of Surgeons of England. 97(3):229-234.
29. Mills. *Histology for pathologists*. 3rd ed. (2004)
30. Cals, Bakker Schut, et al. (2015) *Investigation of the potential of Raman spectroscopy for oral cancer detection in surgical margins.* Laboratory Investigation. 95(10):1186-1196.
31. Cals, Bakker Schut, et al. (2013) *Method development: Raman spectroscopy-based histopathology of oral mucosa.* Journal of Raman Spectroscopy. 44(7):963-972.
32. Jain. *Algorithms for clustering data* 1st ed. (1988)
33. Rosai. *Surgical pathology* 10th ed. (2011)
34. Jolliffe. *Principal component analysis.* 2nd ed. (2002)
35. Tabachnick. *Using multivariate statistics.* 6th ed. (1996)
36. Fan, Upadhye, et al. (2006) *Understanding receiver operating characteristic (roc) curves.* Cancer Journal Emerging Medicine. 8(1):19-20.
37. Youden. (1950) *Index for rating diagnostic tests.* Cancer. 3(1):32-35.
38. Guze, Short, et al. (2011) *Comparison of molecular images as defined by Raman spectra between normal mucosa and squamous cell carcinoma in the oral cavity.* Journal of Raman Spectroscopy. 42(6):1232-1239.
39. Singh, Deshmukh, et al. (2012) *Raman spectroscopy in head and neck cancers: Toward oncological applications.* Journal of Cancer Research and Therapeutics. 8(2):S126-132.
40. Bergholt, Zheng, et al. (2011) *Characterizing variability in in vivo Raman spectra of different anatomical locations in the upper gastrointestinal tract toward cancer detection.* Journal of Biomedical Optics. 16(3):37003-37010.
41. Braakhuis, Leemans, et al. (2004) *A genetic progression model of oral cancer: Current evidence and clinical implications.* Journal Oral Pathology Medicine. 33(6):317-322.
42. Gasparoto, De Oliveira, et al. (2012) *Inflammatory events during murine squamous cell carcinoma development.* Journal of Inflammation. 9(1):1-11.
43. Choi, Myers. (2008) *Molecular pathogenesis of oral squamous cell carcinoma: Implications for therapy.* Journal of Dental Research. 87(1):14-32.
44. Takamori, Kong, et al. (2015) *Optimization of multimodal spectral imaging for assessment of resection margins during mohs micrographic surgery for basal cell carcinoma.* Biomedical Optics Express. 6(1):98-111.
45. Kong, Rowlands, et al. (2013) *Diagnosis of tumors during tissue-conserving surgery with integrated autofluorescence and Raman scattering microscopy.* Proceedings of the National Academy of Sciences. 110(38):15189-15194.

5

Raman spectroscopic analysis of the molecular composition of oral cavity squamous cell carcinoma and healthy tongue tissue structures

Froukje L. J. Cals, Tom C. Bakker Schut, Peter Caspers,
Robert J. Baatenburg de Jong, Senada Koljenović, Gerwin J. Puppels

To be submitted

ABSTRACT

A Raman spectrum is a quantitative representation of the overall molecular composition of a tissue. Raman spectra are often used as tissue fingerprints, without further interpreting them in terms of the information they contain about the tissue's molecular composition. In this study, we analyzed the characteristic spectra of oral cavity squamous cell carcinoma (OCSCC) and healthy tissue structures in oral tongue to define the differences in molecular composition.

A total of 1087 histopathologically annotated spectra (142 OCSCC, 202 surface squamous epithelium, 61 muscle, 65 adipose tissue, 581 connective tissue (CT), 26 gland, and 10 nerve) were obtained from Raman maps of 44 tongue samples from 21 patients. A characteristic, average spectrum per tissue structure was fitted with a set of 55 pure-compound reference spectra, that comprised a representation of proteins, lipids, nucleic acids, carbohydrates, amino acids and miscellaneous, to define the best library of fit-spectra. This was done by using a non-negative least-squares fitting procedure. Next, all individual spectra per histopathological annotation were fitted with this selected library to define the mean and standard deviation of the molecular composition.

The results show that using the set of 55 pure-compound reference spectra all characteristic tissue-type spectra could be explained with a fit-residual of < 4,82%. The carbohydrate, protein and amino acid content were the most important factors to discriminate between tumor and healthy tissue. The combination of these chemical classes were used in a classification model. Validation of this 'tumor' versus 'healthy tissue' classification model on an independent dataset of individual spectra showed a sensitivity of 100% and specificity of 93%.

INTRODUCTION

Tools that provide real-time detection of oral cavity squamous cell carcinoma (OCSCC) may help head and neck surgeons to increase the number of adequate oncological resections and thereby improve patients' outcome.[1,2] The interest in surgery that is guided by optical techniques is increasing because these techniques are generally not invasive, and can provide real-time and objective tissue characterization.[3-6] The applications and performance of (auto) fluorescence,[7-10] narrow-band imaging,[11,12] optical coherence tomography,[13,14] confocal (reflectance) microscopy,[15-18] elastic scattering spectroscopy[19] and Raman spectroscopy[20-23] are being investigated.

Raman spectroscopy is a non-destructive optical technique that is based on the inelastic scattering of light by molecules.[24] The interaction between light and molecules can lead to the excitation of vibrational energy levels in the molecule. Hereby, the incident light loses a quantified amount of energy, which causes a frequency shift in the scattered light. Such shifts in frequency are called 'Raman shifts' and can be plotted in a Raman spectrum. Because the vibrational information is very specific for molecules, Raman spectra can serve as fingerprints, in which molecules can be identified. In the case of a combination of molecules in the measurement volume, they will all add their own specific Raman shifts to the obtained Raman spectrum. The contribution of a specific molecule to a Raman spectrum is proportional to the concentration of that molecule in a measurement volume.[25] The Raman spectrum can therefore be a quantitative representation of the overall molecular composition of a tissue.

Raman spectra are often studied as tissue fingerprints, without further interpreting the spectra in terms of the information they contain about the tissue's molecular composition. A number of such studies have appeared, showing Raman spectroscopy's potential to discriminate between malignant and healthy tissue in several anatomical regions,[26] including the oral cavity.[27-34] The high spatial resolution of the technique allows to define spectral differences between healthy tissue and OCSCC on both subcellular[27] and cellular level[29,32] in sectioned oral tissue.[28,32] However, Raman spectra that are collected from non-sectioned tissue with a fiber-optic probe contain signal contributions of all present molecules. The more heterogeneous the measurement volume, the more complex the obtained Raman spectrum.

Oral tissue is not homogeneous, but rather comprises different tissue structures and layers.[35] The tongue is the most common location of an OCSCC.[36] The keratinized tongue is comprised of mucosa and submucosa. The mucosa includes the stratified squamous epithelium and underlying lamina propria.[35] The lamina propria is a delicate layer, which contains few elastic and collagenous connective tissue (CT) fibers and is rich in blood vessels, lymphatics, and (sensory branches of) nerves. The submucosa is situated beneath the lamina propria and is composed of CT, in which muscle fibers, adipose tissue, nerves, blood vessels, and lymphatics are distributed. The thickness of the epithelium is dependent on sex, age, and tobacco- and alcohol consumption habits.[37,38] The epithelial thickness and the distribution of the different tissue structures in the lamina propria and submucosa vary throughout the tongue.[39]

Each of these tissue structures have a specific Raman spectrum,[21,22] which may make the discrimination between non-sectioned healthy tissue and OCSCC more difficult.[34] Various *ex vivo* studies on oral cavity tissue show that, despite this complexity, healthy tissue and OCSCC can be successfully distinguished.[30,31,33] The discrimination has mostly been attributed to predominant Raman features that can be assigned to

proteins in OCSSC fingerprints, and to predominant lipid features in the Raman fingerprints of normal tissue. Similar results were shown in *in vivo* studies conducted in the oral cavity.[40,41] However, as these measurements were taken on bulky, non-sectioned tissue using a fiber-optic probe, it is not clear how the discrimination between healthy tissue and OCSCC was influenced by the presence and exact proportions of the individual tissue structures in the measurement volume.

A thorough understanding of the spectral contribution of the different tissue structures is essential in optimizing the technique's discriminative power. The aim of this study is to determine and compare the molecular compositions of individual tissue structures within oral tongue tissue. The Raman spectra of the individual tissue structures were analyzed by means of non-negative least-squares fitting with the reference spectra of pure compounds. The molecular compositions of the individual healthy tissue structures were then compared to that of OCSCC. Based on these results, a 'tumor' versus 'healthy tissue' classification model was developed and validated. Finally, simulations of large measurement volumes were performed, in order to demonstrate the impact of their composition on the discrimination between healthy tissue and OCSCC.

MATERIALS AND METHODS

An overview of the steps that were taken to determine the molecular composition of the tissue structures is given in Figure 1, and described in more detail in the paragraphs below.

In summary, the main tissue structures within oral tongue tissue were identified (Figure 1, step 1): surface squamous epithelium, muscle, adipose tissue, CT, gland and nerve.[35] A spectral database was created containing Raman spectra that were correlated to histopathology. This enabled annotation as either OCSCC or one of the healthy tissue structures (Figure 1, step 2). A representative/characteristic Raman spectrum was calculated by averaging all equally annotated spectra per tissue structure, called 'characteristic tissue-type spectrum' (Figure 1, step 3).

The main molecular compounds of these tissue structures were categorized into one of the following chemical classes: proteins, lipids, nucleotides, carbohydrates, amino acids and miscellaneous.[42] A set of pure-compound reference spectra was created representing all these chemical classes. The spectra in this set are called 'fit-spectra' (Figure 1, step 4).

A selection procedure was developed to find the best library, i.e. the optimal combination of fit-spectra to approximate each of the characteristic tissue-type spectra (Figure 1, steps 5 – 7).[43] The best library was defined as having the smallest fit-residual (Figure 1, step 9). The fit residual is that part of the characteristic tissue-type spectrum that cannot be explained by the selected library of fit-spectra (Figure 1, step 8).

Next, the average and standard deviation of the molecular composition per tissue structure were determined by fitting all individual histopathologically annotated spectra with the best library for that tissue structure (Figure 1, step 10 – 13). Quantitative information about the overall molecular composition of the tissue structures is obtained, because the fit coefficients represent the relative proportions in which the molecules contribute to the final spectrum (Figure 1, step 14). An average and standard deviation per chemical class were calculated for each tissue structure (Figure 1, step 15).

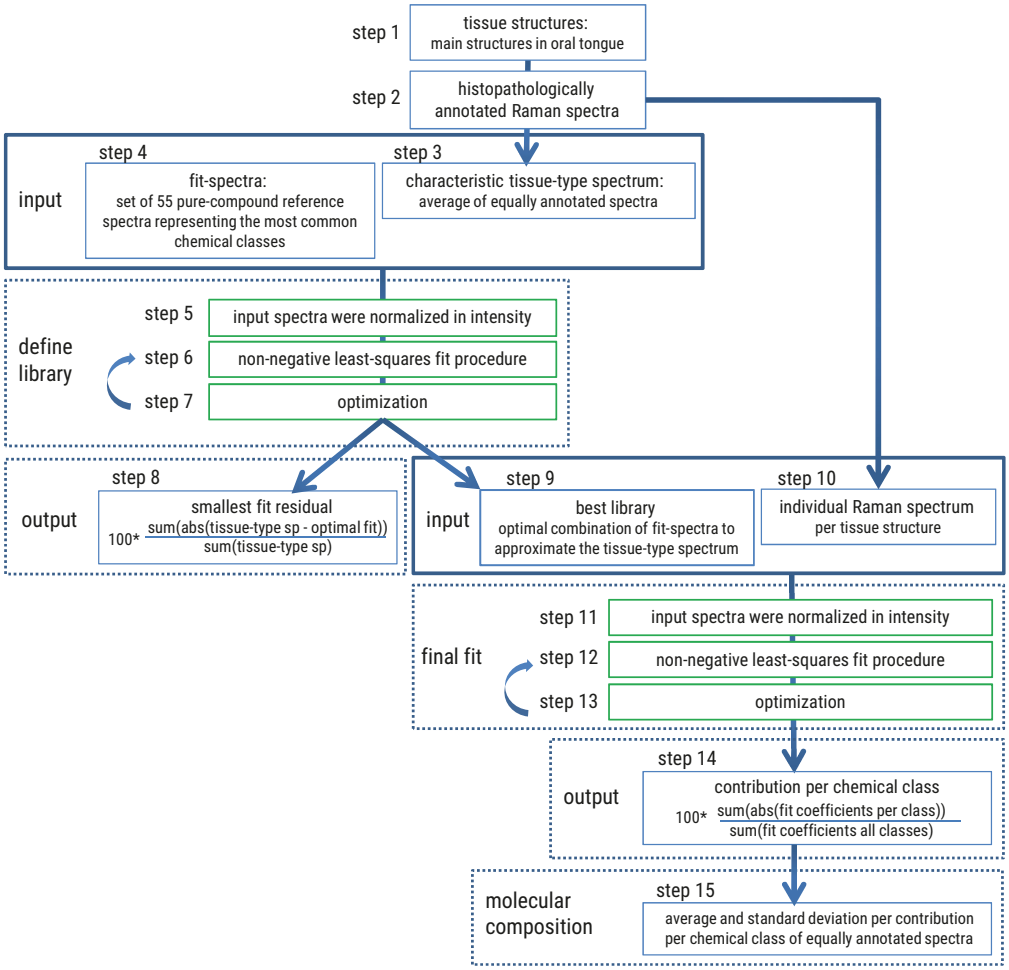

Figure 1. Flowchart of all steps taken to determine the molecular composition of the tissue structures in oral tongue (see text for a detailed description).

Histopathologically annotated Raman spectra

Multiple histopathologically annotated Raman spectra were obtained per tissue structure by performing Raman mapping experiments, as described in detail earlier.[21,22]

At the department of Otorhinolaryngology and Head and Neck Surgery of the Erasmus MC Cancer Institute, tissue samples were collected from patients who had undergone surgery for a primary squamous cell carcinoma of the tongue. Informed consent was obtained prior to the operation according to a protocol which was approved by the Medical Ethics Committee (MEC-2011-450) of the Erasmus MC Cancer Institute, University Medical Center Rotterdam.

A modified SpectraCell RA Bacterial Strain Analyzer (RiverD International B.V., Rotterdam, The Netherlands) was used for Raman mapping experiments on unstained frozen tissue sections of 20 µm in thickness. About 100 mW of laser light (785 nm) was focused on a spot of 2 µm in diameter. The selected regions were scanned point-by-point in a 2-dimensional grid with a step size of 5 µm. At each measurement position a single spectrum was obtained. Raman-scattered light was collected in the wavenumber interval from 300 – 2500 cm^{-1}, with a spectral resolution of 4 cm^{-1}. The wavenumber range of the spectra that were included in the data-analysis was restricted to 400 – 1800 cm^{-1}.

The raw data were processed as described in detail in a previous study.[21,22] Extended multiplicative signal correction procedure combined with spectral interference subtraction (EMSC-SIS)[44] was used for calibration and scaling. The processed spectra were grouped using K-means Cluster Analysis.[45] By assigning a color to each K-means cluster average, pseudo color Raman images were generated. After the Raman experiments, the tissue sections were stained with haematoxylin and eosin (H&E),[46] enabling correlation and then histopathological annotation of the K-means cluster averages as [1] OCSCC, [2] surface squamous epithelium, [3] muscle, [4] adipose tissue, [5] connective tissue, [6] gland or [7] nerve, as described in detail previously (Figure 1, step 2).[21] With OCSCC the epithelial (keratinocytic) component of the tumor is meant.

Set of fit-spectra

In order to create a set of reference spectra, 55 pure compounds were measured which are representative of the following chemical classes: proteins, lipids, nucleic acids, amino acids, carbohydrates and miscellaneous (Figure 1, step 4). All pure compounds were measured using either a modified SpectraCell RA Bacterial Strain Analyzer (RiverD International B.V., Rotterdam, The Netherlands) or a Model 3510 SCA Skin Composition Analyzer (RiverD International B.V., Rotterdam, The Netherlands). Chemicals were purchased from Sigma-Aldrich Chemie B.V. (Zwijndrecht, The Netherlands), Enzo Life Sciences, Inc (Raamsdonksveer, The Netherlands) and MP biochemicals (Santa Ana, USA) and were used without further purification.

All of the spectra were calibrated according to the instructions of the spectrometer's manufacturer. Any spectral contributions of the sample carrier (fused silica) and the solvent were subtracted manually. The pure-compound reference spectra were grouped per chemical class (proteins, lipids, nucleic acids, amino acids, carbohydrates and miscellaneous), as displayed in Figure 2. Hereafter, the pure-compound reference spectra are referred to as 'fit-spectra'.

A complete overview of the specifications (name, CAS-number, chemical class, firm, product number, purity, source, instrument, measured condition (dry/dissolved), solvent, concentration, pH, acquisition time, accumulations, spectral corrections and S/N ratio), as well as the peak positions of all pure-compound measurements are given in Chapter 6.

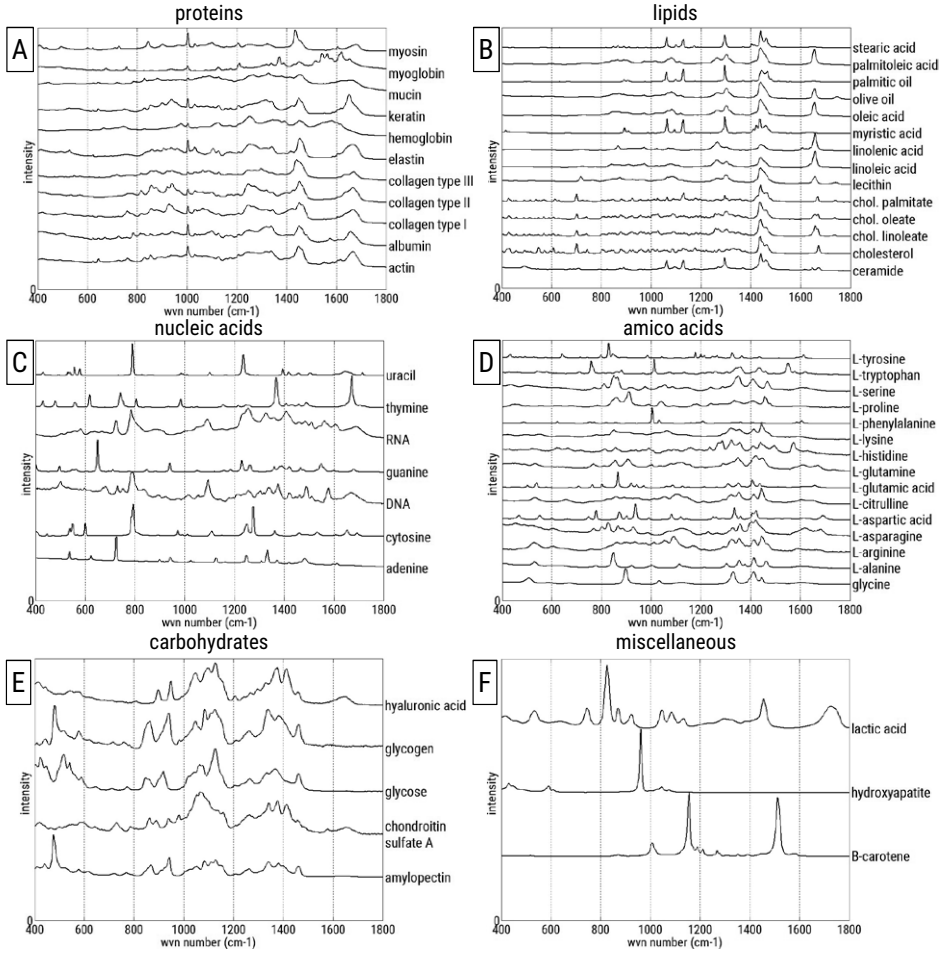

Figure 2. Pure-compound reference spectra grouped per chemical class. A: Proteins. B: Lipids. C: Nucleic acids. D: Amino acids. E: Carbohydrates. F: Miscellaneous.

Fit of characteristic tissue-type spectra to select the best library

In order to find the best spectral representative of a tissue structure, all equally annotated K-means clusters were averaged (Figure 1, step 3). These spectral averages are hereafter referred to as 'characteristic tissue-type spectra' and were fitted according to the following fitting procedure.

Non-negative least-square fitting procedure

A fitting procedure finds the best combination of fit-spectra in order to approximate the characteristic tissue-type spectrum (Figure 1, steps 5 – 9).[43] The software that was used for processing and analysis was developed in-house and operates in a MATLAB environment (MATLAB 7.5.0 (R2007b), MathWorks, MA, USA) with the multivariate toolbox PLS-toolbox 7.0.0c (EigenVector Research, WA, USA).

Pre-processing, fitting and output

Firstly, the characteristic tissue-type spectrum and the fit-spectra were scaled by normalizing the mean intensity of the spectra to a value of 1, after which their offset was removed (Figure 1, step 5). In this way, the intensities of all of the spectra that serve as input to the fitting procedure, become comparable in intensity.

Secondly, the characteristic tissue-type spectrum was fitted with the 55 fit-spectra by using a non-negative least-squares (nn-lsq) fit procedure (Figure 1, step 6).[43] An nn-lsq fit is a constrained version of the least-squares fit in which the fit coefficients are not allowed to become negative. This fit procedure was chosen because only the pure compounds that add positively to the fit (i.e. molecular composition) are of interest. A third order polynomial was included in each fitting step in order to account for spectral backgrounds. The non-negativity constraint is implemented in an iterative optimization procedure, as detailed below.

The quality of the fit is dependent on how well the fit-spectra approximate the characteristic tissue-type spectrum and is defined as the fraction of the tissue-type spectrum that could be explained by the fit-spectra. The fit-residual was calculated by subtracting the fit from the characteristic tissue-type spectrum and was expressed as a percentage of the total intensity of the characteristic tissue-type spectrum (Figure 1, step 8).

Optimization

In order to determine the optimal combination of fit-spectra per characteristic tissue-type spectrum, a multistep fit optimization procedure was used in which the fit-spectra were selected one by one (Figure 1, step 7). This multistep optimization was developed to obtain a reproducible fit and to find the smallest possible fit-residual.

In the first step of the optimization, a nn-lsq fit was performed in which a characteristic tissue-type spectrum was fitted with each of the 55 individual fit-spectra separately. The fit-spectrum that gave the best improvement, i.e. the highest reduction of the fit-residual, was selected. In the next step, the characteristic tissue-type spectrum was fitted with the fit-spectrum that was first selected and with all remaining individual fit-spectra separately. The fit-spectrum that yielded the best fit when it was added (i.e. lowest fit-residual) was selected as second, and so on. The procedure was repeated until the optimal fit was reached. The optimal fit was accomplished when the inclusion of an additional fit-spectrum no longer decreased the fit-residual (Figure 1, step 8). Per tissue structure the best library of fit-spectra was now selected (Figure 1, step 9).

Molecular composition per tissue structure

The molecular composition per tissue structure was determined by fitting all individual histopathologically annotated spectra with the selected library for that tissue structure. Again the multistep optimization fitting procedure was used, as described above (Figure 1, step 11 – 13). Instead of a characteristic tissue-type spectrum, the individual histopathologically annotated Raman spectra served as input (Figure 1, step 10).

The molecular compositions of the different tissue structures were compared by examining the fit contributions per chemical class. The fit coefficients represent the relative proportions in which the

molecular fit-spectra contribute to the spectrum (Figure 1, step 14). The fit coefficients of the included fit-spectra were grouped per chemical class (proteins, lipids, nucleic acids, amino acids, carbohydrates and miscellaneous). An average and standard deviation per chemical class were calculated for each tissue structure (Figure 1, step 15). The molecular compositions of all healthy tissue structures were compared to that of OCSCC.

'Tumor' versus 'healthy tissue' classification model

The significance and consistency of the differences in chemical class fit contributions (ccfc) between OCSCC and the healthy tissue structures were tested by using the ccfc as input for a classification model. The ccfc of spectra annotated as [1] OCSCC were labeled as 'tumor' and the ccfc of spectra from the six individual healthy tissues/tissue structures; [2] surface squamous epithelium, [3] muscle, [4] adipose tissue, [5] connective tissue, [6] gland or [7] nerve, were all marked as 'healthy tissue'.

One half of the spectral database containing annotated Raman spectra of 10 patients (hereafter called the training set) was used to develop a classification model. To ensure an accurate representation of all tissue structures, the training set was created such that each tissue structure was represented in at least three patients. A conditional model was developed in which the most distinctive chemical classes were selected. Based on the fit data from the training set a cut-off was determined per chemical class that distinguished tumor spectra from healthy tissue spectra.

The final tissue classification model was validated using the other half of the spectral database (hereafter called the validation set) that contained annotated Raman spectra of the samples of the 11 different patients not included in the training set.

Spectral simulations of large measurement volumes

In order to investigate the clinical implications of our results, simulations were performed of large measurement volumes (1 mm^3), such as those that can be expected while using fiber-optic probes. In this study, the discriminating differences between OCSCC and healthy tongue tissue collected from the anterior one third and mid one third of the tongue were compared.

The epithelial layer of the dorsal side at the apex, or 'anterior one third of the tongue', has an average thickness of 700 µm.[38] The average subepithelial, deeper soft tissue consists of 33% muscle, 40% adipose tissue, 24% CT, and 2% combined glandular, vascular and nervous tissue.[39] In comparison, the dorsal side at the midpoint between the apex and the foramen caecum, or 'mid one third of the tongue', has an average epithelial layer of 600 µm.[37] The average subepithelial, deeper soft tissue consists of 53% muscle, 6% adipose tissue, 13% CT, and 27% combined glandular, vascular and nervous tissue.[39]

The molecular compositions of the simulated healthy measurement volumes were calculated based on results of the fits of the individual tissue structures. The average molecular composition of gland and nerve were used to represent the combined glandular, vascular and nervous tissue.[39] A similar approach was adopted in order to create simulations representing healthy measurement volumes of the subepithelial, deeper soft tissue layers of the tongue.

RESULTS

Histopathologically annotated Raman spectra

A database containing Raman spectra that were correlated to histopathology was created. The spectra were obtained from the data of 197 Raman mapping experiments on 44 tissue samples from 21 patients. Of these 44 samples, 17 contained OCSCC and surrounding healthy tissue structures (i.e. surface squamous epithelium, CT, muscle, adipose tissue, gland and nerve), and 27 contained healthy tissue structures only. The scanned areas ranged in size between 250 µm x 100 µm and 1005 µm x 470 µm. Adopting a Raman measurement step size of 5 µm resulted in 2700 to 18 894 point spectra per Raman map (mean number of spectra per map: 10 781). The optimal number of K-means clusters per map varied between 3 and 20, resulting in a total of 1087 histopathologically annotated K-means cluster averages.

In total, 142 K-means cluster averages were annotated as OCSCC, 202 as surface squamous epithelium, 581 as CT, 61 as muscle, 65 as adipose tissue, 26 as gland and 10 as nerve. Averaging all equally annotated spectra revealed a representative/characteristic Raman spectrum per tissue structure, or 'characteristic tissue-type spectrum'.

Fit of characteristic tissue-type spectra to select the best library

To select the optimal combination of fit-spectra per tissue structure, the characteristic tissue-type spectra were fit conform the described multistep optimization procedure. The results are plotted in Figure 3 and Figure 4. The selected fit-spectra per tissue structure are summarized in Table 1.

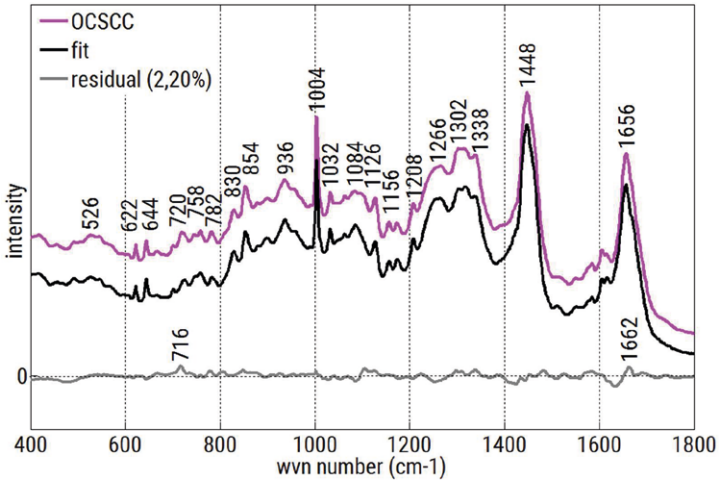

Figure 3. Optimal fit of characteristic OCSCC spectrum.

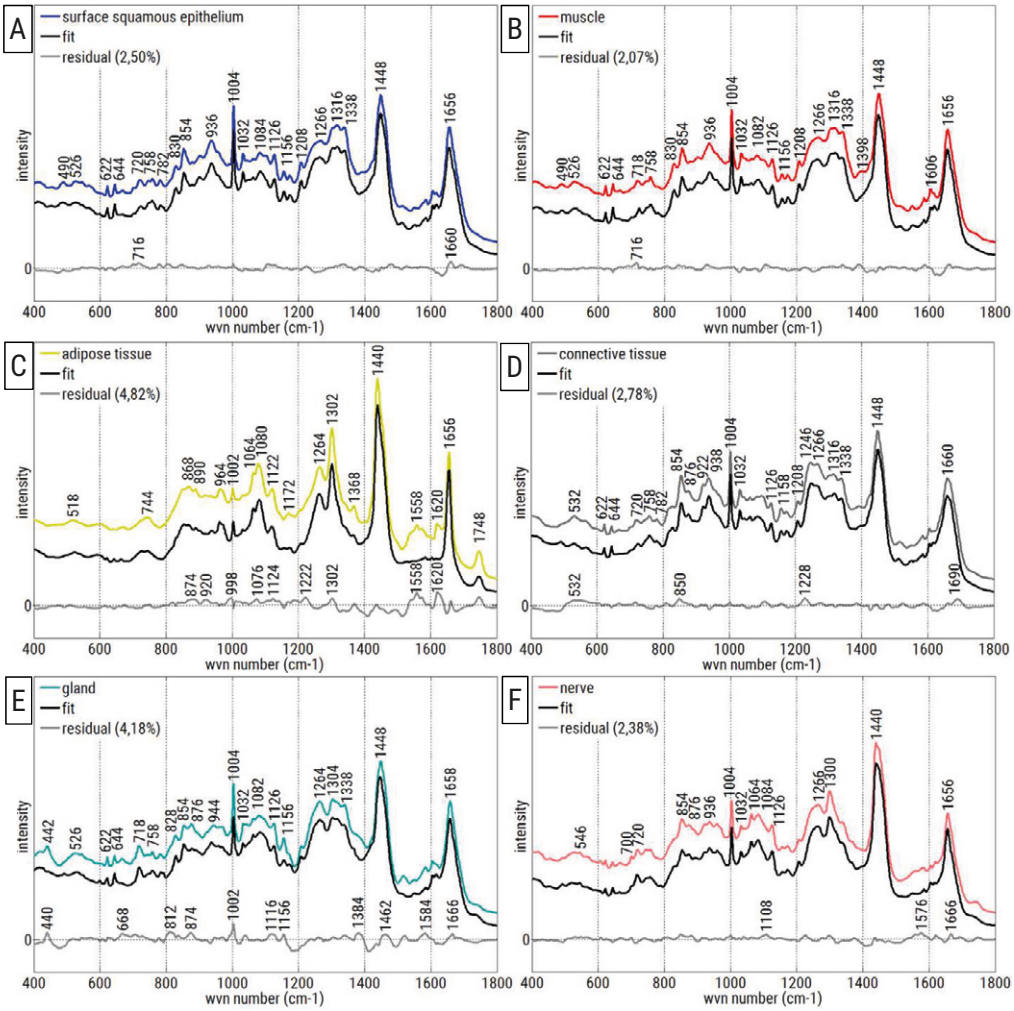

Figure 4. Optimal fits of characteristic healthy tissue-type spectra. A: Surface squamous epithelium. B: Muscle. C: Adipose tissue. D: Connective tissue. E: Gland. F: Nerve.

Molecular composition per tissue structure

The molecular composition per tissue structure was determined by fitting all individual spectra with the selected fit-spectra for that tissue structure. An average and standard deviation per chemical class were calculated. Again the described multistep optimization procedure was used. The compositions of the healthy tissue structures were compared to that of OCSCC, as illustrated in Figure 5A – 5F and summarized in Table 2.

	OCSCC	Surface squamous epithelium	Muscle	Adipose tissue	Connective tissue	Gland	Nerve
Proteins	Actin Albumin Collagen type III Hemoglobin Keratin	Actin Albumin Collagen type III Hemoglobin Keratin Mucin	Actin Collagen type III Hemoglobin Keratin Mucin	Actin Collagen type III Hemoglobin Keratin Myosin	Actin Albumin Collagen type II Collagen type III Elastin Hemoglobin Keratin Mucin	Actin Albumin Collagen type II Elastin Hemoglobin Keratin Mucin	Actin Collagen type III Hemoglobin Keratin Myosin
Lipids	Ceramide Cholesterol Linoleic acid Palmitoleic acid	Ceramide Lecithin Linoleic acid Oleic acid Palmitoleic acid	Chol. linoleate Linoleic acid Oleic acid	Oleic acid Olive oil	Linoleic acid Oleic acid	Lecithin Linolenic acid	Lecithin Linolenic acid Oleic acid
Nucleic acids	Cytosine DNA RNA Thymine	Cytosine DNA Thymine	Adenine Cytosine DNA RNA Thymine	-	Adenine DNA Thymine	Adenine Cytosine DNA Thymine	Adenine Thymine Uracil
Amino acids	L-arginine L-citrulline L-glutamic acid L-phenylalanine L-proline	L-citrulline L-glutamic acid L-lysine L-phenylalanine L-proline	L-citrulline L-glutamic acid L-histidine L-phenylalanine L-proline L-serine	L-arginine L-tyrosine	L-glutamic acid L-histidine L-phenylalanine L-proline	L-citrulline L-serine	L-arginine L-phenylalanine

	OCSCC	Surface squamous epithelium	Muscle	Adipose tissue	Connective tissue	Gland	Nerve
Carbohydrates	Amylopectin	Amylopectin Glycogen	Amylopectin	Chond. sulfate A Glucose	Amylopectin Glycogen	Amylopectin Chond. sulfate A Glycogen	Glucose
Miscellaneous	β-carotene Lactic acid	β-carotene Lactic acid	β-carotene Lactic acid	Hydroxyapatite	β-carotene Lactic acid	β-carotene Hydroxyapatite	Hydroxyapatite Lactic acid

Table 1. The results of the optimal fits are shown.

First column: the chemical classes. Second column: pure compounds included in the optimal fit of characteristic OCSCC spectrum. Third to final column: pure compounds included in the optimal fits of characteristic healthy tissue-type spectra; surface squamous epithelium, muscle, adipose tissue, connective tissue, gland and nerve respectively.

	OCSCC	Surface squamous epithelium	Muscle	Adipose tissue	Connective tissue	Gland	Nerve
Proteins	82 (± 3)	82 (± 6)	83 (± 2)	50 (± 5)	91 (± 4)	71 (± 8)	78 (± 11)
Lipids	6 (± 2)	6 (± 3)	6 (± 2)	45 (± 5)	2 (± 2)	18 (± 5)	18 (± 11)
Nucleic acids	6 (± 3)	5 (± 2)	4 (± 2)	0 (± 0)	3 (± 2)	3 (± 2)	0 (± 0)
Amino acids	5 (± 1)	4 (± 2)	6 (± 1)	3 (± 2)	2 (± 1)	4 (± 3)	1 (± 1)
Carbohydrates	0 (± 0)	2 (± 3)	0 (± 0)	3 (± 1)	1 (± 1)	4 (± 6)	2 (± 1)
Miscellaneous	1 (± 0)	1 (± 0)	2 (± 0)	1 (± 0)	1 (± 0)	0 (± 0)	1 (± 1)

Table 2. Molecular composition in of fitted individual OCSCC and healthy tissue-type spectra.

First column: the chemical classes. Second column: mean percentage ± standard deviation of fitted individual OCSCC spectra. Third to final column: mean percentage ± standard deviation of fitted individual healthy tissue-type spectra; surface squamous epithelium, muscle, adipose tissue, connective tissue, gland and nerve respectively.

OCSCC

The optimal fit included 21 fit-spectra, with which only 2,20% of the characteristic OCSCC spectrum was unexplained (fit-residual) (Figure 3). All 142 individual OCSCC spectra were fitted with these 21 fit-spectra. This resulted in an average molecular composition of 82% proteins, 6% lipids, 6% nucleic acids, 5% amino acids and 1% miscellaneous.

Surface squamous epithelium

The optimal fit included 23 fit-spectra and had 2,50% fit-residual (Figure 4A). The fits of 202 individual surface squamous epithelium spectra resulted in an average molecular composition of 82% proteins, 6% lipids, 5% nucleic acids, 4% amino acids, 2% carbohydrates and 1% miscellaneous. The only two differences with the composition of OCSCC were found in a lower nucleic acid and amino acid content, and in a higher carbohydrate content (Figure 5).

Muscle

The optimal fit included 22 fit-spectra and had 2,07% fit-residual (Figure 4B). All 61 individual muscle spectra were fitted, which resulted in an average molecular composition of 83% proteins, 6% lipids, 4% nucleic acids, 6% amino acids and 2% miscellaneous. A lower nucleic acid content was seen for muscle, compared to OCSCC. Furthermore, muscle had a (slightly) higher contribution of proteins, amino acids and miscellaneous (Figure 5).

Adipose tissue

The optimal fit included 12 fit-spectra and had 4,82% fit-residual (Figure 4C). The fits of 65 individual adipose tissue spectra resulted in an average molecular composition of 50% proteins, 45% lipids, 3% amino acids, 3% carbohydrates and 1% miscellaneous. The composition of adipose tissue comprised a higher lipid and carbohydrate content, and a lower protein, nucleic acid and amino acid content, compared to OCSCC (Figure 5).

Connective tissue

The optimal fit included 21 fit-spectra and had 2,78% fit-residual (Figure 4D). All 581 individual connective tissue spectra were fitted. This resulted in an average molecular composition of 91% proteins, 2% lipids, 3% nucleic acids, 2% amino acids, 1% carbohydrates and 1% miscellaneous. Compared to OCSCC, the CT showed a higher content of proteins and carbohydrates, and a lower content of lipids, nucleic acids and amino acids (Figure 5).

Gland

The optimal fit included 20 fit-spectra and had 4,18% fit-residual (Figure 4E). Twenty-six individual gland spectra were fitted, resulting in an average molecular composition of 71% proteins, 18% lipids, 3% nucleic acids, 4% amino acids and 4% carbohydrates. Compared to OCSCC, gland showed a higher contribution of lipids and carbohydrates, and a lower contribution of proteins, nucleic acids, amino acids and miscellaneous (Figure 5).

Nerve

The optimal fit included 16 fit-spectra and had 2,38% fit-residual (Figure 4F). All 10 individual nerve spectra were fitted with these fit-spectra. This resulted in an average molecular composition of 78% proteins, 18% lipids, 1% amino acids, 2% carbohydrates and 1% miscellaneous. Compared to the composition of OCSCC, nerve was composed of more lipids and carbohydrates, and less proteins, nucleic acids and amino acids (Figure 5).

As shown in Table 2, the main compounds of all of the analyzed tissue structures were proteins and lipids. Whether the contribution of proteins and lipids was higher of lower than OCSCC, depended on the analyzed tissue structure. The molecular composition of adipose tissue, gland and nerve showed a lower contribution of proteins and a higher contribution of lipids than OCSCC. This stands in contrast with CT, which was characterized by more proteins and less lipids, compared to OCSCC. OCSCC differed from all healthy tissue structures by its higher amount of nucleic acids. In all healthy tissue structures the contribution of carbohydrates was higher than in OCSCC, except for muscle. Only muscle had a higher content of amino acids than OCSCC.

'Tumor' versus 'healthy tissue' classification model

Characteristics of the training and validation set

The training set consisted of 127 Raman maps, obtained from 25 (11 OCSCC and 14 healthy) tissue samples from 10 patients. In total 88 K-means clusters averages were annotated as 'tumor', and 632 K-means clusters averages were annotated as 'healthy tissue' (140 surface squamous epithelium, 396 CT, 41 muscle, 33 adipose tissue, 17 gland and 5 nerve). The 'tumor' versus 'healthy tissue' classification model was validated using an independent dataset. This validation set consisted of 70 Raman maps, obtained from 19 (6 OCSCC and 13 healthy) samples from 11 patients that were not included in the training set. In total 54 K-means clusters averages were annotated as 'tumor', and 313 K-means clusters averages were annotated as 'healthy tissue' (62 surface squamous epithelium, 185 CT, 20 muscle, 32 adipose tissue, 9 gland and 5 nerve).

Results of 'tumor' versus 'healthy tissue' classification model

The chemical class fit contributions (ccfc) of carbohydrates, proteins and amino acids revealed to be most discriminative. Setting the cut-off for carbohydrates at < 0,001%, for proteins at < 87% and for amino acids at > 2% resulted in a total of 86 of 88 tumor spectra being classified as 'tumor' and 580 of 632 healthy tissue spectra being classified as 'healthy tissue' in the training set. This matches an accuracy of 93%, a sensitivity of 98% and a specificity of 92%. Validation of this classification model showed an accuracy of 94%, sensitivity of 100% and specificity of 93%, as illustrated in Table 3.

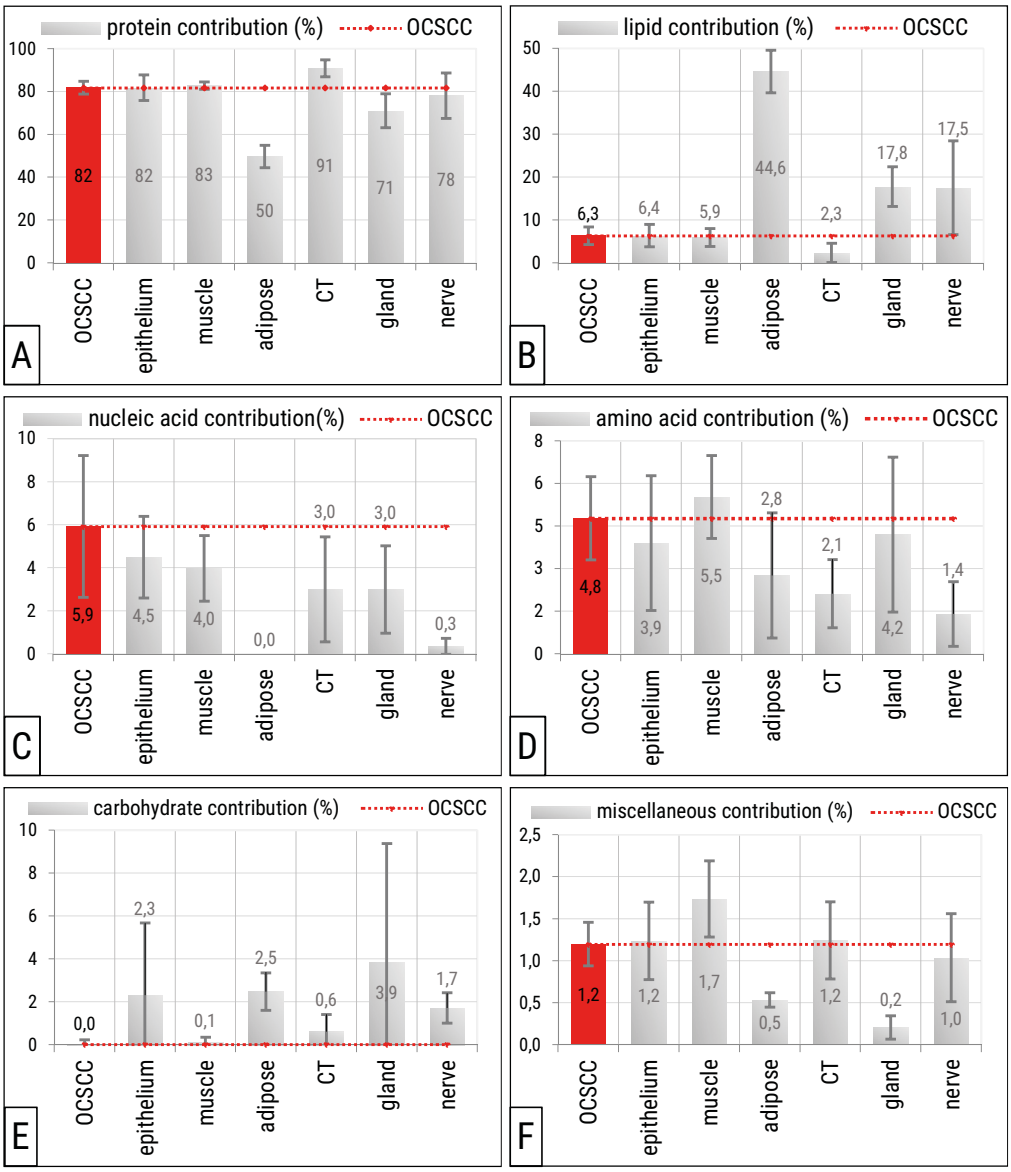

Figure 5. Discriminating differences in molecular composition of fitted individual OCSCC and healthy tissue-type spectra. A: Contribution of proteins. B: Contribution of lipids. C: Contribution of nucleic acids. D: Contribution of amino acids. E: Contribution of carbohydrates. F: Contribution of miscellaneous.

Spectral simulations of large measurement volumes

In most clinical applications of Raman spectroscopy, fiber-optic probes are used with measurement volumes that contain multiple tissue structures. When a probe is placed on the epithelial surface, a signal can be collected from depths up to 1 mm. In the tongue, the epithelial thickness as well as the

distribution of the subepithelial, deeper soft tissue structures is location dependent.[37-39] Simulations of 1 mm^3 measurements representing the distribution of healthy tissue structures at the anterior one third and mid one third of the tongue were created as described in the materials and methods section. Figure 6 shows that although the healthy anterior one third and mid one third of the tongue differed in their distribution of tissue structures and thus in their molecular composition, their distinction with OCSCC remained similar. Nucleic acid, protein and amino acid content were higher in OCSCC, whereas lipid and carbohydrate contributions were higher in healthy tissue.

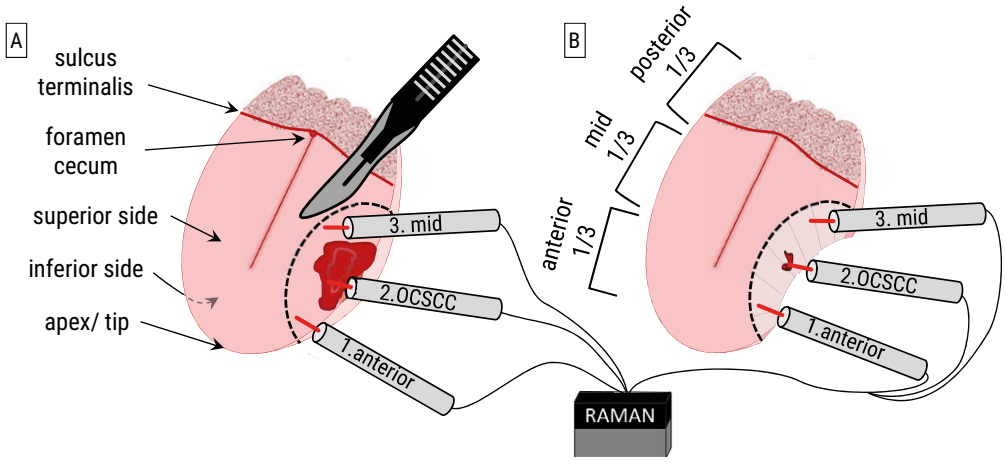

C	OCSCC	Anterior one third	Mid one third	Subepithelial anterior one third	Subepithelial medial one third
Proteins	82	79	81	71	80
Lipids	6	11	8	21	11
Nucleic acids	6	4	4	2	3
Amino acids	5	4	4	4	4
Carbohydrates	0	2	2	1	0
Miscellaneous	1	1	1	1	1

Figure 6. A: Schematic overview of a tongue with an OCSCC on its left edge, with three simulated large-volume measurement points. B: Schematic overview of the tongue wound bed after resection, with residual tumor and three simulated large-volume measurement points. C: Table shows the calculated molecular composition of the simulated points. First column: the chemical classes. Second column: mean percentage of simulated large measurement volume with OCSCC. Third and fourth column: mean percentage of simulated large measurement volume from mucosal surface. Fifth and sixth column: mean percentage of simulated large measurement volume from subepithelial, deeper soft tissue layers.

	Accuracy	Sensitivity	Specificity	True positive	True negative	False positive	False negative
Training set	93%	98%	92%	86	580	52	2
Validation set	94%	100%	93%	54	291	22	0

Table 3. Per dataset the accuracy, sensitivity (true positive rate) and specificity (true negative rate) are shown. The number of correct classified spectra per dataset have been further detailed in the last 4 columns.

The epithelial layer contributes significantly when the probe is placed on the epithelial surface. Regarding the application of Raman spectroscopy as a surgery-guidance tool, it is also of interest to examine how the Raman results of subepithelial, deeper soft tissue are influenced by the distribution of tissue structures. Likewise, simulations were therefore made for the subepithelial anterior one third and the subepithelial mid one third of the tongue. Figure 6 shows that the aforementioned differences between healthy tissue and OCSCC persisted in the subepithelial, deeper soft tissue layers, except for the carbohydrate content.

DISCUSSION

In this study, a set of 55 fit-spectra was used in order to analyze the molecular compositions of OCSCC and individual healthy tissue structures in the oral tongue. The content of carbohydrates was the most important factor to discriminate between tumor and healthy tissue. Only 2 out of 142 OCSCC spectra had a carbohydrate content of > 0%. The markedly increased uptake and utilization of glucose in tumors have been well documented.[47,48] Increased glycolysis allows the change of glycolytic intermediates into various biosynthetic pathways, including those generating nucleic acids and aminos acids.[48] By the additional use of a high protein (> 87%) and low amino acids (< 2%) contribution a high accuracy, sensitivity and specificity was obtained with the developed 'tumor' versus 'healthy tissue' classification model.

The results of this study corroborate those of Deshmukh et al.[28] They compared Raman spectra that were obtained from bulk buccal tissue containing surface squamous epithelium and submucosa, with spectra obtained from sectioned tissue samples containing only surface squamous epithelium. Their samples had an average epithelial thickness of 500 µm and were measured using a probe, collecting signal from a tissue volume with a depth of 1 mm. The analysis of the wavenumber range of 1200 – 1800 cm^{-1} reveals that the spectra of bulk tissues showed features from the epithelial surface as well as from the deeper layers. Independently of the sample type, the cluster analysis demonstrates that tumor spectra with dominating protein features were distinguisable from healthy tissues that had predominant lipid signatures.[28] This was also seen in our simulated larger measurement volumes. The results may be explained by the fact that oral submucosa is characterized by the presence of adipose tissue and glands.[35] However, if on the contrary, a healthy tissue volume consists of a large proportion of CT and muscle, the lipid/protein ratio might approach or be smaller than the one of OCSCC. This confirms that the actual discrimination between an OCSCC spectrum and a spectrum obtained from a larger healthy tissue volume, is dependent on the presence and exact proportion of the individual healthy tissue structures in the measurement volume.

We showed that the molecular composition of OCSCC differs from all other healthy tissue structures by its higher mean content of nucleic acids. However the standard deviation in OCSCC and in the healthy structures was so large that it did not contribute to the classification model. The predominant nucleic acid features in tumor were also described by Sahu et al., who compared 122 *in vivo* acquired spectra of tongue OCSCC, with 137 spectra of tongue from volunteers without tobacco and/or alcohol habits.[41]

As shown by the simulations, the difference in nucleic acid content becomes greater if the subepithelial, deeper soft tissue is studied. This is due to the absence of surface squamous epithelium in the measurement volume. The biochemical compositions of OCSCC and surface squamous epithelium are highly similar, which is not surprising because OCSCC originates from the surface squamous epithelium. In carcinogenesis, stem cells located in the basal epithelial layers acquire genetic alterations, followed by clonal expansion and invasion to the deeper tissue layers.[49] In a previous Raman-fingerprint study,[21] we concluded that squamous epithelium was spectrally distinguishable from OCSCC with lower accuracy (75%), compared to the deeper located healthy tissue structures (adipose tissue, CT, muscle, gland and nerve) (100%, 93%, 97%, 94% and 100% respectively). Within clinical practice, there is especially need for a medical diagnostic device that provides an intraoperative and objective evaluation of the subepithelial, deeper soft tissue resection margins.[1,2,50,51]

However, the developed classification model cannot be directly implemented in such a diagnostic device because it is based on *in vitro* measurements on untreated frozen tissue sections. Water, the most abundant component of human tissue, was not measured in these thin tissue sections. The approach adopted here, however, enabled a detailed analysis of the discriminating differences in the molecular composition of individual tissue structures within oral tongue tissue. The scanning-step size of 5 µm allowed us to obtain information with a minimal interference of spectral contribution from neighboring tissue structures.

In order to define the molecular composition, a set of 55 fit-spectra was created. Some pure compounds that were added to the set were measured in a solid state, while others were dissolved in dissimilar concentrations (see specifications in Chapter 6). A limitation of this study is therefore that the calculated compositions are based on spectral contributions and do not represent the actual chemical composition in the tissues in mass percentages. The set of fit-spectra that was used in this study was extensive but evidently not complete. Nonetheless, the fits of the characteristic tissue-type spectra demonstrate a reasonable spectroscopic representation of the measured frozen tissue section spectra. In the case of adipose tissue, the fit-residual was highest (4,82%) and showed distinct spectroscopic features that can possibly be assigned to heme groups. An expansion of the set of fit-spectra could further reduce the unexplained fit-residual.

The results of this study present important knowledge for future Raman spectroscopic research, as well as for the implementation of the technique as a medical-diagnostic device. This study can help to interpret the results of any *in vivo* acquired tongue spectrum. In the tongue, an OCSCC is surrounded by healthy tissue structures. A mixture of both within a measurement volume can complicate the interpretation of results. In future, this database will be used in order to determine the limit of tumor detection in probe volumes with various mixtures of tissue structures, with and without surface squamous epithelium.

REFERENCES

1. Dillon, Brown, et al. (2015) *How does the close surgical margin impact recurrence and survival when treating oral squamous cell carcinoma?* Journal of Oral and Maxillofacial Surgery. 73(6):1182-1188.
2. Smits, Koljenovic, et al. (2015) *Resection margins in oral cancer surgery: Room for improvement.* Head & Neck. 38(1):E2197-2203.
3. Davies, Connolly, et al. (2015) *Point of care optical diagnostic technologies for the detection of oral and oropharyngeal squamous cell carcinoma.* Surgeon. 13(6):321-329.
4. Green, Cobb, et al. (2014) *Optical diagnostic techniques for use in lesions of the head and neck: Review of the latest developments.* British Journal of Oral and Maxillofacial Surgery. 52(8):675-680.
5. Jerjes, Upile, et al. (2011) *The future of medical diagnostics: Review paper.* Head & Neck Oncology. 3(38):1-8.
6. Singh, Ibrahim, et al. (2016) *Recent advances in optical diagnosis of oral cancers: Review and future perspectives.* Head & Neck. 38(1):1-9.
7. Shin, Vigneswaran, et al. (2010) *Advances in fluorescence imaging techniques to detect oral cancer and its precursors.* Future Oncology. 6(7):1143-1154.
8. Keereweer, Sterenborg, et al. (2012) *Image-guided surgery in head and neck cancer: Current practice and future directions of optical imaging.* Head & Neck. 34(1):120-126.
9. Keereweer, Van Driel, et al. (2013) *Optical image-guided cancer surgery: Challenges and limitations.* Clinical Cancer Research. 19(14):3745-3754.
10. Francisco, Correr, et al. (2014) *Analysis of surgical margins in oral cancer using in situ fluorescence spectroscopy.* Oral Oncology. 50(6):593-599.
11. Tirelli, Piovesana, et al. (2015) *Narrow band imaging in the intra-operative definition of resection margins in oral cavity and oropharyngeal cancer.* Oral Oncology. 51(10):908-913.
12. Vu, Farah. (2016) *Narrow band imaging: Clinical applications in oral and oropharyngeal cancer.* Oral Diseases. 22(5):383-390.
13. Wilder-Smith, Jung, et al. (2004) *In vivo optical coherence tomography for the diagnosis of oral malignancy.* Lasers in Surgery and Medicine. 35(4):269-275.
14. Hamdoon, Jerjes, et al. (2013) *Optical coherence tomography in the assessment of suspicious oral lesions: An immediate ex vivo study.* Photodiagnosis and Photodynamic Therapy. 10(1):17-27.
15. Abbaci, Breuskin, et al. (2014) *Confocal laser endomicroscopy for non-invasive head and neck cancer imaging: A comprehensive review.* Oral Oncology. 50(8):711-716.
16. Anuthama, Sherlin, et al. (2010) *Characterization of different tissue changes in normal, betel chewers, potentially malignant lesions, conditions and oral squamous cell carcinoma using reflectance confocal microscopy: Correlation with routine histopathology.* Oral Oncology. 46(4):232-248.
17. Lucchese, Gentile, et al. (2016) *The potential role of in vivo reflectance confocal microscopy for evaluating oral cavity lesions: A systematic review.* Journal of Oral Pathology and Medicine. 45(10):723-729.
18. Muldoon, Roblyer, et al. (2012) *Noninvasive imaging of oral neoplasia with a high-resolution fiber-optic microendoscope.* Head & Neck. 34(3):305-312.
19. Sharwani, Jerjes, et al. (2006) *Assessment of oral premalignancy using elastic scattering spectroscopy.* Oral Oncology. 42(4):343-349.
20. Barroso, Smits, et al. (2015) *Discrimination between oral cancer and healthy tissue based on water content determined by Raman spectroscopy.* Analytical Chemistry. 87(4):2419-2426.
21. Cals, Bakker Schut, et al. (2015) *Investigation of the potential of Raman spectroscopy for oral cancer detection in surgical margins.* Laboratory Investigation. 95(10):1186-1196.
22. Cals, Bakker Schut, et al. (2013) *Method development: Raman spectroscopy-based histopathology of oral mucosa.* Journal of Raman Spectroscopy. 44(7):963-972.
23. Sahu, Talathi, et al. (2014) *Classification of oral cancers using Raman spectroscopy of serum.* Biomedical Vibrational Spectroscopy. 8939(3):E1-E7.
24. Raman. (1928) *A new type of secondary radiation.* Nature. 121(501-502):365.
25. Koningstein. *Introduction to the theory of the Raman effect.* 1st ed. (1972)
26. Evers, Hendriks, et al. (2012) *Optical spectroscopy: Current advances and future applications in cancer diagnostics and therapy.* Future Oncology. 8(3):307-320.

27. Carvalho, Bonnier, et al. (2015) *Raman micro-spectroscopy for rapid screening of oral squamous cell carcinoma.* Experimental and Molecular Pathology. 98(3):502-509.
28. Deshmukh, Singh, et al. (2011) *Raman spectroscopy of normal oral buccal mucosa tissues: Study on intact and incised biopsies.* Journal of Biomedical Optics. 16(12):127004-127010.
29. Guze, Short, et al. (2011) *Comparison of molecular images as defined by Raman spectra between normal mucosa and squamous cell carcinoma in the oral cavity.* Journal of Raman Spectroscopy. 42(6):1232-1239.
30. Knipfer, Motz, et al. (2015) *Raman difference spectroscopy: A non-invasive method for identification of oral squamous cell carcinoma: Publisher's note.* Biomedical Optics Express. 6(7):3252-3265.
31. Malini, Venkatakrishna, et al. (2006) *Discrimination of normal, inflammatory, premalignant, and malignant oral tissue: A Raman spectroscopy study.* Biopolymers. 81(3):179-193.
32. Su, Sun, et al. (2012) *Raman spectral properties of squamous cell carcinoma of oral tissues and cells.* Laser Physics. 22(1):311-316.
33. Venkatakrishna. (2001) *Optical pathology of oral tissue: A Raman spectroscopy diagnostic method.* Current science. 80(5):665-670.
34. Wu, Xu, et al. (2001) *Distinguishing malignant from normal oral tissues using ftir fiber-optic techniques.* Biopolymers. 62(4):185-192.
35. Mills. *Histology for pathologists.* 3rd ed. (2004)
36. Olaleye, Ekrikpo, et al. (2015) *Incidence and survival trends of lip, intra-oral cavity and tongue base cancers in south-east england.* Annual of the Royal College of Surgeons of England. 97(3):229-234.
37. Sasaki. (1994) *Histomorphometric analysis of age-related changes in epithelial thickness and langerhans cell density of the human tongue.* Tohoku Journal Experimental Medicine. 173(3):321-336.
38. Valentine, Scott, et al. (1985) *A histological analysis of the early effects of alcohol and tobacco usage on human lingual epithelium.* Journal of Oral Pathology. 14(8):654-665.
39. Miller, Watkin, et al. (2002) *Muscle, adipose, and connective tissue variations in intrinsic musculature of the adult human tongue.* Journal of Speech Language and Hearing Research. 45(1):51-65.
40. Krishna, Majumder, et al. (2014) *In vivo Raman spectroscopy for detection of oral neoplasia: A pilot clinical study.* Journal of Biophotonics. 7(9):690-702.
41. Sahu. (2016) *In vivo subsite classification and diagnosis of oral cancers using Raman spectroscopy.* Journal of Innovative Optical Health Sciences. 9(5):1-14.
42. Bettelheim. *Introduction to general, organic and biochemistry.* 10th ed. (2012)
43. Lawson. *Solving least squares problems.* 1st ed. (1995)
44. Patel, Goldstein, et al. (2010) *Impact of positive frozen section microscopic tumor cut-through revised to negative on oral carcinoma control and survival rates.* Head & Neck. 32(11):1444-1451.
45. Jain. *Algorithms for clustering data* 1st ed. (1988)
46. Rosai. *Surgical pathology* 10th ed. (2011)
47. Gillies, Robey, et al. (2008) *Causes and consequences of increased glucose metabolism of cancers.* Journal of Nuclear Medicine. 49(2):24S-42S.
48. Hanahan, Weinberg. (2011) *Hallmarks of cancer: The next generation.* Cell. 144(5):646-674.
49. Braakhuis, Leemans, et al. (2004) *A genetic progression model of oral cancer: Current evidence and clinical implications.* Journal Oral Pathology Medicine. 33(6):317-322.
50. Sutton, Brown, et al. (2003) *The prognostic implications of the surgical margin in oral squamous cell carcinoma.* International Journal of Oral and Maxillofacial Surgery. 32(1):30-34.
51. Woolgar, Triantafyllou. (2005) *A histopathological appraisal of surgical margins in oral and oropharyngeal cancer resection specimens.* Oral Oncology. 41(10):1034-1043.

6

Pure-compound reference spectra

Froukje L. J. Cals, Senada Koljenović, Tom C. Bakker Schut, Gerwin J. Puppels

To be submitted in online database

PURE-COMPOUND REFERENCE SPECTRA

A complete overview of the specifications (name, CAS-number, chemical class, firm, product number, purity, source, instrument, measured condition (dry/dissolved), solvent, concentration, pH, acquisition time, accumulations, spectral corrections and S/N ratio), as well as the peak positions of all pure-compound measurements are given.

Name	**Actin**
CAS-number:	51005-14-2
Chemical class:	Protein, globular
Firm:	Sigma-Aldrich Chemie B.V.
Product number:	A3653
Purity according to firm:	99%
Source:	bovine muscle
Analysis	
Spectral corrections:	automated
Water:	no
Fused silica:	order 1, range 400:2:1800
S/N ratio:	318,50

Measurement	
Condition:	solid
Solvent:	n.a.
Concentration:	n.a.
pH:	n.a.
Instrument:	SpectraCell *RA Bacterial Strain Analyzer*
Acquisition time:	635 x 5 seconds
Remarks:	soluble in H2O, but in different solutions only water bands

Peaks

418, 490, 524, 622, 644, 700, 724, 760, 830, 854, 896, 936, 958, 1004, 1032, 1078, 1126, 1156, 1172, 1208, 1244, 1318, 1338, 1398, 1448, 1552, 1586, 1616, 1668

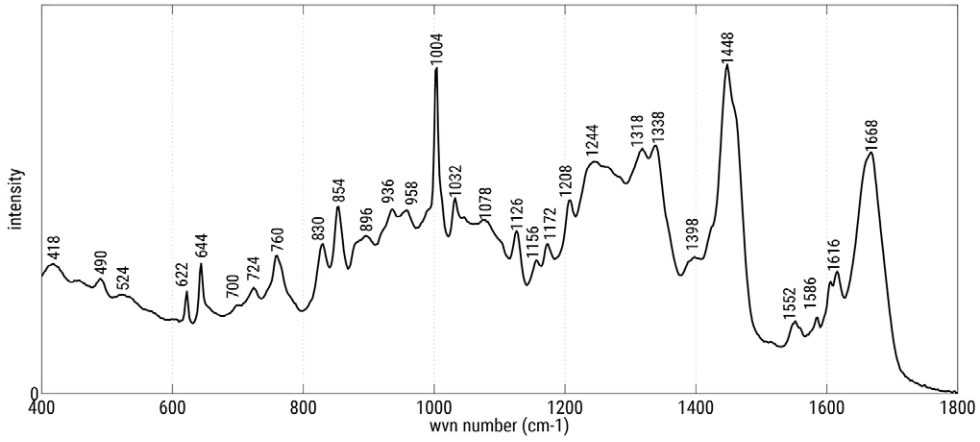

Name	**Adenine**	**Measurement**	
CAS-number:	73-24-5	Condition:	solid
Chemical class:	Nucleotide, purine	Solvent:	n.a.
Firm:	Sigma-Aldrich Chemie B.V.	Concentration:	n.a.
Product number:	A8626	pH:	n.a.
Purity according to firm:	>99%	Instrument:	SpectraCell *RA Bacterial Strain Analyzer*
Source:	not mentioned	Acquisition time:	433 x 1 seconds
		Remarks:	soluble in NaOH 1M
Analysis			
Spectral corrections:	automated		
Water:	no	**Peaks**	
Fused silica:	order 1, range 400:2:1800	536, 560, 622, 724, 796, 796, 898, 942, 1024, 1126, 1162, 1248, 1308, 1332, 1372, 1418, 1462, 1482, 1596, 1612, 1612, 1676	
S/N ratio:	2982,38		

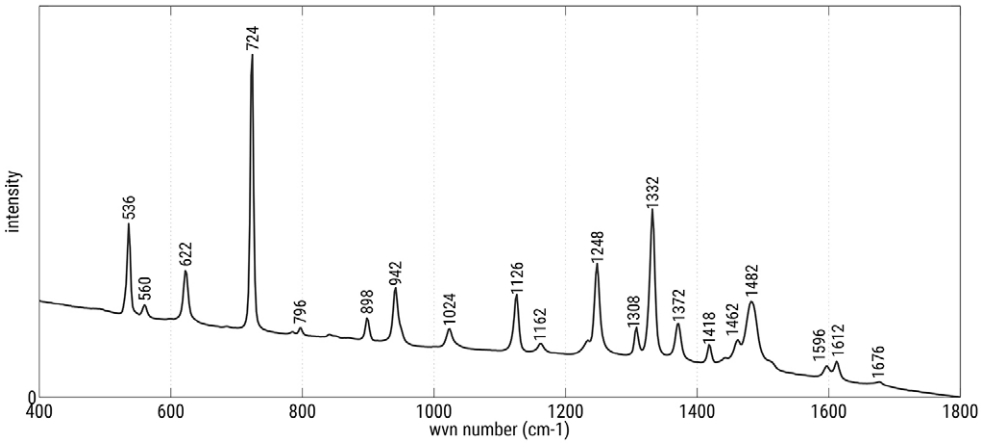

Name	**Albumin**	**Measurement**	
CAS-number:	9048-46-8	Condition:	dissolved
Chemical class:	Protein, globular	Solvent:	purified water
Firm:	Sigma-Aldrich Chemie B.V.	Concentration:	40 mg/ml
Product number:	A9647	pH:	7,5
Purity according firm:	96 - 99%	Instrument:	SpectraCell *RA Bacterial Strain Analyzer*
Source:	bovine	Acquisition time:	273 x 20 seconds
		Remarks:	clear, yellowish solution. Also solid
Analysis			
Spectral corrections:	manually		
Water:	order 0, range 400:2:1000	**Peaks**	
Fused silica:	no	500, 622, 644, 670, 726, 758, 784, 812, 828, 852, 898, 940, 960, 1004, 1032, 1100, 1126, 1158, 1174, 1208, 1248, 1318, 1336, 1450, 1574, 1606, 1656	
S/N ratio:	127,59		

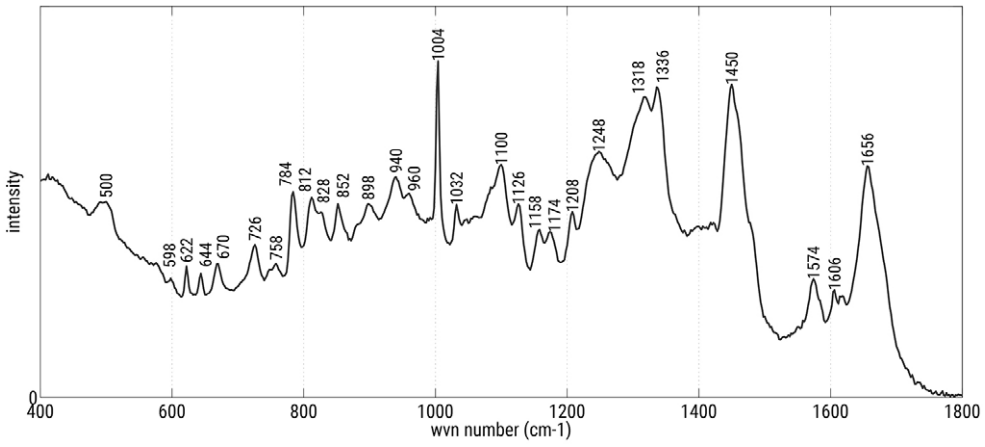

6

Name	**Amylopectin**	**Measurement**	
CAS-number:	9037-22-3	Condition:	dissolved
Chemical class:	Carbohydrate, polysaccharide	Solvent:	purified water
Firm:	Sigma-Aldrich Chemie B.V.	Concentration:	25 mg/ml
Product number:	10120	pH:	7,0
Purity according firm:	not mentioned	Instrument:	*Skin Analyzer*
Source:	maize	Acquisition time:	500 x 5 seconds
		Remarks:	heated, clear solution
Analysis			
Spectral corrections:	automated		
Water:	no	**Peaks**	
Fused silica:	no	410, 440, 476, 522, 578, 614, 720, 770, 868, 910, 942, 1052, 1082, 1110, 1128, 1148, 1210, 1262, 1340, 1380, 1400, 1462	
S/N ratio:	1019,69		

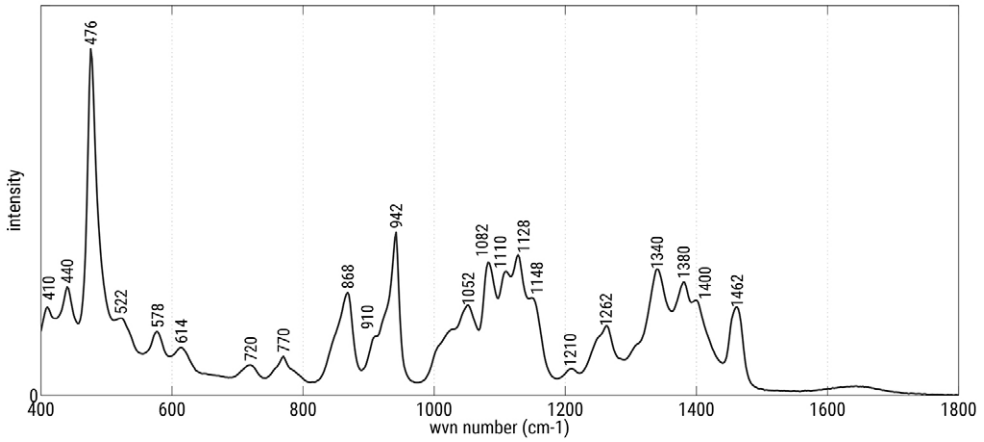

Name	**ß-carotene**	**Measurement**	
CAS-number:	7235-40-7	Condition:	solid
Chemical class:	Miscellaneous, provitamine A	Solvent:	n.a.
Firm:	Sigma-Aldrich Chemie B.V.	Concentration:	n.a.
Product number:	C9750	pH:	n.a.
Purity according firm:	>93%	Instrument:	SpectraCell *RA Bacterial Strain Analyzer*
Source:	synthetic powder	Acquisition time:	909 x 0,00001 seconds
		Remarks:	insoluble
Analysis			
Spectral corrections:	automated		
Water:	no	**Peaks**	
Fused silica:	order 0, range 400:2:1800	518, 870, 1008, 1156, 1190, 1210, 1268, 1278, 1310, 1352, 1394, 1448, 1512, 1576	
S/N ratio:	15375,06		

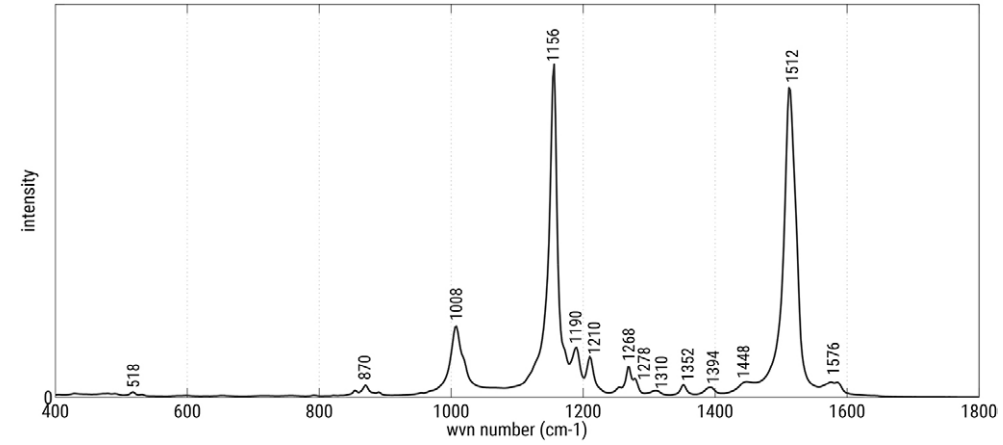

Name	Ceramide	**Measurement**	
CAS-number:	3102-57-6	Condition:	solid
Chemical class:	Lipid, saturated fatty acid	Solvent:	n.a.
Firm:	Enzo Life Sciences, Inc	Concentration:	n.a.
Product number:	ALX303001	pH:	n.a.
Purity according firm:	>98%	Instrument:	SpectraCell *RA Bacterial Strain Analyzer*
Source:	bovine brain	Acquisition time:	1191 x 5 seconds
		Remarks:	insoluble
Analysis			
Spectral corrections:	automated		
Water:	no	**Peaks**	
Fused silica:	no	490, 672, 688, 710, 798, 822, 876, 890, 890, 960, 1010, 1062, 1094, 1128, 1174, 1268, 1294, 1336, 1370, 1440, 1460, 1618, 1648, 1670	
S/N ratio:	280,54		

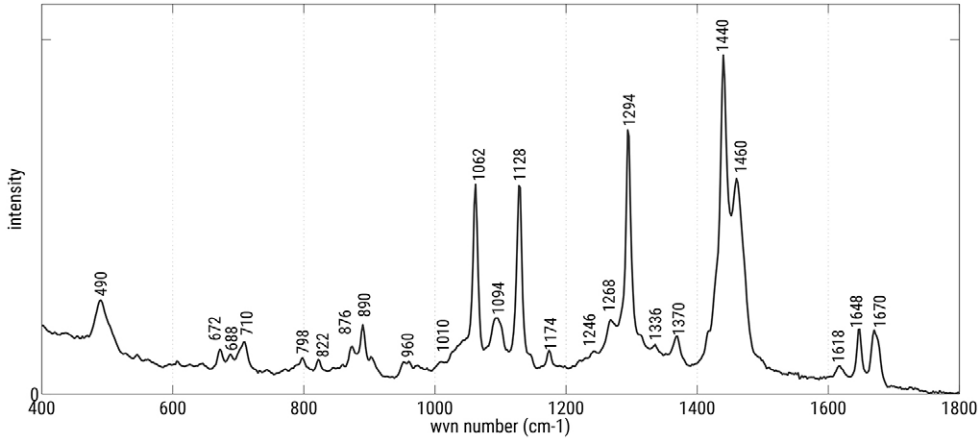

Name	Cholesterol	**Measurement**	
CAS-number:	57-88-5	Condition:	solid
Chemical class:	Lipid, sterol	Solvent:	n.a.
Firm:	Sigma-Aldrich Chemie B.V.	Concentration:	n.a.
Product number:	C8667	pH:	n.a.
Purity according firm:	99%	Instrument:	SpectraCell *RA Bacterial Strain Analyzer*
Source:	not mentioned	Acquisition time:	3000 x 4 seconds
		Remarks:	insoluble
Analysis			
Spectral corrections:	automated	**Peaks**	
Water:	no	422, 430, 456, 492, 504, 516, 548, 570, 594, 608, 628, 644, 700, 730, 742, 804, 828, 840, 850, 878, 914, 926, 936, 960, 988, 1006, 1024, 1040, 1052, 1064, 1084, 1110, 1128, 1142, 1160, 1176, 1194, 1208, 1220, 1238, 1254, 1274, 1304, 1332, 1350, 1376, 1438, 1462, 1672	
Fused silica:	order 0, range 400:2:1800		
S/N ratio:	273,41		

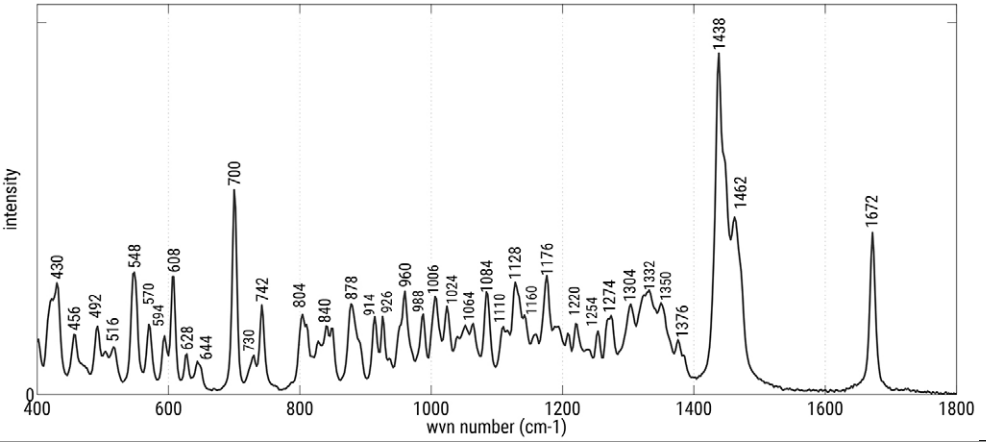

Name	**Cholesteryl linoleate**	**Measurement**	
CAS-number:	604-33-1	Condition:	solid
Chemical class:	Lipid, lipoprotein	Solvent:	n.a.
Firm:	Sigma-Aldrich Chemie B.V.	Concentration:	n.a.
Product number:	C0289	pH:	n.a.
Purity according firm:	>98%	Instrument:	SpectraCell *RA Bacterial Strain Analyzer*
Source:	not mentioned	Acquisition time:	270 x 15 seconds
		Remarks:	insoluble
Analysis		**Peaks**	
Spectral corrections:	automated	404, 428, 458, 490, 510, 546, 568, 590, 606, 626, 700, 726, 738, 802, 812,	
Water:	no	832, 844, 854, 878, 924, 958, 970, 988, 1006, 1028, 1064, 1074, 1088, 1110,	
Fused silica:	order 1, range 400:2:1800	1120, 1132, 1162, 1180, 1196, 1208, 1220, 1258, 1270, 1304, 1324, 1348,	
S/N ratio:	960,58	1378, 1438, 1460, 1658, 1738	

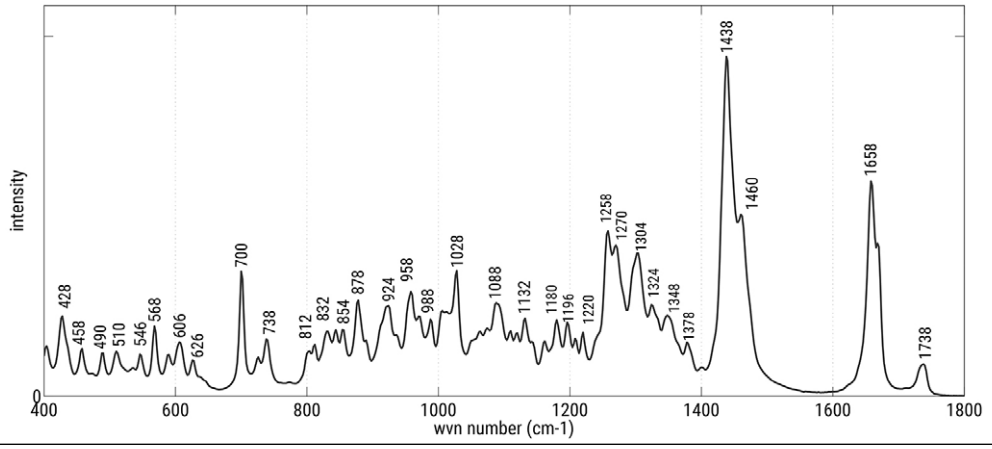

Name	**Cholesteryl oleate**	**Measurement**	
CAS-number:	303-43-5	Condition:	solid
Chemical class:	Lipid, lipoprotein	Solvent:	n.a.
Firm:	Sigma-Aldrich Chemie B.V.	Concentration:	n.a.
Product number:	C9253	pH:	n.a.
Purity according firm:	>98%	Instrument:	SpectraCell *RA Bacterial Strain Analyzer*
Source:	not mentioned	Acquisition time:	647 x 10 seconds
		Remarks:	insoluble
Analysis		**Peaks**	
Spectral corrections:	automated	404, 428, 458, 488, 510, 546, 568, 590, 606, 628, 700, 726, 738, 810, 828,	
Water:	no	844, 856, 876, 890, 924, 938, 958, 970, 988, 1006, 1026, 1064, 1086, 1120,	
Fused silica:	order 1, range 400:2:1800	1130, 1162, 1180, 1196, 1208, 1220, 1244, 1256, 1270, 1302, 1324, 1346,	
S/N ratio:	1381,33	1380, 1438, 1460, 1656, 1670, 1738	

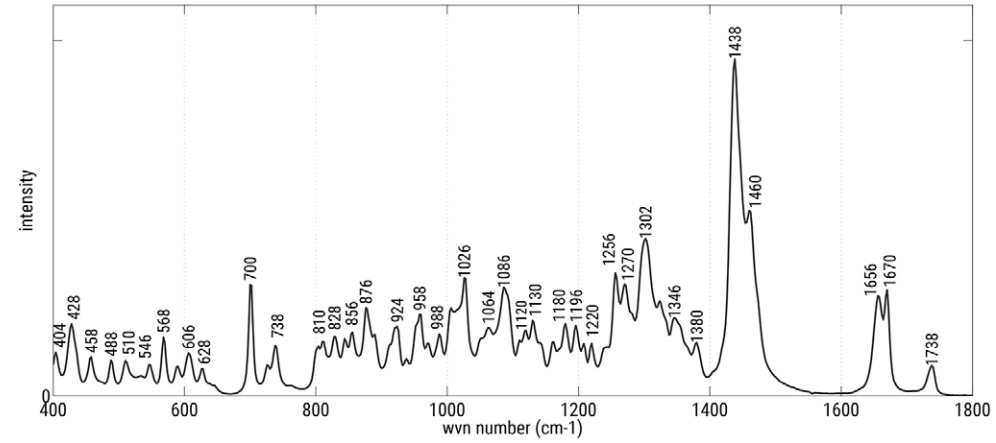

Name	Cholesteryl palmitate	**Measurement**	
CAS-number:	601-34-3	Condition:	solid
Chemical class:	Lipid, lipoprotein	Solvent:	n.a.
Firm:	Sigma-Aldrich Chemie B.V.	Concentration:	n.a.
Product number:	C6072	pH:	n.a.
Purity according firm:	>98%	Instrument:	SpectraCell *RA Bacterial Strain Analyzer*
Source:	not mentioned	Acquisition time:	1584 x 5 seconds
		Remarks:	insoluble
Analysis			
Spectral corrections:	manually	**Peaks**	
Water:	no	402, 428, 446, 456, 476, 490, 514, 538, 550, 570, 594, 614, 628, 646, 700,	
Fused silica:	order 1, range 400:2:1800	724, 740, 802, 826, 848, 880, 924, 960, 972, 988, 1012, 1026, 1050, 1064,	
Background:	removed	1088, 1100, 1130, 1162, 1178, 1196, 1210, 1220, 1238, 1262, 1296, 1330,	
S/N ratio:	347,12	1356, 1378, 1440, 1668, 1738	

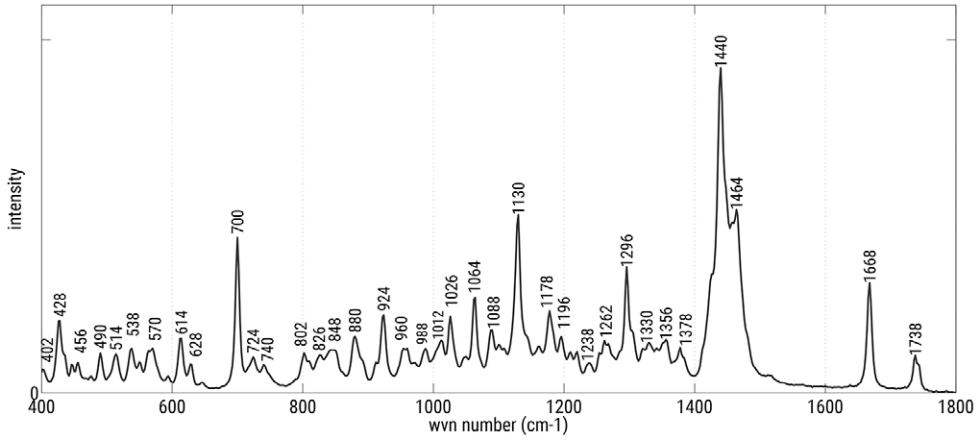

Name	Chondroitin sulfate type A	**Measurement**	
CAS-number:	39455-18-0	Condition:	dissolved
Chemical class:	Carbohydrate, GAG	Solvent:	purified water
Firm:	Sigma-Aldrich Chemie B.V.	Concentration:	100 mg/ml
Product number:	C9819	pH:	6,5
Purity according firm:	>60%	Instrument:	SpectraCell *RA Bacterial Strain Analyzer*
Source:	bovine trachea	Acquisition time:	343 x 20 seconds
		Remarks:	clear, yellowish solution. Also solid
Analysis			
Spectral corrections:	manually		
Water:	order 0, range 1500:2:1800, factor 1/1,35		
Fused silica:	order 1, range 400:2:1800	**Peaks**	
Background:	removed	422, 464, 500, 582, 582, 642, 728, 786, 862, 890, 938, 980, 1052, 1066, 1158,	
S/N ratio:	82,84	1264, 1342, 1376, 1412, 1456, 1578, 1650	

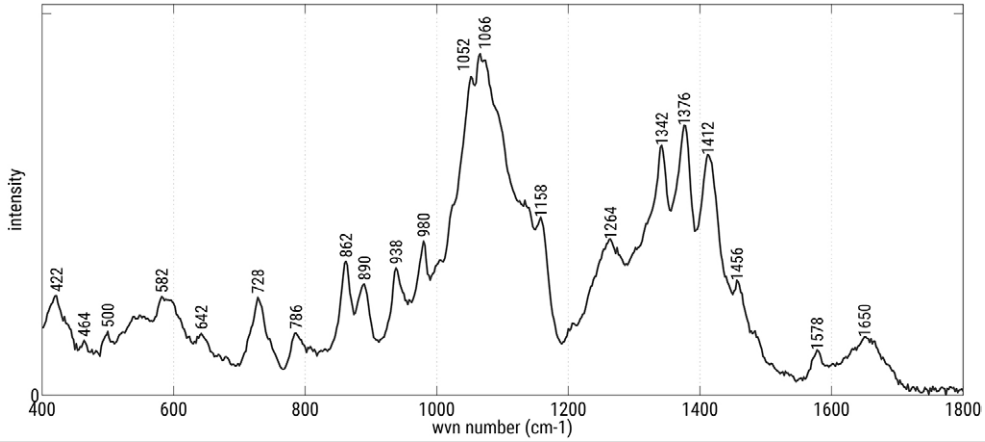

Name	**Collagen type I**
CAS-number:	9007-34-5
Chemical class:	Protein, fibrous
Firm:	Sigma-Aldrich Chemie B.V.
Product number:	C7774
Purity according firm:	not mentioned
Source:	human placenta

Analysis

Spectral corrections:	manually
Water:	order 0, range 1500:2:1800, factor 1/10,5
Fused silica:	order 0, range 400:2:1800
S/N ratio:	167,87

Measurement

Condition:	solid, hydrated with NaCl 0,9%
Solvent:	n.a.
Concentration:	n.a.
pH:	n.a.
Instrument:	SpectraCell *RA Bacterial Strain Analyzer*
Acquisition time:	3721 x 5 seconds
Remarks:	insoluble

Peaks

420, 510, 570, 598, 622, 644, 720, 760, 816, 856, 878, 928, 1004, 1032, 1062, 1126, 1160, 1178, 1206, 1246, 1266, 1318, 1344, 1422, 1452, 1550, 1666

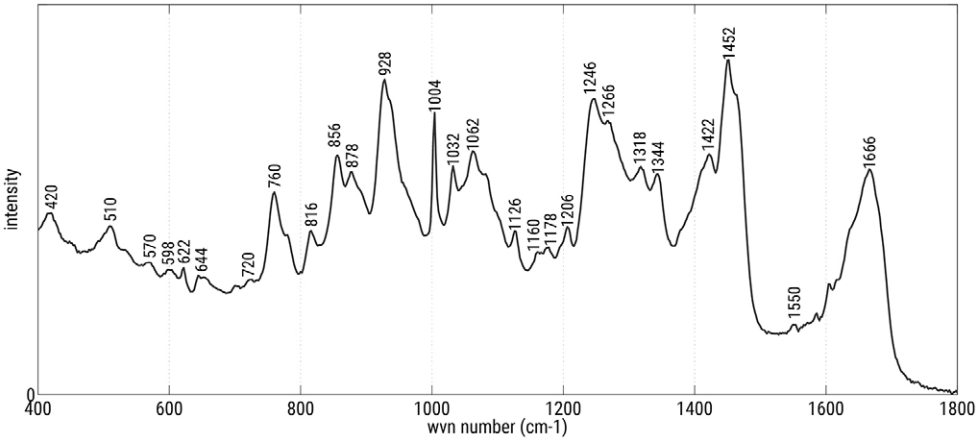

Name	**Collagen type II**
CAS-number:	9007-34-5
Chemical class:	Protein, fibrous
Firm:	Sigma-Aldrich Chemie B.V.
Product number:	C8886
Purity according firm:	not mentioned
Source:	bovine achilles tendon

Analysis

Spectral corrections:	manually
Water:	order 0, range 400:2:1800
Fused silica:	order 1, range 400:2:1800
S/N ratio:	220,37

Measurement

Condition:	solid, hydrated with NaCl 0,9%
Solvent:	n.a.
Concentration:	n.a.
pH:	n.a.
Instrument:	SpectraCell *RA Bacterial Strain Analyzer*
Acquisition time:	345 x 15 seconds
Remarks:	insoluble

Peaks

532, 570, 622, 644, 728, 762, 816, 858, 876, 922, 938, 1004, 1032, 1062, 1082, 1100, 1126, 1164, 1178, 1204, 1246, 1268, 1318, 1340, 1404, 1426, 1452, 1666

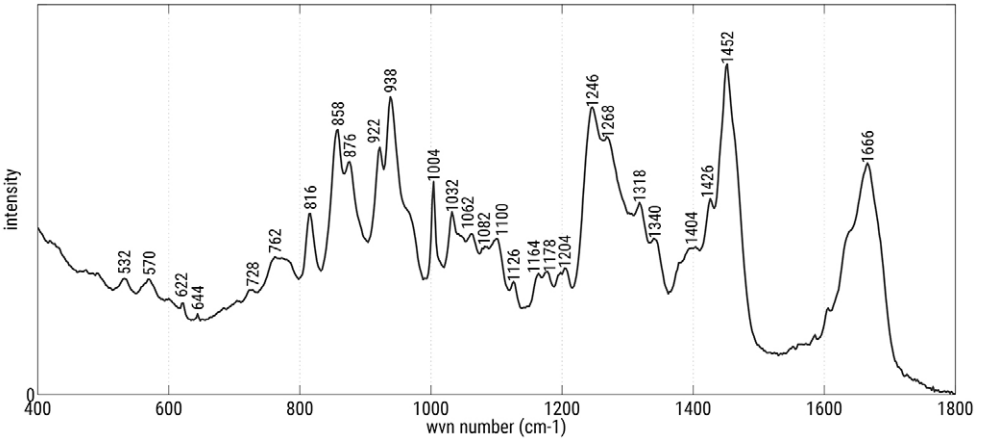

Name	**Collagen type III**	**Measurement**	
CAS-number:	9007-34-5	Condition:	solid, hydrated with NaCl 0,9%
Chemical class:	Protein, fibrous	Solvent:	n.a.
Firm:	Sigma-Aldrich Chemie B.V.	Concentration:	n.a.
Product number:	C4407	pH:	n.a.
Purity according firm:	not mentioned	Instrument:	SpectraCell *RA Bacterial Strain Analyzer*
Source:	human placenta	Acquisition time:	404 x 10 seconds
Analysis		Remarks:	insoluble
Spectral corrections:	manually		
Water:	order 0, range 1500:2:1800, factor 1/2	**Peaks**	
Fused silica:	order 1, range 400:2:1800	492, 546, 570, 608, 622, 646, 700, 718, 770, 816, 856, 876, 922, 938, 1004, 1032, 1064, 1086, 1128, 1162, 1174, 1206, 1246, 1270, 1296, 1340, 1378, 1440, 1634, 1670	
Background:	removed		
S/N ratio:	658,67		

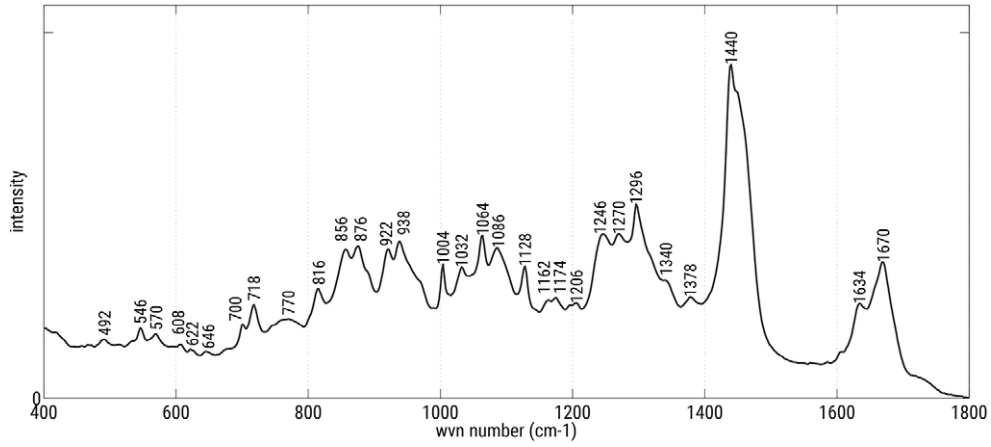

Name	**Cytosine**	**Measurement**	
CAS-number:	71-30-7	Condition:	solid
Chemical class:	Nucleotide, pyrimidine	Solvent:	n.a.
Firm:	Sigma-Aldrich Chemie B.V.	Concentration:	n.a.
Product number:	C3506	pH:	n.a.
Purity according firm:	>99%	Instrument:	SpectraCell *RA Bacterial Strain Analyzer*
Source:	not mentioned	Acquisition time:	420 x 1 seconds
Analysis		Remarks:	soluble in NaOH 1M
Spectral corrections:	automated		
Water:	no	**Peaks**	
Fused silica:	order 0, range 400:2:1800	402, 444, 538, 548, 568, 600, 792, 890, 972, 990, 1010, 1108, 1148, 1250, 1276, 1362, 1460, 1492, 1532, 1608, 1654, 1692	
S/N ratio:	4870,91		

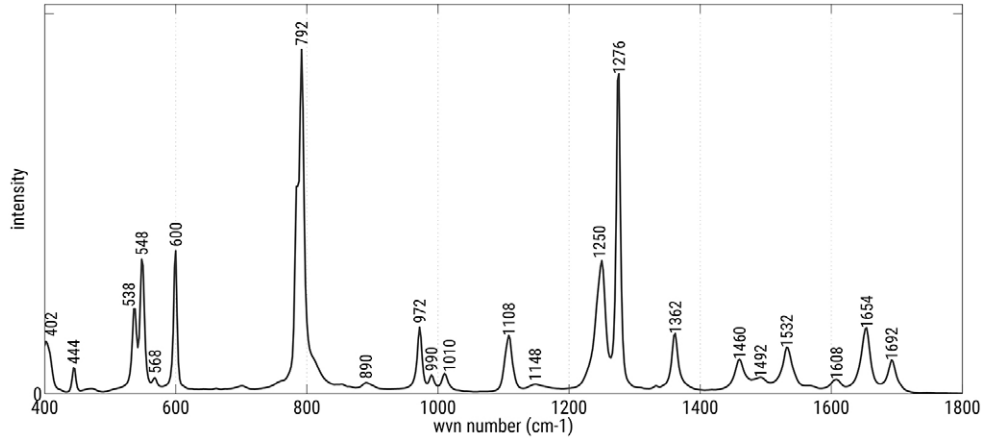

Name	**DNA**
CAS-number:	73049-39-5
Chemical class:	Nucleic acid
Firm:	MP biochemicals
Product number:	195129
Purity according firm:	not mentioned
Source:	not mentioned

Analysis

Spectral corrections:	manually
Water:	order 0, range 1500:2:1800, factor 1/1,25
Fused silica:	order 0, range 400:2:1800, factor 1/1,5
Background:	removed
S/N ratio:	50,80

Measurement

Condition:	dissolved
Solvent:	NaCl 0,9%
Concentration:	1 mg/ml
pH:	6,5
Instrument:	SpectraCell *RA Bacterial Strain Analyzer*
Acquisition time:	365 x 15 seconds
Remarks:	thick, smooth solution. Also solid

Peaks

500, 596, 672, 682, 728, 750, 788, 836, 894, 920, 974, 1014, 1054, 1094, 1144, 1180, 1216, 1256, 1304, 1316, 1334, 1376, 1422, 1446, 1460, 1490, 1510, 1578, 1668

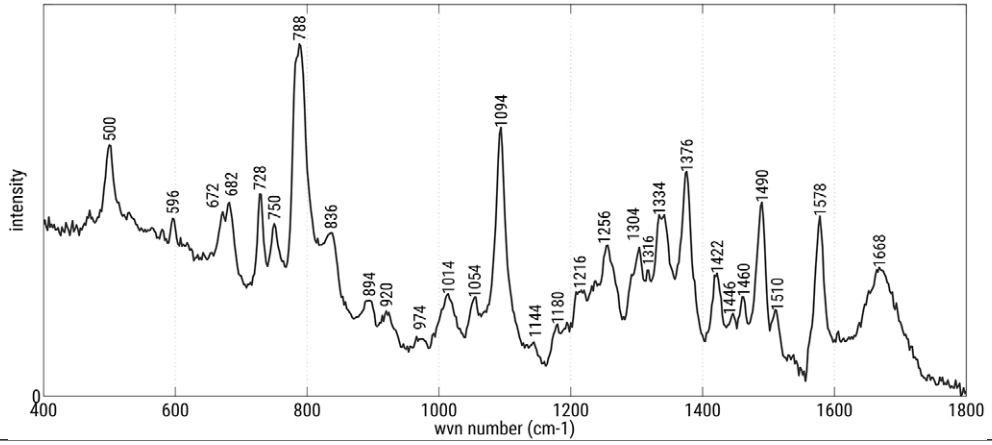

Name	**Elastin**
CAS-number:	9007-58-3
Chemical class:	Protein, fibrous
Firm:	Sigma-Aldrich Chemie B.V.
Product number:	E1625
Purity according firm:	not mentioned
Source:	bovine neck ligament

Analysis

Spectral corrections:	manually
Water:	order 0, range 1500:2:1800, factor 1/2,3
Fused silica:	order 1, range 400:2:1800
S/N ratio:	220,69

Measurement

Condition:	dissolved
Solvent:	purified water
Concentration:	10 mg/ml
pH:	6,0
Instrument:	SpectraCell *RA Bacterial Strain Analyzer*
Acquisition time:	537 x 15 seconds
Remarks:	almost clear solution

Peaks

410, 492, 528, 622, 644, 754, 858, 880, 906, 936, 960, 1004, 1032, 1104, 1126, 1172, 1208, 1252, 1318, 1340, 1390, 1418, 1452, 1586, 1606, 1666

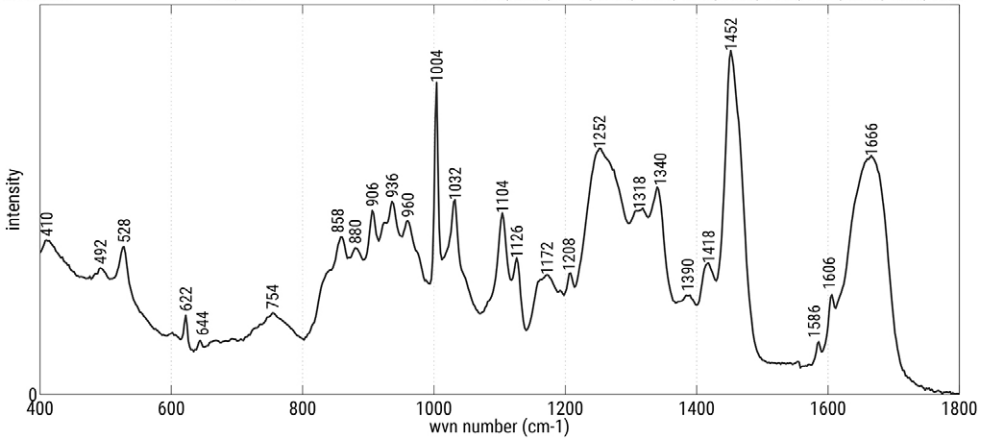

Name	**Glucose**	**Measurement**	
CAS-number:	50-99-7	Condition:	dissolved
Chemical class:	Carbohydrate, monosaccharide	Solvent:	purified water
Firm:	Sigma-Aldrich Chemie B.V.	Concentration:	100 mg/ml
Product number:	G8270	pH:	6,0
Purity according firm:	>99.5%	Instrument:	*Skin Analyzer*
Source:	not mentioned	Acquisition time:	481 x 5 seconds
		Remarks:	heated, clear solution
Analysis			
Spectral corrections:	automated		
Water:	order 0, range 1500:2:1800	**Peaks**	
Fused silica:	no	404, 424, 446, 518, 540, 588, 646, 712, 772, 848, 918, 1020, 1042, 1064,	
S/N ratio:	332,55	1076, 1126, 1206, 1264, 1334, 1368, 1460	

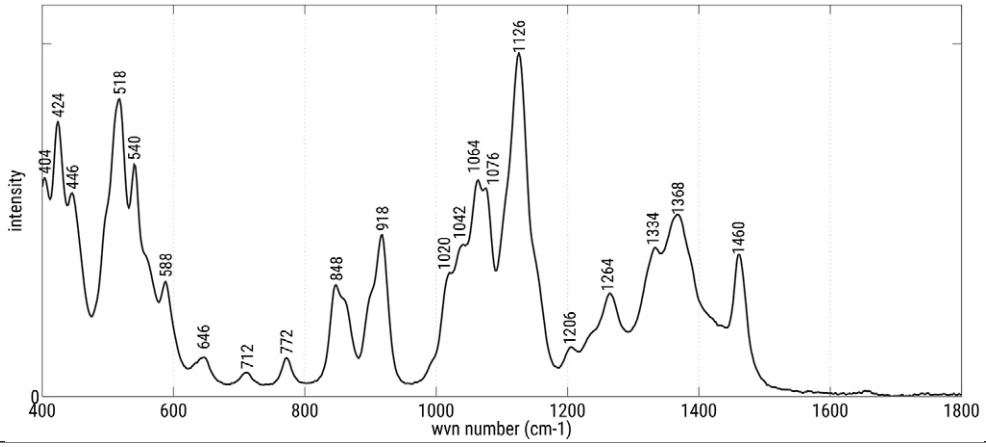

Name	**Glycine**	**Measurement**	
CAS-number:	56-40-6	Condition:	dissolved
Chemical class:	Amino acid, non essential	Solvent:	purified water
Firm:	Sigma-Aldrich Chemie B.V.	Concentration:	200 mg/ml
Product number:	94119 FLUKA	pH:	unknown
Purity according firm:	>99%	Instrument:	SpectraCell *RA Bacterial Strain Analyzer*
Source:	analytical standard	Acquisition time:	820 x 5 seconds
		Remarks:	clear solution. Also solid.
Analysis			
Spectral corrections:	manually		
Water:	order 0, range 1500:2:1800, factor 1/3,1		
Fused silica:	no	**Peaks**	
S/N ratio:	1009,11	508, 586, 670, 898, 1032, 1122, 1330, 1412, 1444, 1502, 1604	

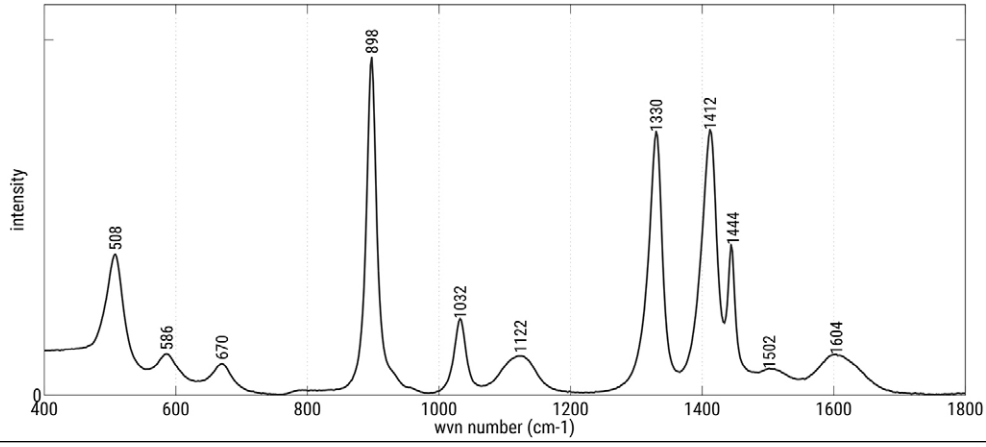

Name	**Glycogen**	**Measurement**	
CAS-number:	9005-72-2	Condition:	dissolved
Chemical class:	Carbohydrate, polysaccharide	Solvent:	purified water
Firm:	Sigma-Aldrich Chemie B.V.	Concentration:	50 mg/ml
Product number:	G8751	pH:	6,5
Purity according firm:	>75%	Instrument:	SpectraCell *RA Bacterial Strain Analyzer*
Source:	oyster	Acquisition time:	1830 x 15 seconds
Analysis		Remarks:	heated, clear solution with bubbles. Also solid
Spectral corrections:	manually		
Water:	order 0, range 1640:2:1720	**Peaks**	
Fused silica:	order 0, range 400:2:1800	410, 442, 480, 518, 546, 576, 618, 718, 760, 864, 940, 980, 1046, 1084, 1108, 1126, 1210, 1262, 1338, 1380, 1462	
S/N ratio:	79,90		

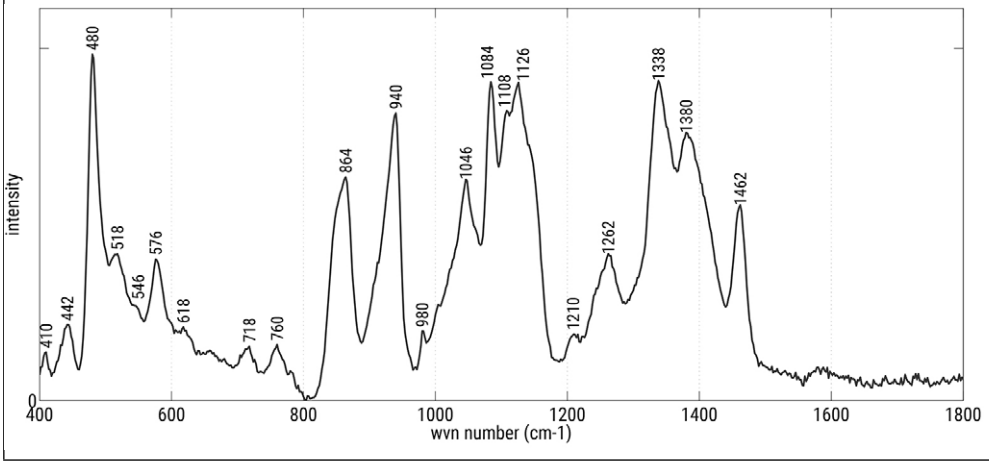

Name	**Guanine**	**Measurement**	
CAS-number:	73-40-5	Condition:	solid
Chemical class:	Nucleotide, purine	Solvent:	n.a.
Firm:	Sigma-Aldrich Chemie B.V.	Concentration:	n.a.
Product number:	G11950	pH:	n.a.
Purity according firm:	98%	Instrument:	SpectraCell *RA Bacterial Strain Analyzer*
Source:	not mentioned	Acquisition time:	1199 x 1 seconds
Analysis		Remarks:	soluble in NaOH 1M
Spectral corrections:	automated		
Water:	no	**Peaks**	
Fused silica:	order 0, range 400:2:1800	496, 548, 562, 606, 650, 692, 710, 778, 846, 884, 940, 1048, 1158, 1184, 1228, 1262, 1360, 1390, 1420, 1466, 1478, 1548, 1600, 1680	
S/N ratio:	1155,32		

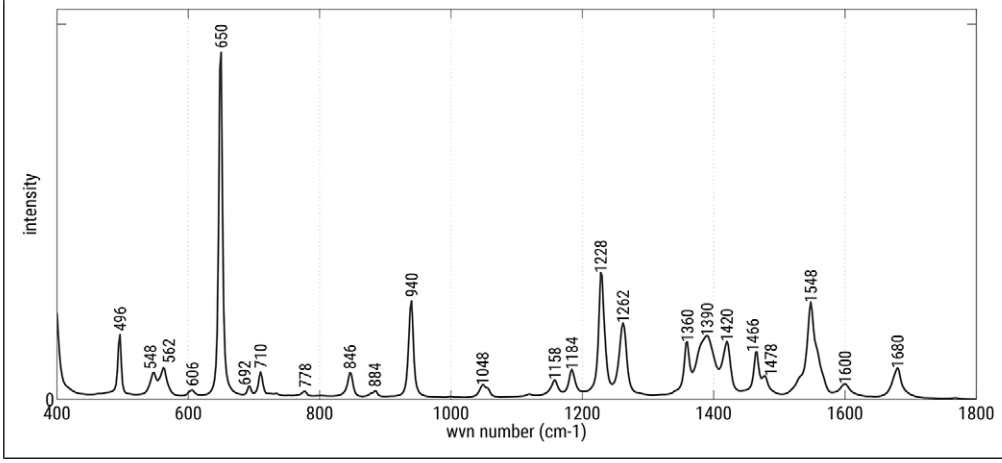

Name	**Hemoglobin**	**Measurement**	
CAS-number:	9008-02-0	Condition:	dissolved
Chemical class:	Protein, globular	Solvent:	purified water
Firm:	Sigma-Aldrich Chemie B.V.	Concentration:	unknown
Product number:	H0267	pH:	6,5
Purity according firm:	>90%	Instrument:	*Skin Analyzer*
Source:	human	Acquisition time:	108 x 1 seconds
		Remarks:	clear reddish solution
Analysis			
Spectral corrections:	manually		
Water:	order 1, range 400:2:1800	**Peaks**	
Fused silica:	no	522, 622, 664, 708, 744, 830, 860, 902, 974, 1004, 1032, 1056, 1126, 1158,	
S/N ratio:	292,85	1172, 1252, 1344, 1368, 1392, 1450, 1582, 1604, 1618	

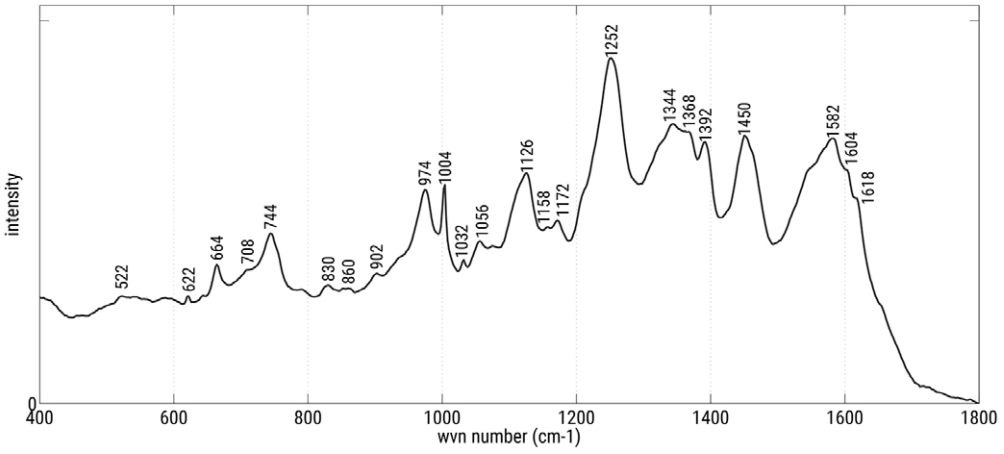

Name	**Hyaluronic acid**	**Measurement**	
CAS-number:	9004-61-9	Condition:	dissolved
Chemical class:	Carbohydrate, GAG	Solvent:	purified water
Firm:	Sigma-Aldrich Chemie B.V.	Concentration:	50 mg/ml
Product number:	53747	pH:	5,5
Purity according firm:	99%	Instrument:	SpectraCell *RA Bacterial Strain Analyzer*
Source:	bacterial (streptococcus equi)	Acquisition time:	485 x 20 seconds
		Remarks:	heated, thick yellowish solution. Also solid
Analysis			
Spectral corrections:	manually		
Water:	order 0, range 1500:2:1800, factor 1/3,1		
Fused silica:	order 1, range 400:2:1800	**Peaks**	
Background:	removed	416, 444, 542, 576, 806, 898, 948, 1048, 1098, 1126, 1206, 1240, 1270, 1296,	
S/N ratio:	133,66	1330, 1376, 1412, 1458, 1644	

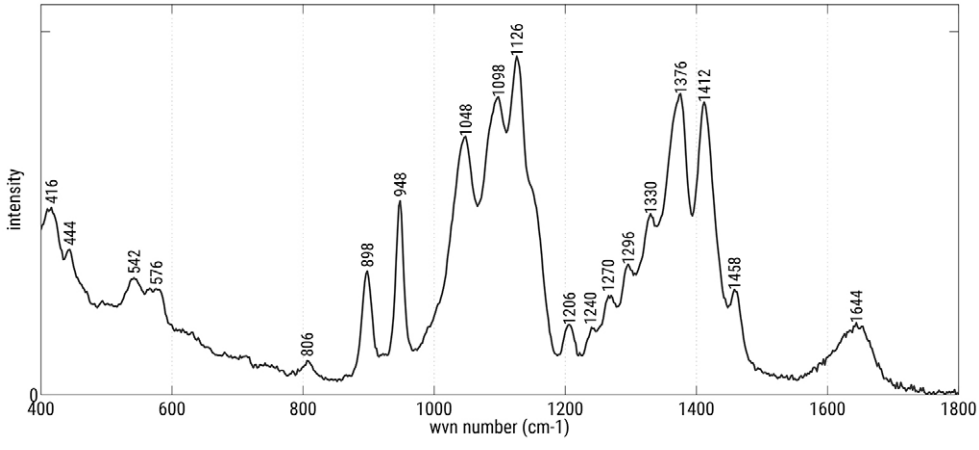

Name	**Hydroxyapatite**	**Measurement**	
CAS-number:	1306-06-5	Condition:	solid
Chemical class:	Miscellaneous, mineral	Solvent:	n.a.
Firm:	Sigma-Aldrich Chemie B.V.	Concentration:	n.a.
Product number:	H0252	pH:	n.a.
Purity according firm:	not mentioned	Instrument:	SpectraCell *RA Bacterial Strain Analyzer*
Source:	not mentioned	Acquisition time:	1156 x 5 seconds
		Remarks:	insoluble
Analysis			
Spectral corrections:	manually		
Water:	no		
Fused silica:	no		
Background:	removed	**Peaks**	
S/N ratio:	1715,1	430, 446, 580, 592, 608, 962, 1046, 1074	

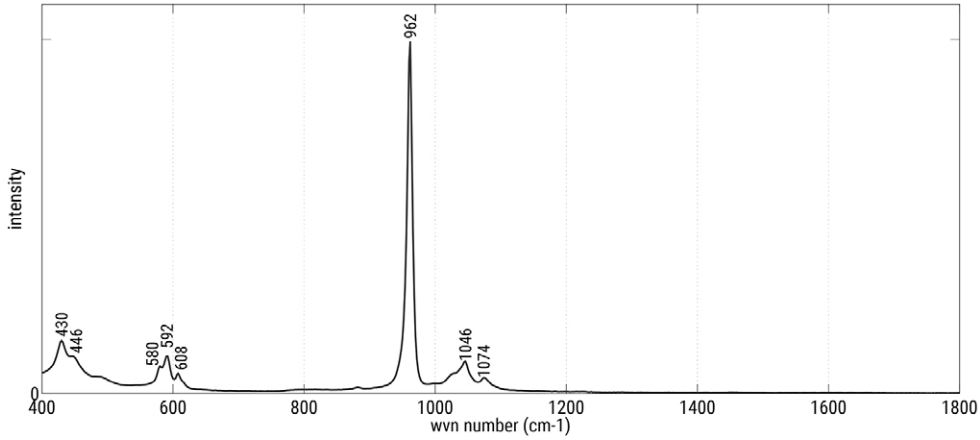

Name	**Keratin**	**Measurement**	
CAS-number:	68238-35-8	Condition:	solid
Chemical class:	Protein, fibrous	Solvent:	n.a.
Firm:	own stock	Concentration:	n.a.
Product number:	n.a.	pH:	n.a.
Purity according firm:	n.a.	Instrument:	SpectraCell *RA Bacterial Strain Analyzer*
Source:	soft keratin	Acquisition time:	66 x 15 seconds
		Remarks:	insoluble
Analysis			
Spectral corrections:	automated	**Peaks**	
Water:	no	412, 456, 492, 524, 564, 622, 644, 722, 748, 828, 854, 900, 936, 1002, 1030, 1080, 1104, 1126, 1156, 1174, 1208, 1316, 1340, 1422, 1448, 1552, 1586, 1616, 1650	
Fused silica:	order 0, range 400:2:1800		
S/N ratio:	782,57		

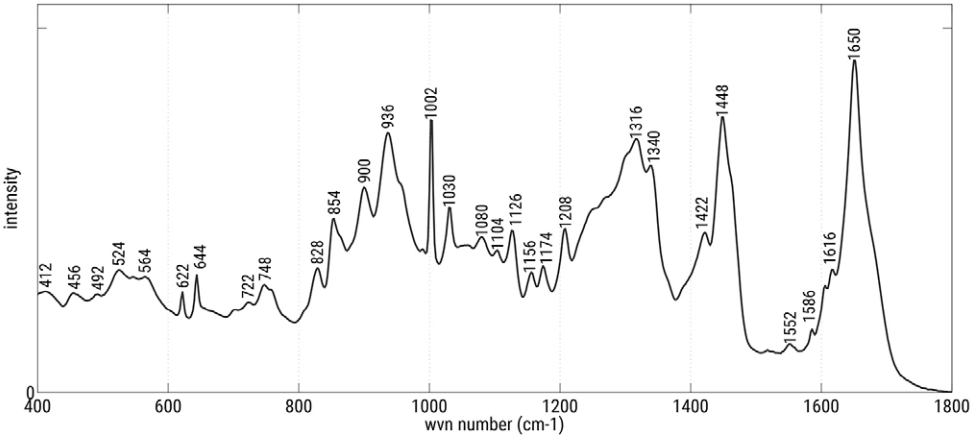

Name	**Lactic acid**	**Measurement**	
CAS-number:	50-21-5	Condition:	fluid
Chemical class:	Miscellaneous, glycogen metabolism product	Solvent:	n.a.
		Concentration:	n.a.
Firm:	Sigma-Aldrich Chemie B.V.	pH:	1,5
Product number:	252476	Instrument:	SpectraCell *RA Bacterial Strain Analyzer*
Purity according firm:	85%	Acquisition time:	624 x 4 seconds
Source:	not mentioned	Remarks:	none
Analysis			
Spectral corrections:	automated		
Water:	no	**Peaks**	
Fused silica:	no	416, 460, 534, 634, 746, 826, 870, 924, 1046, 1086, 1134, 1296, 1320, 1382, 1456, 1726	
S/N ratio:	51,87		

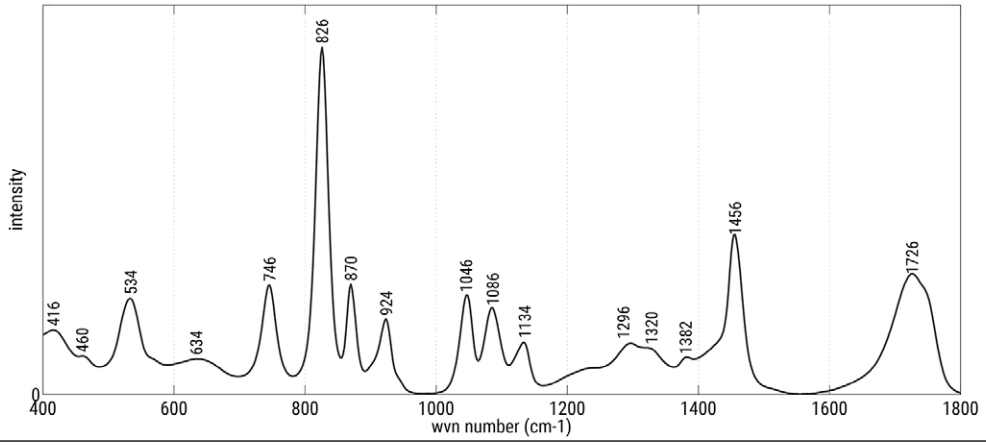

Name	**L-alanine**	**Measurement**	
CAS-number:	56-41-7	Condition:	dissolved
Chemical class:	Amino acid, non essential	Solvent:	purified water
Firm:	Sigma-Aldrich Chemie B.V.	Concentration:	50 mg/ml
Product number:	A26802	pH:	5,5
Purity according firm:	99%	Instrument:	SpectraCell *RA Bacterial Strain Analyzer*
Source:	not mentioned	Acquisition time:	544 x 10 seconds
		Remarks:	clear solution. Also solid
Analysis			
Spectral corrections:	manually		
Water:	order 0, range 1500:2:1800, factor 1/2,4	**Peaks**	
Fused silica:	no	410, 530, 612, 776, 848, 920, 1002, 1112, 1212, 1304, 1354, 1378, 1414, 1462, 1594	
S/N ratio:	190,19		

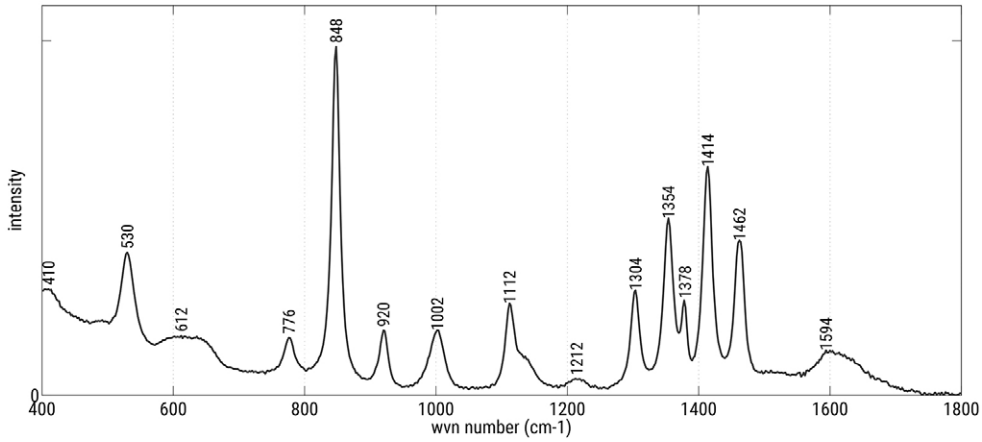

Name	L-arginine	**Measurement**	
CAS-number:	74-79-3	Condition:	dissolved
Chemical class:	Amino acid, essential	Solvent:	purified water
Firm:	Sigma-Aldrich Chemie B.V.	Concentration:	100 mg/ml
Product number:	A92406	pH:	7,0
Purity according firm:	98%	Instrument:	SpectraCell *RA Bacterial Strain Analyzer*
Source:	not mentioned	Acquisition time:	799 x 20 seconds
		Remarks:	heated, clear solution. Also solid
Analysis			
Spectral corrections:	manually	**Peaks**	
Water:	order 0, range 1500:2:1800, factor 1/2,2	530, 604, 760, 862, 892, 934, 978, 1014, 1054, 1092, 1166, 1214, 1290, 1324, 1354, 1388, 1412, 1446, 1590, 1666	
Fused silica:	order 0, range 400:2:1800, factor 1/10,5		
Background:	removed	**Remarks**	
S/N ratio:	32,15	no EMSC scaling	

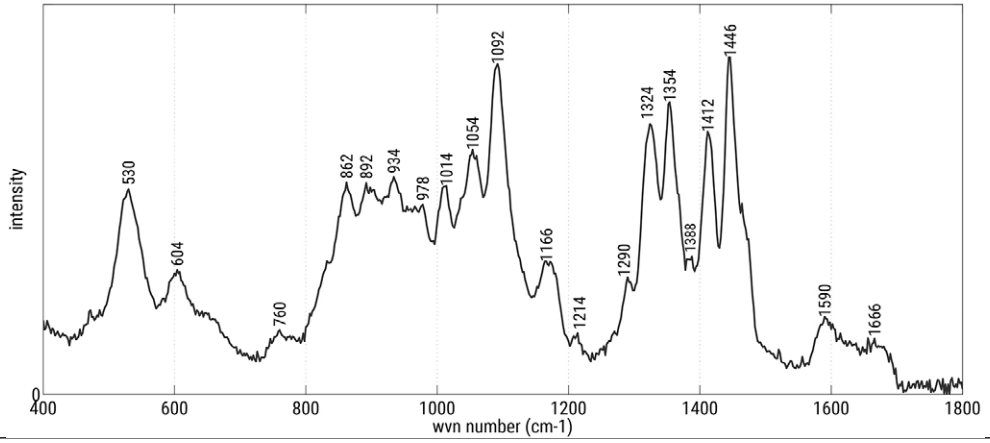

Name	L-asparagine	**Measurement**	
CAS-number:	70-47-3	Condition:	dissolved
Chemical class:	Amino acid, non essential	Solvent:	purified water
Firm:	Sigma-Aldrich Chemie B.V.	Concentration:	33 mg/ml
Product number:	A0884	pH:	5,0
Purity according firm:	98%	Instrument:	SpectraCell *RA Bacterial Strain Analyzer*
Source:	not mentioned	Acquisition time:	254 x 10 seconds
		Remarks:	heated, clear solution. Also solid
Analysis			
Spectral corrections:	manually		
Water:	order 0, range 1500:2:1800, factor 1/1,6		
Fused silica:	no	**Peaks**	
Background:	removed	452, 488, 522, 606, 768, 800, 826, 866, 884, 928, 986, 1122, 1230, 1266, 1328, 1356, 1402, 1420, 1616, 1680	
S/N ratio:	33,0		

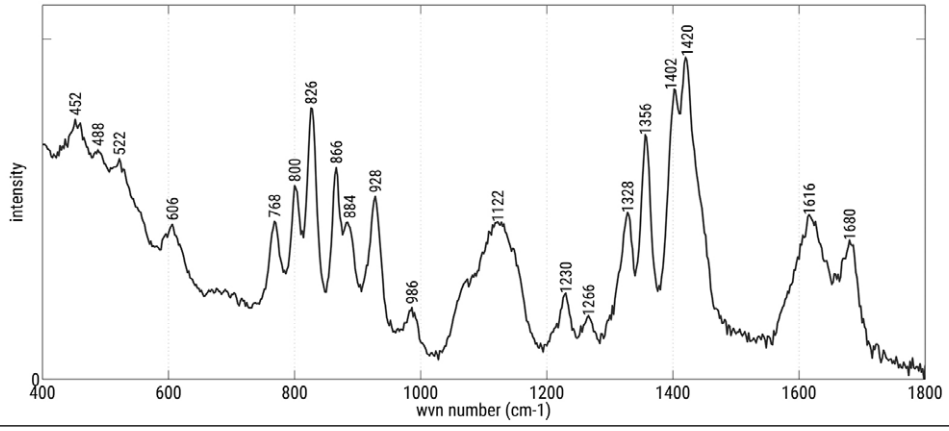

Name	L-aspartic acid	**Measurement**	
CAS-number:	617-45-8	Condition:	solid
Chemical class:	Amino acid, non essential	Solvent:	n.a.
Firm:	Sigma-Aldrich Chemie B.V.	Concentration:	n.a.
Product number:	A93100	pH:	n.a.
Purity according firm:	98%	Instrument:	SpectraCell *RA Bacterial Strain Analyzer*
Source:	not mentioned	Acquisition time:	608 x 10 seconds
Analysis		Remarks:	soluble in H2O, but in different solutions only water bands
Spectral corrections:	automated	**Peaks**	
Water:	no	412, 468, 552, 600, 662, 748, 778, 870, 900, 938, 990, 1082, 1118, 1144, 1250, 1260, 1288, 1336, 1360, 1408, 1422, 1460, 1508, 1550, 1616, 1634, 1692	
Fused silica:	order 0, range 400:2:1800		
S/N ratio:	447,32		

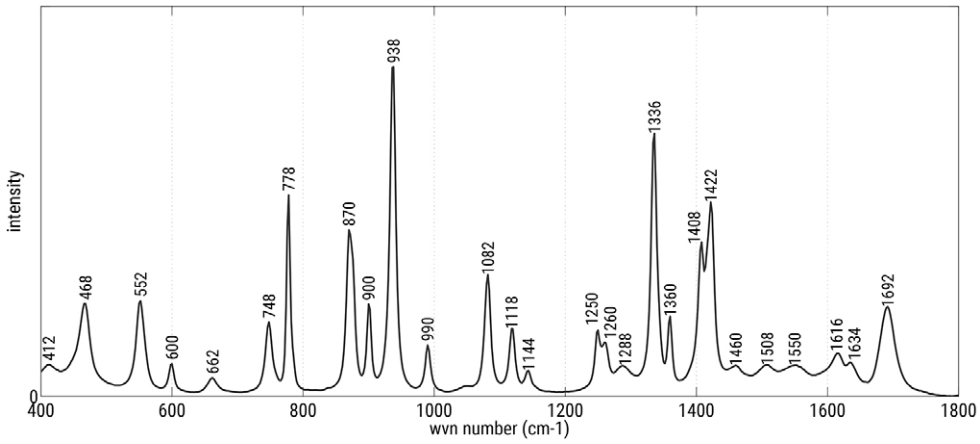

Name	L-citrulline	**Measurement**	
CAS-number:	627-77-0	Condition:	dissolved
Chemical class:	Amino acid, semi essential	Solvent:	water
Firm:	Sigma-Aldrich Chemie B.V.	Concentration:	200 mg/ml
Product number:	C83708	pH:	6,0
Purity according firm:	98%	Instrument:	SpectraCell *RA Bacterial Strain Analyzer*
Source:	not mentioned	Acquisition time:	869 x 5 seconds
Analysis		Remarks:	heated, clear solution. Also solid
Spectral corrections:	manually		
Water:	order 0, range 1500:2:1800, factor 1/3,75		
Fused silica:	order 0, range 1400:2:1800, factor 1/25	**Peaks**	
S/N ratio:	393,20	476, 530, 658, 756, 780, 828, 858, 892, 940, 1012, 1054, 1106, 1142, 1210, 1292, 1322, 1352, 1414, 1444, 1604, 1644	

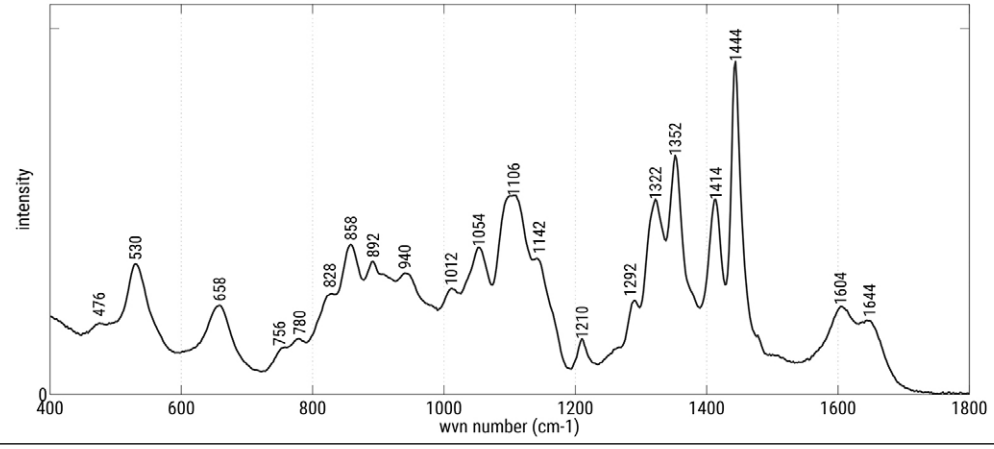

Name	Lecithin	**Measurement**	
CAS-number:	8002-43-5	Condition:	fluid
Chemical class:	Lipid, phospholipid	Solvent:	n.a.
Firm:	Sigma-Aldrich Chemie B.V.	Concentration:	n.a.
Product number:	P5394	pH:	n.a.
Purity according firm:	60%	Instrument:	SpectraCell *RA Bacterial Strain Analyzer*
Source:	dried egg yolk	Acquisition time:	961 x 10 seconds
		Remarks:	thick, brownish
Analysis			
Spectral corrections:	automated		
Water:	no	**Peaks**	
Fused silica:	order 0, range 400:2:1800	414, 456, 606, 718, 764, 848, 874, 924, 954, 970, 1064, 1084, 1122, 1268, 1300, 1366, 1440, 1658, 1740	
S/N ratio:	943,25		

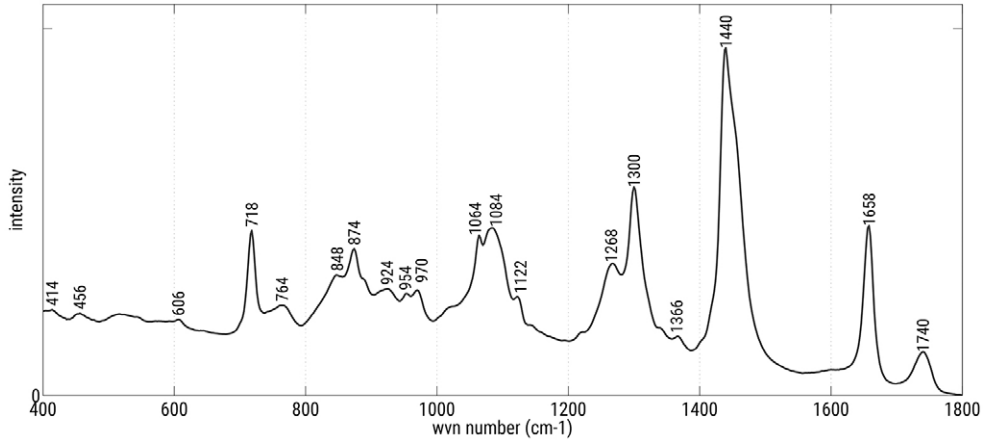

Name	L-glutamic acid	**Measurement**	
CAS-number:	56-86-0	Condition:	solid
Chemical class:	Amino acid, non essential	Solvent:	n.a.
Firm:	Sigma-Aldrich Chemie B.V.	Concentration:	n.a.
Product number:	128430	pH:	n.a.
Purity according firm:	99%	Instrument:	SpectraCell *RA Bacterial Strain Analyzer*
Source:	not mentioned	Acquisition time:	1404 x 10 seconds
		Remarks:	soluble in H2O, but in different solutions only water bands
Analysis			
Spectral corrections:	automated		
Water:	no	**Peaks**	
Fused silica:	order 0, range 400:2:1800	462, 502, 538, 576, 674, 708, 762, 802, 866, 920, 942, 968, 1060, 1086, 1126, 1152, 1216, 1264, 1310, 1350, 1356, 1406, 1436, 1512, 1614, 1630, 1658	
S/N ratio:	1380,55		

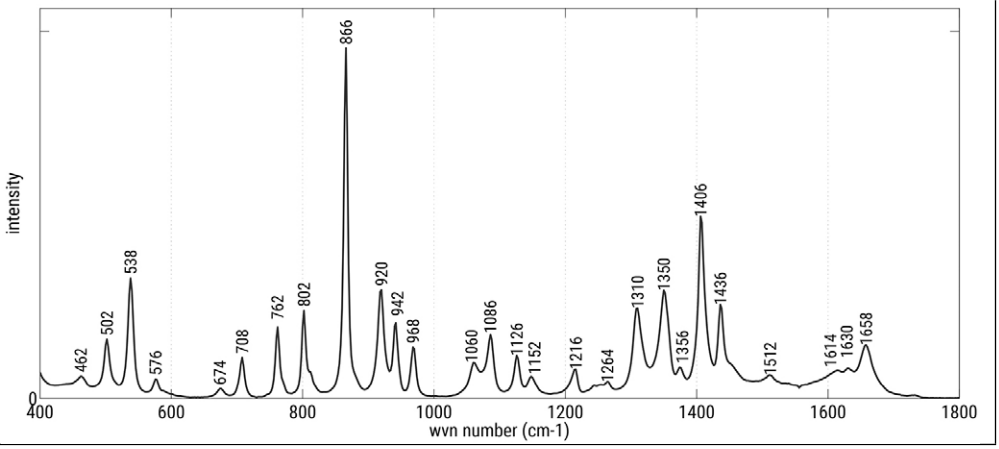

Name	L-glutamine	**Measurement**	
CAS-number:	56-85-9	Condition:	dissolved
Chemical class:	Amino acid, non essential	Solvent:	purified water
Firm:	Sigma-Aldrich Chemie B.V.	Concentration:	50 mg/ml
Product number:	G3202	pH:	5,5
Purity according firm:	99%	Instrument:	SpectraCell *RA Bacterial Strain Analyzer*
Source:	not mentioned	Acquisition time:	2769 x 10 seconds
		Remarks:	heated, clear solution. Also solid
Analysis			
Spectral corrections:	manually		
Water:	order 0, range 1500:2:1800, factor 1/1,5		
Fused silica:	order 1, range 400:2:1800	**Peaks**	
Background:	removed	448, 488, 532, 768, 808, 856, 908, 1002, 1038, 1080, 1124, 1152, 1196, 1292,	
S/N ratio:	67,60	1350, 1422, 1446, 1610, 1672, 1734	

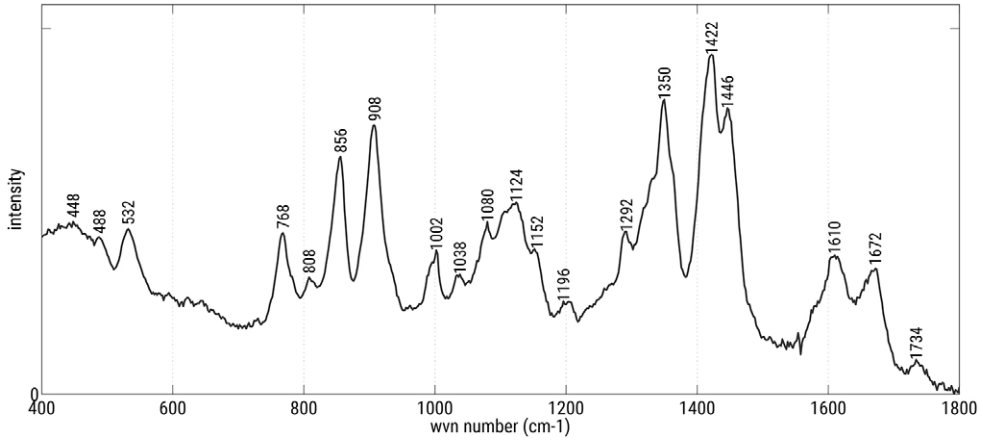

Name	L-histidine	**Measurement**	
CAS-number:	71-00-1	Condition:	dissolved
Chemical class:	Amino acid, semi essential	Solvent:	purified water
Firm:	Sigma-Aldrich Chemie B.V.	Concentration:	50 mg/ml
Product number:	151688	pH:	6,75
Purity according firm:	98%	Instrument:	SpectraCell *RA Bacterial Strain Analyzer*
Source:	not mentioned	Acquisition time:	549 x 15 seconds
		Remarks:	heated, clear solution. Also solid
Analysis			
Spectral corrections:	manually		
Water:	order 1, range 1500:2:1800		
Fused silica:	order 0, range 400:2:1800	**Peaks**	
Background:	removed	470, 520, 622, 664, 716, 814, 854, 916, 938, 966, 992, 1070, 1090, 1108,	
S/N ratio:	30,86	1158, 1192, 1236, 1272, 1286, 1322, 1356, 1414, 1440, 1494, 1574, 1632	

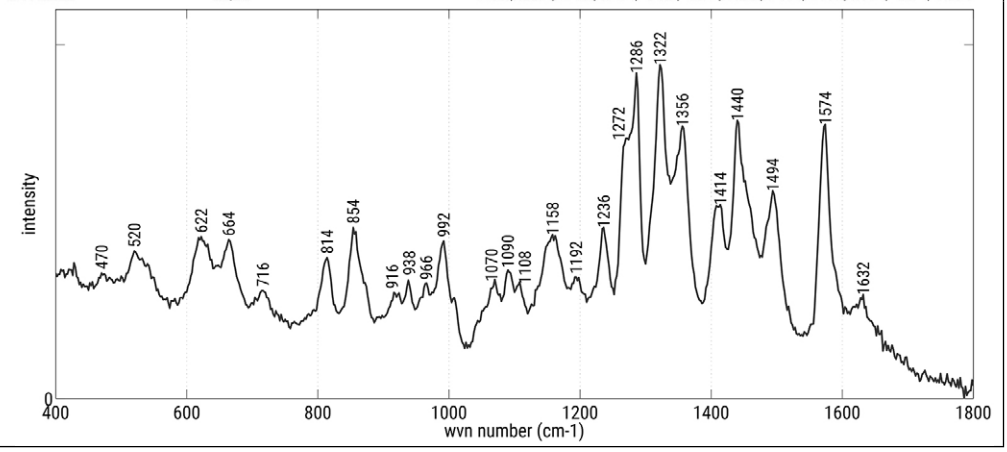

Name	**Linoleic acid**	**Measurement**	
CAS-number:	60-33-3	Condition:	fluid
Chemical class:	Lipid, unsaturated fatty acid	Solvent:	n.a.
Firm:	Sigma-Aldrich Chemie B.V.	Concentration:	n.a.
Product number:	62230 FLUKA	pH:	5,5
Purity according firm:	>98.5%	Instrument:	SpectraCell *RA Bacterial Strain Analyzer*
Source:	analytical standard	Acquisition time:	441 x 1 seconds
		Remarks:	none
Analysis			
Spectral corrections:	automated		
Water:	no		
Fused silica:	order 1, range 400:2:1800	**Peaks**	
S/N ratio:	1880,85	724, 872, 908, 972, 1076, 1094, 1264, 1302, 1440, 1658	

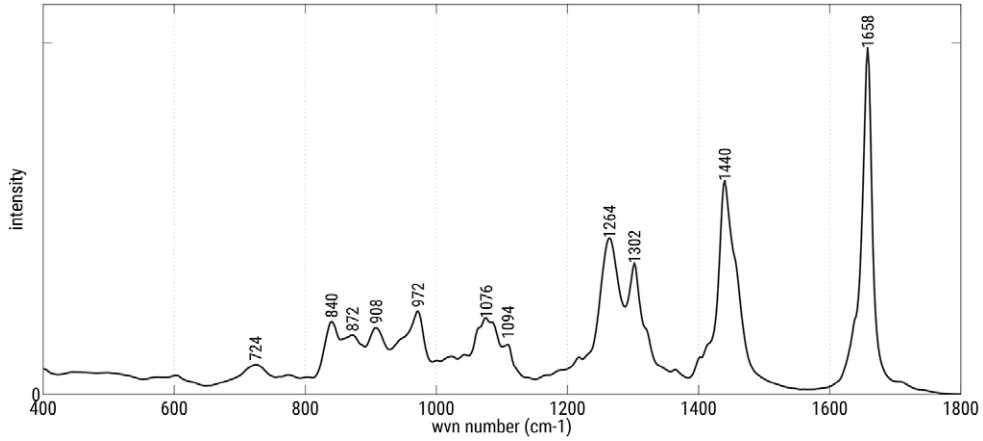

Name	**Linolenic acid**	**Measurement**	
CAS-number:	463-40-1	Condition:	fluid
Chemical class:	Lipid, unsaturated fatty acid	Solvent:	n.a.
Firm:	Sigma-Aldrich Chemie B.V.	Concentration:	n.a.
Product number:	62160 FLUKA	pH:	5,5
Purity according firm:	>98.5%	Instrument:	SpectraCell *RA Bacterial Strain Analyzer*
Source:	analytical standard	Acquisition time:	441 x 1 seconds
		Remarks:	none
Analysis			
Spectral corrections:	automated		
Water:	no		
Fused silica:	order 1, range 400:2:1800	**Peaks**	
S/N ratio:	3549,36	722, 794, 840, 866, 908, 942, 970, 1022, 1070, 1088, 1168, 1266, 1302, 1372, 1440, 1608, 1622, 1658	

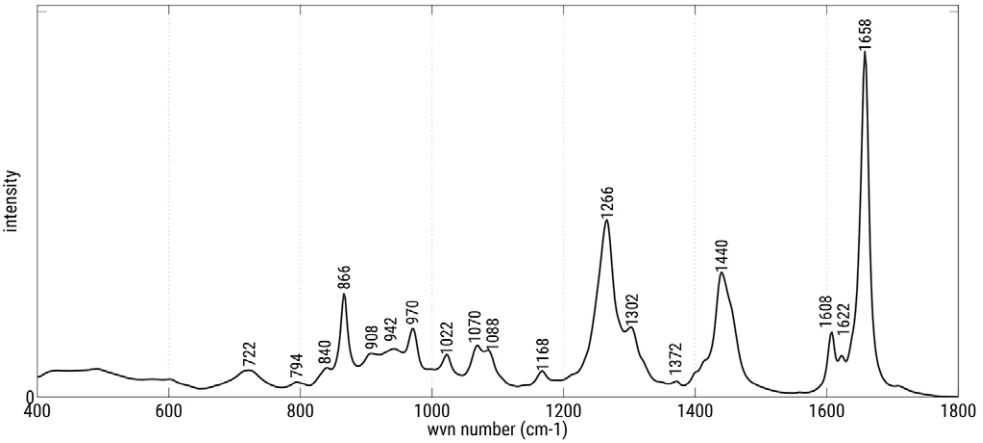

Name	L-lysine	**Measurement**	
CAS-number:	56-87-1	Condition:	dissolved
Chemical class:	Amino acid, essential	Solvent:	purified water
Firm:	Sigma-Aldrich Chemie B.V.	Concentration:	100 mg/ml
Product number:	62840	pH:	9,0
Purity according firm:	>98%	Instrument:	SpectraCell *RA Bacterial Strain Analyzer*
Source:	not mentioned	Acquisition time:	533 x 10 seconds
		Remarks:	clear solution. Also solid
Analysis			
Spectral corrections:	automated		
Water:	order 1, range 1500:2:1800	**Peaks**	
Fused silica:	order 0, range 400:2:1800	426, 496, 548, 658, 780, 822, 850, 902, 942, 962, 1016, 1062, 1128, 1184,	
S/N ratio:	131,73	1232, 1322, 1352, 1412, 1444, 1594	

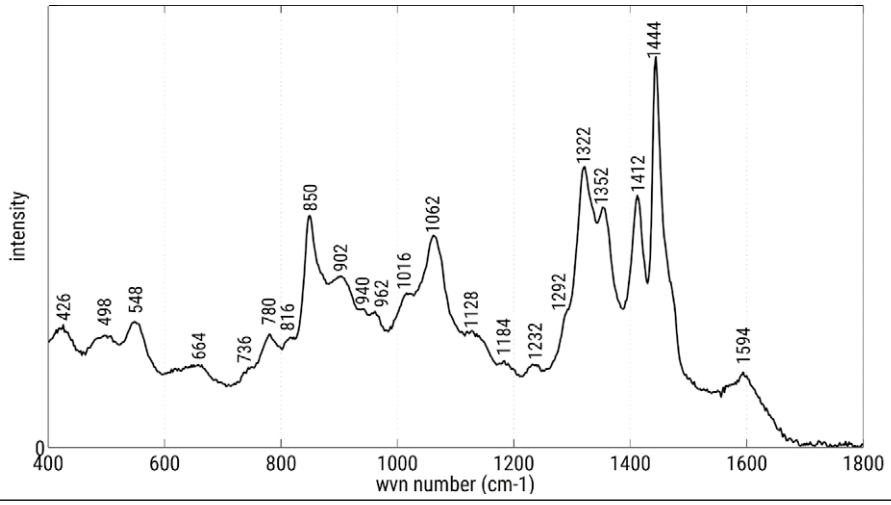

Name	L-phenylalanine	**Measurement**	
CAS-number:	63-91-2	Condition:	dissolved
Chemical class:	Amino acid, essential	Solvent:	purified water
Firm:	Sigma-Aldrich Chemie B.V.	Concentration:	50 mg/ml
Product number:	91331 FLUKA	pH:	unknown
Purity according firm:	>99%	Instrument:	SpectraCell *RA Bacterial Strain Analyzer*
Source:	analytical standard	Acquisition time:	561 x 10 seconds
		Remarks:	unclear solution, reeled off at 9500 rpm, supernatant used. Also solid
Analysis			
Spectral corrections:	automated		
Water:	order 1, range 1500:2:1800	**Peaks**	
Fused silica:	order 0, range 400:2:1800	486, 622, 752, 770, 816, 828, 856, 922, 1004, 1032, 1064, 1160, 1184, 1206,	
S/N ratio:	559,59	1268, 1340, 1360, 1408, 1446, 1586, 1606	

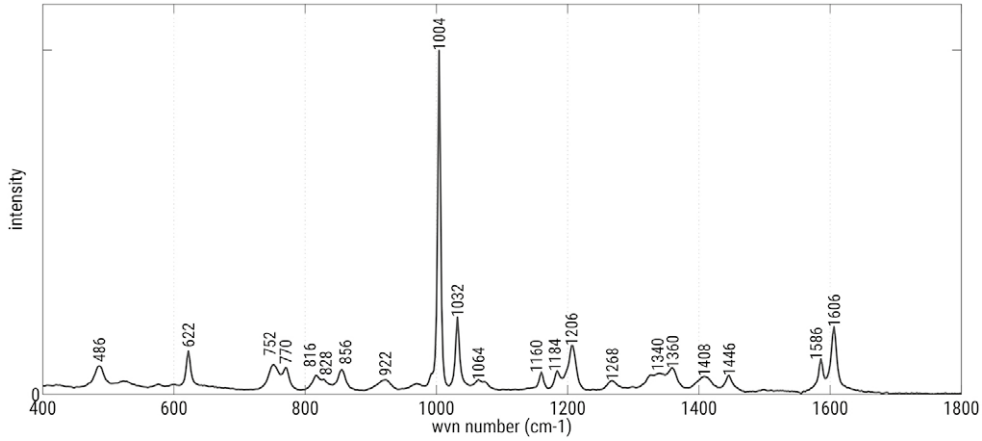

Name	**L-proline**	**Measurement**	
CAS-number:	147-85-3	Condition:	dissolved
Chemical class:	Amino acid, non essential	Solvent:	purified water
Firm:	ICN biochemicals	Concentration:	50 mg/ml
Product number:	102730	pH:	7,0
Purity according firm:	not mentioned	Instrument:	SpectraCell *RA Bacterial Strain Analyzer*
Source:	not mentioned	Acquisition time:	671 x 5 seconds
		Remarks:	clear solution
Analysis			
Spectral corrections:	manually		
Water:	order 0, range 1500:2:1800, factor 1/3,8		
Fused silica:	order 0, range 400:2:1800, factor 1/2,7	**Peaks**	
S/N ratio:	153,31	450, 558, 620, 620, 678, 780, 860, 910, 988, 1040, 1090, 1184, 1242, 1292, 1336, 1408, 1456, 1478, 1604	

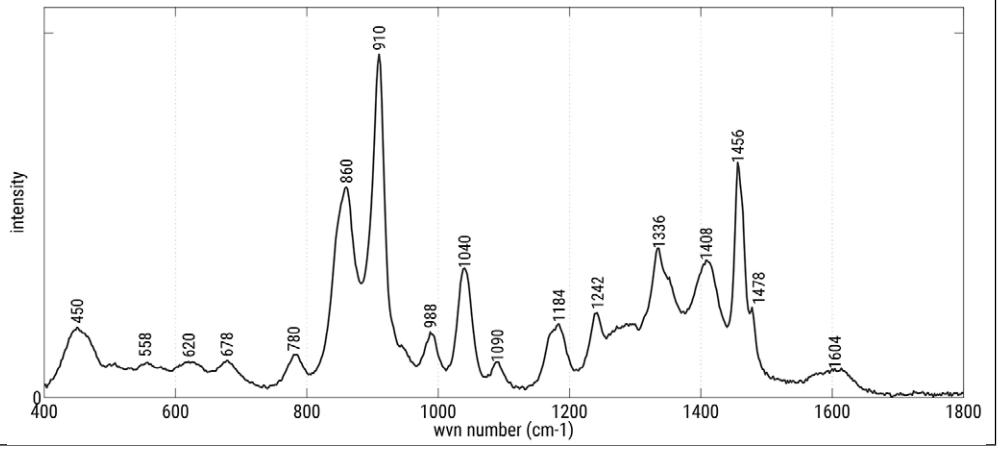

Name	**L-serine**	**Measurement**	
CAS-number:	56-45-1	Condition:	dissolved
Chemical class:	Amino acid, non essential	Solvent:	purified water
Firm:	Sigma-Aldrich Chemie B.V.	Concentration:	100 mg/ml
Product number:	S2600	pH:	5,0
Purity according firm:	99%	Instrument:	SpectraCell *RA Bacterial Strain Analyzer*
Source:	not mentioned	Acquisition time:	906 x 20 seconds
		Remarks:	heated, clear solution. Also solid
Analysis			
Spectral corrections:	manually		
Water:	order 0, range 1500:2:1800, factor 1/2,3		
Fused silica:	no	**Peaks**	
Background:	removed	436, 498, 770, 810, 850, 864, 918, 974, 1056, 1088, 1132, 1240, 1286, 1352, 1408, 1468, 1614	
S/N ratio:	146,68		

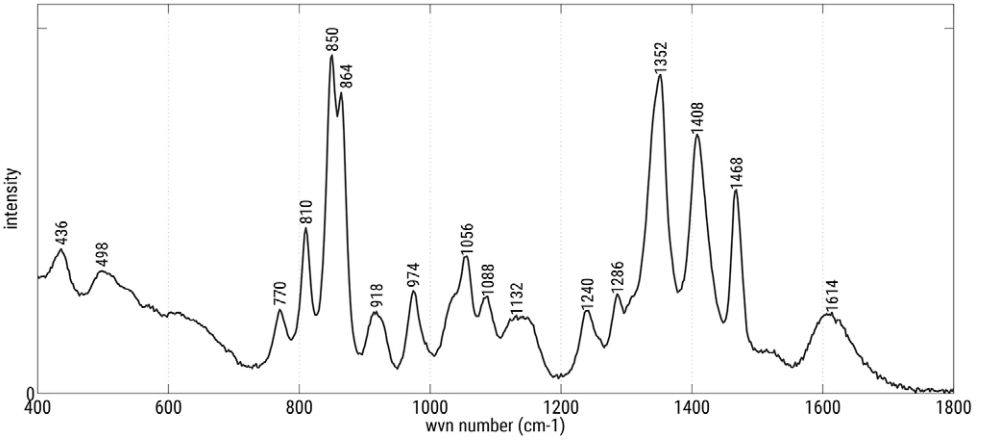

Name	**L-tryptophan**	**Measurement**	
CAS-number:	73-22-3	Condition:	dissolved
Chemical class:	Amino acid, essential	Solvent:	purified water
Firm:	Sigma-Aldrich Chemie B.V.	Concentration:	100 mg/ml
Product number:	T0254	pH:	5,5
Purity according firm:	>98%	Instrument:	SpectraCell *RA Bacterial Strain Analyzer*
Source:	not mentioned	Acquisition time:	445 x 20 seconds
		Remarks:	heated, clear solution. Also solid
Analysis			
Spectral corrections:	automated		
Water:	order 1, range 1500:2:1800	**Peaks**	
Fused silica:	order 0, range 400:2:1800	430, 462, 540, 578, 712, 758, 806, 862, 880, 968, 1012, 1076, 1134, 1204,	
S/N ratio:	99,41	1234, 1258, 1304, 1360, 1434, 1460, 1492, 1550, 1578, 1620	

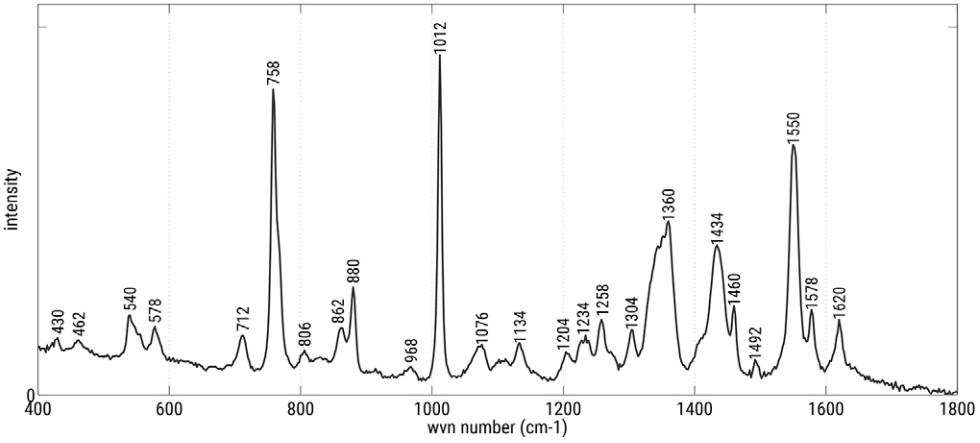

Name	**L-tyrosine**	**Measurement**	
CAS-number:	60-18-4	Condition:	solid
Chemical class:	Amino acid, non essential	Solvent:	n.a.
Firm:	MP biochemicals	Concentration:	n.a.
Product number:	103183	pH:	n.a.
Purity according firm:	not mentioned	Instrument:	SpectraCell *RA Bacterial Strain Analyzer*
Source:	not mentioned	Acquisition time:	553 x 15 seconds
		Remarks:	soluble in H2O, but in different solutions only water bands
Analysis			
Spectral corrections:	automated	**Peaks**	
Water:	no	432, 456, 472, 492, 526, 574, 642, 714, 714, 742, 798, 830, 846, 880, 896,	
Fused silica:	no	938, 984, 1042, 1098, 1114, 1154, 1178, 1200, 1214, 1246, 1264, 1282,	
S/N ratio:	807,82	1326, 1364, 1418, 1434, 1516, 1588, 1602, 1614	

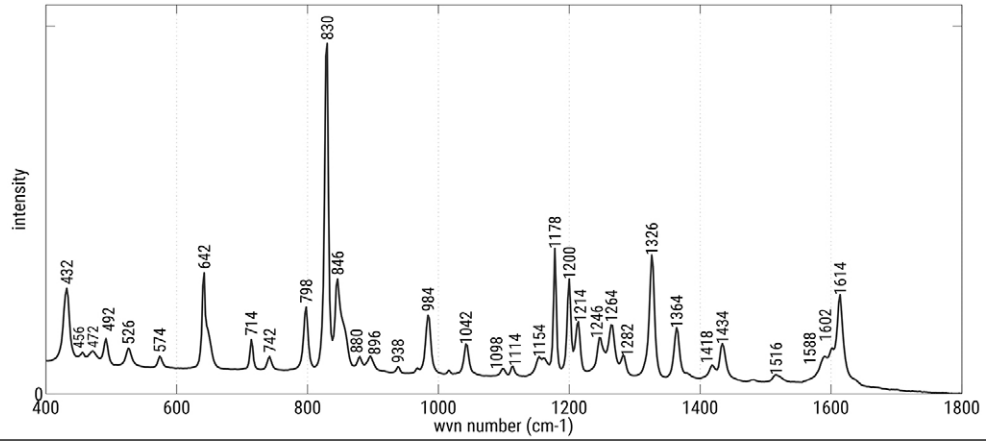

Name	**Mucin**
CAS-number:	84082-64-4
Chemical class:	Protein, glycoprotein
Firm:	Sigma-Aldrich Chemie B.V.
Product number:	M2378
Purity according firm:	not mentioned
Source:	procine stomach

Analysis

Spectral corrections:	manually
Water:	no
Fused silica:	no
Background:	removed
S/N ratio:	145,48

Measurement

Condition:	solid, hydrated with NaCl 0,9%
Solvent:	n.a.
Concentration:	n.a.
pH:	n.a.
Instrument:	SpectraCell *RA Bacterial Strain Analyzer*
Acquisition time:	189 x 10 seconds
Remarks:	insoluble

Peaks

442, 510, 642, 718, 786, 830, 852, 880, 920, 946, 970, 1004, 1064, 1084, 1126, 1154, 1178, 1266, 1326, 1378, 1410, 1452, 1658

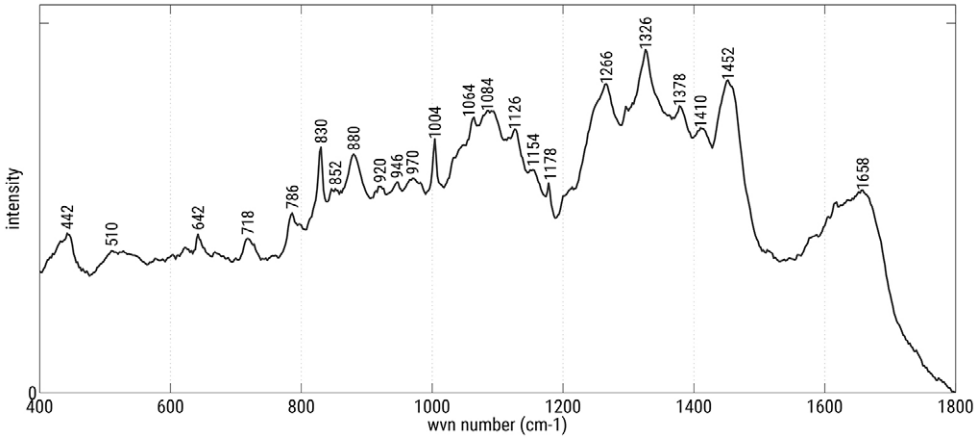

Name	**Myoglobin**
CAS-number:	100684-32-0
Chemical class:	Protein, globular
Firm:	Sigma-Aldrich Chemie B.V.
Product number:	M0630
Purity according firm:	95 - 100%
Source:	equine skeletal muscle

Analysis

Spectral corrections:	manually
Water:	no
Fused silica:	no
Background:	removed
S/N ratio:	263,83

Measurement

Condition:	dissolved
Solvent:	purified water
Concentration:	unknown
pH:	unknown
Instrument:	SpectraCell *RA Bacterial Strain Analyzer*
Acquisition time:	248 x 15 seconds
Remarks:	clear solution

Peaks

408, 490, 622, 642, 674, 714, 756, 790, 828, 854, 896, 938, 1002, 1032, 1056, 1076, 1104, 1126, 1156, 1174, 1210, 1238, 1302, 1318, 1338, 1370, 1388, 1430, 1450, 1520, 1542, 1562, 1582, 1620, 1654

Remarks

correctionType = 'none'

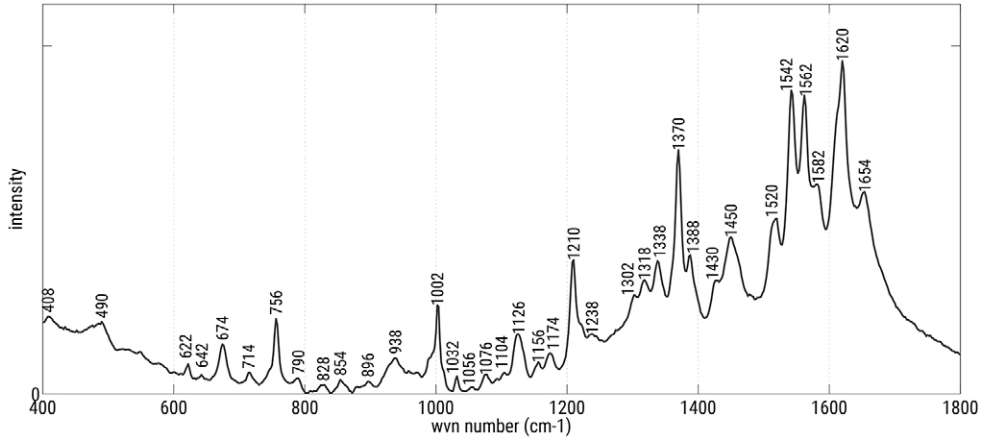

Name	Myosin	**Measurement**	
CAS-number:	86417-96-1	Condition:	dissolved
Chemical class:	Protein, fibrous	Solvent:	purified water
Firm:	Sigma-Aldrich Chemie B.V.	Concentration:	unknown
Product number:	SCP0196	pH:	7,0
Purity according firm:	95% (>62% peptide content)	Instrument:	SpectraCell *RA Bacterial Strain Analyzer*
Source:	rabbit musculus psoas	Acquisition time:	306 x 15 seconds
		Remarks:	clear solution. Also solid
Analysis			
Spectral corrections:	manually		
Water:	order 0, range 400:2:1800		
Fused silica:	order 0, range 400:2:1800, factor 1/7	**Peaks**	
S/N ratio:	171,20	406, 434, 494, 600, 622, 710, 726, 844, 900, 962, 1004, 1032, 1060, 1100, 1160, 1184, 1206, 1248, 1322, 1436, 1524, 1586, 1680	

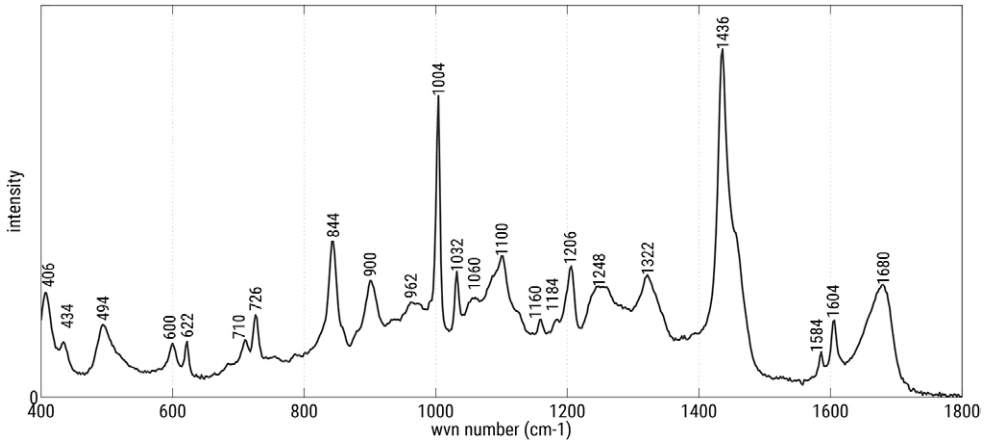

Name	Myristic acid	**Measurement**	
CAS-number:	544-63-8	Condition:	solid
Chemical class:	Lipid, saturated fatty acid	Solvent:	n.a.
Firm:	Sigma-Aldrich Chemie B.V.	Concentration:	n.a.
Product number:	70079 FLUKA	pH:	n.a.
Purity according firm:	>99.5%	Instrument:	SpectraCell *RA Bacterial Strain Analyzer*
Source:	analytical standard	Acquisition time:	441 x 1 seconds
		Remarks:	insoluble
Analysis			
Spectral corrections:	automated		
Water:	no		
Fused silica:	order 0, range 400:2:1800	**Peaks**	
S/N ratio:	727,89	416, 430, 492, 534, 570, 670, 894, 908, 986, 1008, 1040, 1064, 1092, 1128, 1176, 1250, 1296, 1372, 1412, 1422, 1436, 1460, 1508, 1558, 1630	

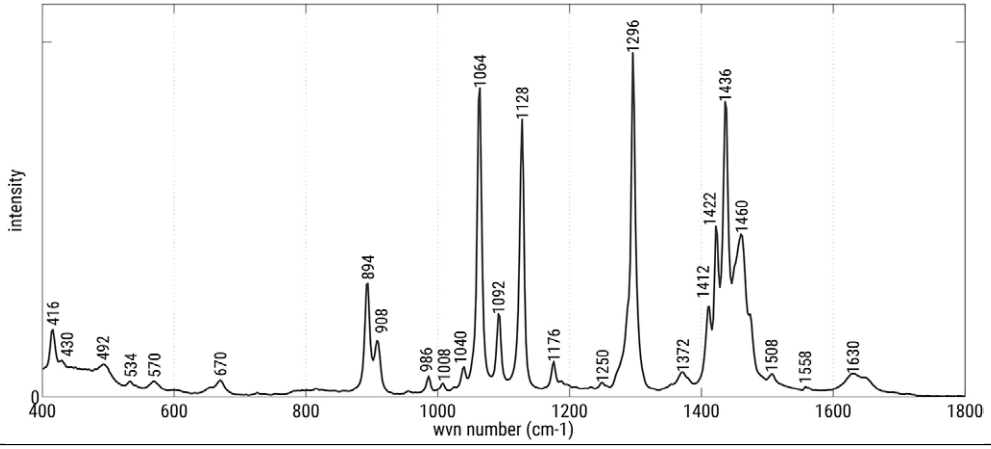

Name	**Oleic acid**	**Measurement**	
CAS-number:	112-80-1	Condition:	fluid
Chemical class:	Lipid, unsaturated fatty acid	Solvent:	n.a.
Firm:	Sigma-Aldrich Chemie B.V.	Concentration:	n.a.
Product number:	75090 FLUKA	pH:	5,5
Purity according firm:	not mentioned	Instrument:	SpectraCell *RA Bacterial Strain Analyzer*
Source:	analytical standard	Acquisition time:	441 x 1 seconds
		Remarks:	none
Analysis			
Spectral corrections:	automated	**Peaks**	
Water:	no	498, 602, 726, 768, 844, 856, 868, 890, 904, 972, 1018, 1066, 1082, 1118, 1266, 1302, 1366, 1440, 1656	
Fused silica:	order 1, range 400:2:1800		
S/N ratio:	1920,23		

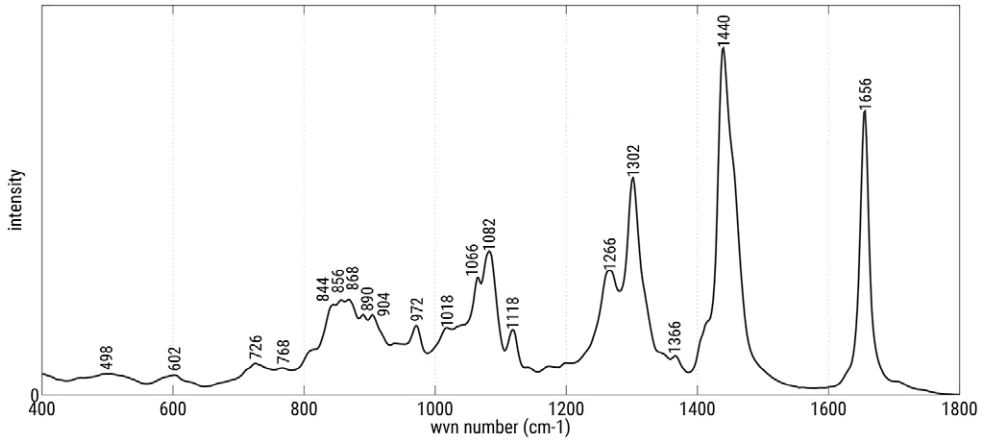

Name	**Olive oil**	**Measurement**	
CAS-number:	8001-25-0	Condition:	fluid
Chemical class:	Lipid, unsaturated fatty acid	Solvent:	n.a.
Firm:	supermarket	Concentration:	n.a.
Product number:	n.a.	pH:	unknown
Purity according firm:	100%	Instrument:	*Skin Analyzer*
Source:	not mentioned	Acquisition time:	100 x 1 seconds
		Remarks:	none
Analysis			
Spectral corrections:	automated		
Water:	no	**Peaks**	
Fused silica:	order 0, range 400:2:1800	520, 600, 726, 766, 854, 870, 888, 972, 1066, 1080, 1120, 1268, 1302, 1366, 1440, 1524, 1656, 1748	
S/N ratio:	364		

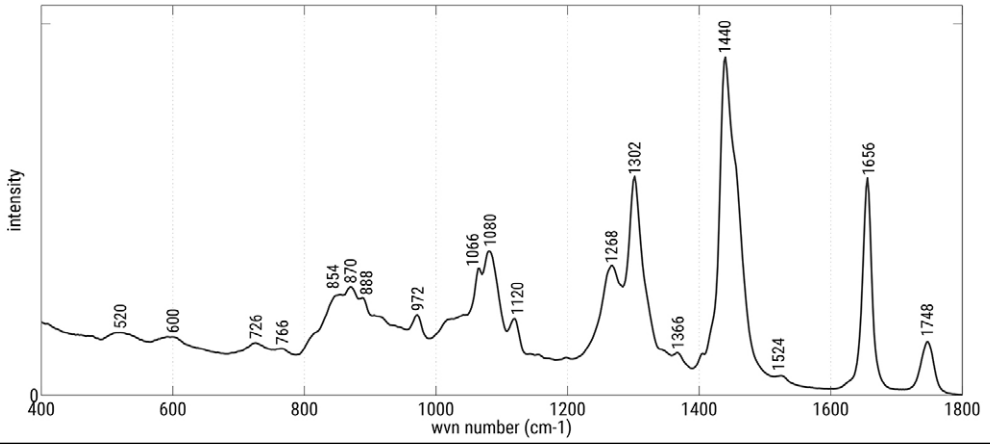

Name	**Palmitic acid**	**Measurement**	
CAS-number:	57-10-3	Condition:	solid
Chemical class:	Lipid, saturated fatty acid	Solvent:	n.a.
Firm:	Sigma-Aldrich Chemie B.V.	Concentration:	n.a.
Product number:	76119 FLUKA	pH:	n.a.
Purity according firm:	>99%	Instrument:	SpectraCell *RA Bacterial Strain Analyzer*
Source:	analytical standard	Acquisition time:	256 x 1 seconds
Analysis		Remarks:	insoluble
Spectral corrections:	automated		
Water:	no	**Peaks**	
Fused silica:	order 1, range 400:2:1800	630, 666, 892, 906, 972, 1012, 1026, 1050, 1060, 1098, 1128, 1176, 1188, 1296, 1370, 1410, 1444, 1466, 1512, 1652	
S/N ratio:	483,34		

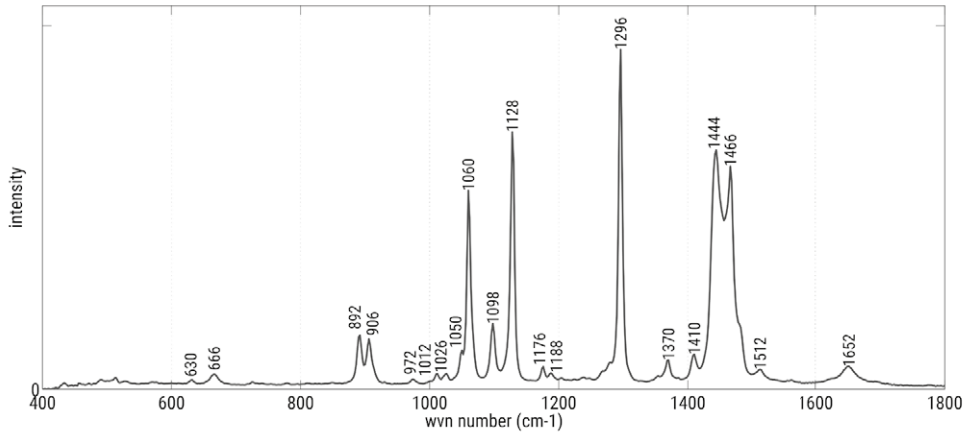

Name	**Palmitoleic acid**	**Measurement**	
CAS-number:	373-49-9	Condition:	fluid
Chemical class:	Lipid, unsaturated fatty acid	Solvent:	n.a.
Firm:	Sigma-Aldrich Chemie B.V.	Concentration:	n.a.
Product number:	76169 FLUKA	pH:	5,5
Purity according firm:	not mentioned	Instrument:	SpectraCell *RA Bacterial Strain Analyzer*
Source:	analytical standard	Acquisition time:	441 x 1 seconds
Analysis		Remarks:	none
Spectral corrections:	automated		
Water:	no	**Peaks**	
Fused silica:	order 1, range 400:2:1800	402, 456, 602, 728, 754, 818, 842, 864, 890, 904, 972, 992, 1016, 1066, 1080, 1114, 1142, 1190, 1208, 1264, 1302, 1366, 1440, 1656	
S/N ratio:	1476,66		

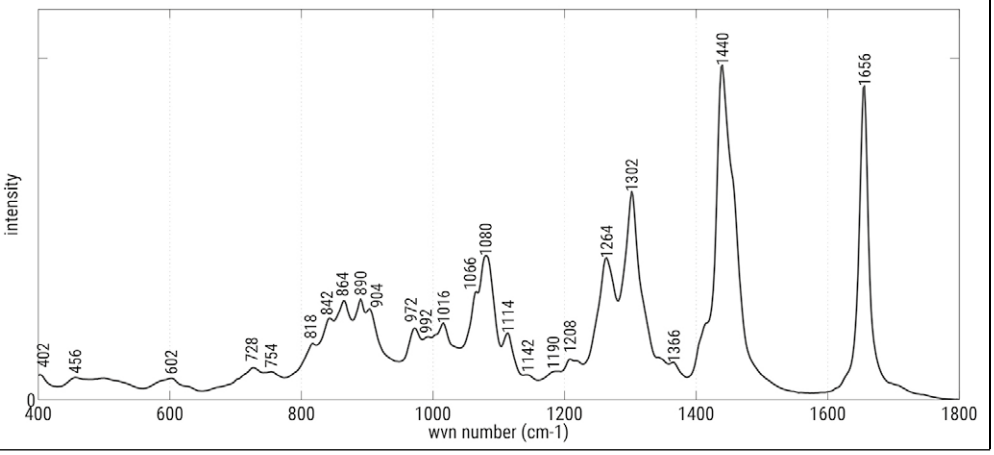

Name	**RNA**
CAS-number:	63231-63-0
Chemical class:	Nucleic acid
Firm:	Sigma-Aldrich Chemie B.V.
Product number:	83850
Purity according firm:	not mentioned
Source:	torula utilis

Analysis

Spectral corrections:	manually
Water:	order 1, range 400:2:1800
Fused silica:	no
Background:	removed
S/N ratio:	300,65

Measurement

Condition:	dissolved
Solvent:	purified water
Concentration:	10 mg/ml
pH:	5,0
Instrument:	SpectraCell *RA Bacterial Strain Analyzer*
Acquisition time:	111 x 10 seconds
Remarks:	yellowish almost clear solution. Also solid

Peaks

504, 528, 558, 580, 620, 636, 666, 724, 784, 886, 974, 1016, 1056, 1092, 1150, 1254, 1326, 1358, 1408, 1458, 1484, 1510, 1542, 1560, 1606, 1686

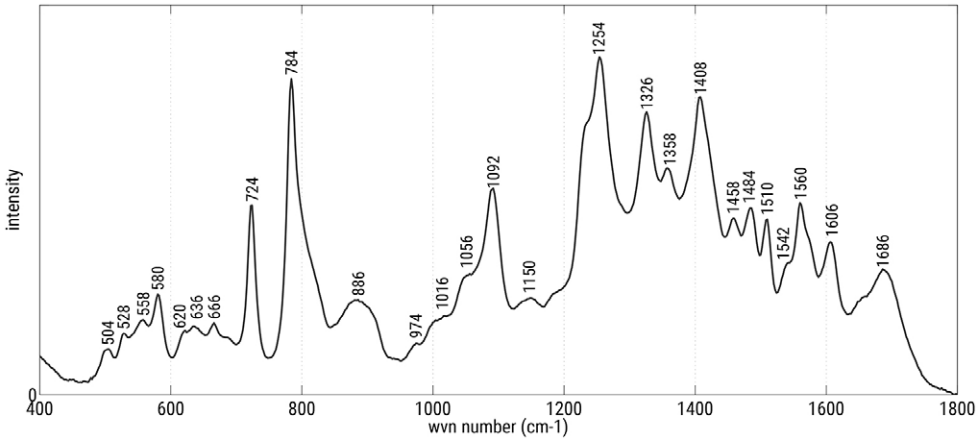

Name	**Stearic acid**
CAS-number:	57-11-4
Chemical class:	Lipid, saturated fatty acid
Firm:	Sigma-Aldrich Chemie B.V.
Product number:	85679 FLUKA
Purity according firm:	not mentioned
Source:	analytical standard

Analysis

Spectral corrections:	automated
Water:	no
Fused silica:	order 1, range 400:2:1800
S/N ratio:	1655,42

Measurement

Condition:	solid
Solvent:	n.a.
Concentration:	n.a.
pH:	n.a.
Instrument:	SpectraCell *RA Bacterial Strain Analyzer*
Acquisition time:	891 x 5 seconds
Remarks:	insoluble

Peaks

406, 558, 572, 632, 818, 848, 866, 890, 910, 944, 980, 1026, 1062, 1100, 1128, 1172, 1186, 1204, 1224, 1262, 1296, 1370, 1402, 1416, 1440, 1462, 1472, 1496, 1532, 1650

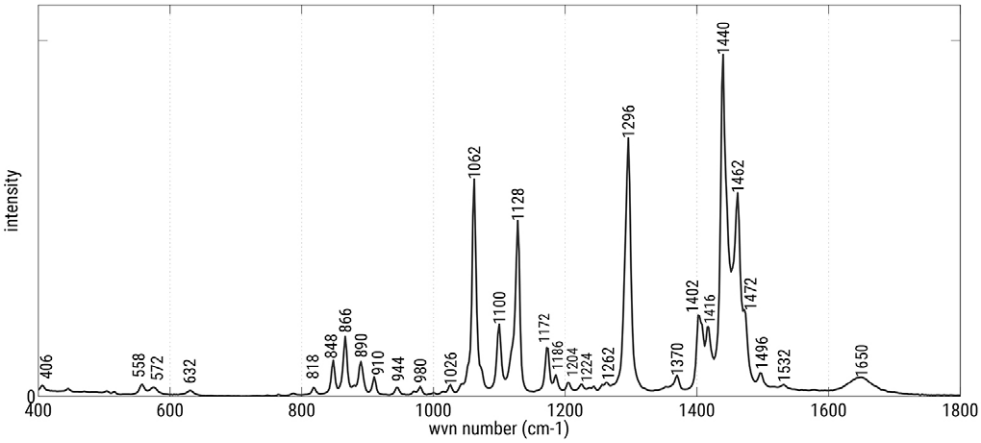

Name	**Thymine**	**Measurement**	
CAS-number:	65-71-4	Condition:	solid
Chemical class:	Nucleotide, pyrimidine	Solvent:	n.a.
Firm:	Sigma-Aldrich Chemie B.V.	Concentration:	n.a.
Product number:	T0376	pH:	n.a.
Purity according firm:	>99%	Instrument:	SpectraCell *RA Bacterial Strain Analyzer*
Source:	not mentioned	Acquisition time:	1857 x 1 seconds
		Remarks:	soluble in NaOH 1M
Analysis			
Spectral corrections:	automated		
Water:	no	**Peaks**	
Fused silica:	order 0, range 400:2:1800	428, 480, 554, 560, 616, 740, 766, 804, 934, 984, 1048, 1154, 1214, 1246, 1258, 1368, 1408, 1426, 1434, 1458, 1488, 1672, 1704, 1722	
S/N ratio:	783,13		

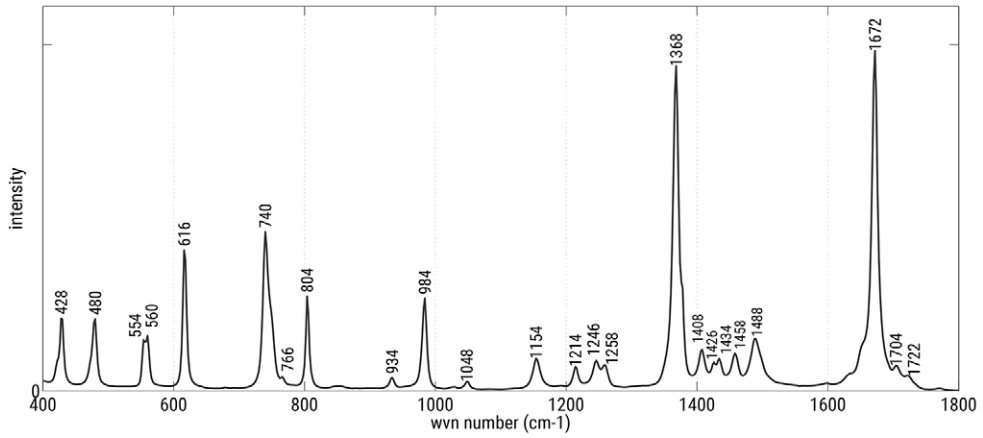

Name	**Uracil**	**Measurement**	
CAS-number:	66-22-8	Condition:	solid
Chemical class:	Nucleotide, pyrimidine	Solvent:	n.a.
Firm:	Sigma-Aldrich Chemie B.V.	Concentration:	n.a.
Product number:	U0750	pH:	n.a.
Purity according firm:	>99%	Instrument:	SpectraCell *RA Bacterial Strain Analyzer*
Source:	not mentioned	Acquisition time:	1792 x 1 seconds
		Remarks:	soluble in NaOH 1M
Analysis			
Spectral corrections:	automated		
Water:	no	**Peaks**	
Fused silica:	order 0, range 400:2:1800	430, 530, 538, 556, 578, 790, 826, 984, 994, 1010, 1100, 1162, 1236, 1254, 1394, 1418, 1454, 1504, 1610, 1646, 1714	
S/N ratio:	1715,25		

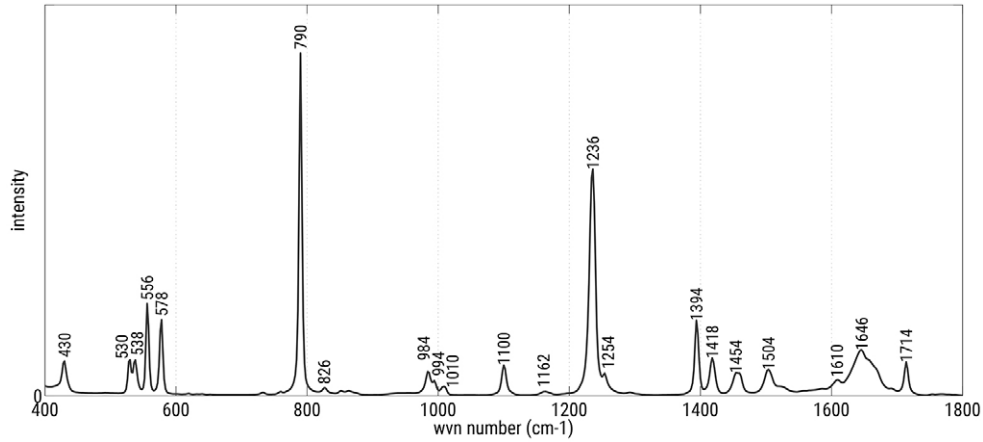

7

General discussion

CLINICAL NEED

In oncology there is increasing interest in optical techniques as diagnostic tools. In daily head and neck oncological care there are three major applications for such techniques: [1] screening of high-risk patients, [2] targeted biopsy of clinically evident lesions with a heterogeneous aspect, and [3] surgery guidance. As all optical techniques tend to provide a real-time, non-invasive signature of the examined tissue, they are ideal for integrating into the oncological workflow without causing harm to the patient or the tissue.[1] Numerous publications demonstrate the potential and feasibility of several optical techniques. Currently the techniques studied most include Raman spectroscopy,[2-7] (auto) fluorescence,[8-11] narrow band imaging (NBI),[12,13] optical coherence tomography (OCT),[14,15] confocal (reflectance) microscopy (C(R)M)[16-19] and elastic scattering spectroscopy (ESS).[20] Several reviews provide an overview of the most recent publications on oncological applications in the head and neck region.[21-28] Each technique is based on a different principle and all have their own advantages and disadvantages. To evaluate the different optical techniques it is important to keep the specific future clinical application in mind, as the technical and discriminatory requirements of a technique may vary (Figure 1). This will be dealt with in more detail in the paragraph 'optical techniques'.

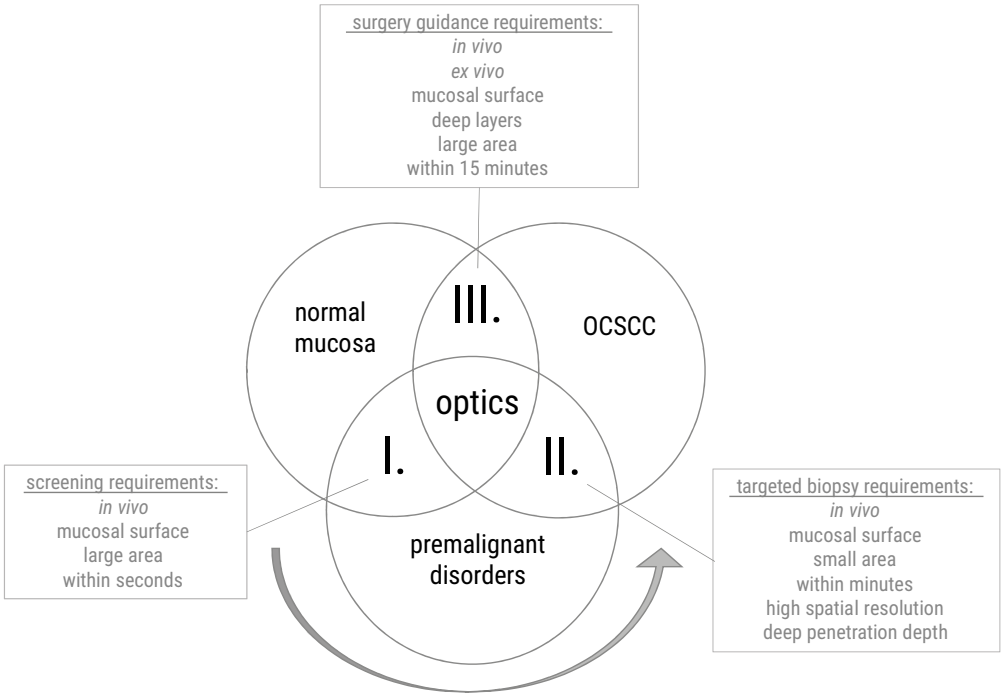

Figure 1. Different applications require different technical and discriminatory specifications. I. Screening of high-risk patients. II. Targeted biopsy of clinically evident lesions. III. Surgery guidance.

Screening of high-risk patients

The Netherlands currently has nationwide screening programs for breast cancer, cervical cancer and colorectal cancer.[29] A screening program for head and neck cancer may be potentially beneficial, not only for the patient but also for society by reducing healthcare costs through earlier detection of malignancies. Screening can be offered to high-risk patients; those that have extensive nicotine and alcohol habits, and those that have had previous malignancies in the aerodigestive tract.[30] For screening purposes the goal would be to scan the mucosal lining of the upper aerodigestive tract in asymptomatic individuals with the intention of examining potentially malignant disorders such as leukoplakia, erythroplakia and lichen planus.[8] When a mucosal lesion is detected the optical technique can also be used to monitor changes over time.

Targeted biopsy of clinically evident lesions with a heterogeneous aspect

With targeted biopsy the goal is to detect the most altered region within a clinically evident mucosal lesion. Mucosal lesions harbor inflammation, dysplastic epithelial changes and cancer,[31-33] which are difficult to distinguish clinically. Histopathological assessment is the gold standard for malignancy diagnosis.[34] Optical techniques can help in the selection of the best area to sample for histological assessment, and thereby minimize the sampling error. This prevents the need for repeated biopsies to achieve an accurate diagnosis, and reduces the risk of patient harm and anxiety.

Surgery guidance

In surgical guidance the goal is to delineate tumor margins. Therefore the tumor needs to be distinguished from the surrounding non-tumorous tissue. Accurate delineation of the tumor is of great importance as inadequate tumor resection is associated with a poor prognosis.[35] Accurate delineation may also limit unnecessary resection of healthy tissue, which in turn preserves organ function and esthetics and improves the patient's quality of life.

Intraoperative assessment of resection margins can be performed in the wound bed (i.e. wound bed-driven assessment/defect-driven assessment, *in vivo*) or on the resection specimen (i.e. specimen-driven assessment, *ex vivo*). Various publications have shown that intraoperative *ex vivo* specimen-driven assessment is superior to *in vivo* defect-driven assessment.[36-38]

An ideal optical technique can be used in all of these applications, and should meet as many as possible of the following requirements: [1] is applicable both *in vivo* and *ex vivo*, [2] requires no pretreatment or use of labels, probes or dyes, [3] provides objective, reproducible data, independent of the operator, [4] provides information on large tissue regions in a limited amount of time, [5] obtains high spatial resolution, [6] obtains sufficient penetration depth, and [7] enables objective result interpretation.

The time required to obtain the results should not far exceed that of the required time for current intraoperative procedures. The average time-span for clinical judgment of a tissue ranges between a few seconds to a few minutes, whereas the histopathological assessment of a frozen tissue section may take up to 15 minutes.[39] The acquired spatial resolution is dependent on the anticipated differences between the tissues to be distinguished. The average cell size is between 10 – 20 μm.[40] Thus, subcellular differences

are noticed from a spatial resolution of ≤ 10 µm. The penetration depth needed for measurements from the mucosal surface should be at least the thickness of the epithelium in order to detect invasion through the basement membrane. The epithelial thickness within the head and neck region varies between 100 µm in the floor of the mouth and up to 700 µm in the dorsal tongue.[41] Regarding the desired penetration depth of an optical technique, one needs to consider that most premalignant disorders are characterized by an increased epithelial thickness, and invasive malignant transformation is characterized by invasion through the basement membrane.[40] Generally, one can distinguish between point measurement techniques (Raman spectroscopy, fluorescence, ESS) and imaging techniques ((auto) fluorescence, NBI, OCT, CRM). With point measurement techniques the scanning size is restricted, whereas with imaging techniques the information per pixel is limited. Point measurement techniques are most useful for suspicious areas that are limited in size, because the user needs to determine the position of the measurement. On the other hand, in imaging technique a learning curve is often experienced before good quality images are obtained. Also result interpretation can be subjectively influenced. The scanning size is dependent on the acquisition time as well as on the size of the probe used. Further technical improvements will solve these drawbacks. The excitation source used is one of the essential factors determining the penetration depth; the longer the wavelength the deeper the penetration.[1]
Below, the principles and characteristics of the following techniques are discussed: Raman spectroscopy, (auto) fluorescence, NBI, OCT, C(R)M, and ESS. Their properties are summarized in Table 1.

OPTICAL TECHNIQUES

Raman spectroscopy

The principle of Raman spectroscopy is described in detail in the introduction of this thesis. Briefly, the technique is based on the inelastic scattering of light by molecules.[42] The contribution of a specific molecule to the Raman spectrum is proportional to the concentration of that molecule in the measurement volume.[43] A Raman spectrum therefore provides both a qualitative and quantitative representation of the molecular composition of the tissue examined.
The technique can be used with UV, visible and near infrared (NIR) light.[26] Usually a NIR excitation source is used to reduce spectral interference from tissue fluorescence. This also ensures a deeper penetration of the light into the tissue, up to 1000 µm.[44] Both the mucosal surface and the deeper soft tissue layers can be investigated without pretreatment of the tissue
Reproducible point measurements can be provided within a second.[45] With a high spatial resolution of up to 1 µm, highly specific information can be obtained. However, this leads to a restricted scanning size. Data interpretation is objective as this is based on statistical and analytical classification algorithms. The technique can be used *in vivo* as well as *ex vivo*.
As is often mentioned, the disadvantage of Raman spectroscopy is the weak signal: this is because only inelastic scattered photons are measured.[27] This requires a longer collection time to obtain an adequate signal. Technical improvements, such as more sensitive detectors, have solved this problem.[46]

	In vivo	*Ex vivo*	Pretreatment needed	Reproducible data	Scanning size	Spatial resolution up to	Penetration depth up to	Objective data interpretation
Raman spectroscopy	Yes	Yes	No	Yes	Restricted	1 µm	1000 µm	Yes
Fluorescence	Yes	Limited	Often use of dyes and probed	Yes	Large	n.a.	500 µm	No
Narrow band imaging	Yes	No	No	No	Large	n.a.	240 µm	No
Optical coherence tomography	Yes	Limited	No	No	Restricted	4 µm	2000 µm	No
Laser scanning confocal endomicroscopy	Yes	No	Use of dyes	No	Restricted	1 µm	300 µm	No
Confocal reflectance endomicroscopy	Yes	No	No	No	Restricted	1 µm	500 µm	No
Elastic scattering spectroscopy	Yes	Yes	No	Yes	Restricted	10 µm	500 µm	Yes

Table 1. Properties and applications of discussed optical techniques.

Several variations of Raman spectroscopy have been developed. Their purpose is to enhance sensitivity (e.g. surface-enhanced Raman scattering (SERS)), or to acquire very specific information (e.g. coherent anti-Stokes Raman scattering (CARS)).[47] However, these techniques have their own limitations.

Fluorescence

Fluorescence is based on the presence of endogenous fluorophores in cells, such as hemoglobin, collagen, elastin, keratin, flavin adenine dinucleotide (FADH) and nicotinamide adenine dinucleotide (NADH).[48] Fluorophores can absorb photons and gain energy when they are illuminated by electromagnetic radiation. The stored energy can be re-emitted as light with a longer wavelength, which is known as fluorescence.[49] Carcinogenesis leads to changes that can alter the concentration and characteristics of the fluorophores.[9] A review of the optimal wavelength showed that the normalized red-to-green fluorescence intensity ratio of 405 nm excitation provided the best discrimination between neoplastic and non-neoplastic oral mucosa.[50] Normal cells emit more green fluorescence, while abnormal cells show a loss of auto-fluorescence and appear darker. This is imaged by using filtered camera systems.

The maximum penetration depth is 500 μm.[10] Reproducible auto-fluorescence is obtained by using a very short acquisition time of less than a second. With commercially available devices the auto-fluorescence of large tissue surfaces is evaluated at once.[51] This results in a modest amount of spectral information, but for a significant area of tissue surface.[52] More detailed spectroscopic information can be provided when single points are measured. However, this naturally limits the total scanning size.

Image interpretation is subjective as it relies on the ability of the examiner to recognize loss of fluorescence. The development of automated classification algorithms, used to quantify the decrease in the ratio of red-to-green auto-fluorescence, tends to reduce this subjective interpretation.[50]

The technique can be used *in vivo* and *ex vivo*. However, within epithelium the most relevant fluorophores are NADH and FADH,[53] which have been reported to lose their fluorescent properties after resection. The oxygenation of tissue leads to a shift from NADH to its oxidized form NAD, which does not fluoresce. This limits the use of the technique after resection.

As is often mentioned, the relatively low specificity of auto-fluorescence is a limitation. This is due to a few fluorophores with broad and overlapping features.[26] Several commonly occurring conditions, such as mucosal pigmentation, hyperkeratosis, ulceration, irritation and gingivitis also show a loss of fluorescence.[54] Therefore the use of exogenous dyes/labels and probes has been explored. A probe is an antibody or ligand conjugated to an optically active reporter that is designed to target specific hallmarks of cancer.[10] The use of probes allows the detection of specific and relatively abundant molecules in malignant tissue, which can be associated with specific characteristics (e.g. invasive, aggressive or metastatic tendency) of the tumor.[10] Topical or intravenous application of tumor selective dyes, such as 5-aminolevulinic acid (5-ALA),[55] hypericin,[56] acriflavine and proflavine[57] can be used to enhance fluorescence. However, this requires preparation of the tissue or patient.

Narrow band imaging

In NBI blue light with a short wavelength (415 nm) penetrates the mucosa and highlights the superficial capillaries, while another wavelength (540 nm) penetrates deeper and identifies prominent vessels in the submucosa.[58] A colored composite image is displayed directly onto a monitor, in which the superficial capillaries are shown as brown and the deeper vessel as cyan.[59] Due to the penetrating depths of the blue (160 μm) and green (240 μm) lights, usage is limited to *in vivo* evaluation of superficial lesions, or the mucosal extension of deeper lesions.[60] There is no need for dyes or probes. As this is a non-contact technique, large areas can be examined at once. Lesions as small as 300 μm in diameter can be detected.[61] Histology and 3D imaging confirm that the further a lesion is along the carcinogenesis continuum, the more pronounced are the microvascular changes. Stepwise changes in these microvascular irregularities form the basis for pattern classifications.[62] Up to 50x magnification can be used to facilitate further the visualization of these changes in the degree of dilation, tortuosity, meandering and the caliber of intra-papillary capillary loops (IPCL).[13] The interpretation of these IPCL patterns is highly subjective. For the development of more objective classification systems, knowledge of the habits and underlying diseases of the study population is crucial, as these can affect the appearance of vessels due to vasoconstriction or vascular complications.[60] Other anatomical and (patho) physiological issues can also affect the appearance of underlying blood vessels. Bleeding, hyperkeratosis, chronic inflammation, postoperative radiotherapy, ulcers and leukoplakia can alter the penetration of light into tissue, precluding NBI evaluation.[12,63] In the oral cavity the reflective shine caused by mucous and salivary secretions also complicates result interpretation.[64]

NBI systems are commercially available, in which switching between white light and NBI modes can be performed.[59] Positioning the rigid endoscope to provide clear images on the monitor can initially be difficult, requiring an experienced operator, particularly in the oral cavity where soft tissues may overlap or become mobile.[13] The technique is not reliable in a surgical field for assessing deep margins because of blood interference, and also because it has been developed to recognize specific mucosal patterns without information on different submucosal tissue structures.[65]

Optical coherence tomography

OCT is an analogue of ultrasound, although infrared light is used instead of sound.[66] Back-scattered signals that reflect from the different layers within the tissue are used to reconstruct cross-sectional structural images.[66] In this way tissue architecture is depicted from the mucosal surface or from the deeper soft tissue.[67] High speed OCT devices with a high spatial resolution (< 4 μm) are currently available.[68] Only a small area can be examined at a time, because of the small size of the OCT probe.[69] OCT records reflections up to a depth of up to 2000 μm per second.[70] There is no need for pretreatment of the tissue.

Providing an image of high quality is however contingent on a learning curve,[71] which makes the technique operator dependent. There are no standards for the evaluation of the OCT images, thus the interpretation is subjective and rests on the experience of the investigator. This could lead to inter-observer inconsistencies.[15] Moreover, interpretation by a more experienced pathologist is often desirable. No quantitative information is provided. Nevertheless, image analysis algorithms for the extraction of morphological features are being investigated in order to achieve a more objective and automated

diagnosis.[72] Certain morphological alterations cause diagnostic difficulties, such as hyperkeratotic lesions (due to increased light reflection), hyperplastic lesions (that exceed the penetration depth) and ulcers (the lack of basement membrane being confused with invasive carcinoma).[73]
The technique can be used to assess *ex vivo* and *in vivo* lesions. However, *ex vivo* samples lack capillary fluid perfusion, which may affect optical scattering properties and image resolution.[15]

Confocal microscopy

Confocal microscopy (CM) involves the examination of tissue *in vivo* at magnifications from 60x to 150x.[23] It differs from conventional microscopy in that it uses a confocal point source of visible light to illuminate a small spot within the tissue. Consecutively scanned points in the x-y-plane produce an image that is oriented parallel rather than perpendicular to the tissue surface.[74] The thin section image illustrates tissue architecture and cellular morphology. By moving the microscope lens closer to or further away from the tissue, images become either deeper or shallower from the surface.[75] However, with a magnification of 60x it only assesses depths of 80 µm, and with a 150x magnification an even shallower depth of 30 µm.[76] When NIR light is used instead of visible light a deeper penetration up to 300 µm can be obtained. This is called laser scanning confocal microscopy (LSCM).[74] The technique can be used both on the mucosal surface and in the deeper soft tissue layers.
In (LS)CM various topical and intravenous antibody targeted dyes are utilized to help highlight the cellular structures. The most commonly used stains include methylene blue, acetic acid, hypericin, acriflavine and fluorescein.[75]
Confocal reflectance microscopy (CRM) differs from LSCM in that fluorescence is not required for imaging. Reflected light from various tissue components is detected only from the plane in focus.[74] Variations in brightness of structures are a function of the light-reflecting properties of tissues. Image contrast is due to local natural variations in the refractive indices of various cellular structures.[17] CRM devices usually operate at a wavelength of 830 nm.[18] Detailed information of the epithelium can be gained up to 500 µm in depth.[75]
In confocal (reflectance) endomicroscopy the technique is integrated into an endoscope. Commercially available endoscopes have an average spatial resolution of 1 µm.[75] Obtaining an image of 10 µm x 10 µm takes minutes. The endomicroscope is available in different sizes. However, its large diameter (up to 5,5 mm) and rigidity limits imaging of certain areas in the mouth.[75]
Confocal (reflectance) microscopy depends on a user's learning curve for a consistent image quality.[23] Image resolution is significantly affected by glare from light reflected in cells not in focus. Additionally, minimal patient movement during the imaging procedure and motion artifacts due to poor soft tissue stability complicates the task of obtaining clear images.[16] Keratinization and hyperplasia can cause background artifacts due to changes in the refractive index.[19] Result interpretation of confocal images is subjective and requires a detailed knowledge of the cellular morphology.

Elastic scattering spectroscopy

In ESS the acquired point spectra reflects both the elastic scattering and absorptive properties of the tissue without separating these contributions.[77] In this way ESS translates tissue micro-morphological

changes into spectral features.[22] Micro-morphological characteristics including the size and density of the nucleus, nucleolus and cytoplasm, will change on transformation to premalignant or malignant conditions.[20] In ESS a width range of wavelengths is used in the visible or NIR region (300 – 900 nm).[23] The average penetration depth is 500 µm.[78] Both the mucosa surface and the deeper tissue layers can be evaluated with the technique.

The entire measurement can be made in less than a second and is operator independent.[23] The technique can be used both *in vivo* and *ex vivo* without tissue preparation. Objective and automated result interpretation is based on a statistical and analytical algorithm of the spectra rather than on a subjective interpretation of images.[25]

The correlation to gold standard histopathology can be a problem, as the optical signature reports changes commonly in a volume of 1 mm^3.[23] False-positive results were found in inflamed tissue.[28] There are limited numbers of publications on its use in the oral cavity.

RAMAN SPECTROSCOPY FOR SURGERY GUIDANCE

None of these techniques discussed meet all the prior stated requirements, and thus none of them is generally superior regarding its future use in the field of head and neck oncological care. As stated, in order to judge which technique should be used it is important to keep the specific future clinical application in mind.

For this thesis we decided to focus on the application in surgery guidance. The majority of head and neck carcinomas arise in the oral cavity, of which the tongue is the most common subsite.[79] Most patients with a carcinoma of the tongue will be treated with surgical excision.[80] The goal of surgery is to excise the tumor with adequate resection margins (> 5 mm distance between tumor border and resection surface).[81] The patient's prognosis is negatively affected when this goal is not accomplished. Nevertheless, to date inadequate resection margins are found in 30% – 85% of the cases.[35,82] Preoperative imaging (magnetic resonance imaging, computed tomography, etc.) combined with intraoperative tactile and visual information is apparently insufficient for guiding the surgeon to an adequate tumor resection. There are several ways to assess resection margins. The most accurate and current gold standard is the postoperative final histopathological assessment on formalin-fixed and paraffin-embedded tissue sections of the resection specimen.[83] This laborious and time-consuming procedure may take up to a couple of days, or even weeks in case of complex cases with, for instance, bone involvement. Due to wound healing and scarring an additional resection in case of an inadequate resection margin is after this time not possible anymore. Therefore, intraoperative histopathological examination of frozen tissue sections from suspicious regions, mostly sampled by the surgeon (from the wound bed), is used to achieve intraoperative feedback on the resection margin.[39,84,85] An additional resection can be taken from the wound bed in case of detected tumor residual. Although state-of-the-art, this so-called frozen section procedure has major limitations: sampling error risks, costs and the time-consuming nature.[38,85,86] Thus an intraoperative tool providing a real-time, non-invasive and objective discrimination between oral cavity

squamous cell carcinoma (OCSCC) and surrounding non-tumorous tissue could help to increase the number of adequate resections and thereby improve the prognosis.
In this thesis we have explored whether Raman spectroscopy is a potential candidate to fulfill this need, because the technique requires no tissue preparation or use of dyes, does not suffer from subjective result interpretation, and requires no learning curve. It also has a favorable spatial resolution and penetration depth, and can be used *in vivo* as well as *ex vivo*.[2-7] Of all the techniques discussed only ESS also meets these requirements.[20] Raman results are a quantitative representation of the molecular composition of the measurement volume. This enables tissue characterization based on biochemical composition rather than on changes in cellular and subcellular size and density, as is the case in ESS.[20] Due to these properties we have focused in this thesis on Raman spectroscopy.

FINDINGS OF THIS THESIS

The main goal of this thesis was to provide a solid foundation for further development of Raman spectroscopic applications in head and neck oncology. This was a multistep process in which we aimed to investigate and thoroughly understand those Raman spectroscopic features that distinguish tongue OCSCC from its surrounding non-tumorous tissue.
The tongue is comprised of different tissue structures (i.e. surface squamous epithelium, connective tissue, muscle, adipose tissue, gland and nerve).[40] In most published Raman studies large measurement volumes are used that contain multiple tissue structures.[6,7,87,88] These structures differ in their molecular composition and consequently have their own characteristic Raman features. Although other authors describe clear spectral differences between tumor and normal tissue, the cause of these differences remains unknown, because histopathological confirmation of the tissue samples examined was often omitted. Our first step was the development of a method to answer these questions. With *in vitro* Raman mapping experiments performed on thin tissue sections, detailed spectral information could be clearly correlated to histopathology.[89]
This method provided clear insight into the spectral characteristics and variance of OCSCC and the individual non-tumorous tissue structures. An accurate distinction (93% – 100%) was possible between OCSCC and individual subepithelial tissue structures.[90] Furthermore, as might be expected by similarities in biochemical composition, the spectroscopic features of OCSCC and surface squamous epithelium were partly overlapping, resulting in a lower discriminatory power of 75%. More specifically, the structures that were most often misclassified as OCSCC were dysplastic epithelium, basal layers of epithelium, inflammation- and capillary-rich connective tissue (CT), and connective and glandular tissue close to OCSCC.[90]
This knowledge was used for the development of a 'tumor' or 'non-tumorous tissue' classification model. A two-step tissue classification model was based on principal components analysis (PCA) followed by hierarchical linear discriminant analysis (hLDA). In the first step the spectra of adipose tissue and nerve were distinguished from all the other spectra. In the second step the spectra of surface squamous epithelium, CT, muscle and gland were distinguished from the spectra of OCSCC. The validated results

showed an accuracy of 91%, a sensitivity of 100% and a specificity of 78%.[91] The suboptimal specificity was mainly due to misclassifications of the surface squamous epithelium spectra.[91] Therefore, it is important to underline the clinical problem. In 30 – 85% of the cases the tumor is excised with inadequate resection margins (< 5 mm distance between tumor border and resection surface).[35] Woolgar et al. found that 87% of the resection specimens with involved margins showed the involvement of a deeper soft tissue margin.[92] This implies that the mucosal margin is not often a clinical problem, and that the imperfect discrimination of surface squamous epithelium and OCSCC by our current Raman spectroscopic classification model should not hamper its future clinical use.

A Raman spectrum of a tissue contains spectroscopic contributions of all molecules present.[93] We investigated these contributions of all tissue structures individually. Pure-compound reference spectra were used that represented the main components of the tongue; proteins, lipids, nucleic acids, amino acids and carbohydrates. A non-negative least-squares fitting procedure found the best combination of these pure-compound reference spectra in order to approximate the representative/characteristic tissue spectra. The fit-results showed that only a small percentage of the characteristic tissue spectra remained unexplained (< 4,82%). Next, all individual annotated Raman spectra per tissue structure were fitted with a selected fit-library. In this way the molecular composition per tissue structure was determined, splitted in an average and standard deviation per chemical class. The carbohydrate, protein and amino acid content were the most important factors to discriminate between tumor and non-tumorous tissue. The combination of these chemical classes were used in a 'tumor' versus 'non-tumorous' tissue classification model. The validated results showed a sensitivity of 100% and a specificity of 93%.

Previous studies concluded that the discrimination between OCSCC and normal tissue was found in predominant protein and nucleic acids features in OCSCC spectra and predominant lipid features in the Raman fingerprints of normal tissue.[87,88,94] However, by analyzing the non-tumorous tissue structures individually, we showed that whether the spectral contributions of proteins and lipids were higher or lower than OCSCC depended on the analyzed normal tissue structure. In contrast to previous studies we now know that CT-rich and muscle-rich normal tissue contains more proteins and less lipids compared to OCSCC. Being aware of this is crucial for an accurate interpretion of Raman results obtained from large measurement volumes.

Only the mean content of nucleic acids was consistently higher in OCSCC, compared to all individual non-tumorous tissue structures. However, the absolute content of nucleic acids was insufficient to be used as a tumor-detection determinant due to a small percentage contribution and a high variance within OCSCC and non-tumorous tissue spectra.

There is a great deal of literature in which the tumor-detection potential of Raman spectroscopy is demonstrated. However, we were the first to answer the question 'what is measured?' sufficiently that the strengths and pitfalls of Raman spectroscopy could be defined. We concluded that: [1] accurate correlation with histopathology is essential for identifying the precise source of the signals needed to interpret the Raman results, [2] it is quite challenging to discriminate surface squamous epithelium from OCSCC, [3] spectroscopic fingerprints can be used to develop highly accurate classification models, [4] decomposing these fingerprints provides more knowledge about them but does not necessarily add to

the discriminative power, and [5] the composition of the measurement volume defines the discriminative features. This knowledge is needed for further technological development, in order to integrate Raman spectroscopy into daily head and neck oncological care.

FUTURE PERSPECTIVES

What are the steps that need to be taken to bring Raman spectroscopy to the head and neck oncological clinics? In 1992 Littenberg published an interesting paradigm for the evaluation of new medical technologies.[95] In this hierarchical assessment scheme he simplifies the process of examining and reporting the properties of medical technologies into a biological plausibility, level I, in which the technology's proposed mode of action is compared with current biological information and theory. At level II, technical feasibility, it is determined whether the technology meets its own performance specifications and can be delivered to the target population. In the case of a diagnostic test, level III, intermediate outcomes, assesses the sensitivity and specificity in a relevant population. The overall medical, psychological and financial impacts of the technology upon the patient, including unintended side effects and long-term morbidity and mortality is investigated in level IV, patient outcomes. Finally, the costs of the technology to society in terms of resource use, ethical issues and social and political hazards are measured in level V, societal outcomes. A technology's success at one level does not guarantee success at another level.[95] The results described in this thesis provide a fundamental basis that contribute to level I, biological plausibility. The methodology that we have developed for tongue can be used as a blueprint for other anatomical regions, and likewise for other types of malignant neoplasms in the head and neck regions. We conclude that the spectral variance found within one tissue structure was not due to sample or patient characteristics.[89] Nevertheless, many interesting fundamental questions remain unanswered. For instance, whether there are discriminative spectral differences between healthy contralateral tissue and healthy-looking tissue adjacent to the tumor, and whether spectral differences exist between tumors or healthy tissue structures at different oral cavity subsites. All subsites have their own architectures of tissue structures, their own thicknesses and degrees of keratinization[40] and therefore their own specific optical signatures. If not taken into account, this may affect the diagnostic accuracy.

Level II, the technical feasibility of Raman spectroscopic measurements to detect tumor in frozen tissue sections, has also been demonstrated in this thesis. However, the measurements are currently too slow to be of any value in daily clinical practice. Future technical improvements could speed up measurement time by, for instance, massive parallel measurements (> 100 points simultaneously). Another possibility is to skip and/or minimize non-informative regions, to limit spectral resolution or to use a larger step size. Research is needed to determine the ideal conditions. The solution to the speed problem might otherwise be found in combinations with other optical techniques. The pioneering work of Notingher et al. shows that auto-fluorescence can be used to determine which regions need a more specified evaluation with Raman spectroscopy.[96] A multimodal approach has the ability to exploit the strengths of several techniques.

Other fundamental research questions may be answered using the methodology developed in this thesis, e.g. whether there are specific spectroscopic features that discriminate metastatic from non-metastatic

tumors. In patients with no clinical evidence of lymph nodal metastasis (N0), there is a percentage of occult metastasis.[97] Whenever it can be reliably predicted which tumors metastasize, this can change the recommended therapy. Furthermore, if it is known which specific cell populations are responsible for invasive behavior and metastasis, then Raman spectroscopy might be helpful in their detection. Subsequently, molecular based targeted-therapy could be performed.
The results of this thesis cannot directly be translated into requirements for *in vivo* applications using a fiber optic probe. The results can be used to make a first estimate to define the ideal measurement volume of a probe and to get a first estimate on the limit of detection, i.e. how many tumor cells need to be in the target volume to be able to recognize them as tumor? However, the answer will be different for detection of tumor in frozen tissue sections compared to the *in vivo* assessment of large measurement volumes. Recent results on freshly excised resection tissue show that the differences between tumor and surrounding healthy tissue may be much larger when measured *in vivo* due to differences in water concentration that are not visible in frozen tissue sections.[2]

In conclusion, this thesis provides a solid foundation for further development of Raman spectroscopic applications in head and neck oncology. Nevertheless, it will take several more years before patients with an OCSCC can experience the benefits of Raman spectroscopy.

REFERENCES

1. Hecht. *Optics*. 4th ed. (2002)
2. Barroso, Smits, et al. (2015) *Discrimination between oral cancer and healthy tissue based on water content determined by Raman spectroscopy.* Analytical Chemistry. 87(4):2419-2426.
3. Carvalho, Bonnier, et al. (2015) *Raman micro-spectroscopy for rapid screening of oral squamous cell carcinoma.* Experimental and Molecular Pathology. 98(3):502-509.
4. Deshmukh, Singh, et al. (2011) *Raman spectroscopy of normal oral buccal mucosa tissues: Study on intact and incised biopsies.* Journal of Biomedical Optics. 16(12):127004-127010.
5. Guze, Pawluk, et al. (2014) *Pilot study: Raman spectroscopy in differentiating premalignant and malignant oral lesions from normal mucosa and benign lesions in humans.* Head & Neck. 37(4):511-517.
6. Krishna, Majumder, et al. (2014) *In vivo Raman spectroscopy for detection of oral neoplasia: A pilot clinical study. Journal of Biophotonics.* 7(9):690-702.
7. Sahu, Deshmukh, et al. (2012) *Raman spectroscopy of oral buccal mucosa: A study on age-related physiological changes and tobacco-related pathological changes.* Technology in Cancer Research and Treatment. 11(6):529-541.
8. Shin, Vigneswaran, et al. (2010) *Advances in fluorescence imaging techniques to detect oral cancer and its precursors.* Future Oncology. 6(7):1143-1154.
9. Keereweer, Sterenborg, et al. (2012) *Image-guided surgery in head and neck cancer: Current practice and future directions of optical imaging.* Head & Neck. 34(1):120-126.
10. Keereweer, Van Driel, et al. (2013) *Optical image-guided cancer surgery: Challenges and limitations.* Clinical Cancer Research. 19(14):3745-3754.
11. Francisco, Correr, et al. (2014) *Analysis of surgical margins in oral cancer using in situ fluorescence spectroscopy.* Oral Oncology. 50(6):593-599.
12. Tirelli, Piovesana, et al. (2015) *Narrow band imaging in the intra-operative definition of resection margins in oral cavity and oropharyngeal cancer.* Oral Oncology. 51(10):908-913.
13. Vu, Farah. (2016) *Narrow band imaging: Clinical applications in oral and oropharyngeal cancer.* Oral Diseases. 22(5):383-390.
14. Wilder-Smith, Jung, et al. (2004) *In vivo optical coherence tomography for the diagnosis of oral malignancy.* Lasers in Surgery and Medicine. 35(4):269-275.
15. Hamdoon, Jerjes, et al. (2013) *Optical coherence tomography in the assessment of suspicious oral lesions: An immediate ex vivo study.* Photodiagnosis and Photodynamic Therapy. 10(1):17-27.
16. Abbaci, Breuskin, et al. (2014) *Confocal laser endomicroscopy for non-invasive head and neck cancer imaging: A comprehensive review.* Oral Oncology. 50(8):711-716.
17. Anuthama, Sherlin, et al. (2010) *Characterization of different tissue changes in normal, betel chewers, potentially malignant lesions, conditions and oral squamous cell carcinoma using reflectance confocal microscopy: Correlation with routine histopathology.* Oral Oncology. 46(4):232-248.
18. Lucchese, Gentile, et al. (2016) *The potential role of in vivo reflectance confocal microscopy for evaluating oral cavity lesions: A systematic review.* Journal of Oral Pathology and Medicine. 45(10):723-729.
19. Muldoon, Roblyer, et al. (2012) *Noninvasive imaging of oral neoplasia with a high-resolution fiber-optic microendoscope.* Head & Neck. 34(3):305-312.
20. Sharwani, Jerjes, et al. (2006) *Assessment of oral premalignancy using elastic scattering spectroscopy.* Oral Oncology. 42(4):343-349.
21. Davies, Connolly, et al. (2015) *Point of care optical diagnostic technologies for the detection of oral and oropharyngeal squamous cell carcinoma.* Surgeon. 13(6):321-329.
22. Green, Cobb, et al. (2014) *Optical diagnostic techniques for use in lesions of the head and neck: Review of the latest developments.* British Journal of Oral and Maxillofacial Surgery. 52(8):675-680.
23. Jerjes, Upile, et al. (2011) *The future of medical diagnostics: Review paper.* Head & Neck Oncology. 3(38):1-8.
24. Liu, Zhao, et al. (2016) *Non-invasive techniques for detection and diagnosis of oral potentially malignant disorders.* Tohoku Journal of Experimental Medicine. 238(2):165-177.
25. Omar. (2015) *Current concepts and future of noninvasive procedures for diagnosing oral squamous cell carcinoma – a systemic review.* Head & Face Medicine. 11(6):1-27.

26. Singh, Ibrahim, et al. (2016) *Recent advances in optical diagnosis of oral cancers: Review and future perspectives.* Head & Neck. 38(1):1-9.
27. Swinson, Jerjes, et al. (2006) *Optical techniques in diagnosis of head and neck malignancy.* Oral Oncology. 42(3):221-228.
28. Upile, Jerjes, et al. (2009) *Head and neck optical diagnostics: Vision of the future of surgery.* Head & Neck Oncology. 1(25):1-9.
29. RIVM. *Bevolkingsonderzoek.* http://www.rivm.nl/Onderwerpen/B/Bevolkingsonderzoeken_en_screeningen [accessed 2017].
30. Warnakulasuriya. (2009) *Causes of oral cancer – an appraisal of controversies.* British Dental Journal. 207(10):471-475.
31. Gasparoto, De Oliveira, et al. (2012) *Inflammatory events during murine squamous cell carcinoma development.* Journal of Inflammation. 9(1):1-11.
32. Pindborg. *Histological typing of cancer and precancer of the oral mucosa.* 2nd ed. (1997)
33. Slaughter, Southwick, et al. (1953) *Field cancerization in oral stratified squamous epithelium; clinical implications of multicentric origin.* Cancer. 6(5):963-968.
34. Rosai. *Surgical pathology* 10th ed. (2011)
35. Smits, Koljenovic, et al. (2015) *Resection margins in oral cancer surgery: Room for improvement.* Head & Neck. 38(1):E2197-2203.
36. Amit, Na'ara, et al. (2016) *Improving the rate of negative margins after surgery for oral cavity squamous cell carcinoma: A prospective randomized controlled study.* Head & Neck. 38(1):E1803-1809.
37. Maxwell, Thompson, et al. (2015) *Early oral tongue squamous cell carcinoma: Sampling of margins from tumor bed and worse local control.* JAMA Otolaryngology Head Neck Surgery. 141(12):1104-1110.
38. Varvares, Poti, et al. (2015) *Surgical margins and primary site resection in achieving local control in oral cancer resections.* Laryngoscope. 125(10):2298-2307.
39. Dinardo, Lin, et al. (2000) *Accuracy, utility, and cost of frozen section margins in head and neck cancer surgery.* Laryngoscope. 110(10):1773-1776.
40. Mills. Histology for pathologists. 3rd ed. (2004)
41. Valentine, Scott, et al. (1985) *A histological analysis of the early effects of alcohol and tobacco usage on human lingual epithelium.* Journal of Oral Pathology. 14(8):654-665.
42. Raman. (1928) *A new type of secondary radiation.* Nature. 121(501-502):365.
43. Hanlon, Manoharan, et al. (2000) *Prospects for in vivo Raman spectroscopy.* Physics in Medicine and Biology. 45(2):R1-59.
44. Mason. *Fluorescent and luminescent probes for biological activity.* 2nd ed. (1999)
45. Guze, Short, et al. (2009) *Parameters defining the potential applicability of Raman spectroscopy as a diagnostic tool for oral disease.* Journal of Biomedical Optics. 14(1):161-169.
46. Boyle. (1970) *Charge coupled semiconductor devices.* Bell systems technical journal. 49(4):587-593.
47. Krafft, Popp. (2015) *The many facets of Raman spectroscopy for biomedical analysis.* Analytical and Bioanalytical Chemistry. 407(3):699-717.
48. Farah, Dalley, et al. (2016) *Improved surgical margin definition by narrow band imaging for resection of oral squamous cell carcinoma: A prospective gene expression profiling study.* Head & Neck. 38(6):832-839.
49. *Chapter 3 absorption, emission, reflection and scattering.* [accessed 2016].
50. Roblyer, Kurachi, et al. (2009) *Objective detection and delineation of oral neoplasia using autofluorescence imaging.* Cancer Prevention Research. 2(5):423-431.
51. Sawan, Mashlah. (2015) *Evaluation of premalignant and malignant lesions by fluorescent light (velscope).* Journal of International Society of Preventive and Community Dentistry. 5(3):248-254.
52. Utzinger, Richards-Kortum. (2001) *Fiber optic probes for biomedical optical spectroscopy.* Journal of Biomedical Optics. 8(1):121-147.
53. Pavlova, Weber, et al. (2009) *Fluorescence spectroscopy of oral tissue: Monte carlo modeling with site-specific tissue properties.* Journal of Biomedical Optics. 14(1):1-16.
54. Huber. (2009) *Assessment of the velscope as an adjunctive examination tool.* Texas Dental Journal. 126(6):528-535.
55. Zhao, Wu, et al. (2013) *Intraoperative fluorescence-guided resection of high-grade malignant gliomas using 5-aminolevulinic acid-induced porphyrins: A systematic review and meta-analysis of prospective studies.* PLoS One. 8(5):1-10.
56. Thong, Olivo, et al. (2009) *Clinical application of fluorescence endoscopic imaging using hypericin for the diagnosis of human oral cavity lesions.* British Journal of Cancer. 101(9):1580-1584.

57. Contaldo, Poh, et al. (2013) *Oral mucosa optical biopsy by a novel handheld fluorescent confocal microscope specifically developed: Technologic improvements and future prospects.* Oral and Maxillofacial Pathology. 116(6):752-758.

58. Tan, Herd, et al. (2012) *The role of narrow band imaging in early detection of head and neck cancer.* British Journal of Oral and Maxillofacial Surgery. 50(2):132-136.

59. Piazza, Cocco, et al. (2010) *Narrow band imaging and high definition television in evaluation of oral and oropharyngeal squamous cell cancer: A prospective study.* Oral Oncology. 46(4):307-310.

60. Sekine, Yakushiji, et al. (2015) *A study on the intrapapillary capillary loop detected by narrow band imaging system in early oral squamous cell carcinoma.* Journal of Oral and Maxillofacial Surgery, Medicine and Pathology. 27(5):624-630.

61. Kumamoto, Sentani, et al. (2012) *Clinicopathological features of minute pharyngeal lesions diagnosed by narrow-band imaging endoscopy and biopsy.* World Journal of Gastroenterology. 18(44):6468-6474.

62. Takano, Yakushiji, et al. (2010) D*etecting early oral cancer: Narrowband imaging system observation of the oral mucosa microvasculature.* International Journal of Oral and Maxillofacial Surgery. 39(3):208-213.

63. Yang, Lee, et al. (2014) *Use of endoscopy with narrow-band imaging system in detecting squamous cell carcinoma in oral chronic non-healing ulcers.* Clinical Oral Investigations. 18(3):949-959.

64. Ugumori, Muto, et al. (2009) *Prospective study of early detection of pharyngeal superficial carcinoma with the narrowband imaging laryngoscope.* Head & Neck. 31(2):189-194.

65. Vicini, Montevecchi, et al. (2015) *A novel approach emphasising intra-operative superficial margin enhancement of head-neck tumours with narrow-band imaging in transoral robotic surgery.* Acta Otorhinolaryngologica Italica. 35(3):157-161.

66. Huang, Swanson, et al. (1991) *Optical coherence tomography.* Science. 254(5035):1178-1181.

67. Fercher, Hitzenberger, et al. (1993) *In vivo optical coherence tomography.* Americal Journal of Ophthalmology. 116(1):113-114.

68. Wojtkowski, Srinivasan, et al. (2004) *Ultrahigh-resolution, high-speed, fourier domain optical coherence tomography and methods for dispersion compensation.* Optics Express. 12(11):2404-2422.

69. Olivo, Bhuvaneswari, et al. (2011) *Advances in bio-optical imaging for the diagnosis of early oral cancer.* Pharmaceutics. 3(3):354-378.

70. Bouma, Tearney. (2002) *Clinical imaging with optical coherence tomography.* Academic Radiology. 9(8):942-953.

71. Wilder-Smith, Holtzman, et al. (2010) *Optical diagnostics in the oral cavity: An overview.* Oral Diseases. 16(8):717-728.

72. Pande, Shrestha, et al. (2014) *Automated classification of optical coherence tomography images for the diagnosis of oral malignancy in the hamster cheek pouch.* Journal of Biomedical Optics. 19(8):60221-602210.

73. 73. Volgger, Stepp, et al. (2013) *Evaluation of optical coherence tomography to discriminate lesions of the upper aerodigestive tract.* Head & Neck. 35(11):1558-1566.

74. Nwaneshiudu, Kuschal, et al. (2012) *Introduction to confocal microscopy.* Journal of Investigative Dermatology. 132(12):1-5.

75. Maher, Collgros, et al. (2016) *In vivo confocal microscopy for the oral cavity: Current state of the field and future potential.* Oral Oncology. 54(3):28-35.

76. Szeto, Wehrli, et al. (2011) *Contact endoscopy as a novel technique in the detection and diagnosis of mucosal lesions in the head and neck: A brief review.* Journal of Oncology. 2011(11):1-6.

77. Bigio, Mourant. (1997) *Ultraviolet and visible spectroscopies for tissue diagnostics: Fluorescence spectroscopy and elastic-scattering spectroscopy.* Physical Medical Biology. 42(5):803-814.

78. Turhan, Yaprak, et al. (2016) *Intraoperative assessment of laryngeal malignancy using elastic light single-scattering spectroscopy: A pilot study.* Laryngoscope. -(8):1-5.

79. WHO. *Mortality database.* http://apps.who.int/healthinfo/statistics/mortality/whodpms/ [accessed 2016].

80. Shah, Gil. (2009) *Current concepts in management of oral cancer--surgery.* Oral Oncology. 45(0):394-401.

81. National Comprehensive Cancer Network (NCCN). *Head and neck cancers.* https://www.nccn.org/professionals/physician_gls/f_guidelines.asp.

82. Dillon, Brown, et al. (2015) *How does the close surgical margin impact recurrence and survival when treating oral squamous cell carcinoma?* Journal of Oral and Maxillofacial Surgery. 73(6):1182-1188.

83. Helliwell. (2013) *Standards and datasets for reporting cancers.*

84. Pathak, Nason, et al. (2009) *Impact of use of frozen section assessment of operative margins on survival in oral cancer.* Oral Surgery, Oral Medicine, Oral Pathology, Oral Radiology and Endodontology. 107(2):235-239.

85. Priya, D'cruz, et al. (2012) *Cut margins and disease control in oral cancers.* Journal of Cancer Research and Therapeutics. 8(1):74-79.

86. Ribeiro, Godden, et al. (2003) *Do frozen sections help achieve adequate surgical margins in the resection of oral carcinoma?* International Journal of Oral and Maxillofacial Surgery. 32(2):152-158.

87. Malini, Venkatakrishna, et al. (2006) *Discrimination of normal, inflammatory, premalignant, and malignant oral tissue: A Raman spectroscopy study.* Biopolymers. 81(3):179-193.

88. Venkatakrishna. (2001) *Optical pathology of oral tissue: A Raman spectroscopy diagnostic method*. Current science. 80(5):665-670.

89. Cals, Bakker Schut, et al. (2013) *Method development: Raman spectroscopy-based histopathology of oral mucosa.* Journal of Raman Spectroscopy. 44(7):963-972.

90. Cals, Bakker Schut, et al. (2015) *Investigation of the potential of Raman spectroscopy for oral cancer detection in surgical margins*. Laboratory Investigation. 95(10):1186-1196.

91. Cals, Koljenovic, et al. (2016) *Development and validation of Raman spectroscopic classification models to discriminate tongue squamous cell carcinoma from non-tumorous tissue*. Oral Oncology. 60(9):41-47.

92. Woolgar, Triantafyllou. (2005) *A histopathological appraisal of surgical margins in oral and oropharyngeal cancer resection specimens.* Oral Oncology. 41(10):1034-1043.

93. Koningstein. *Introduction to the theory of the Raman effect.* 1st ed. (1972)

94. Knipfer, Motz, et al. (2015) *Raman difference spectroscopy: A non-invasive method for identification of oral squamous cell carcinoma: Publisher's note.* Biomedical Optics Express. 6(7):3252-3265.

95. Littenberg. (1992) *Technology assessment in medicine. Academic Medicine.* 67(7):424-428.

96. Kong, Rowlands, et al. (2013) *Diagnosis of tumors during tissue-conserving surgery with integrated autofluorescence and Raman scattering microscopy.* Proceedings of the National Academy of Sciences. 110(38):15189-15194.

97. Van Den Brekel, Stel, et al. (1991) *Lymph node staging in patients with clinically negative neck examinations by ultrasound and ultrasound-guided aspiration cytology.* American Journal of Surgery. 162(4):362-366.

8

Summary & Samenvatting

Summary

Cancer has become a major public health problem as it is now the leading cause of death. In the Netherlands, annually nearly 1000 new patients are diagnosed with cancer of the oral cavity. The majority (90%) originate from the epithelial surface and show squamous cell differentiation. Those oral cavity squamous cell carcinomas (OCSCC) are a source of concern because of the high disease-related mortality: only half of the patients diagnosed with OCSCC will survive the five years following diagnosis.

The majority of patients with an OCSCC will be treated with surgical excision. The ultimate goal of surgery is to excise the tumor with adequate microscopic resection margins (> 5 mm distance between tumor border and resection surface). The prognosis of the patient is negatively affected when this goal is not accomplished. Nevertheless, to date this happens in 30% – 85% of the cases. Preoperative imaging (computer tomography, magnetic resonance imaging, etc.) combined with intraoperative tactile and visual information is apparently insufficient to guide the surgeon to an adequate resection. Biopsy samples can be taken during surgery to evaluate whether suspicious resection margins are tumor free. Although state of art, this so-called frozen tissue section procedure has major limitations, such as sampling error, costs and the time-consuming nature of the procedure.

Thus, an intraoperative tool that provides real-time and objective evaluation of the resection margins would increase the number of adequate resections and thereby improve patient's prognosis. In this thesis we explored whether Raman spectroscopy is a potential candidate to fulfill this need.

Raman spectroscopy is an optical technique named after the Indian scientist, Chandrasekhara Venkata Raman, who discovered in 1928 a new phenomenon of inelastic scattering of light by molecules. A Raman spectrum contains characteristic peaks that are assigned to corresponding molecular structures within the illuminated tissue. Thus, this technique enables nondestructive and objective tissue characterization based on molecular information. Compared to other optical imaging techniques, Raman spectroscopy does not need pretreatment or labeling of the tissue to provide real-time results with sufficient penetration depth (up to 1 mm) and a high spatial resolution.

The tongue, which is the most common subsite of OCSCC, is comprised of different tissue structures (i.e. surface squamous epithelium, connective tissue, muscle, adipose tissue, gland and nerve). These tissue structures differ in their molecular composition and consequently have their own characteristic Raman spectrum. A thorough understanding of the Raman spectroscopic features that distinguish OCSCC from its surrounding non-tumorous tissue structures is needed to provide a solid foundation for further development of a Raman-spectroscopic diagnostic tool.

In **Chapter 2** a standardized method was developed to collect and analyze the Raman spectroscopic features of OCSCC and individual non-tumorous tissue structures in the tongue. *In vitro* Raman mapping experiments performed on tissue sections supplied detailed spectral information that could be correlated to histopathology. The method provided clear insight into the spectral characteristics and variance of OCSCC and the individual non-tumorous tissue structures.

In **Chapter 3** we investigated whether the spectroscopic differences could be used to discriminate between OCSCC and individual non-tumorous tissue structures. A highly accurate distinction (93% – 100%) was

possible between OCSCC and individual subepithelial tissue structures. Furthermore, as might be expected by similarities in biochemical composition, the spectroscopic features of OCSCC and surface squamous epithelium were partly overlapping, resulting in a lower discriminatory power of 75%.

With this knowledge we proved in **Chapter 4** the potential of Raman spectroscopy in classifying unknown Raman tissue spectra obtained from tissue sections. Two tissue classification models were developed using principal components analysis (PCA) followed by (hierarchical) linear discriminant analysis ((h) LDA). The models were validated by means of an independent set of spectra. In our first PCA-LDA model, the spectra of the validation set were classified as either 'tumor' or 'normal' (non-tumorous tissue structures) with an accuracy of 86%, a sensitivity of 100% and a specificity of 66%. The results improved by the use of a two-step PCA-hLDA tissue classification model, showing an accuracy of 91%, a sensitivity of 100% and a specificity of 78%. In the first step of the PCA-hLDA the spectra of adipose tissue and nerve were distinguished from all the other spectra. In the second step the spectra of surface squamous epithelium, CT, muscle and gland were distinguished from the spectra of OCSCC.

The suboptimal specificity was mainly due to misclassifications of the surface squamous epithelium spectra. Therefore, it is important to underline the clinical problem. In 30 – 85% of the cases, the tumor is excised with inadequate resection margins (< 5 mm distance between tumor border and resection surface). The majority (87%) of these tumor-positive margins are located in the depth, in other words in the subepithelial, deeper soft tissue. This implies that the mucosal margin is not often a clinical problem, and that the imperfect discrimination of surface squamous epithelium and OCSCC by our current Raman spectroscopic classification model should not hamper its future clinical use.

A Raman spectrum of a tissue contains spectroscopic contributions of all molecules present. By detailed analysis of these spectroscopic contributions, the molecular composition of a tissue structure can be quantified. In **Chapter 5** we analyzed the Raman spectra of OCSCC and individual healthy tissue structures in terms of the information they contain about the tissue's molecular composition. This was done by using a non-negative least-squares fitting procedure, which finds the best combination of pure-compound reference spectra in order to approximate a representative/characteristic tissue spectrum. **Chapter 6** gives an overview of the 55 pure-compound reference spectra that were used. These reference spectra represented the main components of tongue; proteins, lipids, nucleic acids, amino acids and carbohydrates. The fit-results showed that only a small percentages of the characteristic tissue spectra remained unexplained (< 4,82%).

By analyzing the non-tumorous tissue structures individually, we showed that whether the spectral contributions of proteins and lipids were higher or lower than OCSCC depended on the analyzed normal tissue structure. In contrast to previous studies we now know that CT-rich and muscle-rich normal tissue contains more proteins and less lipids compared to OCSCC. Only the mean content of nucleic acids was consistently higher in OCSCC, compared to all individual non-tumorous tissue structures. However, the absolute content of nucleic acids was insufficient to be used as a tumor-detection determinant due to a small percentage contribution and a high variance within OCSCC and non-tumorous tissue spectra. The carbohydrate, protein and amino acid content were the most important factors to discriminate between tumor and non-tumorous tissue. The combination of these chemical classes were used in a 'tumor' versus

'healthy tissue' classification model. The validated results showed a sensitivity of 100% and a specificity of 93%.
In most clinical applications of Raman spectroscopy, fiber-optic probes are used with measurement volumes that contain multiple tissue structures. Simulations mimicking the sampling of larger measurement volumes demonstrated that the Raman results and the tumor-detection power of the technique are dependent on the presence and exact proportion of the tissue structures in the volume. Being aware of this is crucial for an accurate interpretion of Raman results obtained from large measurement volumes.

To conclude, this thesis provided a thorough understanding of the Raman spectroscopic features that distinguish OCSCC from the individual non-tumorous tissue structures in the tongue. The strengths and limitations of Raman spectroscopy regarding its discriminative potential were elucidated. Raman spectroscopy turned out to be a perfect candidate for OCSCC detection in the tongue. The technique can add value in multiple clinical settings, as discussed in **Chapter 7**. With our work we aimed to help (head and neck) surgeons, pathologists and spectroscopists to understand and adopt the added value of this objective technique in their (future) clinical practice.

Samenvatting

Sinds enkele jaren is kanker wereldwijd doodsoorzaak nummer 1. In Nederland horen jaarlijks bijna 1000 patiënten dat ze een vorm van kanker in de mondholte hebben. Het merendeel (> 90%) van deze tumoren ontstaat in het slijmvlies, ofwel plaveiselepitheel, en worden daarom mondholte plaveiselcel carcinomen (MHPCC) genoemd. MHPCC hebben een slechte prognose; slechts de helft van de patiënten overleeft de eerste 5 jaar nadat de diagnose is gesteld.

De meeste patiënten met een MHPCC worden geopereerd. Het doel van de operatie is om de tumor volledig te verwijderen met adequate microscopische marges (> 5 mm afstand tussen de snijranden en de rand van de tumor). De prognose van de patiënt wordt negatief beïnvloedt indien dit doel niet wordt behaald. Helaas is dit momenteel het geval in 30 – 85% van de operaties. Beeldvorming, zoals magnetic resonance imaging (MRI) of computed tomography, die voor de operatie wordt verricht, wordt tijdens de operatie gecombineerd met de tactiele en visuele informatie van de chirurg. Desondanks zet de chirurg de snee vaak niet op de goede plek. Door vriescoupes te nemen tijdens de operatie, kan een chirurg extra informatie krijgen over de snijranden die verdacht zijn voor tumor residu. Deze procedure heeft echter grote nadelen, zoals hoge kosten en een lange analysetijd waardoor het onmogelijk is om alle snijranden te onderzoeken.

Een hulpmiddel, dat tijdens de operatie direct informatie kan verschaffen over de snijranden, kan het aantal adequate marges vergroten en daarmee de prognose van de patiënten verbeteren. Tijdens deze promotie werd onderzocht of Raman spectroscopie die extra informatie zou kunnen verschaffen.

Raman spectroscopie is een optische techniek die vernoemd is naar een Indische wetenschapper, Chandrasekhara Venkata Raman, die in 1928 een nieuwe vorm van lichtverstrooiing door moleculen heeft ontdekt en daar zijn naam aan heeft verbonden. Een Raman spectrum is een afspiegeling van de moleculen die aanwezig zijn in het weefsel dat wordt belicht. Aan de hand van de pieken in een spectrum is het dus mogelijk om, op een niet invasieve manier, de moleculaire samenstelling van weefsel objectief te analyseren. In vergelijking met andere optische technieken vereist Raman spectroscopie geen voorbehandeling van het weefsel, heeft het voldoende penetratiediepte (tot 1 mm) en een hoge ruimtelijke resolutie.

Tong is de meest voorkomende locatie van een MHPCC en bestaat uit verschillende weefselstructuren (zoals oppervlakte slijmvlies, bindweefsel, spier, vet, speekselklier en zenuw). Deze weefselstructuren verschillen in moleculaire samenstelling en hebben dus hun eigen karakteristieke Raman spectrum. Om een goede basis te leggen voor de toekomstige ontwikkeling van een Raman spectroscopisch hulpmiddel is het noodzakelijk de Raman signalen, die MHPCC onderscheiden van de individuele gezonde weefselstructuren, volledig te begrijpen.

In **hoofdstuk 2** hebben we een gestandaardiseerde methode ontwikkeld om de spectrale informatie van MHPCC en van de individuele gezonde weefselstructuren te verzamelen en te analyseren. *In vitro* metingen op vriescoupes verschaften gedetailleerde spectrale informatie die kon worden gecorreleerd met de histopathologische beoordeling. Deze methode gaf inzicht in de spectrale karakteristieken en variatie van MHPCC en van de individuele gezonde weefselstructuren.

In **hoofdstuk 3** werd onderzocht of de spectrale verschillen konden worden gebruikt om onderscheid te maken tussen MHPCC en de individuele gezonde weefselstructuren. Het bleek mogelijk om met een hoge betrouwbaarheid (93% – 100%) MHPCC te differentiëren van de individuele subepitheliale (onder het oppervlakte slijmvlies gelegen) gezonde weefselstructuren. Zoals kon worden verwacht door de overeenkomsten in moleculaire samenstelling (en dus in spectrale karakteristieken), was het onderscheid tussen MHPCC en het oppervlakte slijmvlies moeilijker. Dit resulteerde in een iets lagere betrouwbaarheid van 75%.

Deze kennis hebben we gebruikt in **hoofdstuk 4** om te bewijzen dat Raman spectroscopie onbekende spectra correct kan classificeren als 'tumor' of 'normaal'. Er werden twee classificatiemodellen ontwikkeld, gebaseerd op een principale-componenten analyse (PCA) gevolgd door een (hiërarchische) lineaire discriminantanalyse ((h)LDA). De modellen werden gevalideerd op een onafhankelijke set van spectra. Met het eerste PCA-LDA classificatiemodel was het mogelijk om de spectra van de validatie set te classificeren als 'tumor' of als 'normaal' met een betrouwbaarheid van 86%, een sensitiviteit van 100% en een specificiteit van 66%. Door in het tweede PCA-hLDA model gebruik te maken van twee opeenvolgende stappen verbeterden de resultaten naar een betrouwbaarheid van 91%, een sensitiviteit van 100% en een specificiteit van 78%.

De suboptimale specificiteit werd voornamelijk veroorzaakt door misclassificaties van het oppervlakte slijmvlies. Hierbij is het van belang om de resultaten te zien in het licht van het klinische probleem. In 30 – 85% van de gevallen wordt de tumor verwijderd met niet-adequate marges (< 5 mm afstand tussen de snijranden en de rand van de tumor). Het merendeel (87%) van deze niet-adequate marges wordt gevonden in de diepte, met andere woorden te midden van de subepitheliale, diepe weefselstructuren. Dit impliceert dat de niet-perfecte differentiatie tussen MHPCC en het oppervlakte slijmvlies het gebruik van onze classificatiemodellen in de kliniek niet in de weg staat.

Een Raman spectrum bevat signaalbijdragen van alle aanwezige moleculen in het belichte weefsel. Door die signaalbijdragen te analyseren is een kwantitatieve uitspraak mogelijk over de moleculaire samenstelling van het weefsel. In **hoofdstuk 5** hebben we de verschillen in moleculaire samenstelling van MHPCC en de individuele gezonde weefselstructuren onderzocht. Hiervoor hebben we gebruik gemaakt van een zogenoemde niet-negatieve least-squares fit procedure die de beste combinatie van referentie spectra zoekt om de representatieve/karakteristieke Raman spectra van MHPCC en van de individuele gezonde weefselstructuren te benaderen. In **hoofdstuk 6** staat het volledig overzicht van de 55 referentie spectra die we hiervoor hebben gebruikt. De referentie spectra zijn een representatie van de belangrijkste bouwstoffen van tong; eiwitten, vetten, nucleotiden, aminozuren en koolhydraten. Met het fitten bleven slechts kleine percentages van de karakteristieke Raman spectra onverklaard (< 4,82%). De hoeveelheid koolhydraten, eiwitten en aminozuren bleken het belangrijkste in het onderscheid tussen tumor en normaal. De combinatie van deze drie werd gebruikt voor de ontwikkeling van een 'tumor' versus 'normaal' classificatie model. De gevalideerde resultaten laten een sensitiviteit van 100% en specificiteit van 93% zien.

Er werden diverse verschillen gevonden tussen de moleculaire samenstelling van MHPCC en van de individuele gezonde weefselstructuren. Het was afhankelijk van de onderzochte gezonde weefselstructuur of de spectrale bijdrage van eiwitten, vetten, aminozuren en koolhydraten hoger of lager was dan die van

MHPCC. Alleen de hoeveelheid nucleotiden was altijd hoger in MHPCC in vergelijking met de gezonde weefselstructuren. Helaas bleek de absolute hoeveelheid nucleotiden, ten gevolge van een grote variatie in MHPCC en gezonde weefsel-spectra, onvoldoende om te gebruiken als tumor-detecterende factor.
Voor de klinische toepassing van Raman spectroscopie worden meestal fiber-optische instrumenten gebruikt met een meetvolume dat meerdere weefselstructuren kan bevatten. Simulaties van grotere meetvolumes werden gebruikt om te demonstreren dat de precieze locatie en samenstelling van het onderzochte meetvolume het Raman signaal en het vermogen van de techniek tot tumor-detectie kan beïnvloeden. Voor een betrouwbare interpretatie van Raman signalen die zijn verkregen van grotere meetvolumes, is het cruciaal om hiervan bewust te zijn.

Ter conclusie, deze promotie verschaft gedetailleerde informatie over de Raman signalen die MHPCC onderscheiden van de individuele gezonde weefselstructuren in tong. De krachten en de beperkingen van Raman spectroscopie werden opgehelderd. Raman spectroscopie kan de extra informatie verschaffen die nodig is om tumor te detecteren in de tong. Hiermee kan de techniek waarde toevoegen in diverse klinische situaties, zoals beschreven in **hoofdstuk 7**. Met ons werk hopen we dat (hoofdhals) chirurgen, pathologen en spectroscopisten de toegevoegde waarde van deze optische techniek in hun toekomstige klinische praktijk zien en begrijpen.

9

Addendum

Affiliations of Co-authors

***Erasmus MC* Cancer Institute, University Medical Center Rotterdam, The Netherlands**
Department of Otorhinolaryngology and Head and Neck Surgery
Robert J. Baatenburg de Jong
José A. Hardillo

Center for Optical Diagnostics and Therapy, Department of Dermatology
Gerwin J. Puppels
Tom C. Bakker Schut
Peter Caspers

Department of Pathology
Senada Koljenović

Abbreviations

5-ALA	5-aminolevulinic acid
AUC	area under the ROC curve
CARS	coherent anti-Stokes Raman scattering
CCD	charge coupled device
ccfc	chemical class fit contributions
CM	confocal microscopy
CRM	confocal reflectance microscopy
CT	connective tissue
EMR	electromagnetic radiation
EMSC-SIS	extended multiplicative signal correction – spectral interference subtraction
EMT	epithelial – mesenchymal transition
ESS	elastic scattering spectroscopy
FADH	flavin adenine dinucleotide
HCA	hierarchical cluster analysis
H&E	haematoxylin and eosin
hLDA	hierarchical linear discriminant analysis
HNSCC	head and neck squamous cell carcinoma
HWVN	high wavenumber
IPCL	intra-papillary capillary loops
KCA	K-means cluster analysis
LDA	linear discriminant analysis
LOPO	leave-one-patient-out
LSCM	laser scanning confocal microscopy
MEC	Medical Ethics Committee
MHPCC	mondholte plaveiselcel carcinoom
MRI	magnetic resonance imaging
NADH	nicotinamide adenine dinucleotide
NBI	narrow band imaging
NIR	near infrared
nn-lsq	non-negative least-squares
n.o.s.	not otherwise specified
OCSCC	oral cavity squamous cell carcinoma
OCT	optical coherence tomography
PCA	principal component analysis
PCs	principal components
ROC	receiver operator characteristic
SCC	squamous cell carcinoma
SERS	surface-enhanced Raman scattering

PhD Portfolio

Name PhD student: F.L.J. Cals
Erasmus MC Cancer Institute, University Medical Center Rotterdam
Department of Otorhinolaryngology and Head and Neck Surgery
Center of Optical Diagnostics and Therapy
PhD period: 2010 – 2017

PHD TRAINING	YEAR
General academic skills	
Endnote and PubMed	2010
Biomedical English Writing and Communication	2011
Masterclass English: Business English	2011
Basic course on Regulations and Organization for Clinical Investigators (BROK)	2012
Basic surgical exam	2014
Reregistration BROK	2016
Other ENT-related courses	
Head and neck anatomy (dissection)	2010, 2012, 2014, 2016
Desiderius school (teamwork, communication, health law, evidence-based medicine, teach the teacher)	2014 – 2015
Ins and outs of nose surgery	2014
Boerhaave: Surgical anatomy of the head and neck region	2014
ENT residency program	
Course on endoscopy and laryngology	2014
Course on nasal surgery	2014
Course on mouth pathology	2015
Course on functional endoscopic sinus surgery	2016
Course on radiology	2016
Course on ear surgery	2017
Other thesis-related courses	
CPO: methodology of clinical trials and preparation of grant applications	2010
NvvO: Introduction in clinical and fundamental oncology	2012
MOLMED: Basic and translational oncology	2012

	YEAR
Other courses	
Automatic external defibrillator	2008
Course on electrocardiogram	2009
MOLMED: Imaging techniques for doctors	2009
Course on Basic Life Support	2010
Extinguish small fire extinguishers	2011
Firefighting and evacuation	2015
Course on Advanced Life Support	2016
Presentations	
TERMIS, Galway (oral and poster)	2010
2nd NWHHT young researcher's day, Groningen (oral)	2011
219th scientific meeting of Dutch society for ENT, Nieuwegein (oral)	2011
5th ECHNO, Poznan (oral)	2012
8th AHNS, Toronto (oral)	2012
223th scientific meeting of Dutch society for ENT, Maastricht (poster)	2014
5th IFHNOS, New York (poster)	2014
SPEC, Krakow (oral and poster)	2014
225th scientific meeting of Dutch society for ENT, Nieuwegein (oral)	2014
9th AHNS, Seattle (oral, presented by R.W.H. Smits)	2016
NWHHT, Utrecht (oral)	2016
230th scientific meeting of Dutch society for ENT, Nieuwegein (oral)	2017
(Inter) national conferences	
Scientific meeting of Dutch society for ENT 2x/year	2009 – 2017
9th congress European Skull Base Society (observer)	2009
6th AHNS Arlington (observer)	2010
5th WIN Paris (observer)	2013
EPIC Bio photonics workshop (observer)	2014
Other activities	
Tissue bank	2009 – 2013
Organization of SEOHS	2010

TEACHING ACTIVITIES	YEAR
Lecturing	
Traumatic ENT for residents emergency medicine	2009 – 2010
Oncology and airway in ENT for operation assistants	2010 – 2014
Vertigo for medicine students	2012
Supervision	
Supervisor of graduation research of Valerie de Water	2013

List of Publications

Froukje L. J. Cals, Janine Goumans, C.M. Zwaan and Johannes A. Borgstein. (2010) Een asymmetrische snel progressieve tonsillaire tumor bij een kind van zes jaar. Nederlands Tijdschrift voor Keel-Neus-oorheelkunde. 16(3): 139-143

Froukje L. J. Cals, Catherina A. hellingman, Wendy Koevoet, Robert J. Baatenburg de Jong and Gerjo J.V.M. van Osch. (2012) *Effects of transforming growth factor-β subtypes on in vitro cartilage production and mineralization of human bone marrow stromal-derives mesenchymal stem cells*. Journal of Tissue Engineering and Regenerative Medicibe. 6: 68-76

Froukje L. J. Cals, Tom C. Bakker Schut, Senada Koljenović, Gerwin J. Puppels and Robert J. Baatenburg de Jong. (2013) *Method development: Raman spectroscopy-based histopathology of oral mucosa*. Journal of Raman Spectroscopy. 44: 693-972

Froukje L. J. Cals, Tom C. Bakker Schut, José A. Hardillo, Robert J. Baatenburg de Jong, Senada Koljenović and Gerwin J. Puppels. (2015) *Investigation of the potential of Raman spectroscopy for oral cancer detection in surgical margins.* Laboratory Investigation. 95: 1186-96

Froukje L. J. Cals, Senada Koljenović, José A. Hardillo, Robert J. Baatenburg de Jong, Tom C. Bakker Schut, Gerwin J. Puppels. (2016) *Development and validation of Raman spectroscopic classification models to discriminate tongue squamous cell carcinoma from non-tumorous tissue.* Oral Oncology. 690: 41-47

Froukje L. J. Cals, Tom C. Bakker Schut, Peter Caspers, Robert J. Baatenburg de Jong, Senada Koljenović, Gerwin J. Puppels. *Raman spectroscopic analysis of the molecular composition of oral cavity squamous cell carcinoma and healthy tongue tissue structures.* To be submitted.

About the Author

Froukje Leontine Joris Cals is geboren op 20 september 1984 te Merselo als dochter van Carolien van Rhijn en Pieter Cals. Samen met haar oudere zus en twee jongere broers groeide zij op in Blerick en doorliep zij de jenaplan basisschool de Omnibus te Baarlo. In haar vrije tijd was zij met de Zeeverkenners veel op het water te vinden en werd vastelaovend elk jaar uitbundig gevierd. In 2002 behaalde zij haar vwo-diploma aan college Den Hulster te Venlo. In datzelfde jaar verliet zij, op 17-jarige leeftijd, het immer gezellige Limburg om Geneeskunde te gaan studeren aan de Erasmus Universiteit te Rotterdam. Ook al was zij ver van huis, door haar altijd positieve blik en aanstekelijke lach werden al snel vele mooie vriendschappen gemaakt. Gedurende haar studie was zij actief lid van de studentenvereniging S.S.R.-Rotterdam waarvoor zij onder andere de Eurekaweek heeft georganiseerd. Daarnaast werkte ze als medisch student op de kraamafdeling van het Sophia kinderziekenhuis en later als triage assistent op de Centrale Huisartsen Posten Rijnmond. Op zoek naar avontuur reisde Froukje, voor aanvang van haar coschappen, 6 maanden door Centraal Amerika, waar zij vrijwilligerswerk verrichtte en kennis maakte met de lokale geneeskunde.

Na een keuzecoschap op de intensive care van het Reinier de Graaf Gasthuis te Delft en op de afdeling hoofdhals oncologie van het Daniel den Hoed Kliniek te Rotterdam, startte zij haar afstudeeronderzoek naar tissue engineering van kraakbeen. Dit werd bekroond met haar eerste publicatie. Froukje studeerde in 2009 cum laude af. Enthousiast geraakt door de KNO, mocht zij, direct na haar oudste coschap, starten als arts-assistent op de afdeling KNO-heelkunde in het Erasmus MC. In de zoektocht naar het juiste promotietraject werd door haar energieke inzet onder andere de weefselbank nieuw leven ingeblazen. In 2010 is zij gestart met haar promotieonderzoek wat leidde tot dit prachtige proefschrift. In 2013 startte Froukje met de opleiding tot KNO-arts onder leiding van prof. R. J. Baatenburg de Jong, dr. R. M.L. Poublon en dr. R.M. Metselaar. Haar perifere stages volgde zij met veel plezier in het HAGA ziekenhuis te Den Haag onder supervisie van dr. H.M. Blom en dr. J.P. Koopman en in het Amphia ziekenhuis te Breda onder supervisie van dr. G.K.A. van Wermeskerken en drs. A.J.M. van der Rijt.

Froukje woont samen met haar verloofde Michiel Droog in Rotterdam en zij verwachten in augustus hun eerste kindje. Wij zijn ontzettend trots op onze energieke, lieve en vrolijke vriendin en wij weten zeker dat Froukje het vandaag, op deze speciale dag, en ook in de toekomst fantastisch zal doen!

Florence en Viola